Transport in isotropic and anisotropic Dirac systems

Zur Erlangung des akademischen Grades einer

DOKTORIN DER NATURWISSENSCHAFTEN (Dr. rer. nat.)

von der KIT-Fakultät für Physik des
Karlsruher Instituts für Technologie (KIT)

genehmigte

DISSERTATION

von

Julia Monika Link, M. Sc.
aus Heidelberg

Tag der mündlichen Prüfung: 01.12.2017
Referent: Prof. Dr. Jörg Schmalian
Korreferent: PD. Dr. Boris Narozhny

I thank the *Carl-Zeiss Stiftung* for financial support during two and a half years of my PhD.

Introduction

inde fluunt lacrimae, stillataque sole rigescunt
de ramis electra *novis, quae lucidus amnis*
excipit et nuribus mittit gestanda Latinis.

Their tears still flow, and hardened by the sun,
fall as amber *from the virgin branches,*
to be taken by the bright river and sent onwards to adorn Roman brides.

—Ovid, Metamorphoses Book II, 364-366

These are the last words of a tragic story. Phaethon, son of the sun god Phoebus, requests to drive his fathers chariot, the sun, over the sky. However, he looses control over the horses and comes too close to earth. In order to save the oceans, rivers, and earth from the fate of being burned by the sun, Jupiter throws a lightning onto Phaethon. Phaethon falls from the sky and dies on the riverside of Eridanus, which is nowadays known as the river Po. His sisters, the Heliads, grieve at his grave for four months without ever leaving it. Then a god takes pity on the sisters and turns the grieving virgins into poplar trees and their tears into amber which falls into the river and is sent onwards to Roman brides.

The reader may now wonder how this mythological tale is connected to ***Transport in isotropic and anisotropic Dirac systems***. It is a story which explains how amber, in Latin electrum and in Greek $\eta\lambda\epsilon\tau\rho o\nu$, comes to exist. This material fascinated many generations, since, besides its beautiful color, it exhibits a mysterious force which attracts dust and paper. This attractive force was already observed by the Roman philosopher Pliny the Elder and is a phenomenon that could not be explained or understood for a long time. In 1600, the English physician and physicist William Gilbert was the first to distinguish between different attractive forces and named this strange attractive force of amber electrium and firstly introduced the term electric force. The physical reason for this attractive force is that amber has a very high relative permittivity and thus becomes electrostatically charged upon applying friction. Hence, amber –or *electrum*– gave its name to a whole field of physics: electrostatics, electrodynamics and quantum electrodynamics.

Now, let us return to the quotation we started with. The tears of the grieving virgins are turned into amber, *electra*, and the *electra* fall into the river and are transported in and by the river to the Roman brides. Just like the amber is transported in the river, we study the transport of electrons in condensed matter systems in this thesis: we investigate the *electrical conductivity* σ and the *viscosity* η of two dimensional (2D) isotropic and anisotropic Dirac systems. These two transport quantities play an important role in the transport theory of electrons (or rather quasiparticles) in condensed matter systems. In the following, we describe these quantities in detail and motivate why they are interesting to study.

The nature of the transport described by the electrical conductivity and by the viscosity is different: The electrical conductivity describes the movement of electrons due to an electric field, while the viscosity of a system describes the resistance of the quasiparticles to an applied gradient of the drift velocity. These two transport quantities are very important for the characterization of materials. Using the conductivity as a criterion, we can categorize different materials into different classes such as insulator, semi-conductor, and metal. Since the viscosity of a fluid describes the resistance to a hydrodynamic flow, the smaller the viscosity becomes, the more turbulent the flow dynamics of the system is. Hence, the size of the viscosity significantly determines the flow dynamics of the system.

In this thesis, these transport quantities are studied in two different regimes: the *hydrodynamic regime* ($\omega \ll \tau^{-1}$) and the *collisionless regime* ($\omega \gg \tau^{-1}$). Very different processes are responsible for the transport of the electrons in the two regimes and as a consequence, we will also find different behavior of the transport properties in the different regimes. In the hydrodynamic regime where the characteristic scattering time τ between collisions is the fastest time scale, the physics is dominated by scattering processes, whereas in the collisionless regime the excitation frequency ω sets the fastest time scale and scattering processes are less dominant. In order to study the two regimes, the kinetic Boltzmann equation is employed in the hydrodynamic regime, and the Kubo formalism in the collisionless regime. Of course, the Kubo formalism works in both regimes, in the hydrodynamic regime using the Boltzmann equation is only easier.

But why do we study the electrical conductivity and the viscosity in the two regimes for *isotropic and anisotropic Dirac systems*? What is so special about Dirac systems? To answer these questions, we refer to the energy-dispersion of these systems. The energy-dispersion relation of Dirac systems is linear and gapless which makes these systems quasi-relativistic. They are *quasi*-relativistic, since the electrons move with the Fermi velocity v_F and not the speed of light c, where v_F is in the case of graphene 300 times smaller than c. The relativistic, gapless energy spectrum results in a distinct behavior of the transport properties which is very different from conventional metal.

The most famous example for a 2D isotropic Dirac system is *graphene* whose transport properties are investigated in this thesis. Graphene is a beautiful material with many fascinating characteristics. On the one hand, it is the thinnest material in the world, since it only consists of one layer of carbon atoms ordered in a honey-comb structure. On the other hand, graphene is one of the strongest materials (even stronger than steal) and simultaneously it is very flexible. Its relativistic behavior is for example reflected in a universal behavior of the conductivity in the optical regime [1], as can be seen in this thesis. In addition, graphene has several symmetries such as the $\mathcal{C}_3$ rotational symmetry, time reversal symmetry and invariance under spatial inversion.

In this thesis, we also want to address the question what happens to the transport properties in systems with lower symmetry. The *anisotropic Dirac systems* (ADSs) are such systems, since they are not rotationally invariant. These systems are formed by the merging of two Dirac cones. One example of such an anisotropic Dirac system (ADS) is the organic charge transfer salt α-(BEDT-TTF)$_2$I$_3$ where two Dirac cones merge under the application of uniaxial pressure. Another example is the heterostructure TiO$_2$/VO$_2$ which has even four anisotropic Dirac cones in the first Brillouin zone. The resulting energy dispersion of an ADS is parabolic in the direction of the merging Dirac cones and linear in the perpendicular one. The anisotropy in the energy spectrum leads to fascinating transport properties which we demonstrate in Chap. 8 and Chap. 9. We find classical and relativistic behavior in the same material.

A common theme in every chapter of this thesis is the question how the *Coulomb interaction* between the electrons influences the transport properties. The Coulomb potential $V(\boldsymbol{r}, \boldsymbol{r}') = e^2/|\boldsymbol{r} - \boldsymbol{r}'|$ is a long-range interaction which is not screened for graphene at the charge neutrality point, since at this point the charge carrier density vanishes. It was a long standing question whether the influence of the Coulomb interaction in graphene is large or not, since many phenomena such as Klein tunneling [2] and the odd-integer quantum hall effect [3] can be explained without taking the Coulomb interaction into account. However, with cleaner samples, evidence for the influence of the Coulomb interaction was seen, including as the fractional quantum hall effect [4, 5] and the logarithmic divergence of the Fermi velocity [6]. There has also been a long dispute over the influence of the Coulomb interaction on the optical conductivity in graphene [7–17], and we finally settle this dispute in this thesis. Furthermore, we demonstrate that in the collisionless regime, the viscosity is a transport property which is strongly influenced by the Coulomb interaction. But we will not only study the influence of the Coulomb interaction in graphene. The effect of the Coulomb potential on the transport properties of the ADSs is investigated as well and we determine how the Coulomb interaction modifies temperature and frequency dependence of the viscosity and conductivity in both regimes.

Structure of the thesis

This thesis is divided into three parts. In the introductory **Part I**, the different regimes, the applied methods and the studied transport properties are introduced and defined. In **Part II**, the essentials of *graphene* are introduced and the electrical conductivity and the shear viscosity of graphene are studied in the two different regimes. **Part III** is devoted to systems with lower symmetry, the *anisotropic Dirac systems*, where the electrical conductivity and the viscosity in both the hydrodynamic and the collisionless regime are studied.

A graphical guide through this thesis can be found in Fig. 1, where the sections indicated in gray recapitulate results obtained by other authors, whereas the sections marked in black refer to my own work. Let me now give a detailed overview of the content of the different chapters.

In **Chap. 1**, the *hydrodynamic* and the *collisionless regime* are introduced. The ratio between the excitation frequency ω and the relaxation rate τ due to collision processes decides which regime is applicable. Depending on the regime, the transport properties are either determined using the Kubo formalism in the collisionless regime or using the Boltzmann equation in the hydrodynamic regime. These different methods are introduced and defined here.

In **Chap. 2**, the *electrical conductivity* is defined, its scaling behavior under a renormalization group (RG) analysis is studied, and we demonstrate how the conductivity is determined using either the Kubo formalism or the Boltzmann equation.

In **Chap. 3**, the concept of the *viscosity* of a fluid is introduced. We summarize how the energy-stress tensor, and thus the viscosity, is connected to the strain generators acting on spatial coordinates. Moreover, we extend the concept of strain generators acting on spatial coordinates to strain generators acting on the pseudospin space and show how the energy-stress tensor for a lattice with a pseudospin is calculated. Furthermore, we show how the viscosity is determined either in the Kubo formalism or in the Boltzmann equation and study how the viscosity scales under an RG flow with the help of the Ward identity. At last, we introduce the famous lower bound of the ratio viscosity over entropy $\eta/s \geq \hbar/(4\pi k_{\mathrm{B}})$ [18] and give a physical interpretation of this lower bound, which gives a limit to the validity of the quasiparticle picture of the system. We also discuss some examples from cosmology and ultra cold atoms which violate the lower bound.

In **Part II**, we focus on graphene. To this end, we introduce the tight-binding description and the Dirac model of *graphene* in **Chap. 4**. Furthermore, we show how the Coulomb interaction acting on the quasiparticles of graphene is implemented via the Wilson RG scheme in this chapter.

After having laid the foundations, the *electrical conductivity of graphene* is studied in **Chap. 5**. For the sake of completeness, the results of the conductivity in the hydrodynamic regime obtained by Fritz *et al.* [19] are discussed in Sec. 5.1, before we study the *optical conductivity* in the remainder of this chapter. In particular, we focus on the question how the Coulomb interaction influences the optical conductivity and settle a long dispute about the correction coefficient in first order of the Coulomb interaction by performing a tight-binding calculation and correcting previous approaches in the Dirac model. These results are based on my work in collaboration with Peter P. Orth, Daniel E. Sheehy and Jörg Schmalian which is published in Ref. 16.

In **Chap. 6**, the *viscosity of graphene* is studied. We recapitulate the results of Müller *et al.* [20] of the viscosity in the hydrodynamic regime. They showed that the quasiparticles of graphene behave as a nearly perfect fluid, i. e., the ratio of viscosity over entropy approaches very closely the lower bound. In addition we present the derivation of the Navier-Stokes equation by Briskot *et al.* [21]. Our contribution to the investigation of the viscosity is the study of the viscosity in the collisionless regime. We show that the viscosity is proportional to the frequency squared and that the Coulomb interaction has a large influence on this transport quantity.

In **Part III**, we study how these transport quantities change for a system with a lower symmetry, namely the anisotropic Dirac systems (ADSs). Hence, in **Chap. 7**, different physical systems are introduced having such an anisotropic energy dispersion where the energy spectrum is parabolic along one axis and linear in the perpendicular one. Furthermore, the Coulomb interaction is implemented by an RG analysis in the large-N limit and in the strong coupling regime, and the collision integral describing the Coulomb interaction in the Boltzmann equation for an ADS is derived.

In **Chap. 8**, building on the theoretical background obtained in the previous chapter, we are able to determine the *conductivity* in the hydrodynamic and in the collisionless regime and demonstrate that the material has the temperature dependence of an insulator in one direction and the temperature dependence of a metal in the perpendicular direction.

In **Chap. 9**, the *viscosity tensor* of ADSs is investigated in both regimes. We demonstrate that these ADSs are, to our knowledge, the first condensed matter realization which violate the lower bound of viscosity over entropy which implies highly turbulent flow behavior of the system.

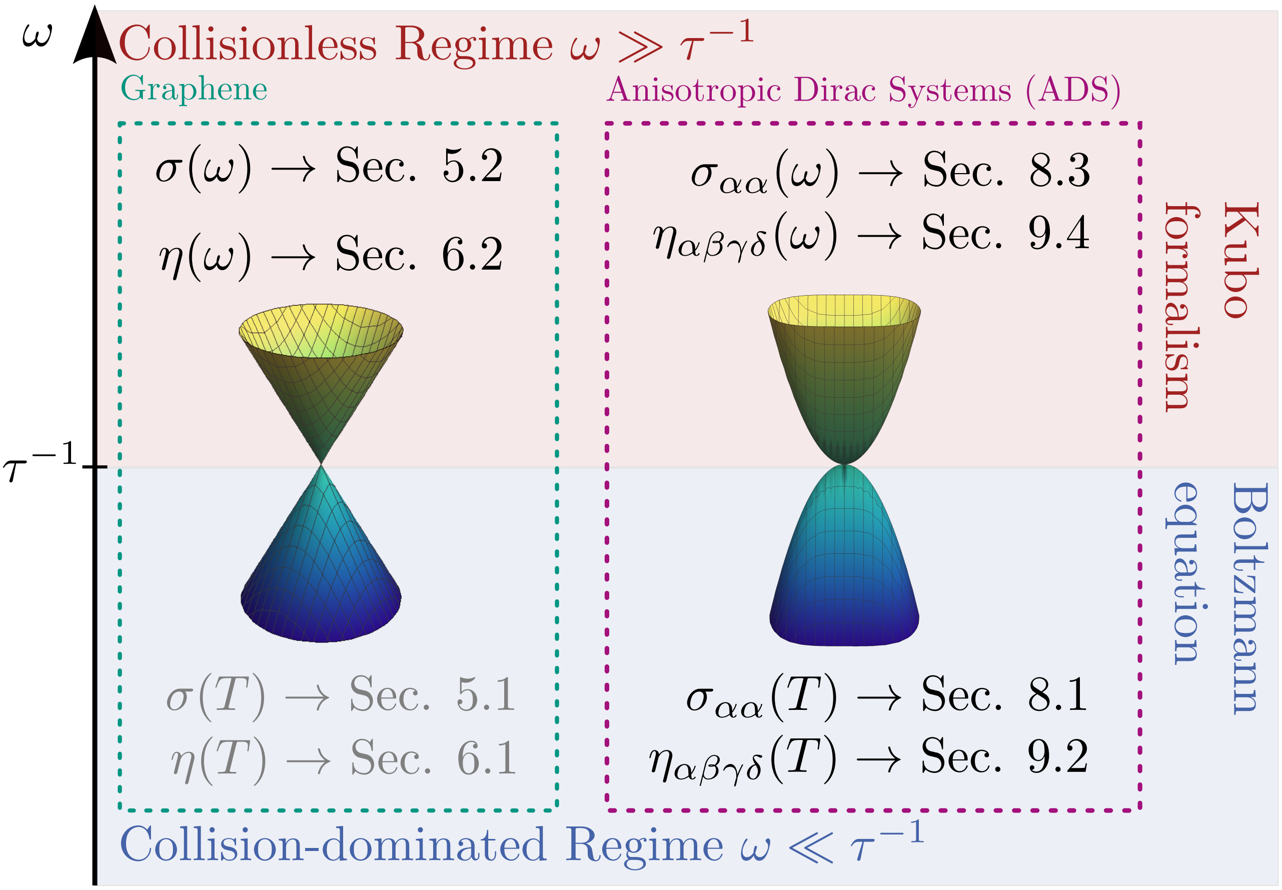

Figure 1: Overview of this thesis. In this thesis, we determine the conductivity σ and the viscosity η of graphene and ADSs as a function of frequency and temperature. Both materials are studied at the charge neutrality point, i. e., their chemical potential μ is zero. The red area indicates the collisionless regime where the Kubo formalism is used, while the blue area indicates the hydrodynamic regime where the transport quantities are calculated using the Boltzmann equation. The sections colored in gray represent results obtained by other authors, while the sections in black represent the results obtained by me and my collaborators.

Contents

Introduction v

I Regimes, Methods and Transport Properties 1

1 Regimes and Methods 3
- 1.1 Collisionless Regime . . . 3
  - 1.1.1 Kubo-Formalism . . . 4
- 1.2 Hydrodynamic Regime . . . 6
  - 1.2.1 Quantum Boltzmann equation . . . 7

2 Conductivity 11
- 2.1 Definition of the Conductivity . . . 11
- 2.2 Kubo-Formalism for the conductivity . . . 12
- 2.3 Scaling behavior of the conductivity . . . 13
- 2.4 Ansatz for Quantum Boltzmann equation . . . 14

3 Viscosity in lattices with pseudospin 17
- 3.1 Definition of the viscosity . . . 17
- 3.2 The strain generator and the energy stress tensor . . . 19
- 3.3 Kubo-Formalism for the viscosity . . . 22
- 3.4 Scaling behavior of the viscosity . . . 23
- 3.5 Ansatz for out-off equilibrium function in the Boltzmann equation . . . 24
- 3.6 The Lower Bound . . . 26
  - 3.6.1 Derivation of the lower bound . . . 26
  - 3.6.2 Violation of the lower bound . . . 28
- 3.7 Summary . . . 29

II Graphene 31

4 Field theoretical description and the Coulomb interaction 33
- 4.1 The tight-binding description . . . 34
- 4.2 The Dirac model . . . 37
- 4.3 Coulomb interaction in Graphene . . . 39
  - 4.3.1 The role of Coulomb interaction in Graphene . . . 39
  - 4.3.2 Wilson RG in Graphene . . . 40

5 The conductivity in graphene 45
- 5.1 ... in the hydrodynamic regime 46
- 5.2 Transmissivity and optical conductivity 48
  - 5.2.1 The light transmissivity of graphene 49
  - 5.2.2 The debate in the literature 50
- 5.3 The tight-binding approach to the optical conductivity 53
  - 5.3.1 The Coulomb interaction Hamiltonian 54
  - 5.3.2 Optical conductivity 57
- 5.4 Field theoretical approach in the Dirac limit 64
  - 5.4.1 Continuum renormalization group and modified minimal subtraction $\overline{\text{MS}}$ scheme 64
  - 5.4.2 Wilson momentum-shell RG combined with dimensional regularization 67
- 5.5 Summary 71

6 The viscosity in Graphene 73
- 6.1 ...in the hydrodynamic regime 74
  - 6.1.1 Navier-Stokes 75
- 6.2 The viscosity in the collisionless regime 76
  - 6.2.1 The viscosity of non-interacting free Dirac fermions in the optical regime 77
  - 6.2.2 The correction coefficient of the viscosity in the optical regime 78
  - 6.2.3 Hall viscosity 83
- 6.3 Summary 84

III Anisotropic Dirac Systems 85

7 Field-theoretical description and Coulomb interaction 87
- 7.1 The model and possible realizations 88
  - 7.1.1 Mergence of two Dirac cones 88
  - 7.1.2 The Heterostructure TiO_2/VO_2 90
  - 7.1.3 The Hamiltonian 92
- 7.2 Coulomb interaction in ADS 93
  - 7.2.1 Large N Renormalization group analysis in the strong coupling limit 93
  - 7.2.2 The collision integral in the hydrodynamic regime 97

8 The conductivity... 99
- 8.1 ...in the hydrodynamic regime 99
- 8.2 Scaling Behavior 103
- 8.3 ...in the collisionless regime 103
- 8.4 Summary 105

9 The viscosity... 107
- 9.1 The energy-stress tensor 108
- 9.2 ...in the hydrodynamic regime 109
  - 9.2.1 The lower bound 111
  - 9.2.2 Scaling of the viscosity tensor 112
- 9.3 ...in the collisionless regime 114

9.4 Navier-Stokes equation 115
9.5 Summary 118

Conclusions **121**

A Graphene **129**
A.1 Derivation of the Transmission coefficient 129
A.2 The optical conductivity of graphene 131
  A.2.1 The non-interacting part of the optical conductivity 131
  A.2.2 Correction coefficient in tight-binding description 135
  A.2.3 Correction coefficient in the Dirac model 141
A.3 Viscosity in the collisionless regime 146
  A.3.1 Non-interacting part of the viscosity 146
  A.3.2 Correction coefficient of the viscosity in the collisionless regime 147

B Anisotropic Dirac System (ADS) **159**
B.1 Derivation of the Scaling behavior of the Conductivity and the Viscosity tensor 159
  B.1.1 Derivation of the Scaling of the Conductivity 159
  B.1.2 Derivation of the Scaling of the Shear viscosity 160
B.2 The viscosity derived by the Boltzmann equation 162

Bibliography **163**

List of Figures **176**

Acronyms **177**

Danksagung **180**

Part I

Regimes, Methods and Transport Properties

1
Chapter 1

Regimes and Methods

In this thesis two transport properties, the electrical conductivity and the viscosity, of graphene and of anisotropic Dirac systems (ADSs) are investigated. Thereby, we distinguish between two different regimes. These regimes are the hydrodynamic regime where collision processes dominate and the collisionless regime. The ratio between excitation frequency ω and the characteristic time scale for the collisions τ decides in which regime we are. If $\omega \ll \tau^{-1}$, the scattering time due to thermal collisions is smaller than the time scale set by the excitation frequency. The dominant process responsible for the transport or relaxation processes are thus collisions due to scattering of thermally excited electrons and holes. However, if $\omega \gg \tau^{-1}$, the fastest time scale is set by the excitation frequency and processes due to thermally excited states can be neglected.

In the following chapter the two different regimes are introduced in detail as well as the different formalisms used which are capable of describing the relevant physics, namely the Kubo formalism and the Boltzmann equation.

1.1 Collisionless Regime

We start with a short introduction of the collisionless regime. In this regime, the excitation frequency sets the shortest time scale and scattering processes of the particles can be neglected, i. e., $\omega \gg \tau^{-1}$. This regime can be experimentally accessed by optical experiments. An example is the measurement of the optical transparency of graphene [22] which measures implicitly the optical conductivity of graphene. In this thesis, the optical conductivity of graphene and the influence of the Coulomb interaction on this transport property is studied in full detail in Chap. 5, while in Sec. 8.3 the optical conductivity of ADSs is investigated. Further, we study the viscosity of graphene and ADSs in the collisionless regime in Sec. 6.2 and in Sec. 9.3, respectively. A related experiment is angle-resolved photoemission spectroscpoy (ARPES) [23] where the band structure of quasi-freestanding graphene can be directly observed.

For a regime with high frequencies, we are going to use the Kubo-formalism in the remainder of this thesis. This does by no means mean that the Kubo-formalism can only be applied in the collisionless regime. With the Kubo-formalism, we are able to make predictions for both regimes, the hydrodynamic and the optical regime. Far more, using the Kubo-formalism, we can access the collisionless regime which could not be accessed by the Boltzmann equation which describes physics that are dominated by collisions.

1.1.1 Kubo-Formalism

In this section we derive the Kubo formalism and thereby follow closely the derivation presented in the book of Elk and Gasser [24]. Here, we study how the mean value of an observable $\hat{A}_i$ of a system with an external perturbation is calculated. The system is described by the Hamiltonian $\mathcal{H} = \mathcal{H}_0 - \mu N$, where $\mathcal{H}_0$ is the Hamiltonian of the non-interacting system, μ is the chemical potential of the system and N the particle number. Next, an external, time-dependent perturbation W_t is introduced to the system

$$W_t = -\sum_j \hat{B}_j F_j(t)\,, \tag{1.1}$$

where $F_j(t)$ is an external, classical time-dependent field and $\hat{B}_j$ a quantum-mechanical operator coupled to $F_j(t)$. In order to evaluate the average of the operator $\hat{A}_i$, we introduce the density operator ρ_t, i. e., $\left\langle \hat{A}_i \right\rangle = \mathrm{Tr}[\hat{A}_i \rho_t]$. The density operator obeys the von-Neumann equation

$$\mathrm{i}\hbar \frac{\partial \rho_t}{\partial t} = [\mathcal{H} + W_t, \rho_t]\,, \tag{1.2}$$

which is the quantum-mechanical analogue of the Liouville equation. In the following, the von-Neumann equation is solved to find the time dependence of the density operator. Firstly, in order to solve this differential equation, the initial condition has to be found. Since the perturbation W_t vanishes for $t \to -\infty$, the density operator is defined over the non-interacting system with $\mathcal{H}$ at $t = -\infty$ which yields the initial condition

$$\rho_{-\infty} = \rho = \frac{\mathrm{e}^{-\mathcal{H}/T}}{\mathrm{Tr}(\mathrm{e}^{-\mathcal{H}/T})}\,. \tag{1.3}$$

Knowing this initial condition, we can now solve the von-Neumann equation. Therefore, we go into the interaction picture[1] where

$$\rho_t(t) = \mathrm{e}^{\mathrm{i}\mathcal{H}t/\hbar} \rho_t \mathrm{e}^{-\mathrm{i}\mathcal{H}t/\hbar}\,. \tag{1.4}$$

The time derivative of this operator is given by

$$\begin{aligned} \mathrm{i}\hbar \frac{\mathrm{d}\rho_t(t)}{\mathrm{d}t} &= -[\mathcal{H}, \rho_t(t)] + \mathrm{e}^{\mathrm{i}\mathcal{H}t/\hbar}\ \mathrm{i}\hbar \frac{\partial \rho_t}{\partial t}\ \mathrm{e}^{-\mathrm{i}\mathcal{H}t/\hbar} \\ &= -[\mathcal{H}, \rho_t(t)] + \mathrm{e}^{\mathrm{i}\mathcal{H}t/\hbar}\ [\mathcal{H} + W_t, \rho_t]\ \mathrm{e}^{-\mathrm{i}\mathcal{H}t/\hbar} \end{aligned} \tag{1.5}$$

which can be rewritten as

$$\mathrm{i}\hbar \frac{\mathrm{d}\rho_t(t)}{\mathrm{d}t} = [W_t(t), \rho_t(t)] \tag{1.6}$$

with $W_t(t) \equiv \mathrm{e}^{\mathrm{i}\mathcal{H}t/\hbar}\ W_t\ \mathrm{e}^{-\mathrm{i}\mathcal{H}t/\hbar}$. Using the initial condition (1.3), we obtain the following expression

$$\rho_t(t) = \rho + \frac{1}{\mathrm{i}\hbar} \int\limits_{-\infty}^{t} \mathrm{d}t' [W_{t'}(t'), \rho_{t'}(t')] \quad \Leftrightarrow \quad \rho_t = \rho + \frac{1}{\mathrm{i}\hbar} \int\limits_{-\infty}^{t} \mathrm{d}t' \mathrm{e}^{-\mathrm{i}\mathcal{H}(t-t')/\hbar} [W_{t'}, \rho_{t'}] \mathrm{e}^{\mathrm{i}\mathcal{H}(t-t')/\hbar}\,. \tag{1.7}$$

This differential equation can be solved by iteration. For the first iteration step, we use that the system is in thermal equilibrium for $t \to -\infty$, insert $\rho_t^{(0)} = \rho$ and obtain

$$\rho_t^{(1)} = \rho + \frac{1}{\mathrm{i}\hbar} \int\limits_{-\infty}^{t} \mathrm{d}t'\ [W_{t'}(t - t'), \rho]\,. \tag{1.8}$$

---

[1] In this section, all operators with the additional time argument $\hat{O}_i(t)$ are in the interaction picture.

This solution is linear in the perturbation and for small fields one can stop the iteration process here. This solution is called linear response and it is the form which is going to be used in the remainder of this thesis.

Now we are able to calculate the mean value of the observable $\hat{A}_i$ in linear response. It is given by

$$\begin{aligned}\left\langle \hat{A}_i \right\rangle_t &= \mathrm{Tr}(\rho \hat{A}_i) + \frac{1}{\mathrm{i}\hbar} \int\limits_{-\infty}^{t} \mathrm{d}t' \, \mathrm{Tr}(\mathrm{e}^{-\mathrm{i}\mathcal{H}t/\hbar}[W_{t'}(t'), \rho]\mathrm{e}^{\mathrm{i}\mathcal{H}t/\hbar}\hat{A}_i) \\ &= \mathrm{Tr}(\rho \hat{A}_i) + \frac{1}{\mathrm{i}\hbar} \int\limits_{-\infty}^{t} \mathrm{d}t'[W_{t'}(t'), \rho]\hat{A}_i(t)) = \mathrm{Tr}(\rho \hat{A}_i) + \frac{1}{\mathrm{i}\hbar} \int\limits_{-\infty}^{t} \mathrm{d}t' \left\langle [\hat{A}_i(t), W_{t'}(t')] \right\rangle \qquad (1.9) \\ &= \mathrm{Tr}(\rho \hat{A}_i) + \frac{1}{\mathrm{i}\hbar} \int\limits_{-\infty}^{t} \mathrm{d}t' \sum_j \left\langle [\hat{A}_i(t), \hat{B}_j(t')] \right\rangle F_j(t') \, .\end{aligned}$$

The mean value of the observable $\hat{A}_i$ in the interacting system is given by the average value of the non-interacting system and a correlation function between the observable and the operator $\hat{B}_j$ coupling to the field $F_j(t)$. This can be rewritten as $\left\langle \hat{A}_i \right\rangle_t = \left\langle \hat{A}_i \right\rangle + \int\limits_{-\infty}^{\infty} \mathrm{d}t \sum_j G_{ij}(t-t')F_j(t')$ with the retarded Green's function $G_{ij}(t-t') = -\mathrm{i}\theta(t-t') \left\langle [\hat{A}_i(t), \hat{B}_j(t')] \right\rangle$. In the following, we demonstrate how this expression can also be cast into a different form. For this purpose, the Kubo-identity is applied which is given by [24]

$$\mathrm{i}[A(t), \rho] = \rho \int\limits_{0}^{\beta} d\tau \dot{A}(t - \mathrm{i}\tau) \, , \qquad (1.10)$$

where the derivative is taken with respect to the imaginary time $\mathrm{i}\tau$ and the boundary β of the integral is proportional to the inverse temperature, i. e., $\beta = (k_\mathrm{B}T)^{-1}$ with k_B being the Boltzmann constant. Hence, upon using the invariance of the trace under cyclic permutations, the retarded Green's function can be written as

$$G_{ij}(t) = -\theta(t) \int\limits_{0}^{\beta} \mathrm{d}\tau \left\langle \dot{B}_j(-t - \mathrm{i}\tau) A_i \right\rangle \, . \qquad (1.11)$$

Upon introducing the Fourier transform $G_{ij}(\omega) = \int\limits_{-\infty}^{\infty} \mathrm{d}t \mathrm{e}^{\mathrm{i}\omega_+ t} G_{ij}(t)$ with $\omega_+ = \omega + \mathrm{i}0^+$, we find for the above expression

$$G_{ij}(\omega) = -\int\limits_{0}^{\infty} \mathrm{d}t \int\limits_{0}^{\beta} \mathrm{d}\tau \mathrm{e}^{\mathrm{i}\omega_+ t} \left\langle \dot{B}_j(-t - \mathrm{i}\tau) A_i \right\rangle \, . \qquad (1.12)$$

This expression can be integrated by parts, which leads to the following expression

$$G_{ij}(\omega) = -\frac{\mathrm{i}}{\omega_+} \int_0^\infty \mathrm{d}t \int_0^\beta \mathrm{d}\tau \mathrm{e}^{\mathrm{i}\omega_+ t} \left\langle \frac{\mathrm{d}}{\mathrm{d}t} \dot{B}_j(-t - \mathrm{i}\tau) A_i \right\rangle + \frac{\mathrm{i}}{\omega_+} \mathrm{e}^{\mathrm{i}\omega_+ t} \int_0^\beta \mathrm{d}\tau \left\langle \frac{\mathrm{d}}{\mathrm{d}t} \dot{B}_j(-t - \mathrm{i}\tau) A_i \right\rangle \Bigg|_0^\infty \, , \qquad (1.13)$$

where in the boundary terms, the term arising due to the the upper boundary vanishes because of the convergence factor in ω_+. Now we apply again the Kubo-identity (1.10) and cast the Fourier transform of the retarded Green's function into the form

$$G_{ij}(\omega) = \frac{\mathrm{i}}{\omega_+}(\chi_{ij}(\omega) - \chi_{ij}^T)\,. \tag{1.14}$$

The correlation function $\chi_{ij}(\omega)$ is the Fourier transform of the retarded Green's function

$$\chi_{ij}(t,t') = -\mathrm{i}\theta(t-t')\left\langle [A_i(t), \frac{\mathrm{d}}{\mathrm{d}t'}B_j(t')]\right\rangle\,, \tag{1.15}$$

while χ_{ij}^T is the Fourier transform of

$$\chi_{ij}^T = \left\langle [A_i(0), B_j(0)]\right\rangle\,, \tag{1.16}$$

which corresponds to the isothermal susceptibility. An important implication of Eq. (1.14) occurs when the zero frequency contribution of $\chi_{ij}(\omega)$ and the value of the isothermal susceptibility are not equal, i. e.,

$$D_{ij} = \chi_{ij}(0) - \chi_{ij}^T \neq 0\,. \tag{1.17}$$

In this case the real part of the Green's function is given by

$$\operatorname{Re} G_{ij}(\omega) = \pi D_{ij}\delta(\omega) - \frac{\operatorname{Im}\chi_{ij}(\omega)}{\omega}\,, \tag{1.18}$$

where D_{ij} denotes the generalized Drude term in the response function. We are going to use this form of the retarded Green's function in order to calculate the conductivity and the shear viscosity of graphene and of ADSs in the collisionless regime.

1.2 Hydrodynamic Regime

In the hydrodynamic regime with $\omega \ll \tau^{-1}$ the shortest time scale is the relaxation time due to collisions and thus scattering processes dominate the physics. But, what exactly is Hydrodynamic? Hydrodynamic describes the dynamic of fluids governed by conservation laws. Thus, it is a powerful description which can be found in many different fields of physics.

An example for the universality of hydrodynamics is the Poiseuille flow of particles through a tube with the radius R. Using the momentum and particle conservation, we find that the current through the tube is $I = (\pi n R^4 \Delta P)/(8\eta l)$ where ΔP denotes the pressure gradient over the distance l, n the particle density and η the viscosity of the fluid, while the resistivity is $\rho = (16e^2\eta R^{-2})/n^2$ which is proportional to the viscosity. This flow behavior becomes very important for the blood circulation in our body. If an artery narrows in the radius by δR, the heart has to increase the pressure gradient by a factor of 4 in order to maintain the same blood current. Astonishingly, the Poiseuille flow is again found in a total different context, namely in solid state systems. Here, we find that the magneto-resistivity of $\mathrm{PdCoO_2}$ depends on the length of the sample [25, 26]. It decreases with increasing width of the sample, since $\rho \propto R^{-2}$. The reason for this behavior is that the friction occurs at the walls where the layers of the fluid have zero velocity. If the sample size increases, this effect decreases. In these two examples we have seen how the same hydrodynamic effect occurs in two very different, physical systems.

Hydrodynamics in condensed matter physics is a very fascinating area of research, since in this regime, it is possible to investigate the universal collision-dominated dynamics of an isolated electron fluid, while the couplings to the lattice and to impurities becomes secondary. The observation of hydrodynamic behavior only became recently experimentally accessible, because, as mentioned before, only the collisions between electrons are the dominating process which requires extreme clean samples. Different examples for the experimentally observed hydrodynamic behavior in many-body physics are as diverse as superfluid Helium [27], the breakdown of the Wiedemann-Franz law in graphene [28, 29], the negative local resistance [30, 31] and the giant magnetodrag [32] in graphene and the above mentioned length dependence of the magentoresistivity of PdCoO_2 [25] and of the (Al, Ga)As heterostructure [33]. A recent review of the hydrodynamics in graphene can be found in Ref. 34.

The main contributions for the conductivity and the shear viscosity in graphene are repeated in Sec. 5.1 and Sec. 6.1, while the new results of the conductivity and the shear viscosity of ADSs are presented in Sec. 8.1 and Sec. 9.2.

1.2.1 Quantum Boltzmann equation

Now, we introduce the method used to determine different transport properties in the hydrodynamic regime. Hydrodynamic processes are described by the Boltzmann equation. The Boltzmann equation determines the distribution function $f_{\lambda\boldsymbol{k}}$ of the quasiparticles and depends on the time t, the spatial coordinate $\boldsymbol{r}$ and the momentum $\boldsymbol{k}$. For a system with two energy bands (the valence and the conductance band) with λ denoting the band index, the Boltzmann equation has the form

$$\left(\frac{\partial}{\partial t} + \boldsymbol{v}_{\lambda\boldsymbol{k}} \cdot \nabla_{\boldsymbol{r}} + \boldsymbol{F} \cdot \nabla_{\boldsymbol{k}}\right) f_{\lambda,t,\boldsymbol{k},\boldsymbol{r}} = I^{\mathrm{coll}}[f_{\lambda\boldsymbol{k}}]\,, \tag{1.19}$$

where the left-hand side of the equation is the Liouville operator describing the time evolution of the system and the right-hand side of the equation is the collision integral which describes changes in the distribution function due to different scattering processes. These scattering processes can have their origin in scattering either due to impurities of the system or due to the Coulomb interaction between the quasiparticles. Furthermore, $\boldsymbol{F}$ is the Lorentz force acting on the electrical charged particles with $\boldsymbol{F} = e(\boldsymbol{E} + \boldsymbol{v}_{\lambda\boldsymbol{k}} \times \boldsymbol{B}/c)$, where $\boldsymbol{E}$ is the electrical field, $\boldsymbol{B}$ the magnetic field and $\boldsymbol{v}_{\lambda\boldsymbol{k}}$ is the velocity of the quasiparticle of the energy band λ. In this thesis, we focus on the electrical transport due to an applied electrical field and are not going to investigate magneto-transport.

The Boltzmann equation and the corresponding collision integral can also be derived using quantum mechanics, or more precisely the Keldysh formalism which can describe out-off equilibrium quantum mechanics. In the following, we roughly sketch the derivation and refer for further details to the corresponding literature [35, 36].

The special characteristic of the Keldysh formalism is its closed time contour which differs from the time contour used in equilibrium physics, where the initial state evolves from $t = -\infty$ to $t = +\infty$. Here, we have a system described by a time-dependent Hamiltonian $\mathcal{H}$, and we assume that the system is in a specific, known many-body state for $t = -\infty$. To calculate the mean value of an observable in the Keldysh formalism, the initial state has to be evolved forward and backwards, i. e.

$$\left\langle \hat{O} \right\rangle (t) \equiv \frac{\mathrm{Tr}[\hat{O}\rho(t)]}{\mathrm{Tr}[\rho(t)]} = \frac{1}{\mathrm{Tr}[\rho(t)]}\,\mathrm{Tr}[\hat{\mathcal{U}}_{-\infty,t}\hat{O}\hat{\mathcal{U}}_{t,-\infty}\rho]\,, \tag{1.20}$$

where $\hat{\mathcal{U}}_{t,t'} = \top \exp(-\mathrm{i}\int_t^{t'} \mathcal{H}(t'')dt'')$ is the time-ordered unitary evolution operator and $\top$ the time-order operator. The time-dependent density matrix is determined using this evolution operator and holds $\rho(t) = \hat{\mathcal{U}}_{t,-\infty}\rho(-\infty)\hat{\mathcal{U}}_{-\infty,t}$ where $\rho = \rho(-\infty)$ is the density matrix at $t = -\infty$. Why do we not have to evolve forward and backwards in time for an equilibrium system which is non-interacting at $t = -\infty$ and where the interaction is adiabatically switched on with increasing time? The reason is that in equilibrium the non-interacting ground state $|0\rangle$ can only collect a phase upon forward and backward evolving in time, i. e., $\hat{\mathcal{U}}_{-\infty,\infty}|0\rangle = \mathrm{e}^{\mathrm{i}L}|0\rangle$. This leads to the fact that it is enough to evolve forwards in time, i. e., $\langle 0|\hat{\mathcal{U}}_{-\infty,t}\hat{O}\hat{\mathcal{U}}_{t,-\infty}|0\rangle = \langle 0|\hat{\mathcal{U}}_{+\infty,t}\hat{O}\hat{\mathcal{U}}_{t,-\infty}|0\rangle \,/\, \langle 0|\hat{\mathcal{U}}_{\infty,-\infty}|0\rangle$ where the denominator describes the accumulated phase factor $\mathrm{e}^{-\mathrm{i}L}$.

After having established the needed time contour in the Keldysh formalism which describes the out-off equilibrium physics, we are now able to derive the Boltzmann equation with the corresponding collision integral. To this end, the equations of motions with the self-energy $\Sigma(1,2)$ for a Green's function $G(1,1')$ are studied. They read

$$\begin{aligned}\left(\mathrm{i}\frac{\partial}{\partial t_1} + \frac{\nabla_1^2}{2m}\right) G(1,1') &= \delta(1,1') + \int_C d2\ \Sigma(1,2)G(2,1') \\ \left(-\mathrm{i}\frac{\partial}{\partial t_1'} + \frac{\nabla_{1'}^2}{2m}\right) G(1,1') &= \delta(1,1') + \int_C d2\ G(1,2)\Sigma(2,1')\,,\end{aligned} \tag{1.21}$$

where $\int_C$ symbolizes that the integral is performed along the closed time contour and we choose the notation $1 \equiv (\boldsymbol{x}_1, t_1)$ and $\delta(1,1') = \delta(\boldsymbol{x}_1 - \boldsymbol{x}_1')\delta_{t_1,t_1'}$. The Green's function is given by

$$G(\boldsymbol{x}_1,t_1,\boldsymbol{x}_2,t_2) = \theta(t_1,t_2)G^>(\boldsymbol{x}_1,t_1,\boldsymbol{x}_2,t_2) + \theta(t_2,t_1)G^<(\boldsymbol{x}_1,t_1,\boldsymbol{x}_2,t_2)\,, \tag{1.22}$$

with $\theta(t_1,t_2)$ being defined on the time contour with $\theta(t_1,t_2) = 1$ if t_1 is later on the contour than t_2 and otherwise zero. The functions $G^>(1,2)$ and $G^<(1,2)$ are the greater and smaller Green's function and they are defined as the average of the following Heisenberg operators, i. e., $-\mathrm{i}G^<(1,2) = \left\langle \hat{\psi}_H^\dagger(2)\hat{\psi}(1)\right\rangle$ and $\mathrm{i}G^>(1,2) = \left\langle \hat{\psi}_H(1)\hat{\psi}_H^\dagger(2)\right\rangle$. Upon introducing relative coordinates in space and time, $\boldsymbol{r} = \boldsymbol{x}_1 - \boldsymbol{x}_2$, $t = t_1 - t_2$ and $\boldsymbol{R} = (\boldsymbol{x}_1 + \boldsymbol{x}_2)/2$, $T = (t_1 + t_2)/2$ and Fourier transforming in the relative coordinates, the lesser and greater Green's functions can be related to the distribution function of the quasiparticles, i. e.,

$$\begin{aligned} f_{\lambda\boldsymbol{k},\boldsymbol{R},\boldsymbol{T}} &= \int \frac{d\omega}{2\pi}(-\mathrm{i})G^<(\boldsymbol{p},\omega,\boldsymbol{R},T) \\ 1 - f_{\lambda\boldsymbol{k},\boldsymbol{R},\boldsymbol{T}} &= \int \frac{d\omega}{2\pi}\mathrm{i}G^>(\boldsymbol{p},\omega,\boldsymbol{R},T)\,.\end{aligned} \tag{1.23}$$

If we fix the time arguments in the equations of motion (1.21) at opposite sides of the contour, we obtain the Kadanoff-Baym equations for upper and lower contour. Under the assumption that the temporal and spatial changes are small and do not vary much from the free evolution of a uniform system, we obtain the Boltzmann equation upon subtracting the Kadanoff-Baym equation of upper branch of the contour and of the lower branch of the contour for the time $t_1 = t_1' = T$. Hence, the Boltzmann equation reads

$$\mathrm{i}\left(\frac{\partial}{\partial T} + \frac{\boldsymbol{p}}{m}\cdot\nabla_{\boldsymbol{R}}\right) G^<(\boldsymbol{p},\boldsymbol{R},T) = \Sigma^>(\boldsymbol{p},\omega;\boldsymbol{R},T)G^<(\boldsymbol{p};\boldsymbol{R},T) - \Sigma^<(\boldsymbol{p},\omega;\boldsymbol{R},T)G^>(\boldsymbol{p};\boldsymbol{R},T)\,, \tag{1.24}$$

where we used that the lesser Green's function is related to the distribution function. The right-hand side of this equation defines the collision integral and we are going to use this definition of the collision integral to determine the collision integral of the ADSs in Sec. 7.2.2.

After having introduced the Boltzmann equation (1.19) and having defined the collision integral (1.24) via the lesser and greater self-energies, we now briefly sketch how the Boltzmann equation is solved in order to determine the distribution function. Thereby, we choose for the distribution function the following ansatz

$$f_{\lambda\boldsymbol{k}} = f^{(0)}_{\lambda\boldsymbol{k}} + \delta f_{\lambda\boldsymbol{k}}\,. \tag{1.25}$$

The distribution function is split up into a part describing the equilibrium distribution function $f^{(0)}_{\lambda\boldsymbol{k}}$ and a part describing the out-off equilibrium correction to the distribution function $\delta f_{\lambda\boldsymbol{k}}$. The equilibrium function of the systems studied in this thesis is given by the Fermi-Dirac distribution function, i. e., $f^{(0)}_{\lambda\boldsymbol{k}} = (1+\mathrm{e}^{(\epsilon_{\lambda\boldsymbol{k}}-\mu_\lambda)/T})^{-1}$, where $\epsilon_{\lambda\boldsymbol{k}}$ is the energy dispersion relation of the system studied, λ the band index of the energy band, and μ_λ the chemical potential. For the out-off equilibrium correction, we assume that the perturbation causing the deviation of the equilibrium of the system is small and thus it is sufficient to take only the linear order in the perturbation into account. Hence, the out-off equilibrium correction is assumed to be the product of the first derivative of the equilibrium distribution and the perturbation and reads

$$\delta f_{\lambda\boldsymbol{k}} = \frac{1}{T} f^{(0)}_{\lambda\boldsymbol{k}}(1-f^{(0)}_{\lambda\boldsymbol{k}}) h_{\lambda\boldsymbol{k}}\,, \tag{1.26}$$

where the function $h_{\lambda\boldsymbol{k}}$ is proportional to the external field perturbing the equilibrium times an unknown function $g_{\lambda\boldsymbol{k}}$. Upon solving the Boltzmann equation, $g_{\lambda\boldsymbol{k}}$ and thus $\delta f_{\lambda\boldsymbol{k}}$ are determined. It is important to know the out-off equilibrium distribution function, since different transport quantities such as the electrical current, $\boldsymbol{j} = \sum_\lambda \int_{\boldsymbol{k}} \boldsymbol{v}_{\lambda\boldsymbol{k}} \delta f_{\lambda\boldsymbol{k}}$, and the energy-stress tensor, $\tau_{\alpha\beta} = \sum_\lambda \int_{\boldsymbol{k}} v^\alpha_{\lambda\boldsymbol{k}} k_\beta \delta f_{\lambda\boldsymbol{k}}$, depend on $\delta f_{\lambda\boldsymbol{k}}$. These quantities will play a crucial role in the remainder of this thesis.

Chapter 2

2 Conductivity

2.1 Definition of the Conductivity

One important property of a material is the electrical conductivity $\sigma_{\alpha\beta}$. The conductivity plays a prominent role in condensed matter physics, since it is the quantity used to characterize different materials, such as insulators having a small conductivity and metals having a large conductivity. It describes the reaction of quasiparticles in a crystal to the perturbation of an electrical field $\boldsymbol{E}$. The electrical conductivity is a rank two tensor which relates the electrical field to the electrical current of the system as shown in Fig. 2.1, i. e.,

$$j_\alpha = \sum_\beta \sigma_{\alpha\beta} E_\beta \,, \tag{2.1}$$

where α, β are the indices for the spatial coordinates. Since we are going to study two-dimensional materials in this thesis, the indices run over $\alpha, \beta \in \{x, y\}$.

One of the first physical models describing the conductivity of materials is the Drude model [37, 38], which was introduced by Paul Drude in the year 1900. He described the movement of a single electron in an electrical field and introduced a scattering time τ defining the time interval between successive collisions in the crystal. He found that the conductivity is proportional to this scattering time, i. e., $\sigma = e^2 n\tau/m$ with m being the mass of the particle and n the particle density. Thereby, it was assumed that all electrons move as single particles which lead to an overestimation of the electrical conductivity by at least a factor of thousand. In the year 1927 Sommerfeld extended this model by taking the quantum statistical distribution functions into account which describe the fact that only fermions at the Fermi surface participate in the transport process and thus corrected the overestimation of the conductivity.

In this thesis, we use a many-body description in order to determine the conductivity of graphene and of a anisotropic Dirac system (ADS). In Sec. 2.2, we introduce the different Kubo formulas for the conductivity which describe the linear response of the material to an external perturbation which is in this case the electrical field $\boldsymbol{E}$. Another method to calculate the conductivity is the Boltzmann equation which gives the distribution function of the quasiparticles when an external perturbation is applied. This distribution function determines the conductivity in the hydrodynamic regime and further details can be found in Sec. 2.4.

An interesting question to ask is how the Coulomb interaction between the electrons influence the conductivity. In order to answer this question, we will perform a renormalization group (RG) analysis

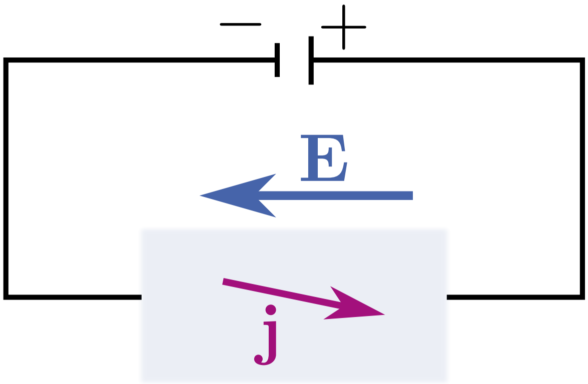

Figure 2.1: The conductivity tensor connects an applied electrical field to an electrical current.

in Chap. 4 and Chap. 7. Here, in Sec. 2.3, we study the scaling behavior of the conductivity under the RG flow.

2.2 Kubo-Formalism for the conductivity

In this section, we derive the expressions defining the conductivity in linear response via the Kubo-formalism. The Kubo-formalism was introduced in Sec. 1.1.1 where we showed how the mean value of an operator can be calculated when an external perturbation W_t occurs in the system. Here, the perturbation generating an electrical current is given by

$$W_t = \hat{\boldsymbol{P}} \cdot \boldsymbol{E}\,, \tag{2.2}$$

where $\boldsymbol{E}$ is the time dependent electrical field coupling to the polarization operator $\hat{\boldsymbol{P}}$. The polarization operator is defined as

$$\hat{\boldsymbol{P}} = \sum_{\boldsymbol{x}} \boldsymbol{x} \hat{\psi}^{\dagger}_{\boldsymbol{x}} \hat{\psi}_{\boldsymbol{x}}\,, \tag{2.3}$$

with $\hat{\psi}^{(\dagger)}_{\boldsymbol{x}}$ denoting the fermionic annihilation (creation) operator. Using the continuity equation of the particle density, one finds that the derivative of the polarization operator determines the electrical current, i. e., $\boldsymbol{j} = \partial \boldsymbol{P}/\partial t$ [39]. As we have seen before, the electrical conductivity is defined over $j_\alpha = \sum_\beta \sigma_{\alpha\beta} E_\beta$ and hence, we have to determine the mean value of the electrical current in order to obtain the electrical conductivity. Using the equations (1.9) and (1.15) of the Kubo formalism derived in the previous chapter, we obtain for the conductivity tensor

$$\begin{aligned} \sigma_{\alpha\beta}(\omega) &= -\frac{\mathrm{i}}{\hbar} \int_{-\infty}^{\infty} \mathrm{d}t\ \mathrm{e}^{\mathrm{i}\omega_+ t} \int_{-\infty}^{t} \mathrm{d}t' \left\langle [j_\alpha(t), P_\beta(t')] \right\rangle \\ &= \frac{\mathrm{i}}{\omega_+} (\chi^T_{j_\alpha j_\beta} - \chi_{j_\alpha j_\beta}(\omega)) \end{aligned} \tag{2.4}$$

where $\chi_{j_\alpha j_\beta}(\omega)$ is the Fourier transform of $\chi_{j_\alpha j_\beta}(t-t') = -\mathrm{i}\theta(t-t') \left\langle [j_\alpha(t), j_\beta(t')] \right\rangle$, while $\chi^T_{j_\alpha j_\beta} = \mathrm{d} \left\langle j_\alpha \right\rangle / \mathrm{d}A_\beta|_{A_\beta=0}$ with $\boldsymbol{A}$ being the vector potential. We find that the real part of the conductivity tensor is given by

$$\sigma_{\alpha\beta}(\omega) = \pi D_{\alpha\beta}\delta(\omega) - \frac{\operatorname{Im}\chi_{J_\alpha J_\beta}(\omega)}{\omega}\,, \tag{2.5}$$

where $D_{\alpha\beta} = \chi_{j_\alpha j_\beta}(\omega)^T - \chi_{j_\alpha j_\beta}(0)$ is the Drude conductivity. Thus, the conductivity is defined over the current-current correlation function. However, we can also express the electrical conductivity by a density-density correlation function. In order to derive the respective Kubo-formula, the continuity equation of the particle density has to be applied. The continuity equation describes the particle conservation and relates the time derivative of the particle density to the divergence of the electrical current, i. e.,

$$\partial_t n(\boldsymbol{r}, t) = -\nabla_{\boldsymbol{r}} \cdot \boldsymbol{j}(\boldsymbol{r}, t)\,. \tag{2.6}$$

The Fourier transform of the continuity equation into momentum and energy space is

$$\omega\; n(\boldsymbol{q}, \omega) = \boldsymbol{q} \cdot \boldsymbol{j}(\boldsymbol{q}, \omega)\,. \tag{2.7}$$

Upon inserting this expression into the Kubo-formula, we obtain

$$\begin{aligned}\sigma_{\alpha\beta}(\omega, \boldsymbol{q}) &= \pi D_{\alpha\beta}\delta(\omega) - \operatorname{Im}\frac{\omega}{q_\alpha q_\beta}\int_0^\infty \mathrm{d}t e^{\mathrm{i}\omega^+ t}\left\langle [n(t), n(0)]\right\rangle \\ &= \pi D_{\alpha\beta}\delta(\omega) - \frac{\omega}{q_\alpha q_\beta}\operatorname{Im}\chi_\rho(\boldsymbol{q}, \omega)\,,\end{aligned} \tag{2.8}$$

where $\chi_\rho(\boldsymbol{q}, \omega)$ is the density-density correlation function. In linear response the electrical conductivity can either be determined by calculating the current-current correlation function or by evaluating the density-density correlator and both methods will lead to the same result.

2.3 Scaling behavior of the conductivity

In the remainder of this thesis we want to study the influence of the Coulomb interaction on different transport properties such as the electrical conductivity and the shear viscosity. To this end, we implement a RG analysis. A detailed discussion of the RG analysis in graphene can be found in Sec. 4.3.2, while the detailed description of the RG analysis in ADS is given in Sec. 7.2.1. Here, we briefly summarize the concept behind the RG and discuss the behavior of the conductivity under the RG. For further details we refer to the corresponding chapters.

In the RG the fermionic operators are split up into fast and slow modes, i. e., $\hat{\psi}_{\boldsymbol{k}} = \hat{\psi}^<_{\boldsymbol{k}} + \hat{\psi}^>_{\boldsymbol{k}}$. The slow modes $\hat{\psi}^<_{\boldsymbol{k}} = \hat{\psi}_{\boldsymbol{k}}$ are defined for momentum $0 \le \boldsymbol{k} \le \Lambda/b$, while the fast modes $\hat{\psi}^>_{\boldsymbol{k}}$ are defined in the momentum integral $\Lambda/b \le \boldsymbol{k} \le \Lambda$, where the parameter Λ is an UV cut-off. As first step, the fast modes are integrated out. Then the momentum $\boldsymbol{k}' = b\boldsymbol{k}$ and the frequency $\omega' = Z_T^{-1}\omega$ are rescaled in such a way that the new variables run up to the old cut-off Λ. During this procedure the transport properties are also rescaled by a scaling factor.

In this section, we determine the scaling factor of the conductivity for a d dimensional system and show that the conductivity is scale invariant for two dimensional systems. The conductivity is given, as we have seen in the previous section, by

$$\sigma(\omega) = \lim_{q\to 0}\frac{e^2\omega}{q^2}\operatorname{Im}\chi_\rho(\boldsymbol{q}, \omega)\,. \tag{2.9}$$

We find that the scaling of the conductivity is determined by

$$\sigma(\omega, T) = Z_T b^2 Z_{\chi_\rho} \sigma_R(Z_T^{-1} T, Z_T^{-1}\omega)\,, \tag{2.10}$$

with Z_{χ_ρ} being the scaling factor of the density-density correlation function consisting of $Z_{\chi_\rho} = Z_n^2 Z_T b^{-d}$. We want to identify the scaling factor Z_n for the particle density and the scaling of the current operator Z_J independent of the order of the RG applied. In an RG analysis up to first loop order, we find that the current operator scales as

$$j_\alpha(\boldsymbol{k}, \Omega) = Z_J j_{\alpha,R}(b\boldsymbol{k}, Z_T^{-1}\Omega) \tag{2.11}$$

with $Z_J = b$. In the following we prove that this scaling relation is correct for every order of the RG. To this end, we use the Ward-identity. The Ward identity represents the conservation of the charged particles and is derived from the continuity equation of the particle density, $\partial_t n(\boldsymbol{r}, t) + \nabla_{\boldsymbol{r}} \cdot \boldsymbol{j}(\boldsymbol{r}, t) = 0$, following the steps in [40, 41]. It reads

$$\begin{aligned} &e\partial_\tau \left\langle T_\tau n(\boldsymbol{r}, \tau)\hat{\psi}_{\boldsymbol{r}_1,\tau_1}\hat{\psi}^\dagger_{\boldsymbol{r}_2,\tau_2}\right\rangle - \mathrm{i}\nabla_{r_\alpha}\left\langle T_\tau j_\alpha(\boldsymbol{r}, \tau)\hat{\psi}_{\boldsymbol{r}_1,\tau_1}\hat{\psi}^\dagger_{\boldsymbol{r}_2,\tau_2}\right\rangle \\ &= -\mathrm{i}e[\delta^{(d)}(\boldsymbol{r} - \boldsymbol{r}_1)\delta(\tau - \tau_1) - \delta^{(d)}(\boldsymbol{r} - \boldsymbol{r}_2)\delta(\tau - \tau_2)]\left\langle \hat{\psi}_{\boldsymbol{r}_1,\tau_1}\hat{\psi}^\dagger_{\boldsymbol{r}_2,\tau_2}\right\rangle\,, \end{aligned} \tag{2.12}$$

where $\tau = \mathrm{i}t$ is the imaginary time and T_τ is the time-ordering operator. The Ward identity has to be fulfilled in all orders of the RG analysis and thus all scaling relations derived from this identity are valid for all orders of the RG. Now we examine the scaling relation of the Ward identity (2.12). To this end, we Fourier transform the electrical current $\boldsymbol{j}(\boldsymbol{q}, \omega)$ and the particle density $n(\boldsymbol{q}, \omega)$ to the real space of a d-dimensional system and obtain the following scaling relations

$$\begin{aligned} j_\alpha(\boldsymbol{r}, \tau) &= Z_J Z_T b^{-d} j_{\alpha,R}(\boldsymbol{r}/b, \tau Z_T)\,, \\ n(\boldsymbol{r}, \tau) &= Z_n Z_T b^{-d} n_R(\boldsymbol{r}/b, \tau Z_T)\,. \end{aligned} \tag{2.13}$$

Inserting these relations into the Ward identity, rescaling $\boldsymbol{r} \to b\boldsymbol{r}$ and $\tau \to \tau/Z_T$ (and similarly for $\boldsymbol{r}_1$, τ_1, etc.), yields for the scaling factors

$$\begin{aligned} Z_J &= b\,, \\ Z_n &= Z_T^{-1}\,. \end{aligned} \tag{2.14}$$

Next these scaling factors are inserted into (2.10) which implies that the conductivity for a d- dimensional system is

$$\sigma(\omega, T) = b^{2-d}\sigma_R(Z_T^{-1}\omega, Z_T^{-1}T)\,. \tag{2.15}$$

For a two dimensional (2D) system, this scaling relation leads to the scale invariance of the conductivity. Independent of the frequency or temperature scale of the system the conductivity will have the same value for two dimensional systems.

2.4 Ansatz for Quantum Boltzmann equation

In the hydrodynamic regime, the conductivity can also be determined using the Boltzmann equation. With the help of the Boltzmann equation, the distribution function of the quasiparticles $f_{\lambda\boldsymbol{k}}$ can be determined. The distribution function consists of the Fermi-Dirac function $f^{(0)}_{\lambda\boldsymbol{k}}$ describing the equilibrium distribution and an out-off equilibrium correction $\delta f_{\lambda \boldsymbol{k}}$. This out-off equilibrium correction arising because of the perturbation due to the electrical field defines the electrical current, i. e.,

$$\boldsymbol{j} = \sum_{\lambda} \int_{\boldsymbol{k}} \boldsymbol{v}_{\lambda \boldsymbol{k}} \delta f_{\lambda \boldsymbol{k}} \,, \tag{2.16}$$

where $\boldsymbol{v}_{\lambda \boldsymbol{k}}$ is the velocity of the quasiparticles and λ is the energy band index of the corresponding quasiparticle. In order to determine this out-off equilibrium correction, the Boltzmann equation needs to be solved. Here, we first study the Boltzmann equation in the relaxation-time approximation which takes only scattering processes due to impurities into account and scattering processes between the particles due to the Coulomb interaction are neglected. The scattering processes due to impurities are characterized by the relaxation time τ_{dis} and the Boltzmann equation in the relaxation-time approximation is

$$\left(\frac{\partial}{\partial t} + e\boldsymbol{E} \frac{\partial}{\partial \boldsymbol{k}} \right) f_{\lambda \boldsymbol{k}} = -\frac{\delta f_{\lambda \boldsymbol{k}}}{\tau_{\text{dis}}} \,, \tag{2.17}$$

where $\delta f_{\lambda \boldsymbol{k}} = f_{\lambda \boldsymbol{k}} - \left\langle f_{\lambda \boldsymbol{k}} \right\rangle_{\varphi}$ with $\langle\rangle_{\varphi}$ denoting the angular average over the directions of $\boldsymbol{k}$ of the distribution function. The momentum derivative of the term proportional to the electrical field can be rewritten as an energy-derivative times the velocity of the quasiparticle, i. e., $\partial/\partial \boldsymbol{k} = \boldsymbol{v}_{\lambda \boldsymbol{k}} \cdot \partial/\partial \epsilon_{\lambda \boldsymbol{k}}$ and thus we obtain for the out-off equilibrium correction of the distribution function is given by

$$\delta f_{\lambda \boldsymbol{k}} = \frac{1}{-\mathrm{i}\omega - \tau_{\text{dis}}^{-1}} T^{-1} f^{(0)}_{\lambda \boldsymbol{k}} (1 - f^{(0)}_{\lambda \boldsymbol{k}}) \boldsymbol{v}_{\lambda \boldsymbol{k}} \cdot \boldsymbol{E} \tag{2.18}$$

which leads to the following electrical current in the relaxation-time approximation

$$\begin{aligned} j_\alpha &= \sum_{\lambda} \int_{\boldsymbol{k}} v^{\alpha}_{\lambda \boldsymbol{k}} \delta f_{\lambda \boldsymbol{k}} \\ &= \sum_{\lambda} \int_{\boldsymbol{k}} v^{\alpha}_{\lambda \boldsymbol{k}} v^{\beta}_{\lambda \boldsymbol{k}} \frac{1}{-\mathrm{i}\omega - \tau_{\text{dis}}^{-1}} T^{-1} f^{(0)}_{\lambda \boldsymbol{k}} (1 - f^{(0)}_{\lambda \boldsymbol{k}}) E_\beta \,. \end{aligned} \tag{2.19}$$

Now we want to generalize the above expression in such a way that we can go beyond the relaxation-time approximation and are thus also able to take scattering processes due to Coulomb interaction into account. To this end, we choose for the out-off equilibrium distribution function the following ansatz

$$\delta f_{\lambda \boldsymbol{k}} = T^{-1} f^{(0)}_{\lambda \boldsymbol{k}} (1 - f^{(0)}_{\lambda \boldsymbol{k}}) h_{\lambda \boldsymbol{k}} \tag{2.20}$$

with

$$h_{\lambda \boldsymbol{k}} = \boldsymbol{v}_{\lambda \boldsymbol{k}} \cdot \boldsymbol{E} \; g_{\lambda \boldsymbol{k}} \,. \tag{2.21}$$

The function $h_{\lambda \boldsymbol{k}}$ is proportional to the scalar product of the velocity $\boldsymbol{v}_{\lambda \boldsymbol{k}}$ and the electrical field $\boldsymbol{E}$ and the term containing the scattering time τ_{dis} is replaced by a by the function $g_{\lambda \boldsymbol{k}} = \sum_n \psi_n \phi^{(n)}_{\lambda \boldsymbol{k}}$, where $\phi^{(n)}_{\lambda \boldsymbol{k}}$ is a set of basis functions weighted by the unknown coefficients ψ_n. The coefficients ψ_n can be calculated by an inversion of the Boltzmann equation. Hence, in the hydrodynamic regime the conductivity is given by

$$\sigma_{\alpha\beta} = \sum_{\lambda} \int_{\boldsymbol{k}} v^{\alpha}_{\lambda \boldsymbol{k}} v^{\beta}_{\lambda \boldsymbol{k}} T^{-1} f^{(0)}_{\lambda \boldsymbol{k}} (1 - f^{(0)}_{\lambda \boldsymbol{k}}) g_{\lambda \boldsymbol{k}} \,. \tag{2.22}$$

This expression of the conductivity is used in Chap. 5 and Chap. 8 in order to calculate the conductivity of graphene and of ADSs.

Chapter 3

3 Viscosity in lattices with pseudospin

An important transport quantity is the viscosity of a material. The viscosity describes the resistivity of a system in response to a hydrodynamic flow. In Sec. 3.1, we define this important transport property and give an intuitive picture of the viscosity before we formalize it. We show in Sec. 3.3 that the viscosity can be calculated using the Kubo-formalism which connects the correlation function of energy-stress tensors to the viscosity tensor. The energy-stress tensor can be determined by the time derivative of the strain generators [42]. Thereby, we extent the study of Bradlyn *et al.* [42] to lattices with a pseudospin in Sec. 3.2. We demonstrate that an additional strain generator acting on the pseudospin is needed to obtain the correct energy-stress tensor. In the same section, we also show how the perturbation of the system due to the gradient of the drift velocity $\partial u_\beta/\partial x_\alpha$ is described by an Hamiltonian, where the velocity gradient couples to the strain generators. This Hamiltonian is used in Sec. 3.5 to derive the ansatz for the out-off equilibrium correction of the distribution function defined by the Boltzmann equation. Furthermore, the scaling behavior of the viscosity under a renormalization group (RG) analysis is determined via a Ward identity in Sec. 3.4. At last the famous lower bound of the ratio viscosity over entropy η/s is introduced [18] and a physical interpretation of this lower bound is given.

3.1 Definition of the viscosity

The viscosity of a fluid describes the effect of energy dissipation in a fluid due to internal friction [43]. This energy dissipation occurs, if different particles of the fluid move with different velocities. Here, we firstly introduce an intuitive picture for the viscosity before we demonstrate how the viscosity modifies the Euler equation which describes the dynamics of an ideal fluid.

Let us start with the following gedankenexperiment: There are two plates, one is fixed, while the other one is moving and there is a liquid between the two plates. This situation is depicted in Fig. 3.1. Due to these boundary conditions (one fixed, one moving plate) a velocity gradient $\partial u/\partial y$ is exhibited in the fluid. Because of interaction, there is an irreversible energy transfer between particles with a large velocity $u(y')$ to particles with a small velocity $u(y)$. In order to maintain this velocity gradient, a shear stress $\tau = F/A$ needs to be applied where F is the force acting on the moving plate with the area A. This force keeps the plate moving. The stronger the force is to obtain the velocity gradient the more viscous the fluid is. The viscosity η connects the shear stress to the velocity gradient

$$\tau = \eta \frac{\partial u}{\partial y} \,. \tag{3.1}$$

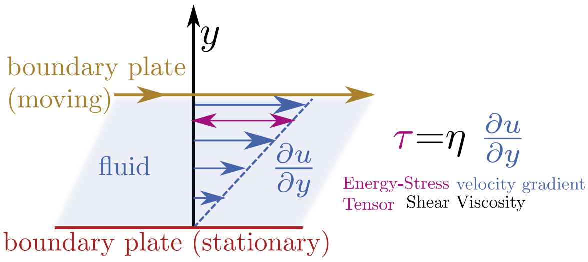

Figure 3.1: Definition of the viscosity. We see two plates, one is moving, the other one is fixed. Between the two plates is a fluid with the velocity gradient $\partial u/\partial y$. The stronger the applied force has to be to maintain the velocity gradient, the more viscous the fluid is.

The viscosity thus describes how resistive a fluid is to an hydrodynamic flow.

Now, we implement the concept of viscosity into the hydrodynamic equations of an ideal, Galilean invariant fluid. An ideal fluid is described by the Euler equations which are defined as

$$\frac{\partial}{\partial t}(\rho u_\alpha) = -\frac{\partial \Pi_{\alpha\beta}}{\partial x_\beta}\,, \tag{3.2}$$

where ρ is the density of the fluid moving with the velocity $\boldsymbol{u}$ and $\Pi_{\alpha\beta}$ is the momentum flux density tensor. The indices α, β denote the spatial components. This momentum flux density consists of the pressure P of the system and the product of two velocity components weighted by the density. It reads

$$\Pi_{\alpha\beta} = P\delta_{\alpha\beta} + \rho u_\alpha u_\beta\,. \tag{3.3}$$

In order to take the dissipative processes due to internal friction into account, the momentum flux density of an ideal gas is modified by adding the viscous energy-stress tensor $-T_{\alpha\beta}$. The form of this viscous energy-stress tensor is derived in the following. Since the irreversible energy transfer only occurs, when the particles of the fluid have different velocities, $T_{\alpha\beta}$ should depend only on space derivatives of the velocity, i. e., $\partial u_\beta/\partial x_\alpha$. Upon assuming the velocity difference to be small, the energy-stress tensor should also only consist of linear combinations of $\partial u_\beta/\partial x_\alpha$. Hence, in the most general form, the viscosity is a rank four tensor which relates the velocity gradient $\partial u_\gamma/\partial x_\delta$ to the viscous part of the energy-stress tensor

$$T_{\alpha\beta} = \sum_{\gamma\delta} \eta_{\alpha\beta\gamma\delta} \frac{\partial u_\delta}{\partial x_\gamma}\,. \tag{3.4}$$

For rotational invariant systems, the above expression can be simplified such that the energy-stress tensor only depends on two viscosities, the shear viscosity η and the bulk viscosity ζ, which are both positive quantities. Thereby, we use the fact that the viscous energy-stress tensor has to vanish when the fluid is in uniform rotation. In the case of a uniform rotation no internal friction occurs. Thus, the viscous part of the energy-stress tensor for a rotational symmetric system has the form [43]

$$T_{\alpha\beta} = \eta \left(\frac{\partial u_\alpha}{\partial x_\beta} + \frac{\partial u_\beta}{\partial x_\alpha} - \frac{2}{d}\delta_{\alpha\beta} \boldsymbol{\nabla}_{\boldsymbol{r}} \cdot \boldsymbol{u} \right) + \zeta\ \delta_{\alpha\beta} \boldsymbol{\nabla}_{\boldsymbol{r}} \cdot \boldsymbol{u}\,, \tag{3.5}$$

where d is the dimension of the system. The viscosity coefficients for rotational invariant systems obey the following condition [44]

$$\eta_{\alpha\beta\gamma\delta} = \eta[\delta_{\alpha\gamma}\delta_{\beta\delta} + \delta_{\alpha\delta}\delta_{\beta\gamma} - \frac{2}{d}\delta_{\alpha\beta}\delta_{\gamma\delta}]\,. \tag{3.6}$$

The shear viscosity of a Galilean invariant system is connected to the non-local conductivity [42, 45], i. e., $\sigma_{\alpha\alpha}(\boldsymbol{q},\omega) \propto \sigma_{\alpha\alpha}(\boldsymbol{0},\omega) + q^2\eta/(m\omega)^2$. Thus, by measuring the non-local conductivity one can gain experimental access to the viscosity of a Galilean invariant system.

3.2 The strain generator and the energy stress tensor

In this section, we show that the energy-stress tensor can also be derived from strain generators, since the viscosity denotes the response of a fluid to the time derivative of strain, i. e., the deformation of the original coordinates of a systems. Furthermore, we demonstrate how a perturbation due to strain is implemented in the Hamiltonian of the fluid and how we can derive a Kubo formula for the viscosity using this perturbation. Thereby, we follow the calculation of Bradlyn *et al.* [42]. However, we are going to extend their considerations to electron liquids in lattices which have a pseudospin due to a multi-atomic basis and show how the pseudospin has to be modified accordingly.

This extension is part of my work in collaboration with Daniel E. Sheehy, Boris N. Narozhny, and Jörg Schmalian which is in preparation to be published [46].

Transformation of the spatial coordinates

Now, let us start with our calculation. The strain acting on the electron fluid is defined as

$$\epsilon_{\gamma\delta}(t) = \frac{\partial \mathrm{u}_\delta(t)}{\partial x_\gamma} \tag{3.7}$$

where $\mathfrak{u}$ denotes the displacement of the coordinates from their original position. The new coordinates under the strain $\epsilon_{\gamma\delta}$ are given by $\boldsymbol{x} \to \boldsymbol{x}' = \boldsymbol{x} + \mathbf{u}(\boldsymbol{x})$ where the deformation is realized by a homogeneous but time-dependent invertible $d \times d$ matrix $\Lambda(t)$

$$\boldsymbol{x}' = \Lambda(t)^T \boldsymbol{x} \qquad \text{with} \qquad \Lambda(t) = \mathrm{e}^{\epsilon(t)}\,. \tag{3.8}$$

The new volume of the fluid becomes time dependent, i. e., $V(t) = \Lambda(t)V_0$ where V_0 is the volume of the undeformed system. In the following, we want to express the Hamiltonian given in the displaced coordinates again by the original coordinates

$$\mathcal{H}_t = \int_{V(t)} \mathrm{d}^2x' \psi^\dagger(\boldsymbol{x}')\epsilon(\boldsymbol{p}')\psi(\boldsymbol{x}') \to \mathcal{H}_t = \int_{V_0} \mathrm{d}^2x \psi^\dagger_\epsilon(\boldsymbol{x})\epsilon\left(\frac{\boldsymbol{p}}{\Lambda(t)}\right)\psi_\epsilon(\boldsymbol{x})\,, \tag{3.9}$$

where $\epsilon(\boldsymbol{p})$ is the energy dispersion of the system. To this purpose, the field operators are transformed as

$$\psi_\epsilon(\boldsymbol{x}) = \sqrt{\det\Lambda(t)}\psi(\Lambda(t)^T\boldsymbol{x})\,, \tag{3.10}$$

where the factor $\sqrt{\det\Lambda(t)}$ ensures the normalization of the field operators, i. e., proper canonical commutation relations. Next, we want to find a unitary transformation, which fulfills the following relation

$$\psi_\epsilon(\boldsymbol{x}) = U_\epsilon(t)\psi(\boldsymbol{x}) \tag{3.11}$$

leading to a Hamiltonian which is completely rewritten in the original coordinates plus an additional part

$$\delta\mathcal{H}_t = -\mathrm{i}\int \mathrm{d}^2x \psi^\dagger(\boldsymbol{x})U_\epsilon(t)(\partial_t U_\epsilon^{-1})\psi(\boldsymbol{x})\,, \tag{3.12}$$

which describes how the system couples to the applied strain. In order to determine the unitary transformation (3.11), we investigate how the fermionic field operators change under the infinitesimal transformation from ϵ to $\epsilon + \delta\epsilon$. We find

$$\frac{\partial}{\partial \epsilon_{\alpha\beta}} \psi_\epsilon(\boldsymbol{x}) = \frac{\delta_{\alpha\beta}}{2} \psi_\epsilon(\boldsymbol{x}) + x'_\alpha \frac{\partial}{\partial x'_\beta} \psi_\epsilon(\boldsymbol{x}) \,, \tag{3.13}$$

where in the last step, we took the derivative with respect to the displaced coordinates. But, since we consider an infinitesimal small change we can set ϵ to zero and there is no distinction between the two sets of coordinates. Hence, the strain generators due to a spatial transformation are

$$\begin{aligned} \mathcal{L}_{\alpha\beta} &= \mathrm{i} x_\alpha \frac{\partial}{\partial x_\beta} + \frac{\mathrm{i}}{2}\delta_{\alpha\beta} \\ &= -\frac{1}{2}\{x_\alpha, p_\beta\} = -x_\alpha p_\beta + \frac{i}{2}\delta_{\alpha\beta} \,. \end{aligned} \tag{3.14}$$

Thus, we find for an infinitesimal transformation of the fermion fields

$$\psi_\epsilon(\boldsymbol{x}) = \psi(\boldsymbol{x}) + \sum_{\alpha\beta} \frac{\partial \psi_\epsilon(\boldsymbol{x})}{\partial \epsilon_{\alpha\beta}}\bigg|_{\epsilon=0} \epsilon_{\alpha\beta} = \Big(1 - \mathrm{i} \sum_{\alpha\beta} \epsilon_{\alpha\beta}\mathcal{L}_{\alpha\beta}\Big)\psi(\boldsymbol{x}) \tag{3.15}$$

which leads to the fact that the unitary transformation is given by

$$U_\epsilon(t) = \mathrm{e}^{-\mathrm{i}\sum_{\alpha\beta} \epsilon_{\beta\alpha}\mathcal{L}_{\alpha\beta}} \,. \tag{3.16}$$

The strain generators due to the spatial transformation of the coordinates $\mathcal{L}_{\alpha\beta}$ fulfill the commutation relation of the corresponding Lie algebra

$$[\mathcal{L}_{\alpha\beta}, \mathcal{L}_{\gamma\delta}] = \mathrm{i}(\delta_{\beta\gamma}\mathcal{L}_{\alpha\delta} - \delta_{\alpha\delta}\mathcal{L}_{\gamma\beta}) \tag{3.17}$$

and the antisymmetric part of $\mathcal{L}_{\alpha\beta}$ determines the angular momentum

$$L_\gamma = -\epsilon_{\alpha\beta\gamma}\mathcal{L}_{\alpha\beta} \,. \tag{3.18}$$

Here, we have seen that under an applied strain which deforms the spatial coordinates, $\mathcal{L}_{\alpha\beta} = -1/2\{x_\alpha, p_\beta\}$ generates the unitary transformation which at the end determines the form of the additional Hamiltonian $\delta\mathcal{H}_t$ by (3.12).

Transformation of the pseudospin

Thus far, we only considered the transformation of the coordinates. However, lattices with a basis consisting of multiple atoms have a pseudospin which we call "lattice spin" that behaves like a real angular momentum. One of these lattices is graphene [47] which has a two-atomic basis and whose Hamiltonian is given by

$$\mathcal{H}_{Dirac} = v_\mathrm{F} \int_{\boldsymbol{p}} \hat{\psi}^\dagger_{\boldsymbol{p}} (p_x\sigma_x + p_y\sigma_y)\hat{\psi}_{\boldsymbol{p}} \,, \tag{3.19}$$

where v_F is the Fermi velocity and the Pauli matrices denote the valence and conductance band[1]. An important example which demonstrates that the pseudospin of graphene is a real angular momentum

---

[1] For a detailed derivation of this Hamiltonian and a far more detailed description of graphene, we refer to Chap. 4. Further, a detailed discussion of the viscosity in graphene will be presented in Chap. 6.

is given by the photon-mediated electron-hole pair production (recombination) in graphene [47]. An electron with its pseudospin parallel to its momentum in the valence band is lifted into the conductance band by absorbing a photon and thereby flipping its pseudospin [48]. Another physical quantity that shows the importance of the pseudospin in graphene is the shear viscosity. This transport quantity is going to be discussed in more detail in Sec. 6.2.1.

In order to treat the deformation of the liquid consistently, we also have to introduce strain generators acting in the spin space. Analogous to the strain generator of the spatial coordinates, we define

$$\mathcal{S}_{\alpha\beta} = \frac{i}{4}[S_\alpha, S_\beta] = -\frac{1}{2}\epsilon_{\alpha\beta\gamma}S_\gamma = -\frac{1}{4}\epsilon_{\alpha\beta\gamma}\sigma_\gamma \,, \tag{3.20}$$

where in the last line we gave the explicit expression for graphene. The antisymmetric part of this strain generator determines again the spin/angular momentum (analogous to $\mathcal{L}_{\alpha\beta}$)

$$S_\gamma = -\epsilon_{\gamma\alpha\beta}\mathcal{S}_{\alpha\beta} \,. \tag{3.21}$$

The total strain generator acting on both spin and real space is thus given by the sum of the above introduced generators. It reads

$$\mathcal{J}_{\alpha\beta} = \mathcal{L}_{\alpha\beta} + \mathcal{S}_{\alpha\beta} \,. \tag{3.22}$$

The unitary matrix $U_\epsilon(t)$, which describes how the fermionic fields transform under the applied strain, and which determines also the additional Hamiltonian $\delta\mathcal{H}_t$, has now the form $U_\epsilon(t) = \mathrm{e}^{-\mathrm{i}\,\mathrm{Tr}\,\epsilon_{\beta\alpha}\mathcal{J}_{\alpha\beta}}$. Hence, we are able to express the influence of the strain on the fluid by the Hamiltonian

$$\mathcal{H}_t = \int_{V_0} \mathrm{d}^d x \psi^\dagger(\mathbf{x})\epsilon(\mathbf{p})\psi(\mathbf{x}) - \int \mathrm{d}^d x \psi^\dagger(\boldsymbol{x})\frac{\partial \epsilon_{\alpha\beta}}{\partial t}\mathcal{J}_{\alpha\beta}\psi(\boldsymbol{x}) \,, \tag{3.23}$$

where the first term describes the unperturbed system, while the second term connects the velocity gradient $\partial u_\beta/\partial x_\alpha$, i. e., the time derivative of the strain tensor, to the total strain generator $\mathcal{J}_{\alpha\beta}$.

The connection between strain generator and energy-stress tensor

As the next step, we have to relate the total strain generator $\mathcal{J}_{\alpha\beta}$ to the energy-stress tensor $T_{\alpha\beta}$, since the energy-stress tensor is proportional to the viscosity tensor as we have seen in the previous section. Therefore, the continuity equation of the momentum density $g_\alpha(\boldsymbol{x}, t)$ is studied, i. e., $g_\alpha(\boldsymbol{x}, t) = \int_{\boldsymbol{x}} \hat{\psi}^\dagger_{\boldsymbol{x},t}(-\mathrm{i}\hbar\partial_{x_\alpha})\hat{\psi}_{\boldsymbol{x},t}$. This continuity equation [49]

$$\partial_t g_\alpha(\boldsymbol{x}, t) = -\partial_{x_\beta} T_{\beta\alpha}(\boldsymbol{x}, t) \tag{3.24}$$

sets the time derivative of the momentum density equal to the negative divergence of the energy-stress tensor $T_{\alpha\beta}(\boldsymbol{x}, t)$. After a Fourier transformation w. r. t. the spatial coordinates, the above continuity equation is given by

$$\partial_t g_\alpha(\mathbf{q}, t) = -iq_\beta T_{\beta\alpha}(\boldsymbol{q}, t) \,. \tag{3.25}$$

Upon expanding the momentum density $g(\boldsymbol{q}, t)$ for small momentum $\boldsymbol{q}$, we find

$$\begin{aligned} g_\alpha(\boldsymbol{q}, t) &= \int \mathrm{d}^d x \mathrm{e}^{\mathrm{i}\boldsymbol{q}\cdot\boldsymbol{x}} g_\alpha(\boldsymbol{x}, t) && (3.26) \\ &= g_\alpha(\mathbf{0}, t) + \mathrm{i}q_\beta \int \mathrm{d}^d x \psi^\dagger(\boldsymbol{x}, t) x_\beta(-\mathrm{i}\partial_{x_\alpha})\psi(\boldsymbol{x}, t) + \cdots \,, && (3.27) \end{aligned}$$

and can identify the following formula for the energy-stress tensor

$$\begin{aligned} T_{\alpha\beta} &= -\partial_t \mathcal{J}_{\alpha\beta} \\ &= -i[H, \mathcal{J}_{\alpha\beta}] \,. \end{aligned} \tag{3.28}$$

The energy-stress tensor is defined as the time derivative of the total strain generator. Here, also the strain generator $\mathcal{S}_{\alpha\beta}$ acting on the spin space is included, since the gradient of an antisymmetric third-rank tensor can always be added without changing the energy-stress tensor, i. e., $T_{\alpha\beta} + \partial_{x_\gamma} Z_{\beta\alpha\gamma}$ [50, 51].

The energy stress tensor and the pressure of the system

In this section, we show that in the hydrodynamic regime the non-dissipative part of the energy-stress tensor $\Pi_{\alpha\beta} = \sum_\lambda \int_{\boldsymbol{k}} v^\alpha_{\lambda\boldsymbol{k}} k_\beta f^{(0)}_{\lambda\boldsymbol{k}}$ and the momentum density $n^\alpha_{\boldsymbol{k}} = \sum_\lambda \int_{\boldsymbol{k}} k_\alpha f^{(0)}_{\lambda\boldsymbol{k}}$ can be set into relation with the pressure P of the system. Here, the distribution function $f^{(0)}_{\lambda\boldsymbol{k}}$ for a two-band lattice system with the energy dispersion $\epsilon_{\lambda\boldsymbol{k}}$ where λ is the band index is given by $f^{(0)}_{\lambda\boldsymbol{k}} = (1 + \mathrm{e}^{(\epsilon_{\lambda\boldsymbol{k}} - \mu_\lambda - \boldsymbol{u}\cdot\boldsymbol{k})/T})^{-1}$. The pressure can be obtained from the thermodynamic potential $\Omega = -PV$. Hence, in the grand canonical ensemble, for a two band system we find the pressure

$$P = T \int \frac{\mathrm{d}^2k}{(2\pi)^2} \log\left(1 + \mathrm{e}^{\frac{-\epsilon_{+\boldsymbol{k}} + \boldsymbol{u}\cdot\boldsymbol{k} + \mu_+}{T}}\right) + T \int \frac{\mathrm{d}^2k}{(2\pi)^2} \log\left(1 + \mathrm{e}^{\frac{-|\epsilon_{-\boldsymbol{k}}| - \boldsymbol{u}\cdot\boldsymbol{k} - \mu_-}{T}}\right) . \tag{3.29}$$

This expression can be simplified further by integration by parts. Thereby, it is important that for an energy spectrum $\epsilon_{\lambda\boldsymbol{k}}$ and small enough $\boldsymbol{u}$, the combination $\epsilon_{+\boldsymbol{k}} - \boldsymbol{u}\cdot\boldsymbol{k}$ tends to infinity for $\boldsymbol{k} \to \pm\infty$ such that the boundary terms of the integration by parts vanish. Thus, we find for the pressure

$$P = \frac{1}{2}\int \frac{\mathrm{d}^2k}{(2\pi)^2} (\boldsymbol{k}\cdot\boldsymbol{v}_{+\boldsymbol{k}} - \boldsymbol{k}\cdot\boldsymbol{u}) f^{(0)}_{+\boldsymbol{k}} + \frac{1}{2}\int \frac{\mathrm{d}^2k}{(2\pi)^2} (\boldsymbol{k}\cdot\boldsymbol{v}_{-\boldsymbol{k}} - \boldsymbol{k}\cdot\boldsymbol{u})(f^{(0)}_{-\boldsymbol{k}} - 1) \,, \tag{3.30}$$

which can also be expressed by the non-dissipative part of the energy-stress tensor and the momentum density as

$$P = \frac{1}{2}\,\mathrm{Tr}\,\Pi_{\alpha\beta} - n_{\boldsymbol{k}}\cdot\boldsymbol{u} \,. \tag{3.31}$$

This formula defining the pressure will become important in Sec. 9.4 where we derive the Navier-Stokes equation for anisotropic Dirac systems (ADSs) which will also contain the pressure of the system.

3.3 Kubo-Formalism for the viscosity

Now, using the Kubo-formalism let us derive the different expressions defining the viscosity tensor which connects the velocity gradient to the energy-stress tensor, i. e., $T_{\alpha\beta} = \sum_{\gamma\delta} \eta_{\alpha\beta\gamma\delta} \partial u_\delta / \partial x_\gamma$. These different expressions for the viscosity can also be found in Ref. 42. We have seen in Sec. 3.2, that the Hamiltonian describing the perturbation due to the velocity gradient is given by

$$\delta\mathcal{H}_t = -\int \mathrm{d}^2x \sum_\alpha \psi^\dagger(\boldsymbol{x}) \frac{\partial u_\beta}{\partial x_\alpha} \mathcal{J}_{\alpha\beta} \psi(\boldsymbol{x}) \,, \tag{3.32}$$

where $\mathcal{J}_{\alpha\beta}$ is the total strain generator which was also defined in the previously mentioned section. We can insert this expression into Eq. (1.9) where the expectation value of the operator $\hat{A}_i$ for the perturbed system was evaluated. In this case, $\hat{A}_i$ is the energy-stress tensor, $\hat{A}_i = T_{\alpha\beta}$, and the operator $\hat{B}_j$ coupling to the external perturbation is the total strain generator, $\hat{B}_j = \mathcal{J}_{\gamma\delta}$. Hence, we obtain

$$\left\langle T_{\alpha\beta} \right\rangle_t = -\frac{\mathrm{i}}{\hbar} \int\limits_{-\infty}^{\infty} \mathrm{d}t' \theta(t-t') \left\langle [T_{\alpha\beta}(t), \mathcal{J}_{\gamma\delta}(t')] \right\rangle \frac{\partial u_\delta}{\partial x_\gamma} \tag{3.33}$$

which leads to the following formula for the real part of the viscosity coefficients

$$\mathrm{Re}\, \eta_{\alpha\beta\gamma\delta}(t) = \mathrm{Im} \int_{-\infty}^{\infty} \mathrm{d}t' \theta(t-t') \left\langle [T_{\alpha\beta}(t), \mathcal{J}_{\gamma\delta}(t')] \right\rangle . \tag{3.34}$$

As seen in Sec. 1.1.1, we can also rewrite this formula by applying the Kubo-identity (1.10) and then integrate by parts which leads to

$$\mathrm{Re}\, \eta_{\alpha\beta\gamma\delta}(\omega) = \frac{\mathrm{i}}{\omega_+} (\chi^T_{T_{\alpha\beta}T_{\gamma\delta}} - \chi_{T_{\alpha\beta}T_{\gamma\delta}}(\omega)) , \tag{3.35}$$

where ω_+ is the imaginary frequency with $\omega_+ = \omega + \mathrm{i}0^+$. The function $\chi_{T_{\alpha\beta}T_{\gamma\delta}}(\omega)$ is the Fourier transform of the retarded Green's function $\chi_{T_{\alpha\beta}T_{\gamma\delta}}(t-t') = -\mathrm{i}\theta(t-t') \left\langle T_{\alpha\beta}(t), T_{\gamma\delta}(t') \right\rangle$ while $\chi^T_{T_{\alpha\beta}T_{\gamma\delta}} = \mathrm{d} \left\langle T_{\alpha\beta} \right\rangle / \mathrm{d}\epsilon_{\alpha\beta}|_{\epsilon_{\alpha\beta}=0}$ being the isothermal susceptibility. Hence, we find for the real part of the viscosity tensor

$$\mathrm{Re}\, \eta_{\alpha\beta\gamma\delta}(\omega) = \pi D_{\alpha\beta\gamma\delta} \delta(\omega) - \frac{\mathrm{Im}\, \chi_{T_{\alpha\beta}T_{\gamma\delta}}}{\omega} , \tag{3.36}$$

where $D_{\alpha\beta\gamma\delta} = D_{\alpha\beta\gamma\delta}(0) - \chi^T_{T_{\alpha\beta}T_{\gamma\delta}}$ determines the Drude peak of the viscosity. This expression for the viscosity tensor is used in Sec. 6.2.1 where the shear viscosity of graphene is determined in the collisionless regime and in Sec. 9.3 where the viscosity tensor of ADSs is calculated.

At last, there is one more expression for the viscosity tensor. Again using Eq. (3.34) and combining it with the fact that the time derivative of the strain tensor is equal to the energy-stress tensor, i. e., $T_{\alpha\beta} = -\partial_t \mathcal{J}_{\alpha\beta}$, we find after an integration by parts (analogous to the one performed in Sec. 1.1.1 form (1.12) to (1.13))

$$\eta_{\alpha\beta\gamma\delta}(\omega) = -\mathrm{i} \left\langle [\mathcal{J}_{\alpha\beta}(0), \mathcal{J}_{\gamma\delta}(0)] \right\rangle + \omega_+ \int_0^{\infty} \mathrm{d}t e^{\mathrm{i}\omega_+ t} \left\langle [\mathcal{J}_{\alpha\beta}(t), \mathcal{J}_{\gamma\delta}(0)] \right\rangle . \tag{3.37}$$

This formula for the viscosity tensor is used in Sec. 9.2.2 where the scaling factor of different contributions of the viscosity tensor for ADSs is determined via the above expression of the viscosity.

3.4 Scaling behavior of the viscosity

Here, the scaling behavior of the viscosity for a d-dimensional system under a RG calculation is investigated. Analogous to the analysis of the conductivity in the previous chapter Sec. 2.3, a Ward identity is used to determine the scaling factor Z_η for two-dimensional, renormalized systems.

Let us shortly repeat the very basics of the RG. After integrating out the fast fermionic modes in the RG process, we obtain an effective theory which has the UV cut-off Λ/b and which only depends on the slow fermionic modes. Next, the momentum and the frequency are rescaled by $\boldsymbol{k}' = b\boldsymbol{k}$ and $\omega' = Z_T^{-1}\omega$ in such a way that these new variables run to the old cut-off Λ. In this process also the viscosity is rescaled.

As seen in the previous section, the viscosity is defined for finite frequency as the correlation function of the energy-stress tensors

$$\eta_{\alpha\beta\gamma\delta}(\omega) = -\operatorname{Im}\frac{\chi_{T_{\alpha\beta}T_{\gamma\delta}}(\omega)}{\omega}\,, \tag{3.38}$$

where the correlation function has the scaling factor $Z_{\chi_{T_{\alpha\beta}T_{\gamma\delta}}} = Z_T b^{-d} {Z_{T_{\alpha\beta}}}^2$, which depends on the scaling of the energy-stress tensor $Z_{T_{\alpha\beta}}$. This implies that the scaling factor of the viscosity has the form

$$\eta_{\alpha\beta\gamma\delta}(\omega, T) = b^{-d} Z^2_{T_{\alpha\beta}} {\eta_{\alpha\beta\gamma\delta}}_R(Z_T^{-1}\omega, Z_T^{-1}T)\,, \tag{3.39}$$

which means that we have to determine $Z_{T_{\alpha\beta}}$. This is done using the Ward identity describing the conservation of the momentum density. By applying the continuity equation for the momentum density, $\partial_t g_\alpha(\boldsymbol{r},t) + \nabla_{r_\beta} T_{\beta\alpha}(\boldsymbol{r},t) = 0$, and following the steps described in Refs. 40 and 41 we obtain the Ward identity

$$\begin{aligned} \partial_\tau \left\langle T_\tau g_\alpha(\boldsymbol{r},\tau)\hat{\psi}_{\boldsymbol{r_1},\tau_1}\hat{\psi}^\dagger_{\boldsymbol{r}_2,\tau_2}\right\rangle - \mathrm{i}\nabla_{r_\beta}\left\langle T_\tau T_{\beta\alpha}(\boldsymbol{r},\tau)\hat{\psi}_{\boldsymbol{r_1},\tau_1}\hat{\psi}^\dagger_{\boldsymbol{r}_2,\tau_2}\right\rangle \\ = -\mathrm{i}[\delta^{(d)}(\boldsymbol{r}-\boldsymbol{r}_1)\delta(\tau-\tau_1)\left\langle(-\mathrm{i}\partial_{r_\alpha})\hat{\psi}_{\boldsymbol{r},\tau}\hat{\psi}^\dagger_{\boldsymbol{r}_2,\tau_2}\right\rangle - \delta^{(d)}(\boldsymbol{r}-\boldsymbol{r}_2)\delta(\tau-\tau_2)\left\langle\hat{\psi}_{\boldsymbol{r_1},\tau_1}(-\mathrm{i}\partial_{r_\alpha})\hat{\psi}^\dagger_{\boldsymbol{r},\tau}\right\rangle]\,. \end{aligned} \tag{3.40}$$

In order to study the scaling of this equation, we Fourier transform the momentum density $g_\alpha(\boldsymbol{q},\omega)$ and the energy-stress tensor $T_{\alpha\beta}(\boldsymbol{q})$ which enter the above Kubo-formula (3.38) to the real space, and find the following scaling behavior

$$\begin{aligned} g_\alpha(\boldsymbol{r},\tau) &= Z_g Z_T b^{-2} {g_\alpha}_R(\boldsymbol{r}/b, \tau Z_T) \\ T_{\beta\alpha}(\boldsymbol{r},\tau) &= Z_{T_{\alpha\beta}} Z_T b^{-2} {T_{\beta\alpha}}_R(\boldsymbol{r}/b, \tau Z_T)\,, \end{aligned} \tag{3.41}$$

where Z_g is the scaling factor of the momentum density in momentum space, and $Z_{T_{\alpha\beta}}$ the one of the energy-stress tensor also in momentum space. Inserting these relations into the Ward identity (3.40), rescaling $\boldsymbol{r} \to b\boldsymbol{r}$ and $\tau \to \tau/Z_T$ (and similarly for $\boldsymbol{r}_1$, τ_1, etc.), the Ward-identity which can also be applied in the renormalized system implies

$$\begin{aligned} Z_g &= b Z_T^{-1}\,, \\ Z_{T_{\alpha\beta}} &= b^0 = 1\,. \end{aligned} \tag{3.42}$$

When we compare the scaling of the momentum density Z_g to the scaling of the particle density Z_n defined in Eq. (2.14), we see that Z_g has an additional b factor. Furthermore, we see that the scaling factor of the energy-stress tensor does neither depend on b nor on Z_T, but is one. Hence, we find the scaling behavior of the viscosity of a renormalized, d-dimensional system with

$$\eta_{\alpha\beta\gamma\delta}(\omega, T) = b^{-d}\ {\eta_{\alpha\beta\gamma\delta}}_R(Z_T^{-1}\omega, Z_T^{-1}T)\,. \tag{3.43}$$

The viscosity of a two dimensional system is thus not scale invariant, but scales with $Z_\eta = b^{-2}$.

3.5 Ansatz for out-off equilibrium function in the Boltzmann equation

As we have seen in the previous chapters, transport properties of materials can also be determined by the Boltzmann equation in the hydrodynamic regime. The Boltzmann equation describes the time evolution of the distribution function of the particles of the fluid. This distribution function $f_{\lambda\boldsymbol{k}}$

consists of an equilibrium distribution of the fluid $f^{(0)}_{\lambda\boldsymbol{k}}$ and an out-off equilibrium correction $\delta f_{\lambda\boldsymbol{k}}$, i. e., $f_{\lambda\boldsymbol{k}} = f^{(0)}_{\lambda\boldsymbol{k}} + \delta f_{\lambda\boldsymbol{k}}$. The equilibrium distribution function is given by a Fermi-Dirac distribution function, while the out-off equilibrium correction denoting the response to a perturbation which in the case of the viscosity the gradient of the drift velocity $\partial u_\beta/\partial x_\alpha$ is unknown.

In this section, we derive an ansatz for this out-off equilibrium distribution function from the Hamiltonian of a perturbed, two-band system. This Hamiltonian is given by

$$\mathcal{H}_t = \int_{V_0} \mathrm{d}^2x \hat{\psi}^\dagger_{\boldsymbol{x}} \epsilon_{\lambda\boldsymbol{p}} \hat{\psi}_{\boldsymbol{x}} - \int \mathrm{d}^2x \hat{\psi}^\dagger_{\boldsymbol{x}} \mathcal{L}_{\alpha\beta} \frac{\partial u_\beta}{\partial x_\alpha} \hat{\psi}_{\boldsymbol{x}} \tag{3.44}$$

with $\mathcal{L}_{\alpha\beta} = -x_\alpha p_\beta + \frac{\mathrm{i}}{2}\delta_{\alpha\beta}$ being the strain generator coupling to a velocity gradient $\partial u_\alpha/\partial x_\beta$. Upon inserting this definition of the strain tensor into the above equation and applying integration by parts for the term proportional to $-x_\alpha p_\beta$ and using that the momentum is defined as $p_\beta = -\mathrm{i}\hbar\partial_{x_\alpha}$ for the term proportional to $\delta_{\alpha\beta}$, we find

$$\mathcal{H}_t = \int_{V_0} \mathrm{d}^2x \hat{\psi}^\dagger_{\boldsymbol{x}} \Big(\epsilon_{\lambda\boldsymbol{p}} - p_\beta u_\beta \Big[1 - \frac{\delta_{\alpha\beta}}{2}\Big]\Big) \hat{\psi}_{\boldsymbol{x}} \,. \tag{3.45}$$

The energy $\epsilon_{\lambda\boldsymbol{p}}$ of the system is modified by the drift velocity $\boldsymbol{u}$. We can thus write for the distribution function

$$f_{\lambda\boldsymbol{p}} = \frac{1}{1 + \mathrm{e}^{\big(\epsilon_{\lambda\boldsymbol{p}} - p_\beta u_\beta (1-\delta_{\alpha\beta}/2)\big)/T}} + \delta f_{\lambda\boldsymbol{p}} \,, \tag{3.46}$$

where the energy dispersion $\epsilon_{\lambda\boldsymbol{p}}$ of the equilibrium distribution function is replaced by the modified energy. In leading order of the velocity gradient $\frac{\partial u_\alpha}{\partial x_\beta}$, we find

$$\frac{\partial f_{\lambda\boldsymbol{k}}}{\partial x_\beta} = -k_\alpha \frac{\partial u_\alpha}{\partial x_\beta} \Big(-\frac{\partial f^{(0)}_{\lambda\boldsymbol{k}}}{\partial \epsilon_{\lambda\boldsymbol{k}}} \Big) \Big[1 - \delta_{\alpha\beta}/2\Big] \,. \tag{3.47}$$

Upon inserting the above expression into the Boltzmann equation, it holds for the Boltzmann equation in the relaxation-time approximation

$$\frac{\partial f_{\lambda\boldsymbol{k}}}{\partial t} + v^\beta_{\lambda\boldsymbol{k}} k_\alpha \Big(1 - \frac{\delta_{\alpha\beta}}{2}\Big) \frac{\partial u_\alpha}{\partial x_\beta} f^{(0)}_{\lambda\boldsymbol{k}} (1 - f^{(0)}_{\lambda\boldsymbol{k}})/T = -\frac{\delta f_{\lambda\boldsymbol{k}}}{\tau_{\mathrm{dis}}} \,, \tag{3.48}$$

where τ_{dis} is the scattering time due to impurities in the system and $\delta f_{\lambda\boldsymbol{k}} = f_{\lambda\boldsymbol{k}} - \big\langle f_{\lambda\boldsymbol{k}} \big\rangle_\varphi$ with $\big\langle f_{\lambda\boldsymbol{k}} \big\rangle_\varphi$ being the angular average performed over the directions of $\boldsymbol{k}$. In the following, we take a closer look at the term proportional to the velocity gradient

$$(v^\beta_{\lambda\boldsymbol{k}} k_\alpha - v^\beta_{\lambda\boldsymbol{k}} k_\alpha \delta_{\alpha\beta}/2) = (v^\beta_{\lambda\boldsymbol{k}} k_\alpha - \underbrace{\frac{\partial \epsilon_{\lambda\boldsymbol{k}}}{\partial k_\alpha} k_\alpha}_{\approx \epsilon_{\lambda\boldsymbol{k}}} \delta_{\alpha\beta}/2) \,. \tag{3.49}$$

The term proportional to $\delta_{\alpha\beta}$ can again be rewritten as the energy $\epsilon_{\lambda\boldsymbol{k}}$ of the unperturbed system. Using this approximation, we obtain, upon solving the Boltzmann equation (3.48), for the out-off equilibrium correction in the relaxation-time approximation[2]

$$\delta f_{\lambda\boldsymbol{k}} = \sum_{\alpha\beta} \frac{T^{-1} f^{(0)}_{\lambda\boldsymbol{k}} (1 - f^{(0)}_{\lambda\boldsymbol{k}})}{-\mathrm{i}\omega - \tau^{-1}_{\mathrm{dis}}} \Big(v^\beta_{\lambda\boldsymbol{k}} k_\alpha - \epsilon_{\lambda\boldsymbol{k}} \delta_{\alpha\beta}/2 \Big) \frac{\partial u_\alpha}{\partial x_\beta} \,. \tag{3.50}$$

---

[2] In the relaxation-time approximation, we assume that the energy can only relax via scattering off impurities within the scattering time τ_{dis} and no other processes are taken into account.

Now, knowing the out-off equilibrium correction, we are able to determine the dissipative part of energy-stress tensor

$$\begin{aligned}\left\langle \tau_{\alpha\beta} \right\rangle &= \sum_{\lambda} \int_{\boldsymbol{k}} v^{\alpha}_{\lambda\boldsymbol{k}} k_{\beta} \delta f_{\lambda\boldsymbol{k}} \\ &= \sum_{\lambda} \int_{\boldsymbol{k}} v^{\alpha}_{\lambda\boldsymbol{k}} k_{\beta} \sum_{\alpha\beta} \frac{T^{-1} f^{(0)}_{\lambda\boldsymbol{k}} (1 - f^{(0)}_{\lambda\boldsymbol{k}})}{-\mathrm{i}\omega - \tau^{-1}_{\mathrm{dis}}} \left(v^{\beta}_{\lambda\boldsymbol{k}} k_{\alpha} - \epsilon_{\lambda\boldsymbol{k}} \delta_{\alpha\beta}/2 \right) \frac{\partial u_{\alpha}}{\partial x_{\beta}} ,\end{aligned} \tag{3.51}$$

which defines the viscosity tensor in the relaxation-time approximation. When we want to go beyond the relaxation-time approximation and take also scattering processes due to Coulomb interaction into account, we generalize the above expression for the out-off equilibrium distribution function to

$$\delta f_{\lambda\boldsymbol{k}} = \frac{1}{T} f^{(0)}_{\lambda\boldsymbol{k}} \left(1 - f^{(0)}_{\lambda\boldsymbol{k}} \right) h_{\lambda\boldsymbol{k}} , \tag{3.52}$$

with

$$h_{\lambda\boldsymbol{k}} = \sum_{\alpha\beta} \left(v^{\beta}_{\lambda\boldsymbol{k}} k_{\alpha} - \epsilon_{\lambda\boldsymbol{k}} \delta_{\alpha\beta}/2 \right) \frac{\partial u_{\alpha}}{\partial x_{\beta}} g_{\lambda\boldsymbol{k}}{}^{\beta} , \tag{3.53}$$

where the function $g^{\beta}_{\lambda\boldsymbol{k}}$ is can be expanded into a set of basis functions which are weighted with unknown coefficients ψ^{β}_{n}, i. e., $g^{\beta}_{\lambda\boldsymbol{k}} = \sum_{n} \psi^{\beta}_{n} \phi^{(n)}_{\lambda,\boldsymbol{k}}$.

3.6 The Lower Bound

So far, we defined the viscosity tensor and showed how the viscosity can be determined in different formalisms. However, we have not introduced a measure for the magnitude of the viscosity, or in other words: we have no indicator if the determined viscosity is large or not. In the following section, the ratio viscosity η over entropy density s is introduced for this purpose. We repeat the arguments of Kovtun, Son, and Starinets [18] and show that there exist a lower bound for the ratio η/s. The closer the ratio η/s of a fluid is to the lower bound, the more perfect the fluid is. Here, a fluid with zero viscosity is referred to as an ideal fluid. Most fluids have a ratio of η/s which is larger than the lower bound, and so far all known condensed matter systems fulfill it. However, there are systems in cosmology [52–57] and an ultra-cold gas system [58, 59] which violate the lower bound in the second part of this section.

Furthermore, in the third part of this thesis, we present the up to our knowledge first condensed matter realization which violates the lower bound of η/s. These systems are the anisotropic Dirac system (ADS) and the viscosity of these systems and the violation of the lower bound is discussed in Chap. 9.

3.6.1 Derivation of the lower bound

In order to derive the famous lower bound of the ratio η/s the anti-de Sitter/conformal field theory (AdS/CFT) correspondence is applied. The AdS/CFT correspondence connects the $\mathcal{N} = 4$ super-symmetric Yang-Mills (SYM) theory in the strong coupling, large N limit with a classical ten-dimensional supergravity theory [60–63].

The idea behind this correspondence is the following. In a type IIB string theory, N black branes are stacked on top of each other [64]. Black branes are black holes with translationally invariant horizons in higher-dimensional gravity theories [18, 65]. The $\mathcal{N}=4$ SYM is the low-energy theory which lives on the branes [64] and the typical parameters are the gauge coupling g and the number of colors N. This theory describes a strongly coupled quark-gluon plasma. For large N the stack of the branes has a large tension, which curves space-time [64]. In the limit of large 't Hooft coupling $\lambda = g^2 N$, the curvature radius of the space-time is large in comparison to the string length, and the string theory can be reduced to a ten-dimensional supergravity theory [66]. Thus, the physics of a strongly coupled field theory can also be described by a higher dimensional, classical gravity theory.

As a consequence of the AdS/CFT correspondence, the viscosity η can be calculated by the absorption cross section $\sigma(\omega)$ of a graviton polarized parallel to the brane which falls in a 90 degrees angle on the brane. This absorption cross section is defined by the correlation function between two energy-stress tensors as it is the case for the viscosity tensor, see (3.36). Hence, the absorption cross section and the viscosity are connected via

$$\begin{aligned}\sigma(\omega) &= \frac{\kappa^2}{\omega}\int \mathrm{d}t\mathrm{d}\boldsymbol{x}\ \mathrm{e}^{\mathrm{i}\omega t}\left\langle T_{xy}(t,\boldsymbol{x}), T_{xy}(0,0)\right\rangle \\ &= 2\kappa^2\eta(\omega)\end{aligned} \tag{3.54}$$

where $\kappa = \sqrt{8\pi G}$ and G is the ten-dimensional gravitational constant [64]. This cross section is calculated upon linearizing the Einstein's equations which connects the Einstein tensor describing the curvature of the space to the energy-stress tensor and thus solving this linearized wave equation.

Furthermore, the entropy of the strongly coupled quantum field theory can also be determined by the AdS/CFT correspondence, since the entropy of the field theory is equal to entropy of a black brane. The entropy of a black brane is proportional to the area A of its event horizon [18]

$$S = \frac{A}{4G}\,. \tag{3.55}$$

The entropy density s is given by $s = a/(4G)$ with $a = A/V$. After determining these quantities, Kovtun *et al.* [18] find

$$\frac{\eta}{s} \geq \frac{1}{4\pi}\frac{\hbar}{k_B} \approx 6.08\times 10^{-13}\mathrm{Ks}\,. \tag{3.56}$$

The ratio of these two quantities cannot become smaller than the ratio of the reduced Planck constant and the Boltzmann factor. Naturally the question of the physical meaning of this lower bound arises. This question can be answered in the following way: The viscosity of a system is proportional to the transport mean free time of a quasi-particle τ and the energy density n_ϵ, i. e., $\eta \propto \tau n_\epsilon$, while the entropy density of the system is proportional to the particle density n and the Boltzmann constant, i. e., $s \propto k_\mathrm{B} n$. Thus, the ratio of viscosity over entropy is proportional to $\eta/s \propto k_\mathrm{B}^{-1}\tau n_\epsilon/n$, where n_ϵ/n is the energy per particle. Due to Heisenberg's uncertainty principle, the product of n_ϵ/n and τ cannot be smaller than $\hbar$ and we find the bound condition $\eta/s \gtrsim \hbar/k_\mathrm{B}$. Another interpretation can be given upon taking into account that the ratio viscosity over entropy is also proportional to

$$\frac{\eta}{s} \sim \frac{\ell_\mathrm{mfp}}{\lambda}\,, \tag{3.57}$$

where ℓ_mfp is the mean free path of the quasiparticles and λ denotes the de Broglie wavelength [66]. If the quasi-particle picture is valid, ℓ_mfp has to be larger than λ which leads again to the lower bound for the ratio.

Up till now, all known condensed matter systems fulfill the lower bound. The temperature dependence of the ratio η/s for different fluids such as helium, nitrogen and water can be found in Fig. 3.2, where we see explicitly that these fluids have a ratio η/s which is well above the lower bound.

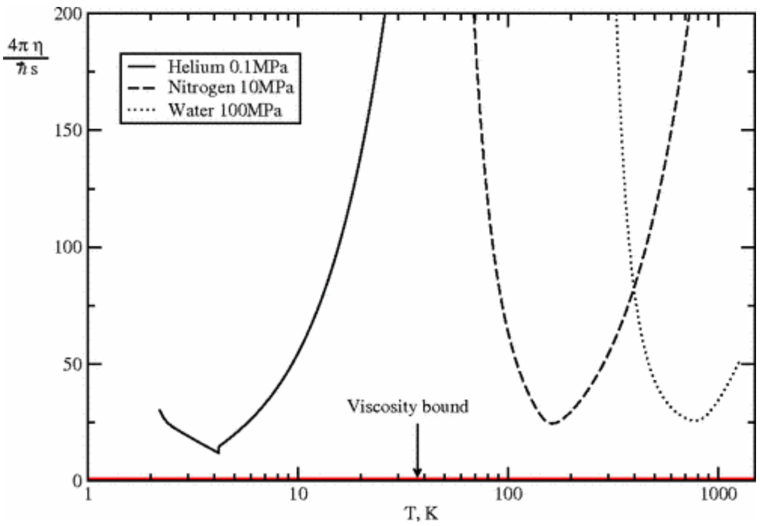

[Reprinted figure with permission from P. K. Kovtun, D. T. Son, and A. O. Starinets, Phys. Rev. Lett. **94**, 111601 (2005). Copyright 2005 by the American Physical Society]

Figure 3.2: The temperature dependence of the ratio η/s for different fluids. The figure was taken from [18].

3.6.2 Violation of the lower bound

Soon after the introduction of the lower bound to the ratio η/s, some counter examples where found. These systems are anisotropic black holes where the anisotropy is introduced by higher order derivative theories of gravity [53–55]. It was shown that when these systems violate the lower bound, the microcausality in the conformal field theory is violated which makes the theory inconsistent [54].

Another example which violates the lower bound is an anisotropic, strongly coupled $\mathcal{N} = 4$ SYM where the anisotropy is introduced by an additional parameter which depends linearly on one of the spatial dimensions [52]. The corresponding gravity theory is given by an anisotropic axion-dilation-gravity background [52].

The violation of the lower bound can also be found in super-conformal gauge theories with non-equal central charge [56] and in black branes which break rotational symmetry while preserving the translational invariance [67].

These are all examples of systems violating the lower bound in cosmology. But, another system violating the lower bound which is not an anisotropic black hole are the ultra-cold atomic gases in an anharmonic trap [58, 59]. The interaction between the ultra-cold gases can be tuned via a Feshbach resonance [68] to the very strong coupling limit. Upon making the trap potential extreme anisotropic, the ratio η/s can theoretically violate the lower bound.

We have seen that anisotropic black holes and ultra-cold atomic gases in an asymmetric trap can violate the lower bound. In Chap. 9, we study the first condensed matter system which will violate the lower bound.

3.7 Summary

In this chapter, we defined the viscosity tensor which connects the energy-stress tensor to the gradient of the drift velocity

$$T_{\alpha\beta} = \sum_{\gamma\delta} \eta_{\alpha\beta\gamma\delta} \frac{\partial u_\delta}{\partial x_\gamma} \,. \tag{3.58}$$

The energy-stress tensor can be derived from the total strain generator $\mathcal{J}_{\alpha\beta}$, i. e., $T_{\alpha\beta} = -\partial_t \mathcal{J}_{\alpha\beta}$. The strain generator consists of a contribution acting on the spatial coordinates $\mathcal{L}_{\alpha\beta} = \{x_\alpha, p_\beta\}/2$, while the other contribution acts on the pseudospin space $\mathcal{S}_{\alpha\beta} = \mathrm{i}[S_\alpha, S_\beta]/2$. Furthermore, we derived the Kubo-formula for the viscosity which is given by

$$\eta_{\alpha\beta\gamma\delta}(\omega) = \pi D_{\alpha\beta\gamma\delta}\delta(\omega) - \frac{\operatorname{Im}\chi_{T_{\alpha\beta}T_{\gamma\delta}}}{\omega} \,, \tag{3.59}$$

where $\chi_{T_{\alpha\beta}T_{\gamma\delta}}$ is the correlation function of two energy-stress tensors and $D_{\alpha\beta\gamma\delta}$ the corresponding Drude peak. In the next section, we derived using momentum conservation and the respective Ward identity the scaling factor of the viscosity under a renormalization group (RG) analysis and found

$$\eta(\omega, T) = b^{-2}\eta_R(Z_T^{-1}\omega, Z_T^{-1}T) \,. \tag{3.60}$$

Next, upon determining the viscosity in the hydrodynamic regime with the help of the Boltzmann equation, we derived the ansatz for the out-off equilibrium contribution $\delta f_{\lambda\boldsymbol{k}} = f^{(0)}_{\lambda\boldsymbol{k}}(1 - f^{(0)}_{\lambda\boldsymbol{k}})h_{\lambda\boldsymbol{k}}/T$ with

$$h_{\lambda\boldsymbol{k}} = \sum_{\alpha\beta} \left(v^\beta_{\lambda\boldsymbol{k}} k_\alpha - \epsilon_{\lambda\boldsymbol{k}}\delta_{\alpha\beta}/2\right) \frac{\partial u_\alpha}{\partial x_\beta} {g_{\lambda\boldsymbol{k}}}^\beta \,. \tag{3.61}$$

In the last section the famous lower bound of the ratio viscosity over entropy density

$$\frac{\eta}{s} \geq \frac{\hbar}{4\pi k_\mathrm{B}} \tag{3.62}$$

was obtained and a physical interpretation was given.

Part II

Graphene

Chapter 4

4 Field theoretical description and the Coulomb interaction

Graphene is a two dimensional material consisting of carbon atoms ordered in a honeycomb lattice. It is a material with many fascinating properties, such as a high mobility of the charge carriers at room temperature, a high transmissivity of optical light and its the strongest material in the world [69–71]. Graphene is also the building block of many carbon based crystals due to its high flexibility. If one rolls graphene up, one obtains the one-dimensional carbon nanotubes, whereas the three dimensional graphite crystal is build up of many different layers of graphene which are stacked on top of each other. It was long believed that graphene does not exist on its own due to the the thermodynamical unstable behavior of two dimensional crystals predicted by Landau and Peierls [70] and manifested further by Mermin [72]. Nevertheless, it rose the interest to theoretical studies as a building block for graphite. Already in 1947, Wallace predicted the band structure of graphene [73] and further studies followed by McClure [74] and Slonczewski [75]. It took almost 60 years untill graphene was experimentally isolated by Novoselov *et al.* in the year 2004 [76]. They used mechanical exfoliating techniques, where they repeatedly peeled different layers from a graphite crystal with the help of an adhesive band until they isolated a graphene flake. In 2010, Andre Geim and Konstantin Novoselov were awarded the Nobel Prize in physics for the discovery of graphene.

A further characteristic of graphene lies in its linear, gapless energy dispersion at the Dirac points. Because of the linear energy dispersion, the quasiparticles of graphene can be described by massless Dirac fermions, which makes graphene a quasirelativistic system. Hence, we have in graphene a condensed matter system that can simulate quantum electrodynamics in $2+1$ dimensions. The difference to QED_{2+1} is that the Dirac fermions of graphene move with the Fermi velocity $v_\mathrm{F} = 1 \cdot 10^6\,\frac{\mathrm{m}}{\mathrm{s}}$ [69] which is approximately 300 times smaller than the speed of light c. The electron-electron Coulomb interaction can thus be regarded as instantaneous.

The influence of the Coulomb interaction can be found in the hydrodynamic regime of graphene, where we see the breakdown of the Wiedemann-Franz law [28], a giant magnetodrag [32], and a local negative resistivity [30]. Further sings of the effect of the Coulomb potential are found in the logarithmic divergence of the Fermi velocity [6], and angular resolved photoemission spectroscopy [23].

In the first part of this chapter, Sec. 4.1 and Sec. 4.2, we will lay the foundations for a theoretical description of graphene. Thereby, we will start with the tight-binding description of graphene and define the most important operators in this description such as the current operator. Further using the tight-binding model as a starting point, we will derive the relativistic Dirac model. After being able

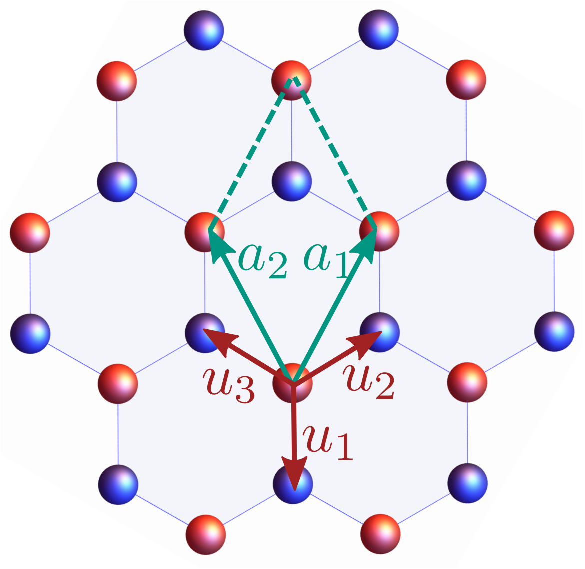

Figure 4.1: The structure of graphene is a honeycomb lattice spanned by the Bravais lattice vector $\boldsymbol{a}_1$ and $\boldsymbol{a}_2$. It has a two-atomic basis with the basis vectors $\boldsymbol{v}_{1,2}$ depicted by the red and blue color of the carbon atoms. The nearest neighbor vectors are $\boldsymbol{u}_\alpha = \boldsymbol{\delta}_\alpha + \boldsymbol{v}_2 - \boldsymbol{v}_1$ with the nearest Bravais lattice vectors $\boldsymbol{\delta}_1 = (0,0)$, $\boldsymbol{\delta}_2 = \boldsymbol{a}_2$, and $\boldsymbol{\delta}_3 = \boldsymbol{a}_2$.

to describe the non-interacting graphene, we want to pose, in the second part of this chapter, Sec. 4.3, one of the main questions asked in this thesis: What is the role of the Coulomb interaction acting on the electrons of the system and how can this influence of the interaction on optical and transport properties be described theoretically.

4.1 The tight-binding description

Graphene as a two dimensional (2D) crystal consists only of one layer of atoms. Due to the sp^2-hybridization of the s- and p-orbitals of the carbon atoms, graphene has a honeycomb structure. This structure can be described by a lattice with a two-atomic basis which is generated by the Bravais lattice vectors $\boldsymbol{R}_i = i_1\boldsymbol{a}_1 + i_2\boldsymbol{a}_2$ with $i_1, i_2 \in \mathbb{Z}$. The primitive vectors have the form

$$\boldsymbol{a}_1 = \frac{a}{2}\begin{pmatrix}\sqrt{3}\\ 3\end{pmatrix} \text{ and } \boldsymbol{a}_2 = \frac{a}{2}\begin{pmatrix}-\sqrt{3}\\ 3\end{pmatrix}, \tag{4.1}$$

where a is the carbon-carbon distance. The two-atomic basis of the lattice is given by the basis vectors $\boldsymbol{v}_{1,2}$ where we choose $\boldsymbol{v}_1 = \boldsymbol{0}$ and $\boldsymbol{v}_2 = \big(0, -a\big)$, and is depicted by the red and blue atoms in Fig. 4.1. The tight-binding Hamiltonian models the kinetic energy of the electrons hopping from one site to another site and is defined as

$$\mathcal{H}_{0,\boldsymbol{r}} = \sum_{\langle \boldsymbol{R}_n, \boldsymbol{R}_m \rangle} -t_{nm}\left(\hat{a}^\dagger_{\boldsymbol{R}_n}\hat{b}_{\boldsymbol{R}_m} + \hat{a}_{\boldsymbol{R}_n}\hat{b}^\dagger_{\boldsymbol{R}_m}\right), \tag{4.2}$$

where the fermionic operator $\hat{a}^\dagger_{\boldsymbol{R}_n}$ creates an electron at the site $\big(\boldsymbol{R}_n, \boldsymbol{v}_1\big)$ and the operator $\hat{b}^\dagger_{\boldsymbol{R}_n}$ creates an atom at the same site $\big(\boldsymbol{R}_n, \boldsymbol{v}_2\big)$, while the operators $\hat{a}_{\boldsymbol{R}_n}$ and $\hat{b}_{\boldsymbol{R}_n}$ annihilate an electron from the

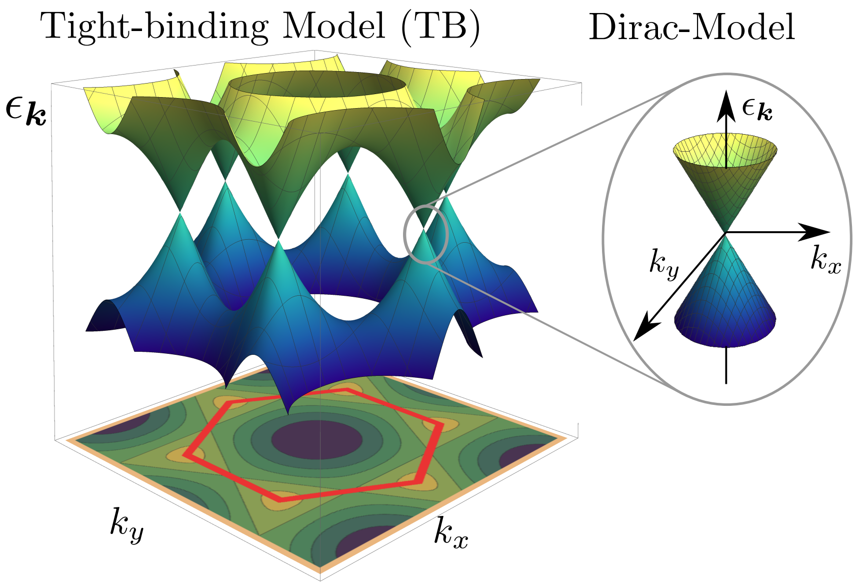

Figure 4.2: The energy dispersion of graphene is shown. The two energy bands touch at two points in the first Brillouin zone indicated by the red line. These points are known as Dirac points and a linear energy spectrum emerges around these points.

respective site. The kinetic energy needed to jump from site $(\boldsymbol{R}_n, \boldsymbol{v}_1)$ to the site $(\boldsymbol{R}_m, \boldsymbol{v}_2)$ is given by the hopping matrix element t_{nm} [1]. In the following, we will restrict ourselves only to nearest neighbor hopping and introduce the Fourier transformation $\hat{c}_{\boldsymbol{R}_i} = \frac{1}{\sqrt{N}} \sum_{\boldsymbol{k}} e^{\mathrm{i}\boldsymbol{k}\boldsymbol{R}_i} \hat{c}_{\boldsymbol{k}}$ with $\hat{c} \in \{\hat{a}, \hat{b}\}$. The Hamiltonian of the tight-binding model in momentum space can now be cast into the form

$$\mathcal{H}_0 = -t \sum_{\boldsymbol{k}} \begin{pmatrix} a^\dagger_{\boldsymbol{k}} & b^\dagger_{\boldsymbol{k}} \end{pmatrix} \begin{pmatrix} 0 & h_{\boldsymbol{k}} \\ h^*_{\boldsymbol{k}} & 0 \end{pmatrix} \begin{pmatrix} a_{\boldsymbol{k}} \\ b_{\boldsymbol{k}} \end{pmatrix}, \tag{4.3}$$

with

$$h_{\boldsymbol{k}} = 1 + e^{\mathrm{i}\boldsymbol{k}\boldsymbol{a}_1} + e^{\mathrm{i}\boldsymbol{k}\boldsymbol{a}_2}\,. \tag{4.4}$$

For our choice of the primitive vectors, we find $h_{\boldsymbol{k}} = 1 + 2\cos\left(\frac{\sqrt{3}}{2}k_x a\right) e^{\mathrm{i}\frac{3}{2}k_y a}$. The energy dispersion of graphene consists of two energy bands which are given by:

$$\epsilon_{\pm\boldsymbol{k}} = \pm t|h_{\boldsymbol{k}}| = \pm t\sqrt{3 + 2\cos\left(\sqrt{3}ak_x\right) + 4\cos\left(\frac{1}{2}\sqrt{3}ak_x\right)\cos\left(\frac{3ak_y}{2}\right)}\,. \tag{4.5}$$

The two energy bands touch at two points in the first Brillouin zone, as can be seen in Fig. 4.2. These two points are known as Dirac points and are positioned at $\boldsymbol{K}_\pm = \frac{2\pi}{3a}\left(\pm\frac{1}{\sqrt{3}}, 1\right)$. A linear energy dispersion emerges around these Dirac points and we will derive the Dirac model for graphene in the next Sec. 4.2. But before we study the Dirac model in more details, we will define different important quantities of the tight-binding description needed in the remainder of the thesis.

---

[1] The braket notation in the summation index should indicate that we do not double count the hopping processes.

One of these quantities is the Matsubara Green's function which is given by $\mathcal{G}_{\boldsymbol{k},\mathrm{i}\omega} = \big(\mathrm{i}\omega - \mathcal{H}_0\big)^{-1}$ and has the explicit form

$$\mathcal{G}_{\boldsymbol{k},\mathrm{i}\omega} = \frac{1}{\omega^2 + t^2|h_{\boldsymbol{k}}|^2} \begin{pmatrix} -\mathrm{i}\omega & t\, h_{\boldsymbol{k}} \\ t\, h^*_{\boldsymbol{k}} & -\mathrm{i}\omega \end{pmatrix} . \tag{4.6}$$

The other quantity which needs to be defined in the tight-binding description is the electrical current $\hat{\boldsymbol{j}}$. This operator can be derived in two different ways. One way is the well known Peierls substitution [77] and the other way is the calculation of the time derivative of the polarization operator after Mahan [39]. In the following, we briefly sketch the two approaches that give identical results. Let us first start with the derivation by Mahan. According to Mahan, the electrical current is defined by the formula

$$\hat{\boldsymbol{J}} = \mathrm{i}[\mathcal{H}, \hat{\boldsymbol{P}}] \tag{4.7}$$

with the polarization $\hat{\boldsymbol{P}} = \sum_i \boldsymbol{R}_i n_i$ which can be derived using the continuity equation of the particle density. In our honeycomb lattice with the two-atomic basis, the polarization operator consists of two parts, one part describing the density of the electrons on the A sublattice and the other part is the density of the B sublattice, leading to the following expression of the polarization operator

$$\hat{\boldsymbol{P}} = -t \sum_{i\in\mathbb{Z}} \left[\big(\boldsymbol{R}_i + \boldsymbol{v}_1\big)\, \hat{a}^\dagger_{\boldsymbol{R}_i} \hat{a}_{\boldsymbol{R}_i} + \big(\boldsymbol{R}_i + \boldsymbol{v}_2\big)\, \hat{b}^\dagger_{\boldsymbol{R}_i} \hat{b}_{\boldsymbol{R}_i} \right] . \tag{4.8}$$

After computing the commutator of Eq. (4.7), we find for the current operator

$$\hat{\boldsymbol{J}}_{\boldsymbol{R}} = -\mathrm{i}t \sum_{i\in\mathbb{Z},\alpha} \big(\boldsymbol{\delta}_\alpha + \boldsymbol{v}_2 - \boldsymbol{v}_1\big) \left(\hat{a}^\dagger_{\boldsymbol{R}_i} \hat{b}_{\boldsymbol{R}_i+\boldsymbol{\delta}_\alpha} - \hat{a}_{\boldsymbol{R}_i} \hat{b}^\dagger_{\boldsymbol{R}_i+\boldsymbol{\delta}_\alpha} \right) , \tag{4.9}$$

with $\boldsymbol{\delta}_1 = \boldsymbol{0}$, $\boldsymbol{\delta}_2 = \boldsymbol{a}_1$ and $\boldsymbol{\delta}_3 = \boldsymbol{a}_2$ and the nearest-neighbor vectors $\boldsymbol{u}_\alpha = \boldsymbol{\delta}_\alpha + \boldsymbol{v}_2 - \boldsymbol{v}_1$.

The same expression can also be obtained by the Peierls substitution [77]. In an electromagnetic vector potential $\boldsymbol{A}$ the hopping element t gains an additional phase when the electron jumps along the direction of the nearest-neighbor vector $\boldsymbol{u}_\alpha$ to a neighboring site, i. e., $t \rightarrow\ t\ e^{\mathrm{i}e\boldsymbol{A}\boldsymbol{u}_\alpha}$. Upon differentiating the modified Hamiltonian with respect to the vector field $\boldsymbol{A}$, one obtains the electrical current, i. e.,

$$\hat{\boldsymbol{J}}_{\boldsymbol{R}} = - \left. \frac{\partial \mathcal{H}_{0,\boldsymbol{r}}(t \rightarrow\ t\ e^{\mathrm{i}e\boldsymbol{A}\boldsymbol{u}_\alpha})}{\partial \boldsymbol{A}} \right|_0 , \tag{4.10}$$

which also leads to Eq. (4.9). The Fourier transform of the current operator is

$$\hat{\boldsymbol{J}}_{\boldsymbol{q}} = \sum_{\boldsymbol{k}} \begin{pmatrix} \hat{a}^\dagger_{\boldsymbol{k}+\boldsymbol{q}} & \hat{b}^\dagger_{\boldsymbol{k}+\boldsymbol{q}} \end{pmatrix} \boldsymbol{\mathcal{J}}(\boldsymbol{k},\boldsymbol{q}) \begin{pmatrix} \hat{a}_{\boldsymbol{k}} \\ \hat{b}_{\boldsymbol{k}} \end{pmatrix} \tag{4.11}$$

with

$$\begin{aligned} \boldsymbol{\mathcal{J}}(\boldsymbol{k},\boldsymbol{q}) &= \begin{pmatrix} 0 & \boldsymbol{j}_{\boldsymbol{k}+\boldsymbol{q}} \\ \boldsymbol{j}^*_{\boldsymbol{k}+\boldsymbol{q}} & 0 \end{pmatrix} \\ &= -\frac{\mathrm{i}t}{\hbar} \left[\boldsymbol{u}_3 \begin{pmatrix} 0 & 1 \\ -1 & 0 \end{pmatrix} + \boldsymbol{u}_1 \begin{pmatrix} 0 & e^{\mathrm{i}\boldsymbol{k}\cdot\boldsymbol{a}_1} \\ -e^{\mathrm{i}(\boldsymbol{k}+\boldsymbol{q})\cdot\boldsymbol{a}_1} & 0 \end{pmatrix} + \boldsymbol{u}_2 \begin{pmatrix} 0 & e^{\mathrm{i}\boldsymbol{k}\cdot\boldsymbol{a}_2} \\ -e^{\mathrm{i}(\boldsymbol{k}+\boldsymbol{q})\cdot\boldsymbol{a}_2} & 0 \end{pmatrix} \right] . \end{aligned} \tag{4.12a}$$

The different components of the current operator can be rewritten using the function $h_{\boldsymbol{k}}$ in the $\boldsymbol{q} \to 0$ limit. We find for the x-component:

$$\begin{aligned}\boldsymbol{\mathcal{J}}^x(\boldsymbol{k},\boldsymbol{q}) &= \frac{\sqrt{3}ta}{\hbar}\sin\left(\frac{\sqrt{3}}{2}k_xa\right)\begin{pmatrix}0 & e^{\mathrm{i}\frac{3}{2}k_ya}\\ e^{-\mathrm{i}\frac{3}{2}k_ya} & 0\end{pmatrix}\\ &= -\frac{t}{\hbar}\begin{pmatrix}0 & \partial_{k_x}h_{\boldsymbol{k}}\\ \partial_{k_x}h^*_{\boldsymbol{k}} & 0\end{pmatrix},\end{aligned} \tag{4.12b}$$

and for the y-component:

$$\begin{aligned}\boldsymbol{\mathcal{J}}^y(\boldsymbol{k},\boldsymbol{q}) &= -\frac{\mathrm{i}ta}{\hbar}\begin{pmatrix}0 & \cos\left(\frac{\sqrt{3}}{2}k_xa\right)e^{\mathrm{i}\frac{3}{2}k_ya}-1\\ -\cos\left(\frac{\sqrt{3}}{2}k_xa\right)e^{-\mathrm{i}\frac{3}{2}k_ya}+1 & 0\end{pmatrix}\\ &= -\frac{t}{\hbar}\begin{pmatrix}0 & \frac{1}{3}\partial_{k_y}h_{\boldsymbol{k}}-a\\ \frac{1}{3}\partial_{k_y}h^*_{\boldsymbol{k}}+a & 0\end{pmatrix}.\end{aligned} \tag{4.12c}$$

4.2 The Dirac model

In this section, we are going to derive the Dirac-Hamiltonian from the tight-binding description and study the symmetries of the system. For a more detailed study of the symmetries of graphene, we refer to Refs. 78 and 79. In the tight-binding description, we have seen that the two energy bands touch in two points of the first Brillouin zone. These points are the Dirac points $\boldsymbol{K}_\pm = \frac{2\pi}{3a}\left(\pm\frac{1}{\sqrt{3}},1\right)$. A linear dispersion relation emerges around these points. By expanding the function $h_{\boldsymbol{K}_\pm+\boldsymbol{k}}$, Eq. (4.4), around these two points we find the Dirac-Hamiltonian[2]

$$\mathcal{H}_D = v_{\mathrm{F}}\int\limits_{\boldsymbol{k}}\begin{pmatrix}\hat{a}^\dagger_{\boldsymbol{K}_++\boldsymbol{k}}\\ \hat{b}^\dagger_{\boldsymbol{K}_++\boldsymbol{k}}\\ \hat{b}^\dagger_{\boldsymbol{K}_-+\boldsymbol{k}}\\ \hat{a}^\dagger_{\boldsymbol{K}_-+\boldsymbol{k}}\end{pmatrix}^T\begin{pmatrix}0 & k_x-\mathrm{i}k_y & 0 & 0\\ k_x+\mathrm{i}k_y & 0 & 0 & 0\\ 0 & 0 & 0 & -k_x+\mathrm{i}k_y\\ 0 & 0 & -k_x-\mathrm{i}k_y & 0\end{pmatrix}\begin{pmatrix}\hat{a}_{\boldsymbol{K}_++\boldsymbol{k}}\\ \hat{b}_{\boldsymbol{K}_++\boldsymbol{k}}\\ \hat{b}_{\boldsymbol{K}_-+\boldsymbol{k}}\\ \hat{a}_{\boldsymbol{K}_-+\boldsymbol{k}}\end{pmatrix}, \tag{4.13}$$

where $\boldsymbol{k}$ is the relative momentum to the Dirac points and $v_{\mathrm{F}} = \frac{3}{2}ta$ is the Fermi velocity with $v_{\mathrm{F}} \simeq 1\cdot 10^6\,\frac{\mathrm{m}}{\mathrm{s}}$ [69]. This Hamiltonian can be compactly written as:

$$\mathcal{H}_D = v_{\mathrm{F}}\int\limits_{\boldsymbol{k}}\hat{\Psi}^\dagger_{\boldsymbol{k}}\tau_z\otimes\left(k_x\sigma_x+k_y\sigma_y\right)\hat{\Psi}_{\boldsymbol{k}}\,, \tag{4.14}$$

where the Pauli-matrices σ_x and σ_y describe the pseudo-spin which arises due to the two sublattices of graphene and the Pauli-matrix τ_z describes the subspace of the two Dirac cones. The system consisting of two Dirac cones is invariant under spatial inversion $\mathcal{P}$, i. e. $\mathcal{H}_D \to \mathcal{P}\mathcal{H}_D\mathcal{P}^{-1} = \mathcal{H}_D$. The

---

[2] Note that we interchanged the operators of the A- and B sites for the Dirac point $\boldsymbol{K}_-$.

spatial inversion exchanges both the A- and B-sublattices as well as the Dirac points and the spinor transform as [78]

$$\hat{\Psi}_{\boldsymbol{k}} = \begin{pmatrix} \hat{a}_{\boldsymbol{K}_+ + \boldsymbol{k}} \\ \hat{b}_{\boldsymbol{K}_+ + \boldsymbol{k}} \\ \hat{b}_{\boldsymbol{K}_- + \boldsymbol{k}} \\ \hat{a}_{\boldsymbol{K}_- + \boldsymbol{k}} \end{pmatrix} \xrightarrow{\mathcal{P}} \mathcal{P}\hat{\Psi}_{\boldsymbol{k}} = \begin{pmatrix} \hat{b}_{\boldsymbol{K}_- - \boldsymbol{k}} \\ \hat{a}_{\boldsymbol{K}_- - \boldsymbol{k}} \\ \hat{a}_{\boldsymbol{K}_+ - \boldsymbol{k}} \\ \hat{b}_{\boldsymbol{K}_+ - \boldsymbol{k}} \end{pmatrix} , \tag{4.15}$$

with $\mathcal{P} = \tau_x \otimes \sigma_0$ and $\mathcal{P}^2 = 1$. Here, σ_0 is the 2×2 unity matrix. The Hamiltonian density $H_{D,\boldsymbol{k}}$ of Eq. (4.13) has to fulfill the condition $\mathcal{P}H_{D,\boldsymbol{k}}\mathcal{P} = H_{D,-\boldsymbol{k}}$, in order to conserve the spatial inversion symmetry. Another symmetry of the system is the time reversal $\mathcal{T}$ which only interchanges the Dirac points and the spin but nothing else. The spinors transform under time reversal as [78]

$$\hat{\Psi}_{\boldsymbol{k}} = \begin{pmatrix} \hat{a}_{\boldsymbol{K}_+ + \boldsymbol{k}} \\ \hat{b}_{\boldsymbol{K}_+ + \boldsymbol{k}} \\ \hat{b}_{\boldsymbol{K}_- + \boldsymbol{k}} \\ \hat{a}_{\boldsymbol{K}_- + \boldsymbol{k}} \end{pmatrix} \xrightarrow{\mathcal{T}} \mathcal{T}\hat{\Psi}_{-\boldsymbol{k}} = \begin{pmatrix} \hat{a}_{\boldsymbol{K}_- - \boldsymbol{k}} \\ \hat{b}_{\boldsymbol{K}_- - \boldsymbol{k}} \\ \hat{b}_{\boldsymbol{K}_+ - \boldsymbol{k}} \\ \hat{a}_{\boldsymbol{K}_+ - \boldsymbol{k}} \end{pmatrix} , \tag{4.16}$$

with $\mathcal{T} = \tau_x \otimes \sigma_x$ and $\mathcal{T}^2 = 1$ [3]. The invariance under time reversal is only fulfilled, if the Hamiltonian density obeys the condition $\mathcal{T}H^*_{D,\boldsymbol{k}}\mathcal{T} = H_{D,-\boldsymbol{k}}$, which is here the case. We have seen that both symmetries $\mathcal{P}$ and $\mathcal{T}$ are only fulfilled upon taking both Dirac cones into account. An other symmetry of the Eq. (4.13) is the chirality. The chirality operator γ^5 can be introduced to the Hamiltonian by defining the γ-matrices: $\boldsymbol{\gamma} = -\mathrm{i}\tau_y \otimes (\sigma_x, \sigma_y, \sigma_z)$, $\gamma^0 = \tau_x \otimes \sigma_0$, and $\gamma^5 = \mathrm{i}\gamma^0\gamma^1\gamma^2\gamma^3$. Since the chirality operator commutates with the Hamiltonian, γ^5 is a conserved quantum number and its eigenvalues denote the chirality and we find that the two Dirac cones have the opposite chirality. In this thesis, the effect of the Coulomb interaction on two different transport quantities, the conductivity σ and the viscosity η, is studied. However, the Coulomb interaction does not break chiral symmetry of graphene except for the Hall conductivity. Thus, we can treat the two Dirac cones separately and the Dirac Hamiltonian of graphene can be described by a 2×2 matrix

$$\mathcal{H}_{\mathrm{Dirac}} = N_{sv} \int\limits_{\boldsymbol{k}} \hat{\psi}^\dagger_{\boldsymbol{k}} v_{\mathrm{F}} \Big(k_x\sigma_x + k_y\sigma_y \Big) \hat{\psi}_{\boldsymbol{k}} \,, \tag{4.17}$$

where $N_{sv} = 4$, since we find two possible spin-directions of the electron and two different Dirac cones. This Hamiltonian describes massless Dirac fermions with the energy dispersion

$$\epsilon_{\lambda\boldsymbol{k}} = \lambda v_{\mathrm{F}}\hbar|\boldsymbol{k}| \,, \tag{4.18}$$

where λ is the band index with $\lambda = +1$ for the conductance and $\lambda = -1$ valence band. What still remains to be done, is to define the Matsubara Green's function of graphene in the Dirac model. It holds

$$G_{\boldsymbol{k},\mathrm{i}\omega} = (\mathrm{i}\omega - \mathcal{H}_{\mathrm{Dirac}})^{-1} = -\frac{\mathrm{i}\omega\sigma_0 + v_{\mathrm{F}}\boldsymbol{k}\boldsymbol{\sigma}}{\omega^2 + \big(v_{\mathrm{F}}k\big)^2} \,. \tag{4.19}$$

The current operator of the Dirac model is derived using the minimal substitution $\boldsymbol{k} \to \boldsymbol{k} - e\boldsymbol{A}$ and taking again the derivative of the modified Hamiltonian with respect to the vector potential $\boldsymbol{A}$. It is

$$\hat{j}_\mu = e \int\limits_{\boldsymbol{k}} \hat{\psi}^\dagger_{\boldsymbol{k}} \sigma_\mu \hat{\psi}_{\boldsymbol{k}} \,. \tag{4.20}$$

---

[3] Here, $\mathcal{T}$ is the unitary part of the time reversal operator $\theta = \mathcal{T}\mathcal{C}$ with $\mathcal{C}$ being the complex conjugation.

This expression is in agreement with the continuum's limit of the current operator of Eq. (4.12).

4.3 Coulomb interaction in Graphene

What role plays the Coulomb interaction in graphene? This frequently asked question is studied in this section. Especially since shortly after the discovery of graphene, many experiments showed no pronounced signature of the Coulomb interaction. The minimal conductivity in disordered samples [80], the odd-integer quantum Hall effect in high magnetic fields [3] and the observation of Klein tunneling through a potential barrier [2] can be explained with a theory of free, noninteracting Dirac fermions. However, while cleaner samples of graphene become accessible, the influence of the electron-electron Coulomb interaction was observed in such phenomena as the fractional quantum Hall effect [4, 5], hydrodynamic behavior [21, 28, 30–32, 34, 81], the logarithmic divergence of the Fermi velocity [6], and angular resolved photoemission spectroscopy [23]. We want to give an overview of the expected role of the Coulomb interaction in this section and show how the Coulomb interaction is theoretically treated in the Wilson RG approach.

4.3.1 The role of Coulomb interaction in Graphene

The repulsive interaction between two equally charged particles is the Coulomb interaction. The interaction Hamiltonian describing the Coulomb potential of two Dirac fermions is

$$\mathcal{H}_C = \frac{1}{2} \int_{\boldsymbol{r}} \int_{\boldsymbol{r}'} \hat{\psi}^\dagger_{\boldsymbol{r}} \hat{\psi}^\dagger_{\boldsymbol{r}'} \frac{e^2}{\epsilon |\boldsymbol{r} - \boldsymbol{r}'|} \hat{\psi}_{\boldsymbol{r}'} \hat{\psi}_{\boldsymbol{r}} \,, \tag{4.21}$$

where $\epsilon = (\epsilon_1 + \epsilon_2)/2$ is the dielectrical constant which consists of the sum of the two dielectrical constants of the materials on either side of the graphene sheet. The Fourier transform of the Coulomb potential is proportional to $V(\boldsymbol{q})_{3D} = \frac{2\pi e^2}{\epsilon |\boldsymbol{q}|^2}$ for three dimensional crystals. However, in the two dimensional graphene, the fermions live in 2D while the Coulomb interaction still acts in the three dimensional space, i. e. $V(\boldsymbol{q})_{3D} = \frac{2\pi e^2}{\epsilon (q_\perp^2 + q_\parallel^2)}$. Thus, the Coulomb interaction has to be projected to the two dimensional space of the fermions by integrating out the perpendicular momentum component $q_\perp$. The Fourier transform of the Coulomb potential for graphene has the form

$$V(\boldsymbol{q}) = \frac{2\pi e^2}{\epsilon |\boldsymbol{q}|} \,, \tag{4.22}$$

where the momentum $\boldsymbol{q}$ now lives in the plane of the honeycomb lattice. At the Dirac point, this Coulomb interaction is not screened because of the vanishing density of charge carriers which will lead to logarithmic divergent corrections, as we will see in the following section. The strength of the Coulomb interaction is governed by the coupling constant

$$\alpha = \frac{e^2}{\epsilon \; \hbar v_{\mathrm{F}}} \,. \tag{4.23}$$

For vacuum $\epsilon = 1$, the coupling constant of graphene is $\alpha \simeq 2.2$ which is approximately 300 times larger than the fine structure constant of QED, $\alpha_{QED} = \frac{1}{137}$, whereas for graphene on a SiO$_2$ substrate with $\epsilon_i \simeq 3.9$ [82], we find $\alpha \simeq 0.79$. Hence, the value of the coupling constant can be manipulated by the substrate on which graphene stands. The influence of the variation of strength of the Coulomb

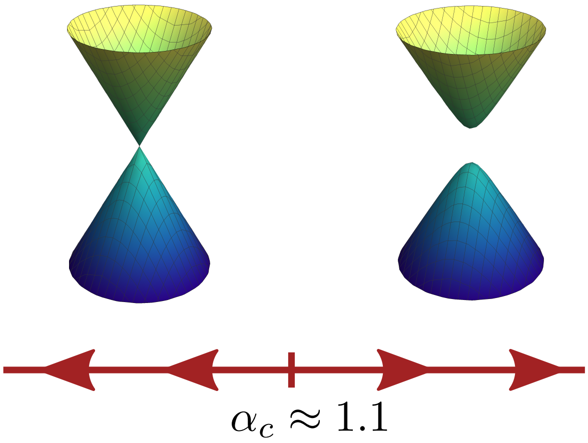

Figure 4.3: The semi-metal to insulator transition induced by the Coulomb interaction calculated by Monte Carlo methods.

interaction was studied by Refs. 83, 84, and 85. Upon applying a lattice Monte Carlo method, they found a phase transition between a semi-metal and an insulator. The critical coupling constant are at $\alpha_c = 1.1$ for the fermion flavor $N_{sv} = 2$ and $\alpha_c = 1.59$ for $N_{sv} = 4$ [84]. This phase transition is depicted in Fig. 4.3. Hence, these lattice Monte Carlo simulations predict that suspended graphene has a gapped energy spectrum. However, the precise value of α_c is expected to depend on microscopic details such as the regularization scheme used to reach the continuum's limit. In addition, there is no experimental evidence that free standing graphene is an insulator and thus we will treat the coupling constant of graphene as being smaller than the critical coupling constant. Thus, because of the experimental observation that the Coulomb interaction does not gap the system, the Coulomb interaction conserves the chiral symmetry.

4.3.2 Wilson RG in Graphene

The renormalization group analysis is a powerful theoretical approach that uses the change of different observables under scale transformation.

In the high-energy physics context, the logic is as follows: Upon calculating the scattering cross section of particles with perturbation theory in the coupling constant α, ultraviolet (UV) divergences were found for the different correction terms, whereas the experiment indicated a finite result. In the RG-analysis, the UV divergences are regularized by a high-energy cut-off Λ and the coupling constants are chosen in such a way that they incorporate the cut-off and thus the final physical observable becomes finite and cut-off independent. That means that for different values of the cut-off one finds different values of the coupling constant. In high energy physics, it is natural to send the cut-off to infinity, $\Lambda \to \infty$, at the end of the day.

In condensed-matter physics applications, the situation is a different one. In contrast to high-energy physics, there is a natural cut-off in the system which is the inverse of the lattice constant, $\Lambda \propto a^{-1}$. Also we are not interested in the regime of high energy but in a low energy description of the system which describes long range physics. This means we use RG in a conceptual different way than in high energy physics. This "new" RG was first thought about by Kadanoff [86] and Wilson [87, 88]. The fermionic fields are separated into slow and fast modes, where the slow modes are given by $\psi^<_{\boldsymbol{k}} = \psi_{\boldsymbol{k}}$ for $0 < \boldsymbol{k} < \Lambda/b$ and the fast modes are $\psi^>_{\boldsymbol{k}} = \psi_{\boldsymbol{k}}$ for $\Lambda/b < \boldsymbol{k} < \Lambda$. The function b is $b = e^l$ with l as

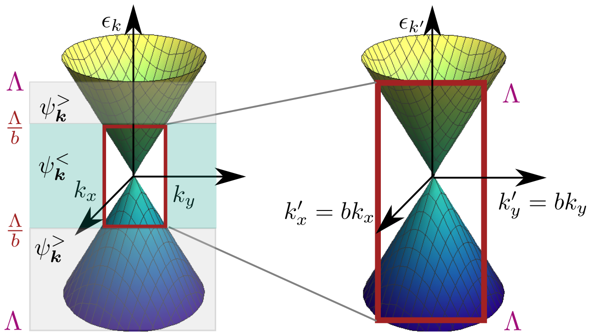

Figure 4.4: The fast modes $\psi^>_{\boldsymbol{k}}$ are integrated out and the action is rescaled to the new cut-off $\Lambda/b \to \Lambda$ by introducing rescaled momenta $\boldsymbol{k}' = b\boldsymbol{k}$.

the RG flow parameter. Next, fast modes are integrated out and the system is described in terms of the slow modes with the new cut-off Λ/b. After rescaling the momenta and frequencies of the system, $\boldsymbol{k}' = b\boldsymbol{k}$ and $\omega' = b\omega$, which now run up to the old cut-off Λ, the only thing which remains to be done, is to introduce rescaled fields $\psi^<_{b^{-1}\boldsymbol{k}',b^{-1}\omega'} = Z_\psi \psi_{\boldsymbol{k},\omega}$. Fig. 4.4 shows schematically this renormalization procedure. For a detailed review on the Wilson RG, we refer to Ref. 89.

Now let us focus on the Wilson RG for clean graphene. The action of clean graphene at the charge neutrality point, i. e., the chemical potential is zero $\mu = 0$, is

$$\mathcal{S} = N_{sv} \int_P \hat{\psi}^\dagger_P \left[-\mathrm{i}\omega_n \sigma_0 + v_\mathrm{F} \boldsymbol{\sigma} \cdot \boldsymbol{p} \right] \hat{\psi}_P + \int_{Q,P_1,P_2} \frac{2\pi e^2}{|\boldsymbol{q}|} \hat{\psi}^\dagger_{P_1} \hat{\psi}_{P_1+Q} \hat{\psi}^\dagger_{P_2} \hat{\psi}_{P_2-Q} \, , \tag{4.24}$$

where P is the four-component vector $P = (\omega_n, \boldsymbol{p})$ with the Matsubara frequency ω_n. Furthermore, it is $\int_P = T \sum_n \int \frac{d^2p}{(2\pi)^2}$ with $T\sum_n$ being the Matsubara sum[4]. The first part of the action describes non-interacting graphene and the second terms arises due to the Coulomb interaction. For the tree-level RG, which is the zeroth order in the RG equation, we introduce the rescaled variables

$$\boldsymbol{p}' = b\boldsymbol{p} \tag{4.25}$$

$$\omega' = b\omega \tag{4.26}$$

$$T' = bT \, . \tag{4.27}$$

It follows for the rescaled fields that the scaling factor is $Z_\psi = b^2$. A consequence of this rescaling is that the Coulomb interaction is marginal for graphene, i. e., it is invariant under the RG flow. This is a consequence of the fact that the kinetic energy of graphene is of the same order of magnitude as the Coulomb interaction. Only further orders of the RG equation will decide, whether the Coulomb interaction is marginal irrelevant or marginal relevant. The next order in the RG-calculation is given by corrections due to one loop diagrams. The crucial diagram which contributes to the quantum corrections is the Fock self energy

$$\begin{aligned} \Sigma(\boldsymbol{k}) &= -T \sum_n \int_{\boldsymbol{k}'}^{\Lambda/b<|\boldsymbol{k}-\boldsymbol{k}'|<\Lambda} \frac{2\pi e^2}{|\boldsymbol{k}-\boldsymbol{k}'|} G_{\boldsymbol{k},\mathrm{i}\omega} \\ &\sim \frac{\alpha}{4} v_\mathrm{F} \boldsymbol{k\sigma} \log b + \mathcal{O}\left(\boldsymbol{k}^2\right) \, . \end{aligned} \tag{4.28}$$

---

[4] Let us also introduce the notation $\int\limits_{\boldsymbol{k}} = \int \frac{d^2k}{(2\pi)^2}$ for the remainder of this thesis.

The Hartee self energy does not contribute to the quantum corrections because of the overall charge conservation of the system and is also responsible that the chemical potential is fixed to zero. Furthermore, the Fock self energy contribution is frequency independent which leads to the fact that the electrical charge e will not be renormalized in the RG-flow. (Only higher order diagrams in the RG [90, 91] or strong coupling effects [92] will lead to a renormalization of the electrical charge.) The rescaling factor of the electrical charge Z_e is defined over the Ward-identity

$$\Gamma_{\boldsymbol{k}} = e\left(1 - \frac{\partial\Sigma(\boldsymbol{k},\omega)}{\partial \mathrm{i}\omega}\right) = eZ_e\,, \tag{4.29}$$

where $\Gamma_{\boldsymbol{k}}$ is the vertex correction. This relation is derived from the charge conservation of the system. Thus, the self energy correction renormalizes only the Fermi velocity of graphene:

$$v_{\mathrm{F}} \to v_{\mathrm{F}}\left(1 + \frac{\alpha}{4}\log b\right)\,. \tag{4.30}$$

A consequence of the renormalization of the Fermi velocity is that the momenta and the frequencies/temperature scale differently. We find for the scaling function $Z_\omega = Z_T$ of the temperature T and the frequency ω

$$Z_T(b) = \left(1 + \frac{\alpha}{4}\log b\right) b^{-1}\,. \tag{4.31}$$

The renormalized temperature is thus given by $T\left(b\right) = Z_T^{-1}T$, where T is the initial value at $b = 1$, i. e., the physical value of the temperature. We see that with increasing RG flow, the renormalized temperature increases. The frequency behaves analogous to the temperature. For the rescaled fermionic fields, the scaling factor is given by $Z_\psi = b\ Z_T^{-1}$. These rescalings also affect the Coulomb interaction. We find for the coupling constant which determines the strength of the Coulomb interaction the following flow equation:

$$\frac{d\alpha(b)}{d\log b} = -\frac{1}{4}\alpha\left(b\right)^2\,. \tag{4.32}$$

The solution to this equation is

$$\alpha(b) = \frac{\alpha}{1 + \frac{\alpha}{4}\log b}\,, \tag{4.33}$$

where α is again the initial value of the RG flow (i. e., the physical value of the coupling constant). Thus, as the RG flow increases with increasing b, the coupling constant decreases. Hence, the Coulomb interaction is a marginal irrelevant interaction in graphene.

As it is shown in Ref. 93, clean graphene is located at a quantum critical point for $T = B = \mu = n = 0$. (Fig. 4.5 shows the quantum critical phase diagram as a function of the carrier density n and the temperature T. At $T = 0$, we see the phase transition from an electron Fermi liquid with a large circular Fermi surface to an hole Fermi liquid with an equally large circular Fermi surface where the phase transition is tuned by varying the doping of the system. Using crossover scaling arguments around the quantum critical point, the behavior of different physical quantities can be predicted. It is

$$O(T,\omega,\alpha) = Z_O O(Z_T^{-1}(b)T, Z_T^{-1}(b)\omega, \alpha(b)) = Z_O O_R \tag{4.34}$$

where $O(T,\omega,\alpha)$ is the physical observable, O_R the renormalized quantity, and Z_O the scaling factor of the observable. One example for the combination of scaling arguments and RG analysis can be given by

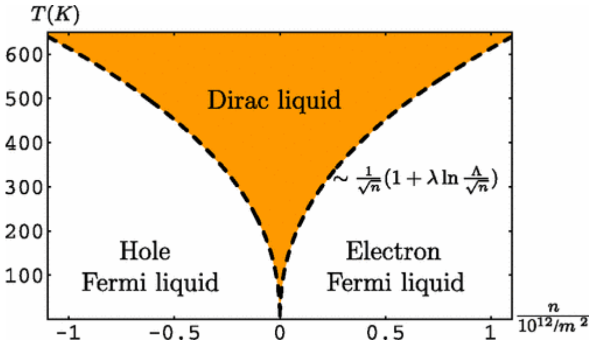

[Reprinted figure with permission from Daniel E. Sheehy and Jörg Schmalian,
Phys. Rev. Lett. **99**, 226803 (2007). Copyright 2007 by the American Physical Society]

Figure 4.5: Quantum critical phase diagram of graphene as a function of the carrier density n and temperature T, for the vacuum case $\epsilon = 1$ taken from [93].

the electronic compressibility $\kappa^{-1}(T)$ of graphene. Hereby, we follow closely the steps of Ref. 93. After renormalization, one finds for the number of charge carriers per area the following scaling behavior $n(T, \mu, \alpha) = b^{-2} n_R$. Since the compressibility is obtained by differentiating the charge carrier density with respect to the chemical potential μ, the scaling of the compressibility is given by $\kappa = b^{-2} Z_T^{-1} \kappa_R$. The renormalized compressibility is defined in a regime with a small effective coupling constant $\alpha(b)$ and a high temperature $T(b)$. Since the temperature cannot become larger than $T_0 = D/k_B$ with the bandwidth $D = \hbar v_\mathrm{F} \Lambda$, we find the renormalization condition $T(b^*) = T_0$. Furthermore, the renormalized high temperature compressibility can be approximated by the free fermion result, i. e., $\kappa_R^{-1} \simeq \pi(\hbar v_\mathrm{F})^2/(4 k_B T_0 \log 2)$. This yields

$$\kappa^{-1}(T) = \frac{\pi(\hbar v_\mathrm{F})^2}{4 k_B T \log 2} \left(1 + \frac{\alpha}{4} \log \frac{T_0}{T}\right)^2 . \tag{4.35}$$

In the same manner, the charge carrier dependence of the incompressibility can be found with $\kappa^{-1}(n) = \hbar v_\mathrm{F} \sqrt{\frac{\pi}{4|n|}} \left(1 + \frac{\alpha}{8} \log \frac{n_0}{|n|}\right)$ with $n_0 = \Lambda^2/\pi$. In Fig. 4.5, the experimental data for the dependence of the inverse compressibility on the charge carrier density measured by Martin *et al.* [94] is shown. There is a very good agreement between the experimental data and the theoretical prediction. Another example for the agreement between the RG prediction and the experiment is the measurement of the Fermi velocity, see Fig. 4.5. In this experiment [6], Elias *et al.* measured for differently doped graphene in a magnetic field $\boldsymbol{B}$ the Shubnikov–de Haas oscillations and deduced from this oscillations the Fermi velocity. The Fermi velocity shows the logarithmic divergence due to the Coulomb interaction predicted by the RG calculation. We can conclude that the RG-analysis captures pretty well the influence of the Coulomb interaction on physical quantities.

In this thesis, we will follow this reasoning, using RG in combination with the scaling behavior of the physical observable, in several different places.

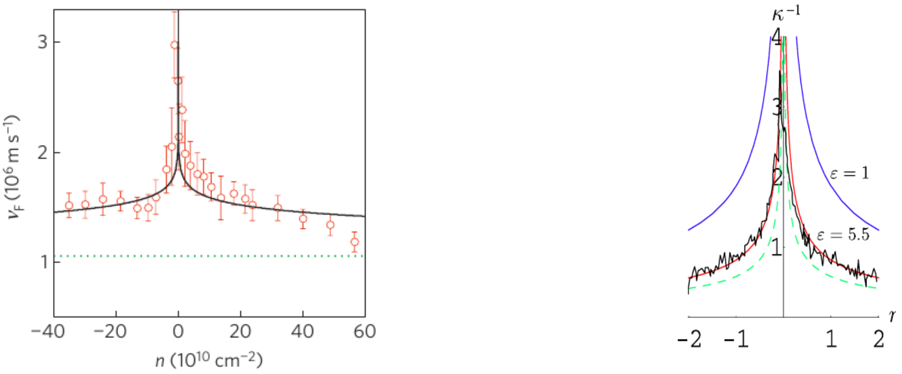

(a) Fermi velocity

(b) inverse compressibility

[Adapted by permission from Springer Nature, *Dirac cones reshaped by interaction effects in suspended graphene*, D. C. Elias, R. V. Gorbachev, A. S. Mayorov, S. V. Morozov, A. A. Zhukov, P. Blake, L. A. Ponomarenko, I. V. Grigorieva, K. S. Novoselov, F. Guinea, and A. K. Geim, Nature Physics **7**, 701, Copyright 2011]

[Reprinted figure with permission from Daniel E. Sheehy and Jörg Schmalian, Phys. Rev. Lett. **99**, 226803 (2007). Copyright 2007 by the American Physical Society]

Figure 4.6: Measured data of the renormalized velocity and inverse compressibility. In panel (a) the experimentally measured Fermi velocity is depicted and we can observe clearly the logarithmic divergence of v_F. (This figure was taken from Ref. 6). In panel (b), we see the inverse compressibility which is also logarithmically diverging. The data of κ^{-1} was measured by Martin *et al.* [94], while the figure was taken from Ref. 93.

5

Chapter 5

The conductivity in graphene

One of the most important transport properties in a condensed matter system is the conductivity. It describes the response of the quasiparticles with an electrical charge to an applied electrical field. In this chapter, the conductivity of graphene at the charge neutrality point is studied in the hydrodynamic and in the collisionless regime. The charge neutrality point is characterized by zero chemical potential μ. In the hydrodynamic regime the shortest time scale is the relaxation time due to collisions, i. e., $\tau^{-1} \gg \omega$, and thus collision processes between the electrons determine the physics, whereas in the collisionless regime the fastest time scale is the excitation frequency of the electrical field, i. e., $\omega \gg \tau^{-1}$, which leads to the fact that collisions can be neglected. For a more detailed description of the two regimes, we refer to Chap. 1.

In Sec. 5.1 we start in the hydrodynamic regime. Here, the conductivity of pristine graphene is proportional to $\alpha(T)^{-2}$ as was shown by Fritz *et al.* in Ref. 19 using the Boltzmann equation. With increasing temperature, the low-frequency conductivity converges to its universal value $\sigma_0(\text{Dirac})_{\text{disorder}} = \frac{2}{\pi^2}\frac{e^2}{\hbar}$, which arises due to disorder in graphene and is determined in the self-consistent Born approximation, see Ref. 95.

In the remainder of this chapter, we will focus on the collisionless regime. First we will point out the connection between the optical conductivity and the light transmissivity through graphene and discuss experimental data of the transmissivity [22]. These data points of the light transmissivity can be theoretically described already quite well by noninteracting Dirac fermions which raises the question of the role of the Coulomb interaction in graphene. This question is a frequently and very controversially discussed question in the literature [7–17]. The course of this discussion is elaborated in Sec. 5.2.2. The reason for this debate is that the involved Feynman diagrams are each logarithmically divergent in the Dirac model and need to be regularized. Depending on the regularization scheme used one finds different answers. In Sec. 5.4, we demonstrate which subtleties have to be considered upon using the different regularization schemes in the correct way. We also show that dimensional regularization (DR) in combination with the Wilson renormalization group (RG) analysis leads to a non-commuting order of limits between the parameter of the dimensionless regularization ϵ and the UV cut-off Λ to which we refer to as UV quirk. And we further elaborate Ref. 15 which shows how DR can be correctly used if it is combined with a continuum field RG.

In the Sec. 5.3, we present a calculation of the optical conductivity of graphene which is independent of any regularization schemes. This calculation of the optical conductivity is performed in the *tight-binding description*. The advantage of the tight-binding model over the Dirac model is the natural momentum cut-off in the system, which is the inverse lattice constant $\Lambda \sim a^{-1}$.

To this end, we give a final answer to the question of the importance of the Coulomb interaction on the optical conductivity in graphene upon presenting a regularization independent calculation and demonstrate the correct way to apply the different regularization schemes in the Dirac model.

Sec. 5.3 and Sec. 5.4 are based on my work in collaboration with Peter P. Orth, Daniel E. Sheehy and Jörg Schmalian which is published in Ref. 16.

5.1 ... in the hydrodynamic regime

In this section, we present the results for the conductivity in the hydrodynamic regime ($\tau^{-1} \gg \omega$) obtained by Fritz *et al.* in Ref. 19. In the hydrodynamic regime, the dominating physical processes are the collisions between the electrons due to Coulomb interaction. In this regime, the method of choice to determine the conductivity is the quantum Boltzmann equation as already pointed out in Sec. 1.2. For a more detailed presentation of the quantum Boltzmann equation, we refer to Sec. 1.2.1. The quantum Boltzmann equation has the form

$$\left(\frac{\partial}{\partial t} + e\boldsymbol{E}\cdot\frac{\partial}{\partial \boldsymbol{k}}\right) f_{\lambda\boldsymbol{k}} = I^{ee}[f_{\lambda\boldsymbol{k}}]\,, \tag{5.1}$$

where $\boldsymbol{E}$ is the electrical field acting on the quasiparticles with the electrical charge e and $I^{ee}[f_{\lambda\boldsymbol{k}}]$ is the collision integral which originates from the Coulomb interaction. The distribution function $f_{\lambda\boldsymbol{k}}$ with λ being the band index of the system is parameterized as

$$f_{\lambda\boldsymbol{k}} = f^{(0)}_{\lambda\boldsymbol{k}} + \delta f_{\lambda\boldsymbol{k}}\,. \tag{5.2}$$

Here, $f^{(0)}_{\lambda\boldsymbol{k}}$ is the Fermi-Dirac distribution function and $\delta f_{\lambda\boldsymbol{k}}$ gives the out-of-equilibrium corrections. In linear response, the out-of-equilibrium correction is $\delta f_{\lambda\boldsymbol{k}} = e\boldsymbol{v}_{\lambda\boldsymbol{k}}\boldsymbol{E} f^{(0)}_{\lambda\boldsymbol{k}}(1-f^{(0)}_{\lambda\boldsymbol{k}})g(\boldsymbol{k},\lambda)$, where $g(\boldsymbol{k},\lambda)$ can be expanded in a set of basis functions $\phi_n(\boldsymbol{k},\lambda)$ which we call the modes of the system, i. e., $g(\boldsymbol{k},\lambda) = \sum_n \psi_n \phi_n(\boldsymbol{k},\lambda)$ and the velocity of the quasiparticles is given by $\boldsymbol{v}_{\lambda\boldsymbol{k}} = \lambda v_{\mathrm{F}}\boldsymbol{k}/k$. The function $g(\boldsymbol{k},\lambda)$ also determines the conductivity tensor, since it holds $\sigma_{\alpha\beta} = e^2 \int_{\boldsymbol{k}} \sum_\lambda v^\alpha_{\lambda\boldsymbol{k}} v^\beta_{\lambda\boldsymbol{k}} f^{(0)}_{\lambda\boldsymbol{k}}(1 - f^{(0)}_{\lambda\boldsymbol{k}})g(\boldsymbol{k},\lambda)$. Next, the collision integral due to Coulomb interaction is to be determined. Due to momentum and energy conservation, not all scattering processes are allowed[1]. The authors of Ref. 19 found that the collision integral including the allowed scattering processes is given by

$$\begin{aligned} I^{ee}[f_{\lambda\boldsymbol{k}}] = -\frac{2\pi}{v_{\mathrm{F}}}\int_{\boldsymbol{k}}\int_{\boldsymbol{q}} \Bigg[& \delta(k - k_1 - |\boldsymbol{k}+\boldsymbol{q}| + |\boldsymbol{k}_1 - \boldsymbol{q}|) R_1(\boldsymbol{k},\boldsymbol{k_1},\boldsymbol{q}) \\ & \times \Big(f_{\lambda\boldsymbol{k}} f_{-\lambda\boldsymbol{k_1}}[1 - f_{\lambda\boldsymbol{k}+\boldsymbol{q}}][1 - f_{-\lambda\boldsymbol{k_1}-\boldsymbol{q}}] - [1 - f_{\lambda\boldsymbol{k}}][1 - f_{-\lambda\boldsymbol{k_1}}] f_{\lambda\boldsymbol{k}+\boldsymbol{q}} f_{-\lambda\boldsymbol{k_1}-\boldsymbol{q}} \Big) \\ & + \delta(k + k_1 - |\boldsymbol{k}+\boldsymbol{q}| - |\boldsymbol{k_1} - \boldsymbol{q}|) R_2(\boldsymbol{k},\boldsymbol{k_1},\boldsymbol{q}) \\ & \times \Big(f_{\lambda\boldsymbol{k}} f_{\lambda\boldsymbol{k_1}}[1 - f_{\lambda\boldsymbol{k}+\boldsymbol{q}}][1 - f_{\lambda\boldsymbol{k_1}-\boldsymbol{q}}] - [1 - f_{\lambda\boldsymbol{k}}][1 - f_{\lambda\boldsymbol{k_1}}] f_{\lambda\boldsymbol{k}+\boldsymbol{q}} f_{\lambda\boldsymbol{k_1}-\boldsymbol{q}} \Big) \Bigg]\,. \end{aligned} \tag{5.3}$$

---

[1] For example Auger-processes or ionization are forbidden. Furthermore, also scattering processes where the two initial states are both in the upper energy band and the final states are both in the lower band, and vice versa, are forbidden due to energy conservation.

The scattering amplitude R_1 corresponds collisions of particles with opposite charge and is defined as

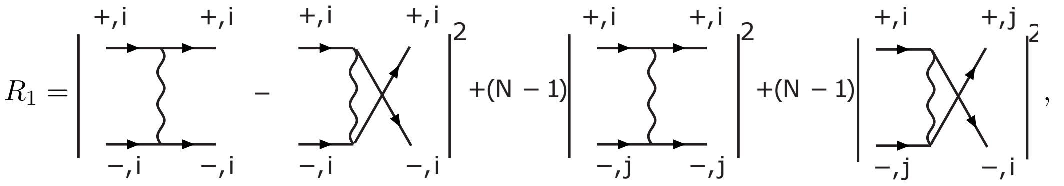

(5.4)

where the additional index i and j indicates the two Dirac cones. The collisions of particles with the same electrical charge are given by the scattering amplitude R_2:

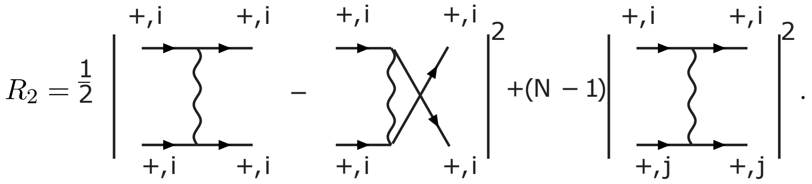

(5.5)

Upon linearization, the collision integral is given by

$$
\begin{aligned}
I^{ee}[g(\boldsymbol{k},\lambda)] = -\frac{2\pi}{v_{\mathrm{F}}} \int\limits_{\boldsymbol{k}} \int\limits_{\boldsymbol{q}} \Bigg[& \delta(k - k_1 - |\boldsymbol{k}+\boldsymbol{q}| + |\boldsymbol{k_1}-\boldsymbol{q}|) R_1(\boldsymbol{k},\boldsymbol{k_1},\boldsymbol{q}) f^{(0)}_{-\boldsymbol{k}} f^{(0)}_{+\boldsymbol{k_1}} f^{(0)}_{+|\boldsymbol{k}+\boldsymbol{q}|} f^{(0)}_{-|\boldsymbol{k_1}-\boldsymbol{q}|} \\
& \Big(\boldsymbol{v}_{\lambda\boldsymbol{k}} g(\boldsymbol{k},\lambda) + \boldsymbol{v}_{-\lambda\boldsymbol{k_1}} g(\boldsymbol{k_1},-\lambda) - \boldsymbol{v}_{\lambda\boldsymbol{k}+\boldsymbol{q}} g(\boldsymbol{k}+\boldsymbol{q},\lambda) - \boldsymbol{v}_{-\lambda\boldsymbol{k_1}-\boldsymbol{q}} g(\boldsymbol{k_1}-\boldsymbol{q},\lambda) \Big) \\
& + \delta(k + k_1 - |\boldsymbol{k}+\boldsymbol{q}| - |\boldsymbol{k_1}-\boldsymbol{q}|) R_2(\boldsymbol{k},\boldsymbol{k_1},\boldsymbol{q}) f^{(0)}_{-\boldsymbol{k}} f^{(0)}_{-\boldsymbol{k_1}} f^{(0)}_{+\boldsymbol{k}+\boldsymbol{q}} f^{(0)}_{+\boldsymbol{k_1}-\boldsymbol{q}} \\
& \Big(\boldsymbol{v}_{\lambda\boldsymbol{k}} g(\boldsymbol{k},\lambda) + \boldsymbol{v}_{\lambda\boldsymbol{k_1}} g(\boldsymbol{k_1},\lambda) - \boldsymbol{v}_{\lambda\boldsymbol{k}+\boldsymbol{q}} g(\boldsymbol{k}+\boldsymbol{q},\lambda) - \boldsymbol{v}_{\lambda\boldsymbol{k_1}-\boldsymbol{q}} g(\boldsymbol{k_1}-\boldsymbol{q},\lambda) \Big) \Bigg] .
\end{aligned}
\tag{5.6}
$$

We find a peculiarity in the collinear scattering limit. The scattering time of nearly collinear particles diverges, since particles with different energies move with the same velocity $\boldsymbol{v}_{\lambda\boldsymbol{k}} = \lambda v_{\mathrm{F}} \frac{\boldsymbol{k}}{k}$, due to the linear energy dispersion. This logarithmic divergence can be seen explicitly in the phase-space density, e. g., for particle-particle scattering processes proportional to R_2. In order to observe the divergence, let us introduce the momenta $\boldsymbol{k} = (k, 0)$, $\boldsymbol{k_1} = (k_1, k_\perp)$, and $\boldsymbol{q} = (q, q_\perp)$ with $k_\perp$ and $q_\perp$ small. (For scattering of particles with opposite charge, the logarithmically divergence occurs for anticollinear collisions since the group velocity depends on λ.) Thus, after expanding in small $q_\perp$, the phase space density can be written as

$$
\begin{aligned}
\int dk_\perp dq_\perp \delta(k + k_1 - |\boldsymbol{k}+\boldsymbol{q}| - |\boldsymbol{k_1}-\boldsymbol{q}|) &= 2\sqrt{\frac{k_1(k+q)(k_1-q)}{k}} \int \frac{dk_\perp}{|k_\perp|} \\
&\propto 2\log\left(\frac{1}{\alpha}\right) ,
\end{aligned}
\tag{5.7}
$$

where the phase-space density is proportional to $\log(1/\alpha)$ with $\alpha = e^2/(\hbar v_{\mathrm{F}})$ being the coupling constant. Now the collision integral can be split into a part arising due to (anti-)collinear scattering and the other one describes the non-collinear scattering, i. e., $I^{ee}[g] = I^{ee}_{\mathrm{nc}}[g] + I^{ee}_{\mathrm{c}}[g]$. In the collinear limit, we find that $\phi_0(\boldsymbol{k},\lambda) = \mathrm{const.}$ is a zero mode of the collinear collision integral I^{ee}_{c}. But if we go

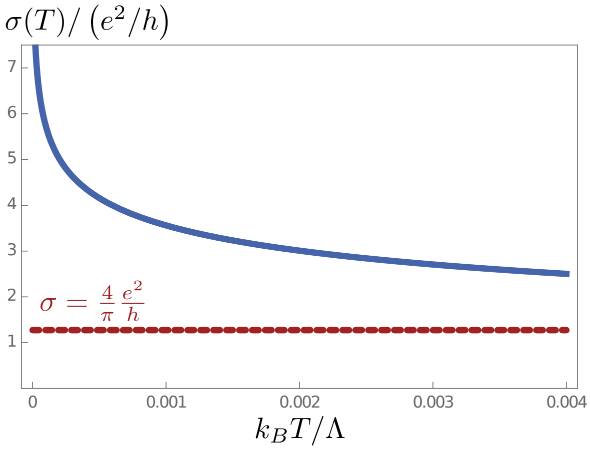

Figure 5.1: Temperature dependence of the dc conductivity in the hydrodynamic regime. The blue line shows the temperature dependence for the dc conductivity which enters via the renormalized coupling constant $\alpha(T)^{-2}$ [19]. Here, the temperature ranges from $T = 0\text{K}$ up to room temperature for a reasonable cut-off Λ of several eV. The red curve indicates the low-frequency value of the dc conductivity with disorder obtained by a self-consistent Born approximation [95].

beyond the collinear scattering regime, this mode will have an eigenvalue which is not proportional to $\log(1/\alpha)$ in the limit of small α. Hence, the Boltzmann equation can be cast into the form

$$\alpha^2 \tilde{I}^{ee}_{\text{nc}}[g] + \alpha^2 \log\left(\frac{1}{\alpha}\right) \tilde{I}^{ee}_{\text{c}}[g] = \varphi\,, \tag{5.8}$$

where φ denotes the left-hand side of the Boltzmann equation defined in Eq. (5.1). In order to obtain the coefficients ψ_n of the different modes $\phi_n(\boldsymbol{k},\lambda)$ which determine the conductivity, we need to invert the Boltzmann equation. Thus, the conductivity is in first order proportional to α^{-2} and the higher corrections in α will be of order $\left|\frac{1}{\alpha^2|\log(\alpha^{-1})|}\right|$. It is

$$\sigma_0(T) = \frac{e^2}{h\alpha^2(T)}\left[0.760 + \mathcal{O}\left(\frac{1}{|\log\alpha(T)|}\right)\right] \tag{5.9}$$

with the renormalized coupling constant $\alpha(T) = \alpha/[1 + \frac{1}{4}\alpha\log\left(\frac{\Lambda}{T}\right)]$ which can be obtained using the Wilson RG. For more details of the Wilson RG in graphene we refer to Sec. 4.3.2. The temperature dependence of the conductivity is shown in Fig. 5.1. The conductivity converges with increasing temperature to the universal value of the dc conductivity at small frequencies $\sigma = \frac{2}{\pi^2}\frac{e^2}{\hbar}$ which was obtained in the presence of disorder within a self-consistent Born-approximation [95].

5.2 Transmissivity and optical conductivity

Now we go into the opposite regime of the hydrodynamic one. This regime is the optical regime where the excitation frequency of the electrical field sets the shortest time scale i. e., $\omega \gg \tau^{-1}$ which leads to the fact that collision processes can be neglected since they occur on a larger time scale. However, now being in a different regime, does not stop us from posing the question how the electrons and

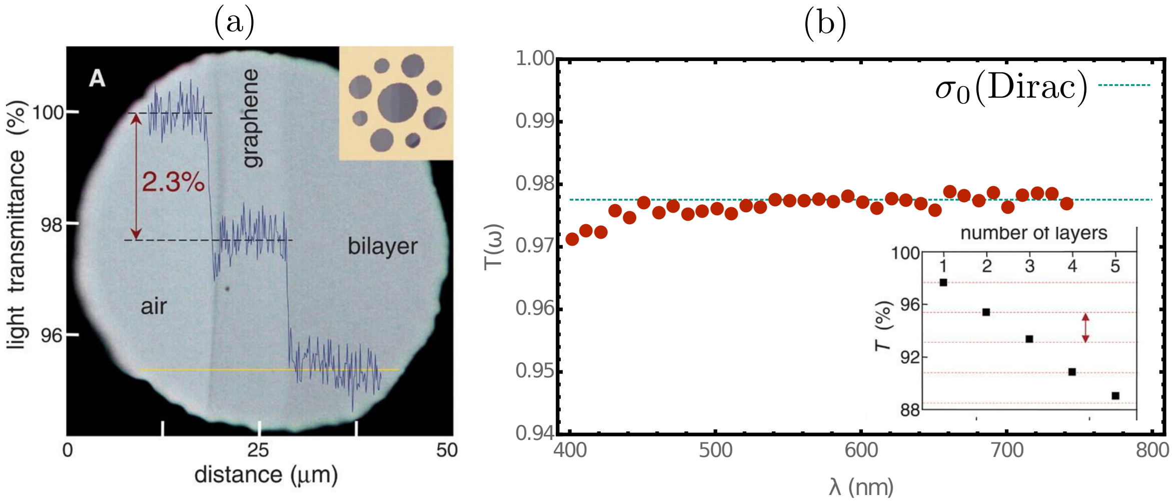

[From R. R. Nair, P. Blake, A. N. Grigorenko, K. S. Novoselov, T. J. Booth, T. Stauber, N. M. R. Peres, and A. K. Geim,
"Fine structure constant defines visual transparency of graphene,"
Science, **320**, 5881, 1308–1308 (2008). Reprinted with permission from AAAS.]

Figure 5.2: Measurement of the transmissivity of light through a graphene sheet. The figure of panel (a) shows how each layer of graphene absorbs 2.3% of the incident light. In figure (b), the experimental data for the light transmissivity in dependence of the wavelength of the incident light is depicted by the red dots. This data is taken from [22]. The green line depicts the theoretical prediction of the transmissivity using the optical conductivity of non-interacting Dirac fermions. (Figure (a) and the inset of Figure (b) was taken from [22].)

holes in graphene respond to an electrical field. Hence, in this section, we want to study the optical conductivity of graphene and the influence of the Coulomb interaction on this transport quantity. The role of the Coulomb interaction for the optical conductivity is a highly controversial discussed question [7–17]. In Sec. 5.2.2, we summarize the course of the debate and give some details of the various methods applied to determine the influence of the Coulomb interaction, before we resolve the dispute in Sec. 5.3 and Sec. 5.4.

5.2.1 The light transmissivity of graphene

One of the fascinating properties of graphene is that it transmits only 97.7% of incident light although graphene consists only of one layer of atoms. This was experimentally measured by Nair *et al.* [22] and Fig. 5.2 (a) shows a graphene flake upon which light falls. One sees clearly, that graphene absorbs 2.3% of the incident light and each new layer absorbs the same amount of light (see inset on the Fig. 5.2 (b)). Furthermore, the transmissivity $T(\omega)$ is almost constant for incident light with wavelength in the range of $480-800$ nm, whereas we see a small decrease of the transmissivity for light with smaller wavelengths. The transmissivity $T(\omega)$ is directly related to the optical conductivity $\sigma(\omega)$. The detailed derivation of this relation can be found in App. A.1. It reads

$$T(\omega) = \left(1 + \frac{\sigma(\omega)}{2\, c\epsilon_0}\right)^{-2}, \tag{5.10}$$

where we assumed a normal incident of p-polarized light to the graphene layer in vacuum[2].

On the one hand, the experimental data of the transmissivity can already be explained by the universal value for the conductivity $\sigma_0(\text{Dirac})$ at high frequencies

$$\sigma_0(\text{Dirac}) = \frac{N_{sv}}{16}\frac{e^2}{\hbar}\,, \tag{5.11}$$

with $N_{sv} = 4$ taking into account the spin degree of freedom and the two Dirac cones in the first Brillouin zone. This value for the optical conductivity is obtained by using the Kubo-Formalism at $T = 0$ for free Dirac fermions [1] and we can rewrite the formula for the transmissivity as $T(\omega) = (1 + \frac{\pi}{2}\alpha_{\text{QED}})^{-2}$ where α_{QED} is $\alpha_{\text{QED}} = e^2/(\hbar c) = 1/137$. This theoretical prediction of the transmissivity using $\sigma_0(\text{Dirac})$ is depicted as the green dashed line in Fig. 5.2 (b). We see that this prediction fits the data already quite well.

On the other hand, $\sigma_0(\text{Dirac})$ was obtained using free Dirac fermions and therefore, the Coulomb interaction was not taken into account. We must ask ourself the question, why we do not see the influence of the Coulomb interaction. What is the reason that already the prediction for non-interacting Dirac fermions fits the experimental data quite well? And can we find an explanation for the deviation between theory and experiment for small wavelengths?

These questions are going to be answered in the following sections.

5.2.2 The debate in the literature

In order to answer the question, why we see no large effect of the Coulomb interaction on the optical conductivity, we will make use of our Wilson renormalization group (RG) analysis introduced in Sec. 4.3.2. Let me briefly repeat here the flow equation for the coupling constant α and the scaling function of the frequency Z_ω. It holds

$$\frac{\mathrm{d}\alpha(b)}{\mathrm{d}\log b} = -\frac{1}{4}\alpha\left(b\right)^2 \qquad \text{and} \qquad Z_\omega(b) = \left(1 + \frac{\alpha}{4}\log b\right) b^{-1}\,, \tag{5.12}$$

with $b = e^l$ and $l > 0$ being the RG flow parameter. We see that with increasing RG flow, the coupling constant decreases, while the frequency increases, i. e., $\omega_R \to Z_\omega^{-1}\omega$. The RG flow can only run to the point where the renormalized frequency has the size of the bandwidth $D = v_{\text{F}}\Lambda$ and we obtain the renormalization condition $\omega_R = D$ and $\alpha(b^*) = \alpha/[1 + \frac{\alpha}{4}\log\frac{D}{\omega}]$. Due to the scale invariance of the conductivity [97], we find

$$\sigma(\omega,\alpha) = \sigma(Z_\omega^{-1}\omega, \alpha(b)) = \sigma(D, \alpha(b^*) \ll 1)\,. \tag{5.13}$$

The optical conductivity at any given frequency $Z_\omega^{-1}\omega$ with the corresponding coupling constant $\alpha(b)$ can also be determined by the value of the optical conductivity where the frequency is equal to the bandwith D of the energy spectrum of graphene. As we have seen before, the coupling constant is extremely small in this regime and hence, we can use it as a small parameter to perform perturbation theory. The optical conductivity $\sigma(\omega)$ can be written as

$$\begin{aligned}\sigma(\omega,\alpha) &= -\frac{\operatorname{Im}\chi_J(\omega)}{\omega}\\ &= \sigma_0\left(1 + \alpha(b^*)\mathcal{C}_\sigma + \mathcal{O}\left(\alpha(b^*)^2\right)\right)\,,\end{aligned} \tag{5.14}$$

---

[2] Another experiment measuring the optical conductivity can be found in Ref. 96.

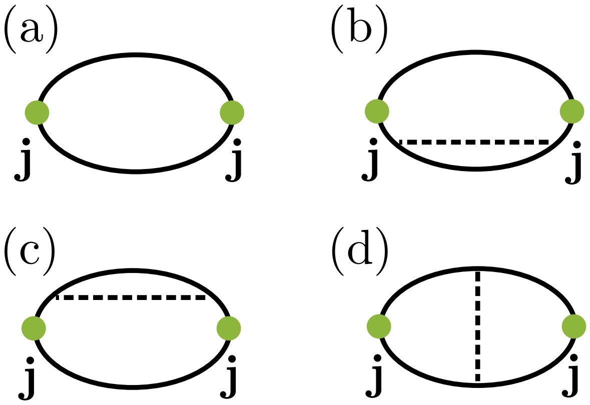

Figure 5.3: Contributions to the current-current correlation function up to first order in α. Panel (a) shows the noninteracting current-current correlation function $\chi_J^{(0)}(\omega)$. The remaining panels show the diagrams contributing to first order in α to the current-current correlation function. Panels (b) and (c) show the self-energy correction to the correlation function and panel (d) the vertex correction.

where we expanded the current-current correlation function $\chi_J(\omega)$ in the small parameter $\alpha(b^*)$, i. e., $\chi_J = \chi_J^{(0)} + \chi_J^{(1)} + \cdots$ with $\sigma^{(i)} = -\operatorname{Im}\chi_J^{(i)}/\omega$. Here, σ_0 refers to the conductivity of free Dirac fermions and $\mathcal{C}_\sigma$ is the correction coefficient of leading-order in α. The conductivity of the free Dirac fermions $\sigma_0 = -[\operatorname{Im}\chi_J^{(0)}(\omega)]/\omega$ is defined in terms of the current-current correlation function $\chi_J^{(0)}(\omega)$ with

$$\chi_J^{(0)}(\omega) = \frac{N_{sv}}{2} \sum_\mu \int \frac{\mathrm{d}\epsilon}{2\pi} \int \frac{\mathrm{d}^2 k}{(2\pi)^2} \operatorname{Tr}\left(\hat{j}_\mu G_{\boldsymbol{k},\mathrm{i}(\epsilon+\omega)} \hat{j}_\mu G_{\boldsymbol{k},\mathrm{i}\epsilon} \right) , \tag{5.15}$$

while the correction coefficient $\mathcal{C}_\sigma$ consists of three contributions: the two *self-energy* diagrams $\chi_J^{(1,bc)}$ and the *vertex-correction* $\chi_J^{(1,d)}$. They are represented in terms of Feynman diagrams in Fig. 5.3. These correlation functions are given by the expressions

$$\begin{aligned} \chi_J^{(1,bc)}(\mathrm{i}\omega) &= -2N_{sv} \int_{\epsilon,\epsilon'} \int_{\boldsymbol{k},\boldsymbol{q}} V(\boldsymbol{q}) \operatorname{Tr}\Big(\hat{j}_\nu G_{\boldsymbol{k},\mathrm{i}(\omega+\epsilon)} \hat{j}_\nu G_{\boldsymbol{k},\mathrm{i}\epsilon} G_{\boldsymbol{k}+\boldsymbol{q},\mathrm{i}\epsilon'} G_{\boldsymbol{k},\mathrm{i}\epsilon} \Big) \\ &= -2N_{sv} \int_\epsilon \int_{\boldsymbol{k}} \operatorname{Tr}\Big(\hat{j}_\nu G_{\boldsymbol{k},\mathrm{i}(\omega+\epsilon)} \hat{j}_\nu G_{\boldsymbol{k},\mathrm{i}\epsilon} \Sigma(\boldsymbol{k}) G_{\boldsymbol{k},\mathrm{i}\epsilon} \Big) , \end{aligned} \tag{5.16}$$

$$\chi_J^{(1,d)}(\mathrm{i}\omega) = N_{sv} \int_{\epsilon,\epsilon'} \int_{\boldsymbol{k},\boldsymbol{q}} V(\boldsymbol{q}) \operatorname{Tr}\Big(\hat{j}_\nu G_{\boldsymbol{k},\mathrm{i}(\omega+\epsilon)} G_{\boldsymbol{k}+\boldsymbol{q},\mathrm{i}(\omega+\epsilon')} \hat{j}_\nu G_{\boldsymbol{k}+\boldsymbol{q},\mathrm{i}\epsilon'} G_{\boldsymbol{k},\mathrm{i}\epsilon} \Big) . \tag{5.17}$$

The three diagrams are individually logarithmically divergent, however, upon adding up the diagrams, the logarithmic divergences cancel each other and we obtain a finite correction coefficient $\mathcal{C}_\sigma$ which does not depend on the cut-off. Different groups have approached this problem [7–17], and one finds three different values for the correction coefficient $\mathcal{C}_\sigma$ in the literature, namely

$$\tilde{\mathcal{C}_\sigma}' = \frac{25-6\pi}{12} \approx 0.51 , \qquad \tilde{\mathcal{C}_\sigma} = \frac{22-19}{12} \approx 0.26 , \qquad \text{and} \qquad \mathcal{C}_\sigma = \frac{19-6\pi}{12} \approx 0.01 . \tag{5.18}$$

These different values have been obtained using different regularization methods. However, the value of the correction coefficient describes the influence of the Coulomb interaction on the optical conductivity and thus, only one value can be correct. Therefore, it is crucial to determine which regularization scheme produces the correct result and also to point out where the other regularization schemes go wrong or where they neglect important subtleties.

First,we demonstrate how it is possible that a hard-momentum cut-off procedure which regularizes the fermionic degrees of freedom yields a different result than a soft-cut-off acting on the Coulomb interaction. To this purpose, we study the self-energy and see that the self-energy can be rewritten as a surface integral and becomes dependent on the parameter ζ. The value of this parameter, determines which cut-off procedure is applied and hence, one has to find a way which fixes ζ.

But now let us start with a more detailed study of the self-energy. The self-energy is independent of the frequency and can be written as

$$\Sigma(\boldsymbol{k}) = -\int_{\epsilon}\int_{\boldsymbol{q}} \frac{2\pi\alpha}{|\boldsymbol{k}-\boldsymbol{q}|} G_{\boldsymbol{q},\mathrm{i}\epsilon} = \phi(\boldsymbol{k})\ \boldsymbol{k}\cdot\boldsymbol{\sigma} \tag{5.19}$$

with $\phi(\boldsymbol{k}) = \frac{\alpha^2}{4\pi k^2}\int_{|\boldsymbol{q}|<\Lambda} \frac{1}{|\boldsymbol{k}-\boldsymbol{q}|}\frac{\boldsymbol{k}\cdot\boldsymbol{q}}{q}$, where the first factor is the Coulomb potential and the second factor comes from the Green's function. Next a shift in the integration variable $\boldsymbol{q} \to \boldsymbol{q} - \zeta\boldsymbol{k}$ is introduced while the cut-off Λ stays fixed. The value of the factor ζ represents which regularization method is used. The function $\phi(\boldsymbol{k})$ can then be rewritten as

$$\phi_\zeta(\boldsymbol{k}) = \frac{\alpha^2}{4\pi k^2}\int_{|\boldsymbol{q}|<\Lambda} \frac{1}{|\boldsymbol{k}(1-\zeta)-\boldsymbol{q}|}\frac{(\boldsymbol{q}+\zeta\boldsymbol{k})\boldsymbol{k}}{|\boldsymbol{q}+\zeta\boldsymbol{k}|}\,, \tag{5.20}$$

and the self-energy is

$$\Sigma_\zeta(\boldsymbol{k}) = \frac{\alpha}{4}\log\left(\frac{4\Lambda\sqrt{e}}{k}\right)\boldsymbol{k}\cdot\boldsymbol{\sigma} + \zeta\frac{\alpha}{4}\boldsymbol{k}\cdot\boldsymbol{\sigma}\,. \tag{5.21}$$

Hence, the self-energy becomes dependent on the regularization scheme used and this leads to different values of the correction coefficient.

On the one hand, according to Eq. (5.20), the integral is regularized by a hard-momentum cut-off for $\zeta = 0$, i. e., $G_{\boldsymbol{q},\mathrm{i}\epsilon} \to G_{\boldsymbol{q},\mathrm{i}\epsilon}\theta\left(\Lambda - \boldsymbol{q}\right)$. In this case, the self-energy is $\Sigma_{\zeta=0}(\boldsymbol{k}) = \frac{\alpha}{4}\log(\frac{4\Lambda\sqrt{e}}{k})\boldsymbol{k}\cdot\boldsymbol{\sigma}$ which produces the value $\tilde{\mathcal{C}_\sigma}'$.

On the other hand, if $\zeta = 1$, the cut-off is introduced for the Coulomb interaction, i. e., $V(\boldsymbol{q}) \to V(\boldsymbol{q})\theta\left(\Lambda - \boldsymbol{q}\right)$. Then the self-energy is given by $\Sigma_{\zeta=1}(\boldsymbol{k}) = \frac{\alpha}{4}\log(\frac{4\Lambda\sqrt{e}}{k})\boldsymbol{k}\cdot\boldsymbol{\sigma} + \frac{\alpha}{4}\boldsymbol{k}\cdot\boldsymbol{\sigma}$, which yields the value $\mathcal{C}_\sigma$.

At last, the value $\zeta = 1/2$, which would correspond to a mixture of both regularization schemes, would yield the value $\tilde{\mathcal{C}_\sigma}$.

Thus, we have to find a method which fixes ζ. In the following, we give an overview of the discourse of the debate and thereby introduce a way to fix ζ, but we will also introduce yet other different approaches yielding one of the three values of the correction coefficient.

In the year 2008, Herbut *et al.* calculated the correction coefficient $\mathcal{C}_\sigma$ for the first time [7] using a hard-momentum cut-off and obtained $\tilde{\mathcal{C}_\sigma}' = \frac{25-6\pi}{12} \approx 0.51$. However, in the same year, Mishchenko determined the correction coefficient by calculating the polarization operator $\Pi(\omega, \boldsymbol{q})$, i. e. $\sigma(\omega) = \lim_{q\to 0} \operatorname{Im} \frac{e^2\omega}{|\boldsymbol{q}|^2}\Pi(\omega, \boldsymbol{q})$, and obtained $\mathcal{C}_\sigma = \frac{19-6\pi}{12} \approx 0.01$, see Ref. 8. The result is one order of magnitude smaller than the previous one. The contradiction between the two values was resolved by Sheehy and Schmalian in Ref. 9. They showed that the hard-momentum cut-off violates the Ward identity (4.29), which describes the charge conservation. This is due the fact that the hard momentum cut off modifies the fermionic density of states. Thus, the hard-momentum regularization scheme should not be used in this case and $\tilde{\mathcal{C}_\sigma}'$ is wrong. Whereas, if the cut-off is at the Coulomb interaction, the Ward-identity is fulfilled and the value $\mathcal{C}_\sigma$ is found. The parameter ζ is thus fixed by charge conservation. Gazzola *et al.* fixed ζ by using the spatial $O(2)$ symmetry which translates to the transversality of the polarization operator [98] and obtained the same result $\mathcal{C}_\sigma$. The discussion seemed to be settled.

However, Juricic *et al.* published a calculation which uses dimensional regularization (DR) and which does not violate the Ward-identity [10] . Their new value for the correction coefficient was $\tilde{\mathcal{C}_\sigma} = \frac{22-6\pi}{12} \approx 0.26$, which is by a factor of two smaller than the previous old wrong value $\tilde{\mathcal{C}_\sigma}'$, but it still deviates from $\mathcal{C}_\sigma$.

In 2012 further work was published by Sodemann and Fogler [13] who found $\mathcal{C}_\sigma$ by using a cut-off in the Coulomb interaction and using the Kubo-formula based on the polarization operator. Teber and Kotikov also obtained $\mathcal{C}_\sigma$ using DR and a continuum RG, see Ref. 15. A list of the different papers with their evaluated value of $\mathcal{C}_\sigma$ and the method applied can be found in Tab. 5.1.

The whole discourse over the correction coefficient $\mathcal{C}_\sigma$ has its origin in the fact that the Dirac theory description has no natural cut-off in its system which leads to the divergent integrals that have to be regularized. Thus, the cut-off has to be introduced "by hand" and a certain regularization method needs to be chosen. In contrast, in the tight-binding description, the cut-off comes in naturally. Here, the cut-off is determined by the lattice constant $\sqrt{3}a$. Furthermore, in contrast to the Dirac model, the energy-dispersion of the tight-binding description is also finite due to its curvature. Hence, a calculation of the correction coefficient in the tight-binding model should give the definite answer.

In 2013, Rosenstein *et al.* claimed that they obtained $\tilde{\mathcal{C}_\sigma}$ in a tight-binding calculation, see Ref. 14. They concluded that a proper treatment of the entire energy spectrum of the first Brillouin zone was needed and that this unexpected behavior is related to a chiral anomaly or due to nonlocal optical effects [99]. However, the supplemental material suggests that they derived an expression for the correction coefficient in the tight-binding description but numerically evaluated the coefficient again in the Dirac approximation. Furthermore, as we are going to show in the next section, they also did not treat the Coulomb interaction on the lattice correctly.

In the following section, we will present a true lattice calculation of the correction coefficient and resolve all issues. We do not only determine the correction value, but also answer the question, whether the correction coefficient is a universal quantity. Or, in other words: Does the correction coefficient depend on microscopic quantities of the system, such as the ratio of the lattice constant over the width of the Wannier orbital λ of the carbon atoms?

This work was done in collaboration with Peter P. Orth, Daniel E. Sheehy, and Jörg Schmalian and can be found in Ref. 16.

5.3 The tight-binding approach to the optical conductivity

In this section, we present a calculation of the optical conductivity and the correction coefficient in the tight-binding description. This section is based on my work in collaboration with Peter P. Orth,

Paper	Year	Method used	$\frac{25-6\pi}{12}$	$\frac{22-6\pi}{12}$	$\frac{19-6\pi}{12}$
Herbut *et al.* [7]	2008	Hard momentum cut-off	⊛		
Mishchenko [8]	2008	Polarization operator			⊛
Sheehy *et al.* [9]	2009	Cut off in the Coulomb-potential & current/current correlation fct			⊛
Juricic *et al.* [10]	2010	Dimensional regularization & Wilson RG		⊛	
Sodemann *et al.* [13]	2012	Cut off in the Coulomb-potential & Polarization operator			⊛
Rosenstein *et al.* [14]	2013	"Tight-binding"-calculation		⊛	
Gazzola *et al.* [98]	2013	spatial $O(2)$ symmetry			⊛
Teber *et al.* [15]	2014	Dimensional regularization & Continuum RG			⊛
Link *et al.* [16]	2016	Tight-binding calculation & UV-Quirk			⊛
Boyda *et al.* [17]	2016	Quantum Monte Carlo			⊛

Table 5.1: List of the different papers calculating the correction coefficient $\mathcal{C}_\sigma$.

Daniel E. Sheehy, and Jörg Schmalian, which was published in Ref. 16.
In order to determine $\mathcal{C}_\sigma$ in a lattice calculation, we first study the Coulomb interaction Hamiltonian and the self-energy in the tight-binding model and answer the question how these quantities depend on the size of the Wannier orbitals λ of the carbon atoms, see Sec. 5.3.1. In contrast to the Dirac approximation, the self-energy is not divergent due to the existence of a natural cut-off, i. e. the lattice constant $\sqrt{3}a$, as can be seen using a real-space analysis.

Furthermore, before we determine the correction coefficient in Sec. 5.3.2, we will see how the curvature of the full energy dispersion influences the non-interacting contribution of the optical conductivity $\sigma_0(\mathrm{TB})$.

5.3.1 The Coulomb interaction Hamiltonian

The interaction between electrons is described by the Coulomb interaction and the corresponding contribution to the Hamiltonian is[3]

$$\mathcal{H}_\mathcal{C} = \frac{1}{2}\int\limits_{\boldsymbol{r}}\int\limits_{\boldsymbol{r'}} \hat{\psi}^\dagger_{\boldsymbol{r}}\hat{\psi}^\dagger_{\boldsymbol{r'}}\frac{e^2}{|\boldsymbol{r}-\boldsymbol{r'}|}\hat{\psi}_{\boldsymbol{r'}}\hat{\psi}_{\boldsymbol{r}}\,. \tag{5.22}$$

The Coulomb interaction acts in the three-dimensional space and thus vectors $\boldsymbol{r}$, $\boldsymbol{r'}$ are three-dimensional real-space position vectors, i. e., $\boldsymbol{r} = (\boldsymbol{\rho}, z)$ with $\boldsymbol{\rho} = (x, y)$. The two-dimensional graphene crystal is considered to be located in the $x-y$ plane with $z = 0$. The fermionic field operators are

$$\hat{\psi}_{\boldsymbol{r}} = \sum_{\boldsymbol{R}_i}\left[\varphi(\boldsymbol{r}-\boldsymbol{R}_i-\boldsymbol{v}_1)\hat{a}_{\boldsymbol{R_i}} + \varphi(\boldsymbol{r}-\boldsymbol{R}_i-\boldsymbol{v}_2)\hat{b}_{\boldsymbol{R_i}}\right]\,, \tag{5.23}$$

where $\varphi(\boldsymbol{r}-\boldsymbol{R}_i-\boldsymbol{v}_\ell)$ are the Wannier p_z-orbitals of the sp^2-hybridized carbon atoms at the site $(\boldsymbol{R}_i, \boldsymbol{v}_\ell)$. We assume that the p_z-orbitals are localized, or with other words that the overlap between

---

[3] Here and in the remainder of this section, we will drop the spin index of the field operators.

neighboring atoms is small in comparison to the on-site overlap $\varphi^*(\boldsymbol{r}-\boldsymbol{R}_i-\boldsymbol{v}_\ell)\varphi(\boldsymbol{r}-\boldsymbol{R}_j-\boldsymbol{v}_{\ell'})$ for $i=j$ and $\ell=\ell'$. The density can thus be approximated by

$$\hat{\psi}^\dagger_{\boldsymbol{r}}\hat{\psi}_{\boldsymbol{r}} \approx \sum_{\boldsymbol{R}_i}\Big[\left|\varphi(\boldsymbol{r}-\boldsymbol{R}_i-\boldsymbol{v}_1)\right|^2 \hat{a}^\dagger_{\boldsymbol{R}_i}\hat{a}_{\boldsymbol{R}_i} + \left|\varphi(\boldsymbol{r}-\boldsymbol{R}_i-\boldsymbol{v}_2)\right|^2 \hat{b}^\dagger_{\boldsymbol{R}_i}\hat{b}_{\boldsymbol{R}_i}\Big]\,. \tag{5.24}$$

In the following, we will use the notation $\hat{c}_{\boldsymbol{R}_i1}=\hat{a}_{\boldsymbol{R}_i}$ and $\hat{c}_{\boldsymbol{R}_i2}=\hat{b}_{\boldsymbol{R}_i}$ for simplicity. The expression for the density thus simplifies to $\hat{\psi}^\dagger_{\boldsymbol{r}}\hat{\psi}_{\boldsymbol{r}}=\sum_{\boldsymbol{R}_i}\sum_{\ell=1,2}\left|\phi(\boldsymbol{r}-\boldsymbol{R}_i-\boldsymbol{v}_\ell)\right|^2\ \hat{c}^\dagger_{\boldsymbol{R}_i\ell}\hat{c}_{\boldsymbol{R}_i\ell}$. Inserting this definition of the density and the Fourier transform $\frac{e^2}{\epsilon|\boldsymbol{r}-\boldsymbol{r}'|}=\int\limits_{\boldsymbol{q}}\int\frac{\mathrm{d}p_z}{2\pi}\mathrm{e}^{\mathrm{i}\boldsymbol{q}(\boldsymbol{\rho}-\boldsymbol{\rho}')}\mathrm{e}^{\mathrm{i}p_z(z-z')}\frac{4\pi}{\epsilon(q^2+p_z^2)}$ into Eq. (5.22), we obtain

$$\begin{aligned}\mathcal{H}_{\mathcal{C}} &= \int \mathrm{d}^3r\int\mathrm{d}^3r'\int\frac{\mathrm{d}^2q}{(2\pi)^2}\int\frac{\mathrm{d}p_z}{2\pi}\mathrm{e}^{\mathrm{i}\boldsymbol{q}(\boldsymbol{\rho}-\boldsymbol{\rho}')}\mathrm{e}^{\mathrm{i}p_z(z-z')}\frac{4\pi}{\epsilon(q^2+p_z^2)}\\ &\quad\times\sum_{\boldsymbol{R}_i,\ell}\sum_{\boldsymbol{R}_j,\ell'}\left|\phi(\boldsymbol{r}-\boldsymbol{R}_i-\boldsymbol{v}_\ell)\right|^2\left|\phi(\boldsymbol{r}'-\boldsymbol{R}_j-\boldsymbol{v}_{\ell'})\right|^2\hat{c}^\dagger_{\boldsymbol{R}_i\ell}\hat{c}^\dagger_{\boldsymbol{R}_j\ell'}\hat{c}_{\boldsymbol{R}_j\ell'}\hat{c}_{\boldsymbol{R}_i\ell}\,.\end{aligned} \tag{5.25}$$

To evaluate the $\boldsymbol{r}$ and $\boldsymbol{r}'$ integration, we shift the integration variable $\boldsymbol{r}\to\boldsymbol{r}+\boldsymbol{R}_i+\boldsymbol{v}_\ell$ and the $\boldsymbol{r}'$ respectively. This shift in the integration variables gives rise to an additional phase factor $\mathrm{e}^{\mathrm{i}\boldsymbol{q}\cdot(\boldsymbol{R}_i+\boldsymbol{v}_\ell)}$. The sum over the lattice vector $\boldsymbol{R}_i$ and $\boldsymbol{R}_j$ implements the lattice Fourier transform of the field operators $\hat{c}_{\boldsymbol{R}_i\ell}=\sum\limits_{\boldsymbol{k}}\hat{c}_{\boldsymbol{k}\ell}\mathrm{e}^{-\mathrm{i}\boldsymbol{k}\cdot\boldsymbol{R}_i}$. We find:

$$\begin{aligned}\mathcal{H}_{\mathrm{int}} &= \frac{1}{2}\int\limits_{\boldsymbol{q}}V(\boldsymbol{q})\sum_{\ell=1,2}\sum_{\ell'=1,2}\mathrm{e}^{\mathrm{i}\boldsymbol{q}\cdot(\boldsymbol{v}_\ell-\boldsymbol{v}_{\ell'})}\sum_{\boldsymbol{k},\boldsymbol{k}'}\hat{c}^\dagger_{\boldsymbol{k}+\boldsymbol{q}\ell}\hat{c}^\dagger_{\boldsymbol{k}'-\boldsymbol{q}\ell'}\hat{c}_{\boldsymbol{k}'\ell'}\hat{c}_{\boldsymbol{k}\ell}\\ &= \frac{1}{2}\int\limits_{\boldsymbol{q}}V(\boldsymbol{q})\sum_{\boldsymbol{k}_1,\boldsymbol{k}_2}\hat{\psi}^\dagger_{\boldsymbol{k}_2-\boldsymbol{q},k}\hat{\psi}^\dagger_{\boldsymbol{k}_1+\boldsymbol{q},i}\hat{\psi}_{\boldsymbol{k}_1,j}\hat{\psi}_{\boldsymbol{k}_2,\ell}M_{ij}(\boldsymbol{q})M_{k\ell}(-\boldsymbol{q})\,,\end{aligned} \tag{5.26}$$

where the matrix

$$M_{\boldsymbol{q}}=\begin{pmatrix}\mathrm{e}^{\mathrm{i}\boldsymbol{q}\cdot\boldsymbol{v}_1} & 0\\ 0 & \mathrm{e}^{\mathrm{i}\boldsymbol{q}\cdot\boldsymbol{v}_2}\end{pmatrix} \tag{5.27}$$

arises because of the two-atomic basis of graphene. The phase factor described by $M_{\boldsymbol{q}}$ is responsible for the convergence of the different contributions to the correction coefficient. The matrix element of the Coulomb interaction of Eq. (5.26) is

$$V\left(\boldsymbol{q}\right)=\int_{-\infty}^{\infty}\frac{dp_z}{2\pi}\frac{4\pi e^2\left|\rho(\boldsymbol{q},p_z)\right|^2}{\epsilon(q^2+p_z^2)}\,, \tag{5.28}$$

where $\rho\left(\boldsymbol{q},p_z\right)$ is the electron density of the three-dimensional orbital with $\rho(\boldsymbol{q},p_z)=\int d^3r|\varphi(\boldsymbol{r})|^2\mathrm{e}^{\mathrm{i}(\boldsymbol{q}\boldsymbol{\rho}+q_zz)}$. Upon using the p_z-orbitals with the effective Bohr radius a_B^*, one obtains $V(\boldsymbol{q})=2\pi e^2\mathcal{F}(\boldsymbol{q})/(\epsilon|\boldsymbol{q}|)$ with the form factor $\mathcal{F}(\boldsymbol{q})=\exp(-|\boldsymbol{q}|a_B^*)$ and $a_B^*\simeq 0.9$ Å [100]. In the following, we will assume that the orbitals are point-like in z-direction, but Gaussian-shaped in the 2D plane, $\varphi(\boldsymbol{r})=\frac{1}{\lambda\sqrt{\pi}}\exp[-(x^2+y^2)/2\lambda^2]\delta(z)$, which leads to the Coulomb matrix element

$$V(\boldsymbol{q})=\frac{2\pi e^2}{\epsilon|\boldsymbol{q}|}\mathrm{e}^{-|\boldsymbol{q}|^2\lambda^2/2}\,. \tag{5.29}$$

The size of the Wannier orbitals λ suppresses the Coulomb potential for large values of the $\boldsymbol{q}$-momentum, whereas for small $\boldsymbol{q}$ the Coulomb interaction is barely affected by the size of the orbitals. Hence, the long-range physics is not determined by the orbital size λ. The above expression simplifies ($\lambda \to 0$) for a point-like orbital to $V(\boldsymbol{q}) = \frac{2\pi e^2}{\epsilon|\boldsymbol{q}|}$.

Crucial for the remainder of the calculation is that the sums $\sum_{\boldsymbol{k},\boldsymbol{k}'}$ in Eq. (5.26) run only over the first Brioullin zone, whereas the integral over $\boldsymbol{q}$ goes over the infinite momentum space. This distinction was ignored in earlier work [14].

The self-energy in the tight-binding description

We have seen in the previous section that the self-energy is logarithmically divergent in the Dirac approximation. Hence, the cut-off Λ needed to be introduced, which results in $\Sigma(\boldsymbol{k})_{\text{Dirac}} \propto \boldsymbol{k} \cdot \boldsymbol{\sigma} \log\left(\frac{4\Lambda\sqrt{e}}{k}\right)$. However, in the tight-binding description, we expect the self-energy to be finite on its own and no cut-off has to be introduced by hand, in spite of the fact that the Coulomb integration runs over the infinite momentum space, since the inverse lattice constant $1/(\sqrt{3}a)$ acts as an ultraviolett cut-off.

The self-energy of graphene in the tight-binding description is given by

$$\Sigma(\boldsymbol{k}) = -\int_{\boldsymbol{q}} V(\boldsymbol{q}) T \sum_{\omega} M_{-\boldsymbol{q}} \mathcal{G}_{\boldsymbol{k}+\boldsymbol{q},\mathrm{i}\omega} M_{\boldsymbol{q}} \,. \tag{5.30}$$

Upon inserting the definition of the Green's function Eq. (4.6) with $\mathcal{G}_{\boldsymbol{k},\mathrm{i}\omega} = \left(\mathrm{i}\omega - \mathcal{H}_0\right)^{-1}$ and $h_{\boldsymbol{k}} = |h_{\boldsymbol{k}}|\mathrm{e}^{\mathrm{i}\phi(\boldsymbol{k})}$ into the above expression and after performing the Matsubara sum over the frequency, we obtain

$$\Sigma(\boldsymbol{k}) = -\frac{1}{2}\int_{\boldsymbol{q}} V(\boldsymbol{q}) M_{-\boldsymbol{q}} \begin{pmatrix} 0 & \mathrm{e}^{\mathrm{i}\phi(\boldsymbol{k}+\boldsymbol{q})} \\ \mathrm{e}^{-\mathrm{i}\phi(\boldsymbol{k}+\boldsymbol{q})} & 0 \end{pmatrix} M_{\boldsymbol{q}} \,. \tag{5.31}$$

For simplicity, in the remainder of the section, we focus on the upper right matrix element of the self-energy which already describes the whole self-energy, since $\Sigma_{21}(\boldsymbol{k}) = \Sigma_{12}^*(\boldsymbol{k})$, and which is given by

$$\Sigma_{12}(\boldsymbol{k}) = -\frac{1}{2}\int_{\boldsymbol{q}} V(\boldsymbol{q}) \mathrm{e}^{\mathrm{i}[\phi(\boldsymbol{k}+\boldsymbol{q}) - \boldsymbol{q}(\boldsymbol{v}_1 - \boldsymbol{v}_2)]} \,. \tag{5.32}$$

The phase factor $\mathrm{e}^{\mathrm{i}\boldsymbol{q}\cdot(\boldsymbol{v}_2-\boldsymbol{v}_1)}$ is highly oscillatory for large $\boldsymbol{q}$ and is thus responsible for the convergence of the self-energy diagram. However, it is numerically very costly to perform the $\boldsymbol{q}$ integration over the infinite momentum space. A better approach is to analyze the self-energy in real space. Since the self-energy is lattice periodic, i. e., $\Sigma(\boldsymbol{k}) = \Sigma(\boldsymbol{k}+\boldsymbol{G})$ with $\boldsymbol{G}$ being the reciprocal lattice vector, the self-energy can be expressed as a function of Bravais-lattice vectors upon applying the Fourier transform

$$\Sigma_{12}(\boldsymbol{R}_i) = \sum_{\boldsymbol{k}} \Sigma_{12}(\boldsymbol{k}) \mathrm{e}^{-\mathrm{i}\boldsymbol{k}\cdot\boldsymbol{R}_i} \,. \tag{5.33}$$

Thus, the Fourier transformation into momentum space of the self energy is given by $\Sigma_{12}(\boldsymbol{k}) = A\sum_{\boldsymbol{R}_i} \Sigma_{12}(\boldsymbol{R}_i)\mathrm{e}^{\mathrm{i}\boldsymbol{k}\cdot\boldsymbol{R}_i}$, where $A = 3\sqrt{3}a^2/2$ is the area of a unit-cell in real-space. The self-energy component in real-space, Eq. (5.33), can be determined by shifting the momentum $\boldsymbol{k} \to \boldsymbol{k} - \boldsymbol{q}$, since the integrand $\Sigma_{12}(\boldsymbol{k})$ is periodic in the reciprocal lattice. $\Sigma_{12}(\boldsymbol{k})$ is not restricted to the first Brillouin zone and can expanded to the whole momentum space, since by adding a reciprocal lattice vectors $\boldsymbol{G}$ to a momentum in the first Brillouin zone, $\boldsymbol{k} \to \boldsymbol{k} + \boldsymbol{G}$, every value of the whole momentum space can be realized. Hence, we find for the self-energy in real-space

$$\Sigma_{12}(\boldsymbol{R}_i) = -\frac{1}{2} \int\limits_{\boldsymbol{q}} V(\boldsymbol{q}) e^{\mathrm{i}\boldsymbol{q}\cdot(\boldsymbol{R}_i + \boldsymbol{v}_2 - \boldsymbol{v}_1)} F(\boldsymbol{R}_i) \tag{5.34}$$

with the coefficients

$$F(\boldsymbol{R}_i) = \sum_{\boldsymbol{k}'} \mathrm{e}^{\mathrm{i}\left[\phi(\boldsymbol{k}') - \boldsymbol{k}'\cdot\boldsymbol{R}_i\right]} . \tag{5.35}$$

Upon inserting the above expression into the Fourier transform into the momentum space, we find the following expression for the self-energy in momentum space with point-like Wannier orbitals, i. e., $\lambda \to 0$:

$$\Sigma_{12}(\boldsymbol{k}) = -\frac{e^2}{2\epsilon} A \sum_{\boldsymbol{R}_i} \mathrm{e}^{\mathrm{i}\boldsymbol{k}\cdot\boldsymbol{R}_i} \frac{1}{\left|\boldsymbol{R}_i + \boldsymbol{v}_2 - \boldsymbol{v}_1\right|} F(\boldsymbol{R}_i) . \tag{5.36}$$

Here, we have exchanged a numerically intensive momentum integration by an infinite sum over Bravais lattice vectors. We can see explicitly that even for $\boldsymbol{R}_i = (0, 0)$ all summands of the self-energy will be finite (since the denominator $\frac{1}{|\boldsymbol{R}_i + \boldsymbol{v}_2 - \boldsymbol{v}_1|}$ never reaches zero). The convergence of the self-energy relies on the fact that the coefficients $F(\boldsymbol{R}_i)$ decay sufficiently fast as a function of $|\boldsymbol{R}_i|$, as can bee seen in Fig. 5.4 (b). If we take the finite size of the Wannier orbitals into account, it holds

$$\Sigma_{12}(\boldsymbol{k}) = -\frac{e^2}{2\epsilon} \frac{A}{\lambda} \sum_{\boldsymbol{R}_i} \mathrm{e}^{\mathrm{i}\boldsymbol{k}\cdot\boldsymbol{R}_i} \sqrt{\frac{\pi}{2}} \mathrm{e}^{-\left|\boldsymbol{R}_i + \boldsymbol{v}_2 - \boldsymbol{v}_1\right|^2/(4\lambda^2)} I_0 \left(\frac{\left|\boldsymbol{R}_i + \boldsymbol{v}_2 - \boldsymbol{v}_1\right|^2}{4\lambda^2} \right) F(\boldsymbol{R}_i) , \tag{5.37}$$

where $I_0(x)$ is the modified Bessel function of the first kind. In order to calculate the self-energy diagram in the tight-binding description we used 4.6×10^4 Bravais lattice vectors. The results are shown in Fig. 5.4 (c), where we see the self-energy for different sizes of the Wannier orbitals. Even for varying size of the Wannier orbitals, the self-energy does not diverge. Only the slope of the self-energy shows logarithmically divergent behavior around the Dirac points, as would be expected in the Dirac approximation. The different sizes of the Wannier orbitals only modify the prefactor of this logarithm.

5.3.2 Optical conductivity

Now, the real part of the optical conductivity is determined via the Kubo formal

$$\sigma(\omega) = -\frac{\operatorname{Im} \chi_J(\omega)}{\omega} , \tag{5.38}$$

where χ_J is the current-current correlation function. As already discussed in the previous sections, we are interested in the high-frequency regime, where the renormalized coupling constant is small, and use perturbation theory to expand the correlation function in small α, i. e., $\chi_J(\omega) = \chi_J^{(0)}(\omega) + \chi_J^{(1)}(\omega) + \cdots$. Here, $\chi_J^{(0)}$ is the non-interacting contribution to the optical conductivity, whereas $\chi_J^{(1)}$ is the leading-order correction in α and consists of the two self-energy diagrams $\chi_J^{(1,bc)}$ and the vertex correction $\chi_J^{(1,d)}$. The different contributions to the current-current correlation function relate to the conductivity via $\sigma^{(i)} = -\operatorname{Im} \chi_J^{(i)}(\omega)/\omega$.

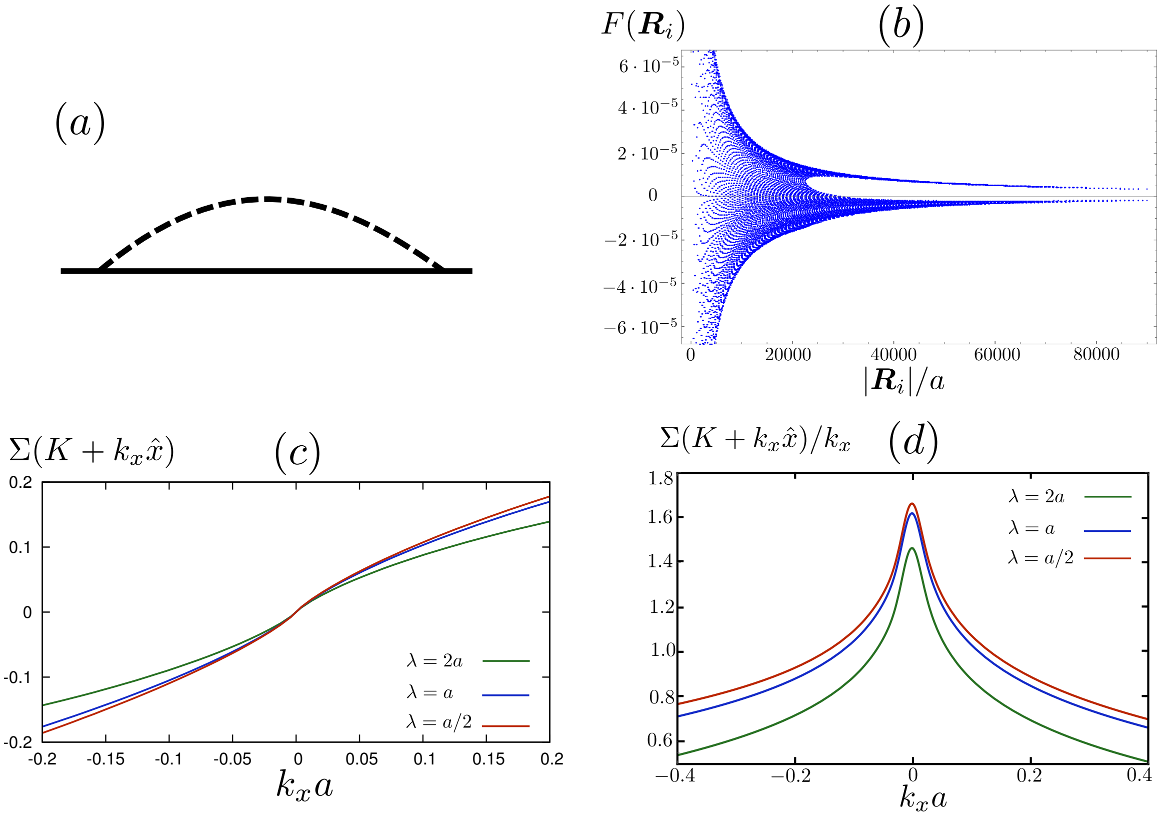

[Reprinted figure with permission from Julia M. Link, Peter P. Orth, Daniel E. Sheehy, and Jörg Schmalian, Phys. Rev. B **93**, 235447 (2016). Copyright 2016 by the American Physical Society.]

Figure 5.4: The self-energy of graphene in the tight-binding description. Panel (a) shows the self-energy diagram. In panel (b), the coefficients $F(\boldsymbol{R}_i)$ are plotted as a function of $|\boldsymbol{R}_i|/a$. They decrease fast and thus ensure the convergence of the self-energy. This convergence is illustrated in panel (c), where we show the self-energy around the Dirac point for different sizes of the Wannier orbitals. Panel (d) shows the slope of the self-energy, and only here we see a logarithmically divergent behavior as the momentum $k_x a$ approaches zero.

Result for non-interacting electrons

The optical conductivity for non-interacting quasiparticles is determined by the free current-current correlation function

$$\begin{aligned}\chi_J^{(0)}(i\omega) &= -\frac{T}{2}\sum_{\boldsymbol{k},\epsilon,\nu}\mathrm{Tr}\left[\mathcal{J}^\nu_{\boldsymbol{k}}\mathcal{G}_{\boldsymbol{k},\mathrm{i}\epsilon}\mathcal{J}^\nu_{\boldsymbol{k}}\mathcal{G}_{\boldsymbol{k},\mathrm{i}(\epsilon+\omega)}\right] \\ &= -\frac{1}{2}\sum_{\boldsymbol{k},\nu}\frac{\left(h_{\boldsymbol{k}}{}^{*}j_{\nu,\boldsymbol{k}} - h_{\boldsymbol{k}}j^{*}_{\nu,\boldsymbol{k}}\right)^2}{t\,|h_{\boldsymbol{k}}|\left(4|h_{\boldsymbol{k}}|^2+\omega^2/t^2\right)}\,, \end{aligned} \tag{5.39}$$

where in the last line, we already performed the sum over the Matsubara frequency $\mathrm{i}\epsilon$ and $\nu = x, y$. The function $h_{\boldsymbol{k}} = 1 + \mathrm{e}^{\mathrm{i}\boldsymbol{k}\cdot\boldsymbol{a}_1} + \mathrm{e}^{\mathrm{i}\boldsymbol{k}\cdot\boldsymbol{a_2}}$ is the off-diagonal element of the tight-binding Hamiltonian in momentum space defined in (4.4), while the current operator $j_{y,\boldsymbol{k}} = -\mathrm{i}ta(h_{\boldsymbol{k}} - 3)/2$ is defined in (4.12a), and t denotes the hopping element. Upon analytically continuing $\mathrm{i}\omega \to \omega + \mathrm{i}\delta$, we find for the denominator of the correlation function

$$\frac{1}{4|h_{\boldsymbol{k}}|^2+\omega^2} \to \mathrm{P.V.}\frac{1}{4|h_{\boldsymbol{k}}|^2-\omega^2} + \mathrm{i}\frac{\pi}{2\omega}\delta\left(\omega - 2|h_{\boldsymbol{k}}|\right) + \mathrm{i}\frac{\pi}{2\omega}\delta\left(\omega + 2|h_{\boldsymbol{k}}|\right)\,, \tag{5.40}$$

where P.V. denotes the principal value integral and it is sufficient to study $\omega > 0$ in the following. The imaginary part of the retarded current-current correlator is thus

$$\mathrm{Im}\,\chi_J^{(0)}(\omega) = \sum_{\boldsymbol{k}}\left(\frac{ta^2\pi}{32}\right)\left[18 + 4\left|h_{\boldsymbol{k}}\right|^2 + 18\frac{\left|\mathrm{Re}\,h_{\boldsymbol{k}}\right|^2 - \left|\mathrm{Im}\,h_{\boldsymbol{k}}\right|^2}{\left|h_{\boldsymbol{k}}\right|^2} - 24\left|h_{\boldsymbol{k}}\right|\right]\delta\left(|h_{\boldsymbol{k}}| - \frac{\omega}{2t}\right)\,. \tag{5.41}$$

The first two terms can be evaluated analytically exact, whereas the remaining terms are going to be Taylor expanded to order $\mathcal{O}((\omega/t)^3)$ around the Dirac points. Hence, the noninteracting optical conductivity in the tight-binding description is, setting $t = 1$,[4]

$$\begin{aligned}\sigma(\omega) &= \frac{\pi}{32\omega}\rho\left(\frac{\omega}{2}\right)(18+\omega^2) - \frac{1}{8}\frac{\omega^2}{36} & (5.42)\\ &\approx \sigma_0\left(1 + \frac{1}{9}\omega^2 + \mathcal{O}(\omega^3)\right) & (5.43)\end{aligned}$$

with the density of state

$$\rho(E) = \frac{1}{(2\pi)^2}\frac{32E\sqrt{1-\frac{E}{3}}K\left[\frac{-16E}{(E-3)(1+E)^3}\right]}{3(3-E)(1+E)^{3/2}}\,. \tag{5.44}$$

Here, $K[m]$ is the complete elliptic integral of the first kind and $\sigma_0 = \frac{N_s}{8}\frac{e^2}{\hbar}$ is the result for the non-interacting optical conductivity in the Dirac approximation. (The factor $N_s = 2$ arises because our fermions have a spin degree of freedom. The valley degree of freedom was already taken into account by the tight-binding calculation.) As shown in Fig. 5.5, the Dirac approximation is valid for $\omega \ll t$ and breaks down close to the van Hove singularity at $\omega = 2t$, where the optical conductivity increases proportional to ω^2. This effect of the curvature of the energy spectrum can also be seen

---

[4] The frequencies are now measured in units of the hopping element.

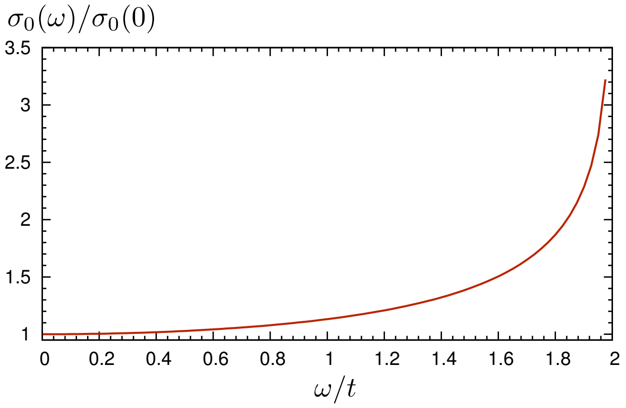

[Reprinted figure with permission from Julia M. Link, Peter P. Orth, Daniel E. Sheehy, and Jörg Schmalian, Phys. Rev. B **93**,235447 (2016). Copyright 2016 by the American Physical Society.]

Figure 5.5: Conductivity $\sigma_0(\omega)$ for noninteracting electrons in the tight-binding approximation with only nearest-neighbor interaction. For small frequencies, the Dirac approximation $\sigma_0(0) = \frac{1}{4}\frac{e^2}{\hbar}$ is valid, whereas it breaks down at the van Hove singularity at $\omega = 2t$.

in the experimental data of the light transmissivity of graphene, which decreases for increasing light frequency.
We want to emphasize that our results differ from previously reported ones [22, 101]. This is of tremendous importance for the prediction of the light transmissivity which differs more strongly from the non-interacting Dirac limit than previously reported. The transmissivity will decrease faster for decreasing wavelength as was predicted by Stauber *et al.* [101]. The detailed calculation of the non-interacting optical conductivity can be found in App. A.2.1.

Interaction corrections to the optical conductivity

The correction coefficient $\mathcal{C}_\sigma$ is determined by three diagrams: the two self-energy diagrams (diagram (b) and (c) in Fig. 5.3) and the vertex correction (diagram (d) shown in Fig. 5.3). The corresponding current-current correlation functions are

$$\chi_J^{(1,bc)}(i\omega) = -T^2 \sum_{\boldsymbol{k}\epsilon\epsilon'\nu} \int \frac{d^2q}{(2\pi)^2} V(\boldsymbol{q}) \mathrm{Tr}\Big(\mathcal{J}_{\boldsymbol{k}}^{\nu} \mathcal{G}_{\boldsymbol{k},\mathrm{i}(\omega+\epsilon)} \mathcal{J}_{\boldsymbol{k}}^{\nu} \mathcal{G}_{\boldsymbol{k},\mathrm{i}\epsilon} M_{\boldsymbol{q}} \mathcal{G}_{\boldsymbol{k}+\boldsymbol{q},\mathrm{i}\epsilon'} M_{-\boldsymbol{q}} \mathcal{G}_{\boldsymbol{k},\mathrm{i}\epsilon}\Big) \tag{5.45}$$

$$\chi_J^{(1,d)}(i\omega) = \frac{T^2}{2} \sum_{\boldsymbol{k}\epsilon\epsilon'\nu} \int \frac{d^2q}{(2\pi)^2} V(\boldsymbol{q}) \mathrm{Tr}\Big(\mathcal{J}_{\boldsymbol{k}}^{\nu} \mathcal{G}_{\boldsymbol{k},\mathrm{i}(\omega+\epsilon)} M_{\boldsymbol{q}} \mathcal{G}_{\boldsymbol{k}+\boldsymbol{q},\mathrm{i}(\omega+\epsilon')} \mathcal{J}_{\boldsymbol{k}}^{\nu} \mathcal{G}_{\boldsymbol{k}+\boldsymbol{q},\mathrm{i}\epsilon'} M_{-\boldsymbol{q}} \mathcal{G}_{\boldsymbol{k},\mathrm{i}\epsilon}\Big) . \tag{5.46}$$

In order to evaluate these expressions, we will implement a crucial simplification: we rewrite these integrals in such a way that the $\boldsymbol{q}$ integral can be done analytically. Therefore, we will evaluate the diagrams by going to real-space and re-express them as sums over Bravais lattice vectors.

In the following, we roughly sketch how the diagrams are evaluated. For a detailed version of the calculation, we refer to App. A.2.2.

Let us start with the two *self-energy diagrams*. After the frequency integration, the self-energy diagrams can be cast into the form

$$\chi_J^{(1,bc)}(\mathrm{i}\Omega) = -\sum_{k} \frac{1}{4|h_{\boldsymbol{k}}|^2} \left[\frac{D_1(\boldsymbol{k})}{4|h_{\boldsymbol{k}}|^2 + \Omega^2} + D_2(\boldsymbol{k}) \frac{4|h_{\boldsymbol{k}}|^2 - \Omega^2}{\left(4|h_{\boldsymbol{k}}|^2 + \Omega^2\right)^2} \right] , \tag{5.47}$$

where $D_1(\boldsymbol{k})$ and $D_2(\boldsymbol{k})$ are functions of combinations of $h_{\boldsymbol{k}}$, $\Sigma_{12}(\boldsymbol{k})$ and $\boldsymbol{j}_{\boldsymbol{k}}$. The explicit expression can be found in App. A.2.2. The analytical continuation $\mathrm{i}\Omega \to \omega + \mathrm{i}\delta$ can be performed, using Eq. (5.40) for the term proportional to $D_1(\boldsymbol{p})$, and

$$\frac{4|h_{\boldsymbol{k}}|^2 - \Omega^2}{\left(4|h_{\boldsymbol{k}}|^2 + \Omega^2\right)^2} \to \frac{d}{d\omega} \frac{\omega}{4|h_{\boldsymbol{k}}|} \left[\frac{1}{2|h_{\boldsymbol{k}}| + \omega + \mathrm{i}\delta} + \frac{1}{2|h_{\boldsymbol{k}}| - \omega - \mathrm{i}\delta} \right] \tag{5.48}$$

for the term proportional to $D_2(\boldsymbol{k})$. After taking the imaginary part of the current-current correlation function and assuming $\omega > 0$, it holds

$$\operatorname{Im} \chi_J^{(1,bc)}(\mathrm{i}\Omega) = -\pi \sum_{k} \frac{1}{16|h_{\boldsymbol{k}}|^4} D_1(\boldsymbol{k}) \delta(\omega - 2|h_{\boldsymbol{k}}|) - \pi \frac{d}{d\omega} \sum_{k} \frac{\omega}{16|h_{\boldsymbol{k}}|^2} D_2(\boldsymbol{k}) \delta(\omega - 2|h_{\boldsymbol{k}}|) . \tag{5.49}$$

To evaluate this term, we determine $\Sigma_{12}(\boldsymbol{k})$ for $\boldsymbol{k}$ within the first Brillouin zone by evaluating the sum over 4.6×10^4 Bravais lattice vectors. What then remains to be done is to perform the $\boldsymbol{k}$ integration, which is pinned to equal energy contours around the Dirac points, due to the δ-functions.

Now let us turn our attention to the *vertex correction.* The current-current correlation function can be written even more compactly by introducing the quantity

$$I_\mu(\boldsymbol{k}, \mathrm{i}\Omega) = \int \frac{d\omega}{2\pi} \mathcal{G}_{\boldsymbol{k},\mathrm{i}\omega} \mathcal{J}^\mu_{\boldsymbol{k}} \mathcal{G}_{\boldsymbol{k},\mathrm{i}(\omega-\Omega)} = \frac{1}{|h_{\boldsymbol{k}}|(4|h_{\boldsymbol{k}}|^2 + \Omega^2)} V_\mu(\boldsymbol{k}, \Omega) , \tag{5.50}$$

where $V_\mu(\boldsymbol{k}, \omega)$ is a matrix whose matrix elements depend on the functions $h_{\boldsymbol{k}}$, and $\boldsymbol{j}_{\boldsymbol{k}}$. (For the exact definitions, we again refer to the App. A.2.2.) Hence, after performing the frequency integration, the correlation function is given by the expression

$$\chi_J^{(1,d)} = \sum_{k} \frac{1}{|h_{\boldsymbol{k}}|(4|h_{\boldsymbol{k}}|^2 + \Omega^2)} \operatorname{Tr} \left[V_\mu(\boldsymbol{k}, \Omega) Q_\mu(\boldsymbol{k}, -\Omega) \right] \tag{5.51}$$

with

$$Q_\mu(\boldsymbol{k}, -\Omega) \equiv \int_{\boldsymbol{q}} V(\boldsymbol{q}) \frac{M_{-\boldsymbol{q}} V_\mu(\boldsymbol{k} + \boldsymbol{q}, -\Omega) M_{\boldsymbol{q}}}{|h_{\boldsymbol{k}+\boldsymbol{q}}|(4|h_{\boldsymbol{k}+\boldsymbol{q}}|^2 + \Omega^2)} . \tag{5.52}$$

Analogous to the self-energy, we rewrite $Q_\mu(\boldsymbol{k}, -\Omega)$ as a sum over Bravais lattice vectors by applying the Fourier transform, i. e., $Q_\mu(\boldsymbol{k}, -\Omega) = A \sum_{\boldsymbol{R}_i} Q_\mu(\boldsymbol{R}_i, -\Omega) \mathrm{e}^{\mathrm{i}\boldsymbol{k}\cdot\boldsymbol{R}_i}$. Here again, the matrix $M_{\boldsymbol{q}}$ ensures the convergence for the $\boldsymbol{q}$-integration. After analytical continuation, we find for the retarded correlator:

$$\begin{aligned} \chi_J^{(1,d)}(\omega) = -e^2 A \sum_{\mu=x,y} \sum_{\boldsymbol{R}_i} \sum_{\boldsymbol{k},\boldsymbol{k}'} & \mathrm{e}^{\mathrm{i}(\boldsymbol{k}-\boldsymbol{k}')\cdot\boldsymbol{R}_i} [h_{\boldsymbol{k}} \boldsymbol{j}^*_{\mu,\boldsymbol{k}} - h^*_{\boldsymbol{k}} \boldsymbol{j}_{\mu,\boldsymbol{k}}][h_{\boldsymbol{k}'} \boldsymbol{j}^*_{\mu,\boldsymbol{k}'} - h^*_{\boldsymbol{k}'} \boldsymbol{j}_{\mu,\boldsymbol{k}'}] \\ \times \left[\frac{\omega^2}{2|\boldsymbol{R}_i|} + \frac{h^*_{\boldsymbol{k}} h_{\boldsymbol{k}'}}{|\boldsymbol{R}_i - a\hat{y}|} + \frac{h_{\boldsymbol{k}} {h_{\boldsymbol{k}'}}^*}{|\boldsymbol{R}_i + a\hat{y}|} \right] & \frac{\pi}{2\omega} \delta(\omega - 2|h_{\boldsymbol{k}}|) \frac{1}{|h_{\boldsymbol{k}}||h_{\boldsymbol{k}'}|} \mathrm{P.V.} \frac{1}{4|h_{\boldsymbol{k}'}|^2 - \omega^2} . \end{aligned} \tag{5.53}$$

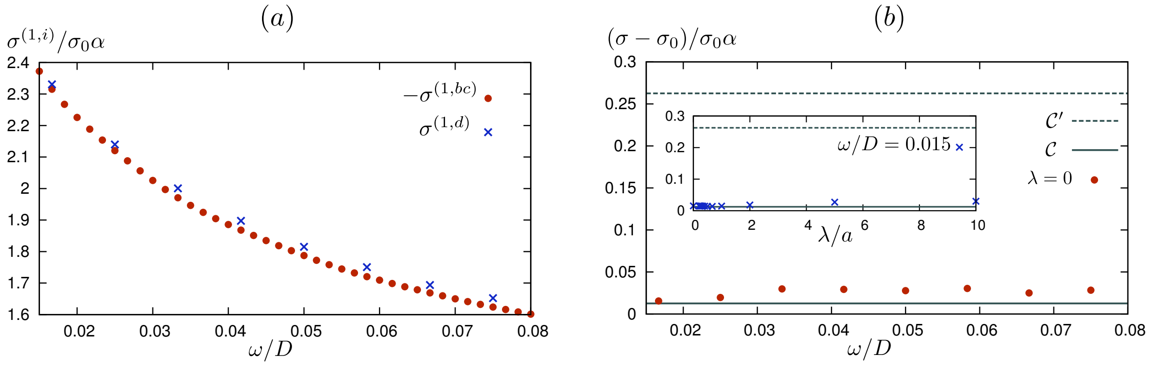

[Reprinted figure with permission from Julia M. Link, Peter P. Orth, Daniel E. Sheehy, and Jörg Schmalian, Phys. Rev. B **93**, 235447 (2016). Copyright 2016 by the American Physical Society.]

Figure 5.6: In panel (a), the self-energy $\sigma^{(1,bc)}$ and vertex-correction $\sigma^{(1,d)}$ contribution to the frequency-dependent conductivity, normalized to $\sigma_0\alpha$.
In panel (b), the red dots depict our results for the interaction coefficient as a function of the frequency ω/D, where $D = 6t$ is the bandwidth of graphene. They are clearly in agreement with the analytical prediction $\mathcal{C}_\sigma = \frac{19-6\pi}{22}$. The inset shows the dependence of the correction coefficient on the size of the Wannier orbitals for $\omega/D = 0.015$. The correction coefficient is independent of λ and thus universal.

To evaluate this expression, we numerically evaluate the integrations over the first Brillouin zone and sum over all Bravais lattice vector $\boldsymbol{R}_i$. The above formula is deduced from point-like Wannier orbitals. Upon substituting the expression $\frac{1}{|\boldsymbol{R}_i-a\hat{y}|}$ by $\sqrt{\frac{\pi}{2}}\frac{1}{\lambda}I_0(\frac{|\boldsymbol{R}_i-a\hat{y}|^2}{4\lambda^2})\mathrm{e}^{-|\boldsymbol{R}_i-a\hat{y}|^2/(4\lambda^2)}$ and analogously for $\frac{1}{\boldsymbol{R}_i}$ and $\frac{1}{|\boldsymbol{R}_i+a\hat{y}|}$, Eq. (5.53) can be extended to Wannier orbitals with finite size λ.

Both contributions, the two self-energy diagrams and the vertex diagram, diverge logarithmically in the low-frequency limit $\omega/D \to 0$, where $D = 6t$ is the bandwidth of graphene. This can be seen in Fig. 5.6 (a), where the different contributions to the conductivity (normalized to $\sigma_0\alpha$) are depicted as a function of the frequency. Upon adding up the self-energy and the vertex contribution, the value of the correction coefficient is determined by

$$\sigma^{(1)} = \sigma^{(1,bc)} + \sigma^{(1,d)} = \sigma_0\alpha\left(\mathcal{C}_{\sigma bc} + \mathcal{C}_{\sigma d}\right) = \sigma_0\alpha\mathcal{C}_\sigma\,. \tag{5.54}$$

In Fig. 5.6 (b), the correction coefficients determined by our tight-binging calculation (red dots) are shown as a function of the frequency of the incoming light. Our numerical values of the correction coefficient are in very good agreement with the analytical value $\mathcal{C}_\sigma = \frac{19-6\pi}{12}$ and clearly rules out $\tilde{\mathcal{C}_\sigma} = \frac{22-6\pi}{12}$. Furthermore, we are able to study the possible dependence of the correction coefficient on the size of the Wannier orbitals λ. The inset in Fig. 5.6(b) shows the calculated values of the correction coefficient for different sizes of the Wannier orbitals at $\omega/D = 0.015$. No dependence of the correction coefficient on the size of the Wannier orbitals can be observed. Hence, the correction coefficient

$$\mathcal{C}_\sigma = \frac{19-6\pi}{22} \tag{5.55}$$

is *universal*, i. e., it neither depends on the frequency nor on the size of the Wannier orbitals.

Now let us compare the results of our tight-binding calculation to the experimental data of the

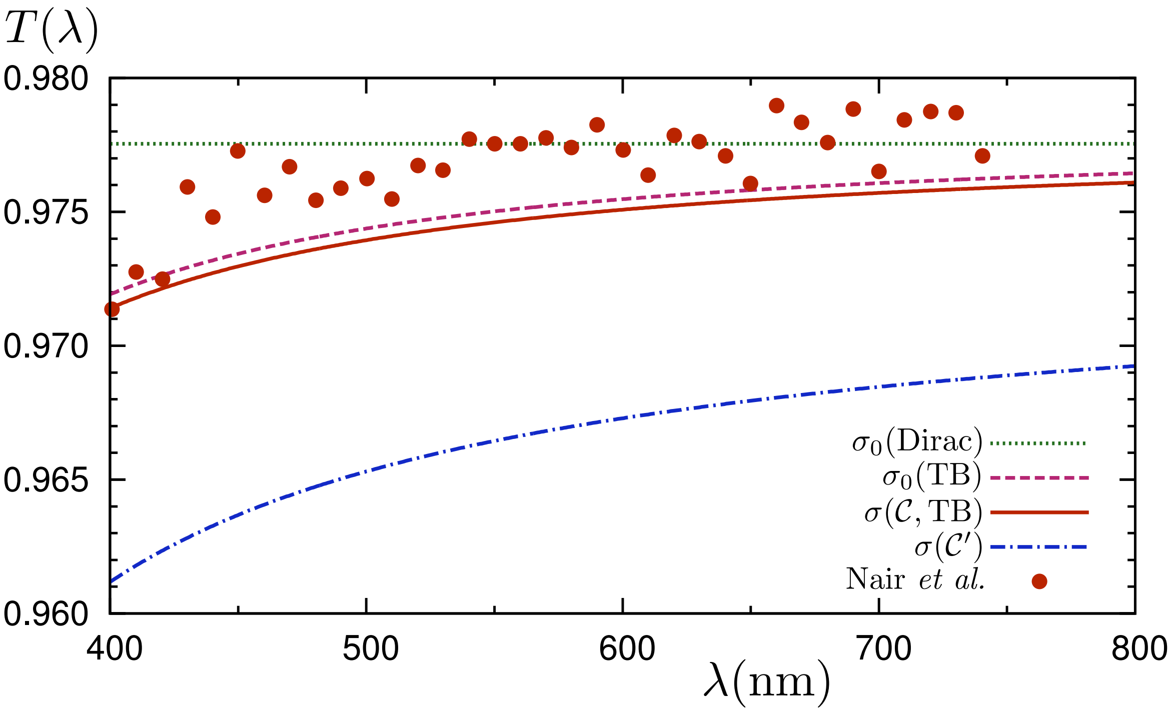

[Reprinted figure with permission from Julia M. Link, Peter P. Orth, Daniel E. Sheehy, and Jörg Schmalian, Phys. Rev. B **93**, 235447 (2016). Copyright 2016 by the American Physical Society.]

Figure 5.7: Optical transmission through graphene as a function of the wavelength λ_ω.

light transmissivity through graphene $T(\lambda_\omega)$, which were measured by Nair *et al.* [22]. Upon relating our frequency-dependent result of the non-interacting optical conductivity to the wavelength of the incoming light by $\lambda_\omega = 2\pi c/\omega$, we find different theoretical predictions for the transmissivity. These predictions are shown as different curves in Fig. 5.7. As we have already seen at the beginning of this section, the prediction obtained using free Dirac fermions $\sigma_0(\text{Dirac})$ (green, dashed line) does not capture the decrease of the transmissivity for smaller wavelengths. However, already the non-interacting conductivity of the tight-binding model $\sigma_0(\text{TB})$ (red, dashed curve) describes this decrease quite well, since it takes into account the nonlinearity of the energy spectrum and the resulting parabolic increase of the conductivity with increasing frequency.

Finally, we want to answer the question "what role plays the Coulomb interaction in graphene". Therefore, we include the corrections to the non-interacting part of the optical conductivity which are proportional to $\sigma_0(\text{TB})\alpha(\lambda_\omega)\mathcal{C}_\sigma$. The incorrect value of the correction coefficient $\tilde{\mathcal{C}_\sigma}$ strongly decreases the transmissivity (blue, dashed line) and is not in agreement with the experimental data. However, our value of the correction coefficient $\mathcal{C}_\sigma$ only introduces a small shift of the non-interacting optical conductivity in the tight-binding description (red, full line) which is in full agreement with the experimental data. In conclusion, we do not see any big influence of the Coulomb interaction on the optical conductivity, since the correction coefficient is small by chance.

5.4 Field theoretical approach in the Dirac limit

In this section, we reconcile the result $\tilde{\mathcal{C}_\sigma} = \frac{22-6\pi}{12}$ obtained by Juricic, Vafek and Herbut (JVH) from the dimensional regularization (DR) scheme [10] combined with the Wilson-renormalization group (RG) analysis with our result $\mathcal{C}_\sigma = \frac{19-6\pi}{12}$ obtained in the tight-binding calculation.

To this end, we first present a DR scheme combined with the modified minimal subtraction $\overline{\text{MS}}$ scheme (a continuum RG) as was published by Teber and Kotikov (TK) in Ref. 15. Determining the two self-energy diagrams and the vertex correction in the DR scheme, TK also find $\tilde{\mathcal{C}_\sigma}$ which was previously obtained by JHV. However, upon combining this result of the DR with the $\overline{\text{MS}}$ scheme, counter terms canceling the divergences are introduced which lead to a renormalization of the bare bubble diagram. This renormalization will fix the value of the correction coefficient to $\mathcal{C}_\sigma$. In the first part of the section, we elaborate this calculation in detail and confirm the TK results.

In the second part of the section, we present how the DR scheme is correctly implemented in the context of Wilson-momentum RG analysis. We show that upon calculating the correction coefficient in $d = 2 - \epsilon$ with an ultraviolet momentum cut-off Λ, a UV quirk arises, i. e., the limits of $\Lambda \to \infty$ and $\epsilon \to 0$ do not commute. By describing Mishchenko's approach, where he used the density-density correlator χ_ρ to calculate the correction coefficient [8], we will locate the origin of the UV quirk at the self-energy of the Dirac model.

This section is based again on my work in collaboration with Peter P. Orth, Daniel E. Sheehy and Jörg Schmalian published in Ref. 16.

5.4.1 Continuum renormalization group and modified minimal subtraction $\overline{\text{MS}}$ scheme

Here, we demonstrate how the DR scheme produces the correct value of the correction coefficient by combining it with a continuum-field RG. Thereby, we follow closely Teber and Kotikov [15] and give a more detailed presentation of the calculation. The difference between Wilson RG and the modified minimal subtraction scheme $\overline{\text{MS}}$ is emphasized. In contrast to the Wilson RG, no UV momentum cut-off

Λ is introduced in the $\overline{\text{MS}}$ scheme. Here, a physical energy scale μ renders the in $1/\epsilon$ diverging observables finite, where ϵ is the parameter of the DR. As shown by JVH and TK, the self-energy diagram and the vertex correction yield $\tilde{\mathcal{C}}_\sigma = \frac{22-6\pi}{12}$ in the dimensional-regularization scheme. However, TK realized that the theory is divergent and needs to be be regularized by the continuum-renormalization group analysis. This is done by introducing counter terms, which remove the divergences. After the regularization procedure, we obtain the correction value $\mathcal{C}_\sigma = \frac{19-6\pi}{12}$.

Let us start with the action of graphene

$$\mathcal{S} = \int d\tau \int d^d x \hat{\psi}_0^\dagger \left(\partial_\tau + \mathrm{i}e_0 A_0^0 + v_{\mathrm{F}0}(-\mathrm{i}\boldsymbol{\nabla}\cdot\boldsymbol{\sigma})\right)\hat{\psi}_0 + \int d\tau \int d^{d_\gamma} x (\partial_x A_0^0)^2 \,, \tag{5.56}$$

where $d = 2-\epsilon$ is the spatial dimension of the electronic degrees of freedom while for the gauge fields $A_0^\nu \equiv A_0$ with $\nu \in \{\tau, x, y\}$ it is $d_\gamma = 3$. The subscript “0” denotes the bare physical quantities, such as the bare fermionic fields $\hat{\psi}$ and the gauge fields A_0 which mediate the Coulomb potential

$$V(\boldsymbol{q}) = \frac{2\pi e^2}{|\boldsymbol{q}|}\frac{r_0^{-\epsilon}\pi^{\epsilon/2}\,\Gamma\left(\frac{1}{2}\right)}{\Gamma\left(\frac{1-\epsilon}{2}\right)}\,, \tag{5.57}$$

where the length scale r_0 is introduced in such a way that the Coulomb potential has the correct units in $d = 2-\epsilon$ dimensions. This action yields physical observables which are divergent in the limit $\epsilon \to 0$. One of these quantities is the self energy

$$\Sigma(\boldsymbol{p}) = \phi(\boldsymbol{p})\; v_{\mathrm{F}}\boldsymbol{p}\cdot\boldsymbol{\sigma} = \alpha_0 \frac{2^{2\epsilon-3}\,\Gamma\left(\frac{\epsilon}{2}\right)}{\Gamma\left(1-\frac{\epsilon}{2}\right)}(r_0 p)^{-\epsilon}\; v_{\mathrm{F}}\boldsymbol{p}\cdot\boldsymbol{\sigma}\,. \tag{5.58}$$

The self-energy is divergent in the limit $\epsilon \to 0$, since it is proportional to $1/\epsilon$, as can be seen explicitly by expanding the function $\phi(\boldsymbol{p})$

$$\phi(\boldsymbol{p}) \approx \frac{\alpha_0}{4\epsilon} + \frac{\alpha_0}{4}\left(\log(4) - \log(pr_0) - \gamma\right)\,. \tag{5.59}$$

In order to render the theory finite, we introduce renormalized quantities, i.e., $\psi_0 = \sqrt{Z_\psi}\psi_R$, $A_0 = \sqrt{Z_A}A_R$, $v_{\mathrm{F}0} = Z_v v_{\mathrm{F}R}$ and $e_0 = Z_e e_R$, which leads to the following renormalized Lagrangian density

$$\mathcal{L}_R = Z_\psi\; \hat{\psi}_R^\dagger \partial_\tau \hat{\psi}_R + \mathrm{i}e_0\sqrt{Z_A}Z_\psi\; \hat{\psi}_R^\dagger A_R^0 \hat{\psi}_R + Z_v Z_\psi\; v_{\mathrm{F}R}\hat{\psi}_R^\dagger(-\mathrm{i}\boldsymbol{\nabla}\cdot\boldsymbol{\sigma})\hat{\psi}_R + Z_A\;\left(\partial_x A_R^0\right)^2\,. \tag{5.60}$$

Next, counter terms are introduced by parameterizing the scaling factors with $Z_i \to 1+\delta_i$. The counter terms δ_i are chosen in such a way that they cancel the divergences of the system. In the renormalized self-energy, the following counter terms occur

$$\Sigma(\boldsymbol{p})_R \sim \phi_R(\boldsymbol{p})\; v_{\mathrm{F}R}\boldsymbol{p}\cdot\boldsymbol{\sigma} + \delta_v\; v_{\mathrm{F}R}\boldsymbol{p}\cdot\boldsymbol{\sigma} + \delta_\psi\;\left(\mathrm{i}\Omega + v_{\mathrm{F}R}\boldsymbol{p}\boldsymbol{\sigma}\right)\,. \tag{5.61}$$

Due to the self-energy being frequency independent, the counter term of the fermionic fields is zero, $\delta_\psi = 0$, which leads to the scaling factor $Z_\psi = 1$. However, the velocity counter term must cancel the divergence of the self-energy, which yields

$$\delta_v = -\frac{\alpha_R}{4}\frac{1}{\epsilon} \;\to\; Z_v = \left(1 - \frac{\alpha_R}{4\epsilon}\right)\,. \tag{5.62}$$

To obtain a finite physical quantity, we the modified minimal subtraction $\overline{\mathrm{MS}}$ scheme to the self-energy. In the $\overline{\mathrm{MS}}$ scheme, a physical energy scale μ is introduced in such a way that the physical observable becomes dimensionless and the divergence is removed [41]. Hence, the divergence $1/\epsilon$ will be substituted by a logarithm depending on the physical scale μ

$$\frac{1}{\epsilon} \to \log\big(\mu/\omega\big)\ . \tag{5.63}$$

Thus upon applying the $\overline{\mathrm{MS}}$ scheme to the self-energy, we find

$$\phi(\boldsymbol{p}) = \frac{\alpha_R}{4}\frac{1}{\epsilon} + \frac{\alpha_R}{4}\big(\log(4) - \log(pr_0) - \gamma\big) \to -\frac{\alpha_R}{4}\log\left(\frac{pr_0}{\tilde{\mu}/\omega}\right) \tag{5.64}$$

with $\tilde{\mu} = 4\mathrm{e}^{-\gamma}\mu$. Here, let us stress the difference of this continuum-field RG to the Wilson momentum RG: In the Wilson RG, due to the UV momentum cut-off Λ, the self-energy does not diverge but depends logarithmically on Λ. In the DR scheme, the self-energy is divergent, as seen above, and only introducing the physical scale μ (using a continuum RG) renders the quantity finite.

Now, let us focus again on the remaining physical observables, the Fermi velocity and the coupling constant, and see how these quantities are rendered finite. Firstly, the dependence of the electrical charge on the physical scale is studied. The electrical charge stays unrenormalized in graphene, i. e., $Z_e = 1$. The dimensionality of the electrical charge is $[e] = \epsilon$, which can be deduced from the fact that the action is a dimensionless quantity and the dimension of the fermionic fields are $[\psi_0] = d/2$ and the bosonic fields are $[A_0^\nu] = 1 - \epsilon$. Thus, in order to have a dimensionless electrical charge, we introduce again the physical scale μ and obtain for the electrical charge the following dependence on μ

$$\frac{e_0^2}{\mu^{2\epsilon}} = e^2(\mu)Z_e \Leftrightarrow e_0^2 = \frac{e^2(\mu)}{4^\epsilon}\mathrm{e}^{2\gamma\epsilon}\tilde{\mu}^{2\epsilon} \Leftrightarrow e^2(\mu) = e_0^2 4^\epsilon \mathrm{e}^{-2\gamma\epsilon}\tilde{\mu}^{-2\epsilon}\,. \tag{5.65}$$

For the Fermi velocity, $v_{\mathrm{F}0} = Z_v v_{\mathrm{F}R}$, we find the following renormalization using the counter term δ_v defined in Eq. (5.62)

$$v_{\mathrm{F}0} = \left[1 - \frac{\alpha(\mu)}{4\epsilon}\right]v_{\mathrm{F}}(\mu) \Leftrightarrow v_{\mathrm{F}}(\mu) = \frac{4\epsilon v_{\mathrm{F}0}}{4\epsilon - \alpha(\mu)}\,. \tag{5.66}$$

Upon combining the Eq. (5.65) and Eq. (5.66), the coupling constant can be rewritten as

$$\alpha(\mu) = \frac{e^2(\mu)}{v_{\mathrm{F}}(\mu)} = \frac{\alpha_0 4^\epsilon \mathrm{e}^{-2\gamma\epsilon}\tilde{\mu}^{-2\epsilon}}{1 + \frac{\alpha_0}{4}\frac{1}{\epsilon}4^\epsilon\mathrm{e}^{-2\gamma\epsilon}\tilde{\mu}^{-2\epsilon}} \to \alpha(\mu) = \frac{\alpha_0}{1 + \frac{\alpha_0}{4}\log\left(\frac{\mu}{\omega}\right)}\,, \tag{5.67}$$

where in the last step, we again applied the $\overline{\mathrm{MS}}$ scheme, substituting $1/\epsilon$ by $\log\big(\mu/\omega\big)$, and took the limit $\epsilon \to 0$. Analogously, we find for the velocity

$$v_{\mathrm{F}0} = v_{\mathrm{F}}(\mu) - \frac{1}{4\epsilon}e^2(\mu) \Leftrightarrow v_{\mathrm{F}}(\mu) = v_{\mathrm{F}0} + \frac{1}{4\epsilon}e_0^2 4^\epsilon\mathrm{e}^{-2\gamma\epsilon}\tilde{\mu}^{-2\epsilon} \to v_{\mathrm{F}}(\mu) = v_{\mathrm{F}0} + \frac{e_0^2}{4}\log\left(\frac{\mu}{\omega}\right)\,. \tag{5.68}$$

Now, we are able to study the noninteracting conductivity of Dirac fermions in $d = 2 - \epsilon$ dimensions. The unrenormalized optical conductivity is given by

$$\sigma_{0,0}(\omega) = e_0^2 N_{sv} A_\epsilon \left|\frac{v_0}{\omega}\right|^\epsilon\,, \tag{5.69}$$

with

$$A_\epsilon = 4^{-2+\epsilon}\pi^{\epsilon/2}\frac{(1-\epsilon)}{\Gamma\left(1-\frac{\epsilon}{2}\right)} \,. \tag{5.70}$$

In order to obtain a theory which does not have any divergences, we have to express the above expression by the renormalized physical quantities. This procedure gives us the following expression

$$\sigma_{0,R}(\omega) = \frac{e^2(\mu)}{4^\epsilon} e^{2\gamma\epsilon}\tilde{\mu}^{2\epsilon} N_{sv} A_\epsilon \left|\frac{\left(1-\frac{\alpha(\mu)}{4\epsilon}\right) v_R}{\omega}\right|^\epsilon \,. \tag{5.71}$$

Since there exists a regime where the coupling constant is small, as can be seen in Eq. (5.67), we can expand the following expression in small $\alpha(\mu)$ and obtain

$$\left(1-\frac{\alpha(\mu)}{4\epsilon}\right)^\epsilon \approx 1 - \frac{\alpha(\mu)}{4} \,. \tag{5.72}$$

After inserting this approximation into Eq. (5.71) and taking the limit $\epsilon \to 0$, the noninteracting conductivity is given by

$$\sigma_0(\omega) = \frac{N_{sv}}{16}\frac{e_0^2}{\hbar}\left(1-\frac{\alpha(\omega)}{4}\right) , \tag{5.73}$$

where $\sigma_0(\text{Dirac}) = \frac{N_{sv}}{16}\frac{e_0^2}{\hbar}$ is the universal value of the optical conductivity for noninteracting Dirac fermions. Upon combining this frequency dependence of $\sigma_0(\omega)$ with the value of the correction coefficient $\tilde{\mathcal{C}_\sigma}$ obtained in DR, we find

$$\sigma(\omega) = \sigma_0(\text{Dirac})\left(1-\frac{\alpha(\omega)}{4} + \tilde{\mathcal{C}_\sigma}\ \alpha(\omega)\right) = \sigma_0(\text{Dirac})\left(1+\mathcal{C}_\sigma\ \alpha(\omega)\right) \,. \tag{5.74}$$

Thus, at the end of the continuum RG procedure, the correction coefficient is $\mathcal{C}_\sigma = \frac{19-6\pi}{12}$. The additional term associated with $\left(-\frac{\alpha(\omega)}{4}\right)$ in the noninteracting conductivity arising due to the continuum RG, corrects the value $\tilde{\mathcal{C}_\sigma}$ of the dimensional regularization scheme. Hence, if *no* UV cut-off Λ is introduced to the system and the diagrams are regularized only by DR, one has to combine this DR-scheme with a continuum-field RG and not with a Wilson RG. Only by applying the continuum RG, divergent physical observables will become finite.

5.4.2 Wilson momentum-shell RG combined with dimensional regularization

In this section, we combine the Wilson RG and the DR scheme and demonstrate how the correct value of the correction coefficient $\mathcal{C}_\sigma$ is obtained in the combination of DR and Wilson RG. To this end, the optical conductivity is calculated in $d = 2-\epsilon$ dimensions and an ultraviolet momentum cut-off Λ is introduced. In $d = 2-\epsilon$ dimensions, the flow equation of the Wilson RG for the coupling constant α and the scaling factor Z_T will become ϵ-dependent and we find

$$\alpha(b) = \frac{4\epsilon\alpha b^\epsilon}{4\epsilon + \alpha\left(b^\epsilon - 1\right)} \quad \text{and} \quad Z_T(b) = \frac{4\epsilon + \alpha\left(b^\epsilon-1\right)}{4\epsilon b} \,, \tag{5.75}$$

with $b = e^l$ and $l > 0$. Furthermore, we will identify which integral is responsible for obtaining the different values of the interaction coefficient via the Mishchenko's approach, where the conductivity is determined by the density-density correlator. With the help of this integral, we can demonstrate how the DR obtains $\tilde{\mathcal{C}_\sigma}$, where on the first glance only $\log\Lambda$ is substituted by $1/\epsilon$. Finally, we show that the limits $\lambda \to \infty$ and $\epsilon \to 0$ do not commute, a phenomenon which we call the UV quirk. Only when the UV cut-off is send to infinity at the very last step of the calculation, we obtain $\mathcal{C}_\sigma$. Hence, we find for the conductivity

$$\sigma(\omega,\alpha) = \lim_{\Lambda\to\infty}\lim_{\epsilon\to 0} b^\epsilon \sigma(Z_T^{-1}\omega, \alpha(b), \Lambda)\,. \tag{5.76}$$

Conductivity via Mishchenko's approach

Let us now identify the origin of the different values of the interaction coefficient by studying the optical conductivity in the Mishchenko approach. The optical conductivity is determined by the density-density correlation function χ_ρ via

$$\sigma(\omega) = \lim_{\boldsymbol{q}\to 0}\frac{\omega}{q^2}\mathrm{Im}\chi_\rho(\boldsymbol{q},\omega)\,. \tag{5.77}$$

The bare bubble diagram, describing the noninteracting contribution to the optical conductivity, yields $\chi_\rho^{(0)}(\boldsymbol{q},\omega) = \frac{N_{sv}}{16}\frac{\omega^2}{\sqrt{\omega^2-|\boldsymbol{q}|^2}}\frac{e^2}{\hbar}$ which simplifies to the well known $\sigma_0(\text{Dirac}) = \frac{N_{sv}}{16}\frac{e^2}{\hbar}$ in the limit $\boldsymbol{q}\to 0$. The self energy is given, as already seen in Eq. (5.19), by

$$\Sigma(\boldsymbol{k}) = -\int_\epsilon\int_{\boldsymbol{q}}\frac{2\pi\alpha}{|\boldsymbol{q}|}G_{\boldsymbol{q}+\boldsymbol{k},\mathrm{i}\epsilon} = \frac{\alpha}{4}\log\left(\frac{4\Lambda\sqrt{e}}{k}\right)\boldsymbol{k}\cdot\boldsymbol{\sigma}\,, \tag{5.78}$$

where Λ is the UV cut-off which restricts the $\boldsymbol{q}$-momentum of the Coulomb interaction to a finite value. The density-density correlator describing the correction due to the self-energy is

$$\chi_\rho^{(1,bc)}(\boldsymbol{q},\omega) = T\sum_\epsilon\int_{\boldsymbol{k}}\mathrm{Tr}\left[G_{\boldsymbol{k},\mathrm{i}\epsilon}\Sigma(\boldsymbol{k})G_{\boldsymbol{k},\mathrm{i}\epsilon}G_{\boldsymbol{k}+\boldsymbol{q},\mathrm{i}(\epsilon+\omega)}\right]\,. \tag{5.79}$$

After performing the Matsubara sum and expanding the correlation function for small $\boldsymbol{q}$, we find

$$\begin{aligned}\chi_\rho^{(1,bc)}(\boldsymbol{q},\omega) &= -\frac{1}{2}N_{sv}e^2\alpha\frac{q^2}{8\pi^3}\frac{1}{\omega}\int_0^\infty \tilde{p}\mathrm{d}\tilde{p}\log\left(\frac{v_\mathrm{F}\Lambda\sqrt{e}}{\tilde{p}\omega}\right)\frac{\pi^2(4\tilde{p}^2-1)}{\tilde{p}(4\tilde{p}^2+1)^2} && (5.80)\\ &= \frac{q^2N_{sv}\alpha}{64\omega}\,, && (5.81)\end{aligned}$$

where $\tilde{p}$ is a dimensionless variable. Let us note here that the integral over $\boldsymbol{p}$ is consisting of the sum of two integrands, since the logarithm can be rewritten as

$$\log\left(\frac{v_\mathrm{F}\Lambda\sqrt{e}}{\tilde{p}\omega}\right) = \log\left(\frac{v_\mathrm{F}\Lambda\sqrt{e}}{\omega}\right) - \log\left(\tilde{p}\right)\,. \tag{5.82}$$

The first integrand depending on the cut-off will vanish upon performing the $\tilde{p}$-integral. Only the integrand proportional to $\log\left(\tilde{p}\right)$ will yield a finite result. Thus, the contribution to the correction coefficient due to the divergent self-energy will be finite and cut-off independent. This integral will

play an important role in our further discussion of the origin of the different values of $\mathcal{C}_\sigma$.
Now let us turn back to the leading-order corrections in α. After evaluating the density correlation function $\chi_\rho^{(1,bc)}$, we find the following contribution to the conductivity

$$\sigma^{(1,bc)}(\omega) = \frac{\alpha(\omega)}{4}\sigma_0(\text{Dirac}) \,, \tag{5.83}$$

which agrees with Eq. (13) of Ref. 8. The advantage of determining the conductivity via the density-density correlation function is that the vertex correction diagram has no logarithmic dependence on the cut-off Λ and yields the finite result

$$\sigma^{(1,d)}(\omega) = \frac{8-3\pi}{6}\alpha(\omega)\sigma_0(\text{Dirac}) \,, \tag{5.84}$$

which finally leads to

$$\sigma(\omega) = \sigma_0(\text{Dirac})\left(1 + \alpha(\omega)\frac{19-6\pi}{12}\right) . \tag{5.85}$$

Hence, the correction coefficient is $\mathcal{C}_\sigma = \frac{19-6\pi}{12}$ which is in agreement with our tight-binding calculation.

Dimensional regularization

How can the dimensional regularization (DR) produce a different result for the correction coefficient? In order to answer this question, we first study the self-energy in $d = 2 - \epsilon$ dimensions. It is

$$\begin{aligned} \Sigma(p) \quad &\propto \quad p^{-\epsilon}\frac{\Gamma\left[\frac{1-\epsilon}{2}\right]\Gamma\left[\frac{3-\epsilon}{2}\right]\Gamma\left[\frac{\epsilon}{2}\right]}{\pi\Gamma[2-\epsilon]} , &(5.86)\\ &\simeq \quad \frac{1}{\epsilon} - \frac{1}{2}\gamma + \log 4 - \log p \,. &(5.87)\end{aligned}$$

Upon comparing this expression of the self-energy in $d = 2 - \epsilon$ to the one obtained in $d = 2$ with an ultraviolet cut-off, Eq. (5.78), we see that the cut-off-dependent term $\log(\Lambda)$ is replaced by $1/\epsilon$. But both expressions of the self-energy are proportional to $\log(p)$. As we have seen before, only this term contributes to the finite value of the self-energy diagram and naively one would expect the same result, $\sigma^{(1,bc)} \propto \frac{\alpha}{4}$, as in the previous section. Thus, in strictly two dimensions we find for $\chi_\rho^{(1,bc)}$ with an self-energy evaluated in $d = 2 - \epsilon$ and the cut-off Λ set to infinity

$$\begin{aligned} I_{d=2,\Lambda=\infty} &\equiv \chi_\rho^{(1,bc)}\frac{16\pi^3}{N_{sv}e^2\alpha q^2} \\ &= \int_0^\infty p\mathrm{d}p\left[\frac{1}{\epsilon} - \frac{1}{2}\gamma + \ln\frac{4}{p}\right]\frac{4p^2-1}{p(4p^2+1)^2} = \int_0^\infty p\mathrm{d}p \ln\frac{1}{p}\frac{4p^2-1}{p(4p^2+1)^2} = -\frac{\pi}{4} , \end{aligned} \tag{5.88}$$

which would be lead to $\mathcal{C}_\sigma$. However, in $d = 2-\epsilon$ dimensions, the measure of the p-momentum integral changes and it is

$$I_{d=2-\epsilon,\Lambda=\infty} = \int_0^\infty p^{1-\epsilon}\mathrm{d}p\left[\frac{1}{\epsilon} - \frac{1}{2}\gamma + \ln\frac{4}{p}\right]\frac{4p^2-1}{p(4p^2+1)^2} = -\frac{\pi}{2} , \tag{5.89}$$

where we took the limit $\epsilon \to 0$ at the end of the calculation. Now, the momentum-independent terms in Eq. (5.89) do not vanish anymore. They are proportional to ϵ and yield a finite contribution when multiplied by $1/\epsilon$. This small difference is seen to double the size of the $\chi_\rho^{(1,bc)}$ diagrams. Since the vertex diagram $\chi_\rho^{(1,d)}$ is convergent and thus has the same value regardless of whether it is calculated in $d = 2$ or $d = 2 - \epsilon$, one finds for the correction coefficient $\tilde{\mathcal{C}_\sigma} = \frac{22-6\pi}{12}$ using dimensional regularization. However, as we have seen previously, dimensional regularization has to be combined with the modified subtraction scheme in order to obtain the correct value. But if one wants to use dimensional regularization in combination with Wilson RG, the momentum cut-off Λ must be kept finite and only at the end of the calculation, it can be send to infinity. The reason for this is that the Wilson RG implicitly requires a momentum cut-off which divides the fermionic fields into fast and slow modes. In the following section, we will see explicitly that the two limits $\epsilon \to 0$ and $\Lambda \to \infty$ do not commute, which we call UV quirk.

Spatial dimension $d = 2 - \epsilon$ but sharp cut-off

Now let us assume that we evaluate the diagrams in $d = 2-\epsilon$ dimensions but maintain the momentum cut-off Λ, since as above mentioned the Wilson RG implicitly requires the cut-off Λ around which the momentum shells are integrated out. The self-energy is then given by

$$\Sigma(\boldsymbol{p}) \propto \int_p^\Lambda \frac{q^{d-1}\mathrm{d}q}{q^2} = \frac{1}{\epsilon}\Big(p^{-\epsilon} - \Lambda^{-\epsilon}\Big) \, . \tag{5.90}$$

Upon inserting this expression into Eq. (5.80), we find

$$I_{d=2-\epsilon,\Lambda} = \int_0^\infty \mathrm{d}p \; p^{1-\epsilon}\frac{1}{\epsilon}\Big(p^{-\epsilon} - \Lambda^{-\epsilon}\Big)\frac{4(v_{\mathrm{F}}p)^2 - \omega^2}{p(4(v_{\mathrm{F}}p)^2+\omega^2)^2} = \left(\frac{\omega}{v_{\mathrm{F}}}\right)^{1-2\epsilon} \frac{\frac{\pi}{4}\left(\frac{\omega}{v_{\mathrm{F}}\Lambda}\right)^{\epsilon} - \frac{\pi}{2}}{\omega^2} , \tag{5.91}$$

which leads to the following form of the correction coefficient

$$\mathcal{C}_\sigma\left(\epsilon, \frac{\omega}{\Lambda}\right) = \frac{22 - 6\pi - 3\left(\frac{\omega}{v_{\mathrm{F}}\Lambda}\right)^{\epsilon}}{12} \, . \tag{5.92}$$

Here we see the UV quirk clearly: The order of limits of the UV cut-off Λ and the dimensional parameter ϵ do not commute. If we first take the limit of $\epsilon \to 0$ before subsequently taking the limit $\Lambda \to \infty$, we obtain $\mathcal{C}_\sigma$. However, if we instead take $\Lambda \to \infty$ first before subsequently taking $\epsilon \to 0$, we obtain $\tilde{\mathcal{C}_\sigma}$:

$$\lim_{\epsilon\to 0}\left(\lim_{\Lambda\to\infty}\left[C\left(\epsilon, \frac{\omega}{\Lambda}\right) = \frac{22 - 6\pi - 3\left(\frac{\omega}{v\Lambda}\right)^{\epsilon}}{12}\right]\right) \;=\; \tilde{\mathcal{C}_\sigma} \, , \tag{5.93}$$

$$\lim_{\Lambda\to\infty}\left(\lim_{\epsilon\to 0}\left[C\left(\epsilon, \frac{\omega}{\Lambda}\right) = \frac{22 - 6\pi - 3\left(\frac{\omega}{v\Lambda}\right)^{\epsilon}}{12}\right]\right) \;=\; \mathcal{C}_\sigma \, . \tag{5.94}$$

The same UV quirk is also found when the dimensional regularization scheme is combined with a smooth cut-off on the Coulomb potential which is implemented by

$$V(\boldsymbol{q}) \to V_\eta(\boldsymbol{q}) = \frac{2\pi\alpha}{|\boldsymbol{q}|^{1+\eta}} \, . \tag{5.95}$$

After some tedious calculation (the details can be found in the App. A.2.3) and combining the DR with the smooth cutoff on the Coulomb potential, we obtain for the correction coefficient

$$\mathcal{C}_\sigma(\eta,\epsilon) = \frac{1}{\eta+\epsilon}\left(\frac{(16-6\pi)(\eta+\epsilon)+3\eta+6\epsilon}{12}\right) . \tag{5.96}$$

Here again, we only find the correct value of the correction coefficient, if we take the limit $\eta \to 0$ at the very end of the calculation.

In conclusion, we showed that it is crucial, if one wants to combine DR with Wilson RG, the UV cut-off Λ (or in the case of the smooth cut-off η) must be kept till the very end of the calculation and should be the last limit being performed.

5.5 Summary

In this chapter, we investigated as important transport property of graphene at the charge neutrality point the electrical conductivity in linear response.

In the hydrodynamic regime, due to the diverging scattering time in the collinear scattering regime, the conductivity is proportional to the square of the inverse coupling constant, i. e., $\sigma(T) = \frac{0.760}{\alpha(T)^2}\frac{e^2}{\hbar}$ [19]. It converges for increasing temperatures to the universal conductivity value of low frequencies $\sigma_0(\text{Dirac})_{\text{disorder}} = \frac{2}{\pi^2}\frac{e^2}{\hbar}$ [95].

Now, in the the optical regime, we determined the noninteracting optical conductivity and its leading order correction in $\alpha(\omega)$ in the *tight-binding* description. We could correct the expression for the non-interacting optical conductivity obtained by Stauber *et al.* in Ref. 101 and found that the non-linearity of the full energy spectrum leads to the following correction

$$\sigma^{(0)}(\omega) = \sigma_0(\text{Dirac})\left(1+\frac{1}{9}\omega^2+\mathcal{O}(\omega^3)\right) . \tag{5.97}$$

Furthermore, we determined the value of the correction coefficient in the tight-binding model to be

$$\mathcal{C}_\sigma = \frac{19-6\pi}{12} . \tag{5.98}$$

We showed that $\mathcal{C}_\sigma$ is universal and does neither depend on the frequency of the incoming light nor on the size of the Wannier orbitals of the carbon atoms. Hence, we could settle the debate over the correct value of $\mathcal{C}_\sigma$, since the tight-binding description yields no diverging quantity having as natural cut-off the inverse lattice constant $\Lambda \sim a^{-1}$. Moreover, we demonstrated the many subtleties which needed to be taken care of, if the correction coefficient is evaluated in the Dirac model via dimensional regularization (DR). We come to the conclusion that it is crucial to combine the DR with a continuum-renormalization group analysis, namely the minimal subtraction scheme, if no UV cut-off is being introduced to the system. However, if the DR is combined with the Wilson RG which has an implicit UV cut-off, the UV momentum cut-off has to be kept finite till the very end of the calculation in order to avoid the UV quirk.

6

Chapter 6

The viscosity in Graphene

So far, we have studied the conductivity of graphene which describes the response of the quasiparticles to an electrical field and thus represents an important transport quantity. However, the electrons and holes in graphene can also be described as a quasiparticle fluid. This fluid is a non-ideal fluid and its characteristics is determined by the shear viscosity, where the viscosity describes the resistance of the fluid to a hydrodynamic flow and connects the gradient of the drift velocity $\partial u_\beta / \partial x_\alpha$ to the dissipative part of the energy-stress tensor $T_{\alpha\beta}$. For a two-dimensional, rotational invariant system, such as graphene, the energy-stress tensor is connected to the drift velocity via

$$T_{\alpha\beta} = \eta \left(\frac{\partial u_\alpha}{\partial x_\beta} + \frac{\partial u_\beta}{\partial x_\alpha} - \delta_{\alpha\beta} \boldsymbol{\nabla} \cdot \boldsymbol{u} \right) + \zeta \delta_{\alpha\beta} \boldsymbol{\nabla} \cdot \boldsymbol{u} \, , \tag{6.1}$$

where η is the shear viscosity and ζ the bulk viscosity which vanishes for graphene. In this chapter, we investigate the shear viscosity of graphene at the charge neutrality point in the hydrodynamic and in the collisionless regime.

In Sec. 6.1 we start with the study of the viscosity in the hydrodynamic regime ($\omega \ll \tau^{-1}$) and show that graphene is a nearly perfect fluid [20] which leads to highly turbulent flow behavior of the quasiparticles [31] and a highly non-linear Navier-Stokes equation [21].

The shear viscosity in the collisionless regime ($\omega \gg \tau^{-1}$) is investigated in Sec. 6.2. Here, we demonstrate that the pseudospin of graphene has an important influence on the shear viscosity and leads, if it is not taken into account, to a shear viscosity tensor which does not fulfill the symmetry property (3.6) introduced in Sec. 3.1.

Furthermore, we consider the question, how the Coulomb interaction influences this important transport property. To this end, we apply again the renormalization group (RG) analysis, go to the regime with the small renormalized coupling constant and perform a perturbation theory. The correction coefficient $\mathcal{C}_\eta$ defines the correction due to the Coulomb potential in the first order of perturbation theory. This coefficient is given by individually divergent diagrams, i. e., the self-energy diagram, the vertex diagram and the honey diagram. In order to cancel the individually divergences of the self-energy and the vertex diagram, an additional diagram needs to be introduced, the honey diagram. This diagram describes the interacting part of the energy-stress tensor and is derived in Sec. 6.2.2. We will regularize all these diagrams with a soft cut-off acting on the Coulomb potential which is a regularization scheme that avoids the UV quirk, as we have demonstrated in the previous chapter. At last we will determine the Hall viscosity of graphene in the collisionless regime.

Sec. 6.2 is based on my work in collaboration with Daniel E. Sheehy, Boris N. Narozhny and Jörg Schmalian which is going to be published in [46].

6.1 ...in the hydrodynamic regime

In this section, we present the properties of the shear viscosity of graphene at the charge neutrality point in the hydrodynamic regime which were obtained by Müller *et al.* in Ref. 20. The calculation of the shear viscosity is analogous to the determination of the conductivity in the hydrodynamic regime, described in Sec. 5.1. Again the quantum Boltzmann equation is used in order to obtain the distribution function of the quasiparticles $f_{\lambda \boldsymbol{k}} = f_{\lambda \boldsymbol{k}}^{(0)} + \delta f_{\lambda \boldsymbol{k}}$, where $f_{\lambda \boldsymbol{k}}^{(0)}$ is the equilibrium Fermi-Dirac distribution and $\delta f_{\lambda \boldsymbol{k}}$ describes the out-off equilibrium contribution to the total distribution function. This time, $\delta f_{\lambda \boldsymbol{k}} = \sum_\lambda \int_{\boldsymbol{k}} f_{\lambda \boldsymbol{k}}^{(0)}(1 - f_{\lambda \boldsymbol{k}}^{(0)}) I_{\alpha\beta} \frac{\partial u_\beta}{\partial x_\alpha} g_{\lambda \boldsymbol{k}}^{\beta}$ with $I_{\alpha\beta} = \lambda(v_{\lambda \boldsymbol{k}}^{\alpha} k_\beta - \delta_{\alpha\beta}\epsilon_{\lambda \boldsymbol{k}}/2)$ is chosen as ansatz for the out-off equilibrium correction as described in Sec. 3.5. The three modes defining $g_{\lambda \boldsymbol{k}}^{\beta} = \sum_n \psi_n \phi_n(\boldsymbol{k}, \lambda)$ are a constant $\phi_0 = \psi_0$, the band index $\phi_1 = \lambda$, and the energy of the system $\phi_2 = \lambda\epsilon_{\lambda \boldsymbol{k}}$, which describe respectively the conservation of the total charge, of the total number of particles and holes, and of the energy. The corresponding coefficients ψ_n are determined by the inversion of the linearized quantum Boltzmann equation and at last the shear viscosity can be evaluated by $\eta_{\alpha\beta\gamma\delta} = \sum_{\lambda} \int_{\boldsymbol{k}} \lambda v_{\lambda \boldsymbol{k}}^{\alpha} k_\beta \left(v_{\lambda \boldsymbol{k}}^{\gamma} k_\delta - \delta_{\gamma\delta}\epsilon_{\lambda \boldsymbol{k}}/2 \right) g_{\lambda \boldsymbol{k}}^{\beta} f_{\lambda \boldsymbol{k}}^{(0)}(1 - f_{\lambda \boldsymbol{k}}^{(0)})/T$. Hence, the smallest eigenvalue of the collision integral determines the shear viscosity $\eta = \eta_{xyxy} = \eta_{yxyx} = \cdots$. Again, in the collinear scattering regime the scattering time diverges logarithmically which leads to the fact that the shear viscosity is (similar to the conductivity) proportional to $\alpha(T)^{-2}$ and higher order corrections will be of order $1/\log\alpha(T)$. The shear viscosity is thus given by [20]

$$\eta(T) = 0.449 \frac{N_{sv}}{4} \frac{1}{\hbar} \frac{\left(k_{\mathrm{B}} T\right)^2}{\left(v_{\mathrm{F}}(T)\alpha(T)\right)^2} \left[1 + \mathcal{O}\left(\frac{1}{\log\alpha} \right) \right] , \tag{6.2}$$

where $N_{sv} = 4$ because of the spin degree of freedom and the additional degree of freedom due to the two Dirac points in the first Brillouin zone. Now as in Sec. 3.6, we want to compare the shear viscosity to the entropy of graphene. The entropy is

$$s = \frac{9\zeta(3)}{\pi} k_{\mathrm{B}} \frac{\left(k_{\mathrm{B}} T\right)^2}{\left[\hbar v_{\mathrm{F}}(T)\alpha(T)\right]^2} \alpha(T)^2 . \tag{6.3}$$

Hence, the ratio of viscosity over entropy can be written as

$$\eta/s = \frac{\hbar}{k_{\mathrm{B}}} \frac{0.499\pi}{9\zeta(3)} \frac{1}{\alpha(T)^2} \simeq 0.00815 \cdot \left(\log \frac{T_\Lambda}{T} \right)^2 . \tag{6.4}$$

The ratio η/s decreases logarithmically with increasing temperature as shown in Fig. 6.1. Due to the small numerical prefactor, the ratio approaches the famous lower bound $\eta/s \geq \frac{\hbar}{4\pi k_B}$ [18], see Eq. (3.56) and Sec. 3.6 for a more detailed discussion, which makes graphene a nearly perfect fluid. Its ratio is even smaller than the ratio of ultra cold atoms with diverging scattering length [102, 103] and of Helium at the λ-point [20]. The small viscosity will lead to highly turbulent flow dynamics. The flow dynamics are governed by the Navier-Stokes equation which will be derived for graphene in the following subsection.

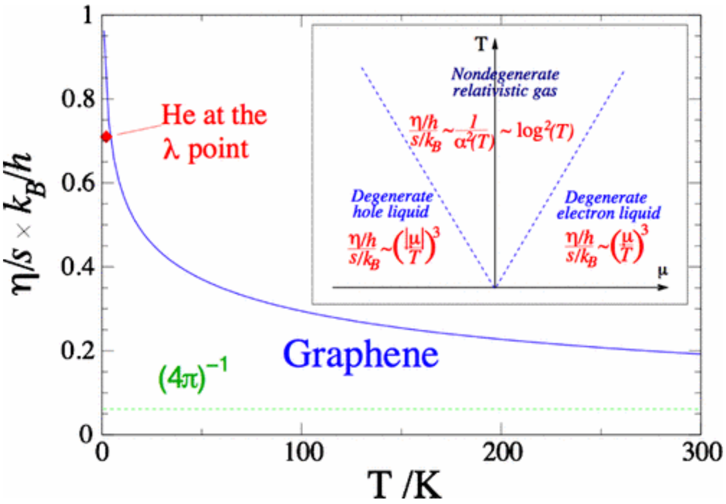

[Reprinted figure with permission from Markus Müller, Jörg Schmalian, and Lars Fritz, Phys. Rev. Lett. **103**, 025301 (2009). Copyright 2009 by the American Physical Society.]

Figure 6.1: Graphene is a nearly perfect liquid. The ratio viscosity over entropy approaches for increasing temperature the famous lower bound of this ratio [18] which is indicated by the green dashed line. The figure is taken from [20].

6.1.1 Navier-Stokes

In this section, we sketch the derivation of the Navier-Stokes equation. Thereby, we follow closely the derivation presented by Briskot *et al.* in Ref. 21. The following three continuity equations can be derived from the quantum Boltzmann equation

$$\partial_t n \quad + \boldsymbol{\nabla}_{\boldsymbol{r}} \cdot \boldsymbol{j} \quad = 0 \tag{6.5}$$

$$\partial_t n_I \quad + \boldsymbol{\nabla}_{\boldsymbol{r}} \cdot \boldsymbol{j}_I \quad = 0 \tag{6.6}$$

$$\partial_t n_\epsilon \quad + \boldsymbol{\nabla}_{\boldsymbol{r}} \cdot \boldsymbol{j}_\epsilon \quad = e\boldsymbol{E} \cdot \boldsymbol{j} \,. \tag{6.7}$$

The first one, Eq. (6.5), describes the continuity equation for the total charge carrier density $n = n_+ - n_-$, where n_+ is the number of charge carriers in the upper energy band and n_- in the lower one. It relates the time derivative of the total charge carrier density to the electrical current $\boldsymbol{j} = n\boldsymbol{u} + \delta\boldsymbol{j}$, where $\delta\boldsymbol{j}$ is the dissipative part of the current arising due to the viscosity of the system. The hydrodynamic (or "drift") velocity is denoted by $\boldsymbol{u}$. The second equation, Eq. (6.6), is the continuity equation of the imbalance density, i. e., the total quasiparticle density $n_I = n_+ + n_-$, with the imbalance current $\boldsymbol{j}_I = n_I\boldsymbol{u} + \delta\boldsymbol{j}_I$. While the last of the three continuity equations, Eq. (6.7), connects the time derivative of the energy density n_ϵ to the divergence of the energy current $\boldsymbol{j}_\epsilon = {v_\mathrm{F}}^2 n_{\boldsymbol{k}} + \delta\boldsymbol{j}_\epsilon = \frac{3n_\epsilon \boldsymbol{u}}{2+u^2/{v_\mathrm{F}}^2} + \delta\boldsymbol{j}_\epsilon$. Here, we see a special feature of graphene. Due to its linear energy spectrum, the energy current $\boldsymbol{j}_\epsilon$ is equal to the momentum density $n_{\boldsymbol{k}}$ whose continuity equation is given by

$$\partial_t n^\alpha_{\boldsymbol{k}} + \boldsymbol{\nabla}^\beta_{\boldsymbol{r}} \Pi_{\beta\alpha} - enE^\alpha + \frac{e}{c}\left[\boldsymbol{j} \times \boldsymbol{B}\right]^\alpha = -\frac{n^\alpha_{\boldsymbol{k}}}{\tau_\mathrm{dis}} \,, \tag{6.8}$$

where $\Pi_{\alpha\beta}$ is the energy-stress tensor and τ_dis is the scattering time due to disorder. In the case of graphene, the energy-stress tensor depends on the energy density and the hydrodynamic velocity and is

$$\Pi_{\alpha\beta} = \frac{n_\epsilon}{2 + u^2/{v_\mathrm{F}}^2} \left[\delta_{\alpha\beta} \left(1 - \frac{u^2}{{v_\mathrm{F}}^2} \right) + \frac{3u_\alpha u_\beta}{{v_\mathrm{F}}^2} \right] + \tau_{\alpha\beta} \,. \tag{6.9}$$

where $\tau_{\alpha\beta}$ describes the dissipative part proportional to the shear viscosity, see Eq. (6.1). Now, according to Eq. (3.31), we can relate the elements of the energy-stress tensor to the pressure of the system, which is

$$P = n_\epsilon \frac{1 - (u/v_\mathrm{F})^2}{2 + (u/v_\mathrm{F})^2} \,. \tag{6.10}$$

Already here, it can be seen that the Navier-Stokes equation will be highly nonlinear due to the quadratic dependence of the pressure on $\boldsymbol{u}$. However, for small velocity $\boldsymbol{u}$, the standard value of a scale-invariant gas $P_0 = n_\epsilon/2$ is recovered. The enthalpy of the system is

$$W = n_\epsilon + P = \frac{3n_\epsilon}{2 + (u/v_\mathrm{F})^2} \,. \tag{6.11}$$

Upon inserting these definitions into Eq. (6.8) and applying the continuity equations Eq. (6.5) to Eq. (6.7), we find the Navier-Stokes equation

$$W\partial_t \boldsymbol{u} + W \left(\boldsymbol{u} \cdot \boldsymbol{\nabla} \right) \boldsymbol{u} + \boldsymbol{\nabla} P + \boldsymbol{u} \partial_t P + \boldsymbol{u} \left(\delta \boldsymbol{j} \cdot \boldsymbol{E} \right) = en \Big[\boldsymbol{E} - \boldsymbol{u} \left(\boldsymbol{u} \cdot \boldsymbol{E} \right) \Big] + \eta \nabla^2 \boldsymbol{u} \,. \tag{6.12}$$

This Navier-Stokes equation differs from the one of a Galilean invariant system by the additional term $\boldsymbol{u}\partial_t P$. This term arises due to the linear energy spectrum and describes the relativistic nature of the quasiparticles in graphene. This equation governs the flow dynamics of the liquid. If the viscosity is very small, as in the case of graphene, the nonlinearities will be the dominant process which will lead to a highly turbulent flow. An example for the viscous flow pattern was given for graphene with a finite chemical potential by Levitov and Falkovich in Ref. 31. Vortices appear in the viscous flow pattern as can be seen in Fig. 6.2.

Further investigations of the hydrodynamics in graphene for all regimes, both the degenerate regime $\mu \gg T$ and the charge neutrality point, can be found in Ref. 81.

6.2 The viscosity in the collisionless regime

Now, the shear viscosity of graphene is determined in the collisionless regime. In the collisionless regime, the excitation frequency sets the dominant energy scale compared to the inverse scattering time, i. e., $\omega \gg \tau^{-1}$. The time scale on which collisions occur is much larger than the time scale set by the frequency and thus the collisions can be neglected and the only relevant interaction is the Coulomb potential. In the second part of this section, we are going to determine the influence of the Coulomb interaction on the shear viscosity by calculating the corresponding correction coefficient $\mathcal{C}_\eta$ in the Dirac model. Thereby, we use a smooth cut-off on the Coulomb interaction, $V(\boldsymbol{q}) \to V_\eta(\boldsymbol{q}) = 2\pi\alpha/|\boldsymbol{q}|^{1+\eta}$, which is a regularization scheme that avoids the previously mentioned UV quirk and yields the correct result for the correction coefficient of the conductivity $\mathcal{C}_\sigma$, see Sec. 5.4. But before the correction coefficient $\mathcal{C}_\eta$ is determined, the non-interacting contribution to the shear viscosity at finite frequencies is investigated and in Sec. 6.2.3, the Hall viscosity η_{xxxy} for graphene is studied.

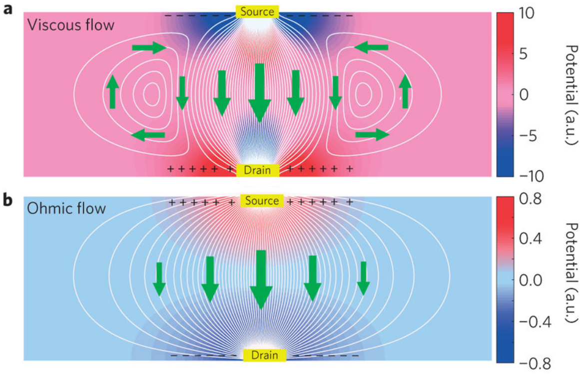

[Reprinted by permission from Springer Nature,
Electron viscosity, current vortices and negative nonlocal resistance in graphene,
Leonid Levitov and Gregory Falkovich, Nature Physics **12**, 672-676 (2016),
Copyright 2016.]

Figure 6.2: Viscous flow of graphene. The viscosity generates vorticity. The figure is taken from [31].

6.2.1 The viscosity of non-interacting free Dirac fermions in the optical regime

In order to study the shear viscosity of graphene in the collisionless regime, the Kubo-formula for the viscosity coefficient $\eta_{\alpha\beta\gamma\delta}$ defined in Sec. 3.3 is being used. The expression is given by

$$\eta_{\alpha\beta\gamma\delta} = -\operatorname{Im} \frac{\chi_{T_{\alpha\beta}T_{\gamma\delta}}}{\omega} \,, \tag{6.13}$$

where $\chi_{T_{\alpha\beta}T_{\gamma\delta}}$ is the correlation function between two energy-stress tensors having the form

$$\chi_{T_{\alpha\beta}T_{\gamma\delta}} = \int_\omega \int_{\boldsymbol{k}} \operatorname{Tr}\left[G_{\boldsymbol{k},\mathrm{i}\omega} T_{\alpha\beta}(\boldsymbol{k}) G_{\boldsymbol{k},\mathrm{i}(\omega+\Omega)} T_{\gamma\delta}(\boldsymbol{k}) \right] . \tag{6.14}$$

The Green's function $G_{\boldsymbol{k},\mathrm{i}\omega} = -(\mathrm{i}\omega\sigma_0 + v_\mathrm{F}\boldsymbol{k}\cdot\boldsymbol{\sigma})/(\omega^2+(v_\mathrm{F}k)^2)$ is defined in Sec. 4.2. Hence, to calculate this correlation function, we need to determine the energy-stress tensor $T_{\alpha\beta}(\boldsymbol{k})$ of graphene. Thereby, we follow the procedure introduced in Sec. 3.2, where we showed that the energy-stress tensor is related to the time derivative of the strain generators. These strain generators describe the transformation of the system due to external strain. Let us first determine the part of the energy-stress tensor due to the strain generator acting on the spatial coordinates of the system $\mathcal{L}_{\alpha\beta} = -\{x_\alpha, p_\beta\}$. We find for the energy-stress tensor

$$\begin{aligned} T^{\mathcal{L}}_{\alpha\beta}(\boldsymbol{k}) &= -\mathrm{i}[\mathcal{H}_\mathrm{Dirac}, \mathcal{L}_{\alpha\beta}] \\ &= \sigma_\alpha k_\beta \,. \end{aligned} \tag{6.15}$$

This energy-stress tensor is not symmetric and upon determining the different viscosity coefficients we find

$$\begin{aligned} \eta_{xxxx}(\omega) &= \frac{N_{sv}}{256}\omega^2 & \eta_{yyyy}(\omega) &= \frac{N_{sv}}{256}\omega^2 & \eta_{xxyy}(\omega) &= -\frac{N_{sv}}{256}\omega^2 \\ \eta_{xyyx}(\omega) &= -\frac{N_{sv}}{256}\omega^2 & \eta_{xyxy}(\omega) &= 3\frac{N_{sv}}{256}\omega^2 & \eta_{yxyx}(\omega) &= 3\frac{N_{sv}}{256}\omega^2 \,, \end{aligned} \tag{6.16}$$

where $N_{sv} = 4$. These evaluated viscosity coefficients do not fulfill the symmetry properties of a rotational invariant system [44]

$$\eta_{\alpha\beta\gamma\delta}(\omega) = \eta(\omega)[\delta_{\alpha\gamma}\delta_{\beta\delta} + \delta_{\alpha\delta}\delta_{\beta\gamma} - \delta_{\alpha\beta}\delta_{\gamma\delta}] \,. \tag{6.17}$$

However, graphene is a rotational invariant system and should fulfill this symmetry property. The reason for this peculiar behavior is that we have not taken the pseudospin of graphene into account. The pseudospin describes the two sub-lattices of graphene and it behaves as a real angular momentum [47]. The strain generator acting on the pseudospin space $\mathcal{S}_{\alpha\beta} = \mathrm{i}[S_\alpha, S_\beta]/4$ yields the following contribution to the energy-stress tensor of graphene

$$\begin{aligned} T^{\mathcal{S}}_{\alpha\beta}(\boldsymbol{k}) &= -\mathrm{i}[\mathcal{H}_{\mathrm{Dirac}}, \mathcal{S}_{\alpha\beta}] \\ &= \frac{1}{2}(\sigma_\beta k_\alpha - \sigma_\alpha k_\beta) \,, \end{aligned} \tag{6.18}$$

which leads when all contributions are added up to the symmetrized energy-stress tensor

$$T^{\mathcal{J}}_{\alpha\beta}(\boldsymbol{k}) = T^{(0)}_{\alpha\beta}(\boldsymbol{k}) = \frac{1}{2}(\sigma_\beta k_\alpha + \sigma_\alpha k_\beta) \,. \tag{6.19}$$

The viscosity coefficients determined with this symmetrized energy-stress tensor fulfill the symmetry property (6.17) of a rotational invariant system and yields after inserting $\hbar$ and v_{F}

$$\eta_0(\omega) = \frac{\hbar}{v_{\mathrm{F}}^2}\frac{N_{sv}}{256}\omega^2 = \frac{1}{64}\frac{\hbar}{v_{\mathrm{F}}^2}\omega^2 \,. \tag{6.20}$$

The shear viscosity of graphene is not universal but depends on the square of the frequency and has a small prefactor.

6.2.2 The correction coefficient of the viscosity in the optical regime

It is again natural to ask the question, how the Coulomb interaction influences the transport quantity. In order to answer this question, we apply a RG analysis analogous to the previous chapter and go to the regime where the coupling constant is small and perform a perturbation theory in $\alpha(b^*)$ for the shear viscosity. Hence, the frequency-dependent shear viscosity is given by

$$\eta(\omega) = \eta_0\left(1 + \mathcal{C}_\eta \alpha(b^*) + \mathcal{O}(\alpha(b^*)^2)\right) \,, \tag{6.21}$$

where the non-interacting shear viscosity of graphene η_0 was calculated in the previous section. Here, we want to determine the value of the correction coefficient $\mathcal{C}_\eta$ in first order of perturbation theory and want to find out, if this value is small as it is in the case of the optical conductivity in graphene or if the influence of the Coulomb interaction on the shear viscosity is large. The value of the correction coefficient $\mathcal{C}_\eta$ is determined by four different contributions, the self-energy diagram, the vertex diagram and the honey diagram. The corresponding Feynman diagrams are depicted in Fig. 6.3 (b)-(d). We are going to find again that each of these diagrams is individually logarithmically divergent but when they are summed up the divergences cancel each other and we obtain a finite correction coefficient.

Upon comparing these diagrams with the diagrams contributing to the correction coefficient $\mathcal{C}_\sigma$ of the optical conductivity, we see that an additional Feynman diagram needs to be calculated. This diagram is the honey diagram which is going to be derived in this section.

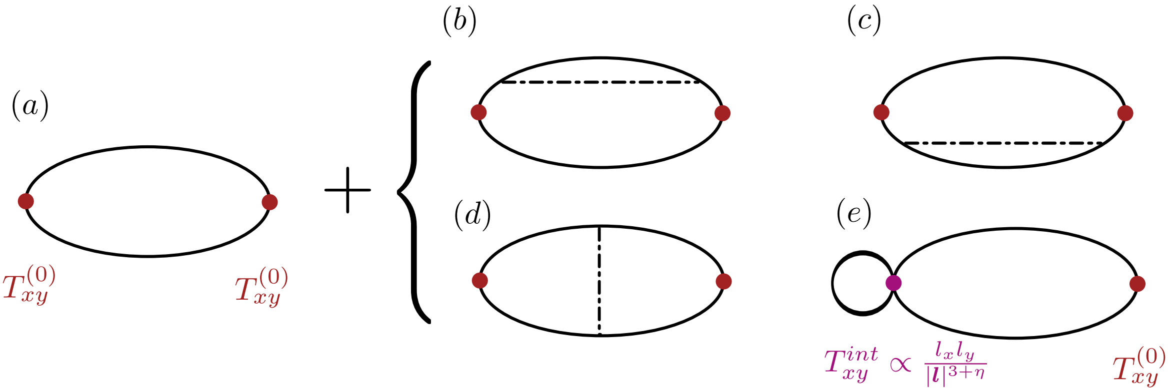

Figure 6.3: The Feynman diagrams defining the shear viscosity in graphene up to the first order in perturbation theory in $\alpha(\omega)$. Panel (a) illustrates the bare bubble diagram describing the non-interacting shear viscosity. The diagrams (b) to (e) depict the different contributions to the correction coefficient $\mathcal{C}_\eta$. Diagrams (b) and (c) are the self-energy diagrams, diagram (d) is the vertex diagram, and diagram (e) represents the honey diagram.

By the way, the great viscosity of honey is caused by the great interaction between the honey molecules. Thus by analogy, we call this additional diagram honey diagram, since it is the diagram which takes the interacting part of the energy-stress tensor into account.

But, let us now start with the calculation of the different Feynman diagrams contributing to the correction coefficient.

Self-energy diagram

The self-energy diagram is defined via the correlation function

$$\chi^{(1,bc)}_{T^{(0)}_{xy}T^{(0)}_{xy}}(\mathrm{i}\Omega) = -2\int_{\boldsymbol{p}}\int_{\omega} \mathrm{Tr}\left[G_{\boldsymbol{p},\mathrm{i}(\omega+\Omega)}T^{(0)}_{xy}(\boldsymbol{p})G_{\boldsymbol{p},\mathrm{i}\omega}\Sigma(\boldsymbol{p})G_{\boldsymbol{p},\mathrm{i}\omega}T^{(0)}_{xy}(\boldsymbol{p})\right]\,, \tag{6.22}$$

where the self-energy for a Coulomb potential with a soft cut-off $V_\eta = 2\pi\alpha/|\boldsymbol{q}|^{1+\eta}$ is given by $\Sigma(\boldsymbol{p}) = \phi(\boldsymbol{p})\boldsymbol{p}\cdot\boldsymbol{\sigma}$ with

$$\phi(\boldsymbol{p}) = \alpha r_0^{-\eta}\frac{2^\eta\,\Gamma\left(\frac{\eta}{2}\right)}{8\,\Gamma\left(\frac{4-\eta}{2}\right)}p^{-\eta}\,, \tag{6.23}$$

where r_0 is an additional length scale introduced in such a way that the Coulomb potential still has the correct dimension. In order to calculate the diagram, we proceed the following way. First the frequency integral is evaluated. After the integration, we subtract twice the zero-frequency part of the above correlation function. Now, why do we subtract the zero-frequency part here? We know that the imaginary part of the correlation function of two non-interacting enery-stress tensors is proportional to ω^3. With the help of the Kramer-Kronig relation [24], the form of the correlation function $\chi_{T^{(0)}_{xy}T^{(0)}_{xy}}$ can be deduced, ie., $\chi_{T^{(0)}_{xy}T^{(0)}_{xy}}(\omega) \propto a\Lambda^3 + b\Lambda\omega^2 + c\mathrm{i}\omega^3$, where Λ is the UV cut-off and a, b, and c are constants. In the complex plane this expression is related to $\chi_{T^{(0)}_{xy}T^{(0)}_{xy}}(\mathrm{i}\Omega) \propto a\Lambda^3+b\Lambda\Omega^2+c|\Omega|^3$. In order to obtain the coefficient c, which we are interested in, first the difference $f^{(0)}_{xyxy}(\mathrm{i}\Omega) = (\chi_{T^{(0)}_{xy}T^{(0)}_{xy}}(\mathrm{i}\Omega) -$

$\chi_{T^{(0)}_{xy}T^{(0)}_{xy}}(0))/\Omega^2 = b\Lambda + c|\Omega|$ is to be taken and than we have to calculate $(f^{(0)}_{xyxy}(\mathrm{i}\Omega) - f^{(0)}_{xyxy}(0))/\Omega = c$. The same procedure is applied in order to evaluate the self-energy diagram and is also going to be applied in the case of the vertex diagram.

We find for the self-energy diagram

$$\begin{aligned}
\frac{f^{(1,bc)}_{xyxy}(\mathrm{i}\Omega) - f^{(1,bc)}_{xyxy}(0)}{\Omega} &= -\frac{4^{\eta-6}(\eta-4)\Omega\left(\frac{1}{\Omega^2}\right)^{\frac{\eta+1}{2}}\sec\left(\frac{\pi\eta}{2}\right)\Gamma\left(\frac{\eta}{2}\right)}{\Gamma\left(2-\frac{\eta}{2}\right)} \\
&\approx \frac{N_{sv}\alpha}{512\eta} + N_{sv}\alpha\frac{-4\log(r_0\Omega) - 4\gamma + 1 + 4\log(4)}{2048} + \mathcal{O}(\eta)\,,
\end{aligned} \tag{6.24}$$

which is divergent in the parameter $1/\eta$ and has a finite value.

Vertex diagram

Next, we evaluate the vertex diagram. This vertex diagram is defined by the correlation function

$$\chi^{(1,d)}_{T^{(0)}_{xy}T^{(0)}_{xy}}(\mathrm{i}\Omega) = -\frac{N_{sv}\alpha_\eta}{4}\int_{\boldsymbol{p},\omega}\int_{\boldsymbol{k},\omega'}\frac{2\pi}{|\mathbf{p}-\mathbf{k}|^{1+\eta}}\,\mathrm{Tr}\left[G_{\boldsymbol{p},\mathrm{i}\omega}T^{(0)}_{xy}(\boldsymbol{p})G_{\boldsymbol{p},\mathrm{i}(\omega+\Omega)}G_{\boldsymbol{k},\mathrm{i}(\omega'+\Omega)}T^{(0)}_{xy}(\boldsymbol{k})G_{\boldsymbol{k},\mathrm{i}\omega'}\right]\,, \tag{6.25}$$

with $\alpha_\eta = \alpha r_0^{-\eta}2^\eta\,\Gamma\big((1+\eta)/2\big)\,/\,\Gamma\big((1-\eta)/2\big)$. Again, after the two frequency integrations are performed, we subtract twice the zero-frequency part of the correlation function and obtain

$$\frac{f^{(1,d)}_{xyxy}(\mathrm{i}\Omega) - f^{(1,d)}_{xyxy}(0)}{\Omega} = Q_1 + Q_2 + Q_3\,, \tag{6.26}$$

which consists of three different integrals Q_1, Q_2, and Q_3. The first two integrals are convergent for $\eta = 0$ and are given by

$$\begin{aligned}
Q_1 &= -\frac{N_{sv}\alpha_\eta}{8(2\pi)^2}\Omega^{-\eta}\int_0^\infty dp\int_0^\infty dq\; 2\int_0^\pi d\varphi\frac{pq}{32p^2q^2\left(4p^2+1\right)\left(4q^2+1\right)}\frac{4pq\cos(2\varphi) + 16p^2q^2\cos(\varphi)\cos(2\varphi)}{\left(p^2+q^2-2pq\cos(\varphi)\right)^{\frac{1+\eta}{2}}} \\
&= -\frac{N_{sv}\alpha_\eta}{960}
\end{aligned} \tag{6.27}$$

and

$$\begin{aligned}
Q_2 &= -\frac{N_{sv}\alpha_\eta}{4}\frac{\Omega^{-\eta}}{(2\pi)^2}\int_0^\infty dp\frac{1}{p(4p^2+1)}\int_0^\infty dq\frac{1}{q(4q^2+1)}\int_0^\pi d\varphi\frac{p^3q\cos(2\varphi)}{(p^2+q^2-2pq\cos(\varphi))^{\frac{1+\eta}{2}}} \\
&= -\frac{N_{sv}\alpha_\eta}{4}\frac{\Omega^{-\eta}}{(2\pi)^2}2^{\eta-4}\pi\sec\left(\frac{\pi\eta}{2}\right)\frac{\pi}{6}(11-3\pi) \\
&\approx -\frac{N_{sv}\alpha}{2}\left(\frac{11}{768} - \frac{\pi}{256}\right)\,,
\end{aligned} \tag{6.28}$$

where the detailed calculation can be found in the App. A.3. The last integral Q_3 diverges when η goes to zero. It reads

$$\begin{aligned}
Q_3 = &-\frac{N_{sv}\alpha_\eta}{8}\frac{1}{(2\pi)^2}\frac{\Omega^{-\eta}}{32}\int\limits_0^\infty dp\frac{p}{p^2(4p^2+1)}\int\limits_0^\infty dq\frac{q}{q^2(4q^2+1)}\int\limits_0^{2\pi} d\varphi\frac{\cos(\varphi)\cos(2\varphi)}{\Big(p^2+q^2-2pq\cos(\varphi)\Big)^{\frac{1+\eta}{2}}} \\
&\times\{4p^2(4p^2+1)+4q^2(4q^2+1)\} \\
=&-\frac{N_{sv}\alpha_\eta}{32}\frac{\Omega^{-\eta}}{(2\pi)^2}2^{-2+\eta}\pi\frac{\sec\left(\frac{\pi\eta}{2}\right)}{\Gamma\left(\frac{1+\eta}{2}\right)}\frac{\pi(\eta+2)\Gamma\left(\frac{1}{2}-\frac{\eta}{2}\right)\Gamma\left(\frac{\eta}{2}\right)}{4\Gamma\left(3-\frac{\eta}{2}\right)} \\
\approx&-\frac{N_{sv}\alpha}{1024\eta}-\frac{\alpha N_{sv}(4\log(r_0\Omega)+4\gamma-5-8\log(2))}{4096}+\mathcal{O}(\eta)\,.
\end{aligned}\tag{6.29}$$

The vertex diagram is also divergent in the parameter $1/\eta$. However, when the self-energy diagram and the vertex diagram are summed up, the two divergences do not cancel each other. A third diagram, namely the honey diagram, has to be introduced that all divergences cancel each other.

The honey diagram

So far we only took the non-interacting part of the energy-stress tensor into account. In order to calculate the energy-stress tensor we determined the time derivative of the strain generator $\mathcal{J}_{\alpha\beta}$, i. e., $T^{(0)}_{\alpha\beta}(\boldsymbol{p}) = -\mathrm{i}[\mathcal{H}_{\text{Dirac}}, \mathcal{J}_{\alpha\beta}]$. However, graphene is described by the non-interacting Hamiltonian $\mathcal{H}_{\text{Dirac}}$ and the Coulomb interaction $\mathcal{H}_{\mathcal{C}} = \int_{\boldsymbol{r},\boldsymbol{r}'}\hat{\psi}^\dagger_{\boldsymbol{r}}\hat{\psi}^\dagger_{\boldsymbol{r}'}V(\boldsymbol{r},\boldsymbol{r}')\hat{\psi}_{\boldsymbol{r}'}\hat{\psi}_{\boldsymbol{r}}$ with $V(\boldsymbol{r},\boldsymbol{r}') = \frac{r_0^{-\eta}}{|\boldsymbol{r}-\boldsymbol{r}'|^{1-\eta}}$. Hence, there exists also a contribution of the energy-stress tensor $T^{int}_{\alpha\beta}$ which represents the Coulomb interaction in the system. This contribution is again determined by calculating the commutator of the Coulomb Hamiltonian and the total strain generator $\mathcal{J}_{\alpha\beta}$. The part of the strain generator acting in the pseudospin space commute with the interaction Hamiltonian and we only have to determine

$$T^{int}_{\alpha\beta}(\boldsymbol{r}) = -\mathrm{i}[\mathcal{H}_{\mathcal{C}},\mathcal{L}_{\alpha\beta}] = \frac{1}{2}(1-\eta)r_0^{-\eta}\int\limits_{\boldsymbol{r_1},\boldsymbol{r_2}}\hat{\psi}^\dagger_{\boldsymbol{r_1}}\hat{\psi}^\dagger_{\boldsymbol{r_2}}\hat{\psi}_{\boldsymbol{r_2}}\hat{\psi}_{\boldsymbol{r_1}}\frac{(\boldsymbol{r_1}-\boldsymbol{r_2})_\alpha(\boldsymbol{r_1}-\boldsymbol{r_2})_\beta}{|\boldsymbol{r_1}-\boldsymbol{r_2}|^{3-\eta}}\,. \tag{6.30}$$

This result is in agreement with the expression of the interacting energy-stress tensor which was obtained in the derivation by Martin and Schwinger in Ref. 49, where the authors derived the interacting part of the energy-stress tensor using the continuity equation of the momentum density (3.24). The Fourier transform of the interacting energy-stress tensor is

$$\begin{aligned}
T^{int}_{\alpha\beta}(\boldsymbol{q}=0,\tau) =&\frac{1}{2}(1-\eta)r_0^{-\eta}2^{1-\eta}\pi\frac{\Gamma\left(\frac{3+\eta}{2}\right)}{\Gamma\left(\frac{3-\eta}{2}\right)}\int\limits_{\boldsymbol{k},\boldsymbol{p},\boldsymbol{l}}\frac{l_\alpha l_\beta}{|\boldsymbol{l}|^{3+\eta}}\hat{\psi}^\dagger_{\boldsymbol{k}}(\tau)\hat{\psi}^\dagger_{\boldsymbol{p}}(\tau)\hat{\psi}_{\boldsymbol{p}-\boldsymbol{l}}(\tau)\hat{\psi}_{\boldsymbol{k}+\boldsymbol{l}}(\tau) \\
=&\frac{1}{2}(1-\eta)r_0^{-\eta}2^{1-\eta}\pi\frac{\Gamma\left(\frac{3+\eta}{2}\right)}{\Gamma\left(\frac{3-\eta}{2}\right)}\int\limits_{\boldsymbol{l}}\frac{l_\alpha l_\beta}{|\boldsymbol{l}|^{3+\eta}}n(\boldsymbol{l},\tau)n(-\boldsymbol{l},\tau)\,,
\end{aligned}\tag{6.31}$$

with

$$n(\boldsymbol{l},\tau) = \int\limits_{\boldsymbol{p}}\hat{\psi}^\dagger_{\boldsymbol{p}}(\tau)\hat{\psi}_{\boldsymbol{p}+\boldsymbol{l}}(\tau)\,. \tag{6.32}$$

This interacting part of the energy-stress tensor contributes to the correction coefficient of the shear viscosity due to the Coulomb interaction, when the correlation function of an interacting energy-stress tensor $T^{int}_{\alpha\beta}$ with a non-interacting part of the energy-stress tensor $T^{(0)}_{\alpha\beta}$ is calculated. We refer to this Feynman diagram depicted in Fig. 6.3 (d) as the honey diagram.

The honey diagram is defined as

$$\chi_{T^{int}_{\alpha\beta},T^{(0)}_{\gamma\delta}}(\mathrm{i}\nu_r) = -\frac{1}{2}(1-\eta)r_0^{-\eta}2^{1+\eta}\pi\frac{\Gamma\left(\frac{3+\eta}{2}\right)}{\Gamma\left(\frac{3-\eta}{2}\right)}\int_{\boldsymbol{k},\boldsymbol{l},\boldsymbol{m},\boldsymbol{s}}\frac{l_\alpha l_\beta}{|\boldsymbol{l}|^{3+\eta}}\,\mathrm{Tr}\left[G_{\boldsymbol{k}+\boldsymbol{l},\mathrm{i}\omega_s}G_{\boldsymbol{k},\mathrm{i}(\omega_m+\nu_r)}\left(k_\gamma\sigma_\delta+k_\delta\sigma_\gamma\right)G_{\boldsymbol{k},\mathrm{i}\omega_m}\right]. \tag{6.33}$$

After performing the two frequency integrations, we find

$$\begin{aligned}\chi_{T^{int}_{\alpha\beta},T^{(0)}_{\alpha\beta}}(\mathrm{i}\nu_r) =& \frac{1}{2}(1-\eta)r_0^{-\eta}2^{1+\eta}\pi\frac{\Gamma\left(\frac{3+\eta}{2}\right)}{\Gamma\left(\frac{3-\eta}{2}\right)}\frac{1}{(2\pi)^4}\\ &\times\int_0^\infty \mathrm{d}k\int_0^\infty \mathrm{d}l\int_0^{2\pi}\mathrm{d}\alpha\int_0^{2\pi}\mathrm{d}\beta\frac{k^3\sin(2\alpha)\cos(2\beta)l^{1-\eta}\sin(\alpha-\beta)}{\left(4k^2+\Omega^2\right)\sqrt{k^2+2kl\cos(\alpha-\beta)+l^2}}\,.\end{aligned} \tag{6.34}$$

This expression can be analytically continued ($\mathrm{i}\Omega\to\omega+\mathrm{i}\delta$), using the relation

$$\frac{1}{4k^2+\Omega^2}\to P.V.\frac{1}{4k^2-\omega^2}+\frac{\mathrm{i}\pi}{4\omega}\delta\left(k-\frac{\omega}{2}\right)+\frac{\mathrm{i}\pi}{4\omega}\delta\left(k+\frac{\omega}{2}\right), \tag{6.35}$$

with *P.V.* denoting the principal value integral, which yields after taking the imaginary part of the above expression

$$\begin{aligned}\mathrm{Im}\,\chi_{T^{int}_{\alpha\beta},T^{(0)}_{\alpha\beta}}(\mathrm{i}\nu_r) =& \frac{2^{2\eta-11}(\eta-1)\omega^3\left(\omega^2\right)^{-\frac{\eta}{2}}r_0^{-\eta}\Gamma\left(\frac{\eta}{2}\right)}{\Gamma\left(3-\frac{\eta}{2}\right)}\\ \approx& -\frac{\omega^3}{2048\eta}-\frac{-4\omega^3\log(r_0)-4\gamma\omega^3-\omega^3+8\omega^3\log(2)-2\omega^3\log\left(\omega^2\right)}{8192}+\mathcal{O}(\eta)\,.\end{aligned} \tag{6.36}$$

This expression also diverges in $1/\eta$ and has a finite part. An important fact is that we have to multiply the above expression by the factor 2, since both correlation functions $\left\langle T^{(0)}_{\alpha\beta}T^{int}_{\alpha\beta}\right\rangle$ and $\left\langle T^{int}_{\alpha\beta}T^{(0)}_{\alpha\beta}\right\rangle$ give the same result.

Hence, upon combining the self-energy diagram, the vertex-diagram and the honey-diagram, the logarithmic divergences cancel and the following value of the correction coefficient is found

$$\mathcal{C}_\eta = \frac{89-20\pi}{40}\approx 0.65\,. \tag{6.37}$$

We find that the additional diagram which describes the interacting part of the energy-stress tensor reduces the shear viscosity, since it makes a before diverging quantity (the sum of the self-energy diagram and the vertex diagram) finite. Furthermore, we see that the value of the correction coefficient is quite large and thus found a transport quantity in graphene, which shows a big influence of the Coulomb interaction. The frequency dependence of the non-interacting shear viscosity and the influence of the Coulomb interaction is shown in Fig. 6.4.

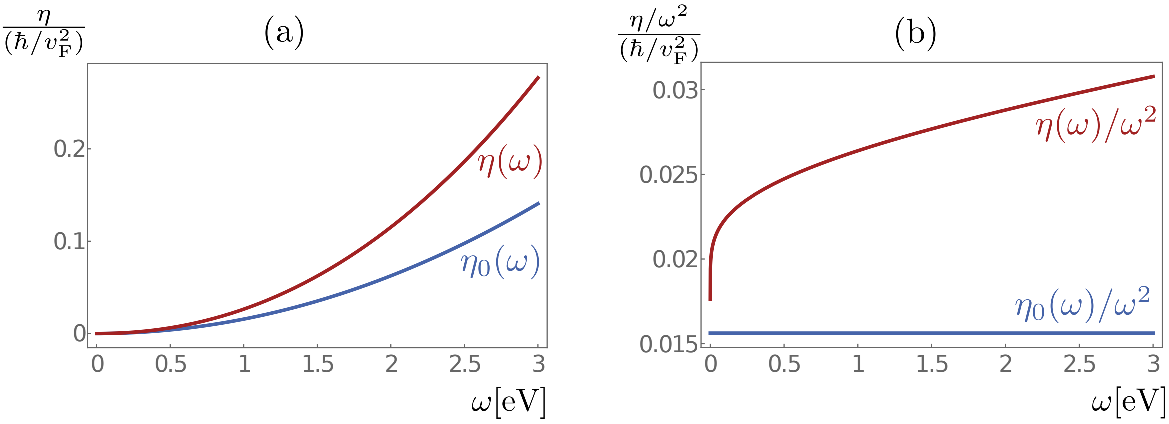

Figure 6.4: The frequency dependence of the shear viscosity of graphene in the collisionless regime. The frequency ranges up to the optical regime. The blue curve depicts the non-interacting part of the viscosity, while the red curve shows the the viscosity modified by the Coulomb interaction. In panel (a) the parabolic frequency dependence of the shear viscosity is presented, while in panel (b), where $\eta(\omega)/\omega^2$ is depicted, we see clearly that the Coulomb interaction enhances the viscosity of graphene logarithmically.

6.2.3 Hall viscosity

As last topic in this chapter, we study the Hall viscosity η_{xxxy} and η_{yyyx} of a single Dirac cone in graphene. In order to render the integrals to be calculated analytically, we introduce a mass term m to the system. The Green's functions are than modified the following way

$$G_{\boldsymbol{k},\mathrm{i}\omega} = -\frac{\mathrm{i}\omega + v_\mathrm{F}\boldsymbol{k}\cdot\boldsymbol{\sigma} + m\sigma_z}{\omega^2 + (v_\mathrm{F}k)^2 + m^2}\,, \tag{6.38}$$

with the dispersion relation $\epsilon_{\lambda\boldsymbol{k}} = \lambda\sqrt{(v_\mathrm{F}k)^2 + m^2}$, where the introduced mass opens a gap in the energy spectrum of graphene. Next, the imaginary part of the correction function

$$\chi_{T^{(0)}_{\alpha\alpha}T^{(0)}_{\alpha\beta}}(\mathrm{i}\Omega) = v_\mathrm{F}\int_{\boldsymbol{k}}\int_{\omega}\mathrm{Tr}[T^{(0)}_{\alpha\alpha}(\boldsymbol{k})G_{\boldsymbol{k},\mathrm{i}\omega}T^{(0)}_{\alpha\beta}(\boldsymbol{k})G_{\boldsymbol{k},\mathrm{i}(\omega+\Omega)}] \tag{6.39}$$

is determined. Thereby, we find that the evaluation of the trace over the pseudospin yields an additional imaginary unit i in comparison to the shear viscosity $\eta_{xyxy} = \eta$. Hence, the on-shell processes of the correlation function are now entering the real part of the correlator, while the imaginary part of the correlator is governed by off-shell excitations. After evaluating the corresponding integrals and introducing an UV cut-off, we find for the Hall viscosities

$$\begin{aligned} \eta_{xxxy} &= -\frac{1}{16\pi v_\mathrm{F}^2}m\Lambda - \mathrm{sign}(m)\frac{1}{96\pi v_\mathrm{F}^2}\omega^2 \\ \eta_{yyyx} &= +\frac{1}{16\pi v_\mathrm{F}^2}m\Lambda + \mathrm{sign}(m)\frac{1}{96\pi v_\mathrm{F}^2}\omega^2\,. \end{aligned} \tag{6.40}$$

The Hall viscosities are not universal, since they depend on the UV cut-off Λ. Furthermore, similar to the Hall conductivity of graphene with $\sigma_{xy} = -\mathrm{sign}(m)/(8\pi)$, the Hall viscosities also consist of a term proportional to the sign of the mass m.

6.3 Summary

In the first part of this chapter, we presented calculations of the shear viscosity of graphene in the hydrodynamic regime [20] and showed that graphene is a nearly perfect liquid [20], i. e., its ratio of shear viscosity over entropy approaches the famous lower bound of this physical quantity [18]. Further, the derivation of the Navier-Stokes equation [21] was shown, since the Navier-Stokes equation gives experimental access to the shear viscosity.

In the second part of this chapter, we presented our calculation of the shear viscosity in the collisionless regime. Thereby, we demonstrated that the pseudospin of graphene has to be taken into account in order to obtain a viscosity tensor with the symmetry properties of a two-dimensional, rotational invariant system. Furthermore, we determined the influence of the Coulomb interaction on the shear viscosity upon calculating the corresponding correction coefficient $\mathcal{C}_\eta$ using a soft cut-off on the Coulomb interaction. We find

$$\eta(\omega) = \frac{1}{64}\frac{\hbar}{v_\mathrm{F}^2}\omega^2\left[1 + \frac{89 - 20\pi}{40}\alpha(\omega)\right], \tag{6.41}$$

with $\alpha(\omega) = \alpha/(1+\alpha/4\log(\Lambda/\omega))$. The shear viscosity is not universal, but proportional to the square of the frequency. The correction coefficient is with $\mathcal{C}_\eta \approx 0.65$ large and thus we find a transport quantity of graphene which is greatly influenced by the Coulomb interaction. Furthermore, we found the Hall viscosity of graphene, which is given by $\eta_{yyyx,xxxy} = \pm\frac{1}{16\pi v_\mathrm{F}^2}m\Lambda \pm \mathrm{sign}(m)\frac{1}{96\pi v_\mathrm{F}^2}\omega^2$.

Part III

Anisotropic Dirac Systems

7

Chapter 7

Field-theoretical description and Coulomb interaction

In the previous part, we have studied the conductivity and viscosity of graphene and the influence of the Coulomb interaction on these transport properties. We found that in the collisionless regime the conductivity is universal and the Coulomb interaction has no large impact on it [1, 16]. In the hydrodynamic regime the temperature dependence of the conductivity only enters via the renormalized coupling constant [19]. Furthermore, we have seen that in the collisionless regime graphene behaves as a nearly perfect fluid [20], i. e., the ratio of shear viscosity over entropy decreases with increasing temperature and approaches the lower bound [18]. In the course of this, it was important that graphene is invariant under spatial inversion and time reversal and that the energy dispersion relation is isotropic.

However, the reader may wonder what happens with these transport quantities in systems with lower symmetry. Do the conductivity and the shear viscosity show a different characteristic behavior or do they stay unchanged? And we can ask ourself one more time the question, how the Coulomb interaction influences the transport properties of a system with lower symmetry. These questions are going to be answered in the following three chapters.

In this chapter, we want to introduce two dimensional systems which have a lower symmetry than graphene. These systems are the anisotropic Dirac systems (ADSs). Their peculiarity is that their energy spectrum is anisotropic at the Dirac point, i. e., in one direction the energy spectrum is linear, as it is the case in graphene, whereas in the perpendicular direction we will find a parabolic energy dispersion [104–111]. The anisotropic energy dispersion will give rise to classical and relativistic behavior depending on the chosen direction and leads to fascinating properties of the transport quantities. In Chap. 8, we will demonstrate that both in the hydrodynamic and in the collisionless regime, the system is either metallic or insulating depending on the direction of the applied electrical field. Furthermore, the shear viscosity coefficients of an ADS exhibit fundamentally different scaling with temperature, depending on the direction of the momentum flow, as is shown in Chap. 9. Even more drastically, some of these viscosity coefficients will violate the famous lower bound of viscosity over entropy [18]. The origin of the violation lies in the emergence of two different length scales due to the anisotropy of the energy spectrum which will lead to different scaling laws of the viscosity coefficients.

Now let us focus on the content of this chapter. In Sec. 7.1, as mentioned above, we will introduce the ADSs and their Hamiltonian and the most important physical quantities. Also different materials which exhibit an anisotropic energy spectrum are presented, such as the organic conductor α-(BEDT-TTF)$_2$I$_3$ [112–115] and the heterostructure 5/3 TiO$_2$/VO$_2$ [108, 109]. In Sec. 7.2 we will include the

Coulomb interaction and study the influence of the Coulomb potential on the ADSs. For this purpose, a large N renormalization group analysis of ADSs in the strong coupling limit [116] is presented in Sec. 7.2.1. Also the collision integral of the quantum Boltzmann equation arising due to the Coulomb interaction is derived in the last section.

7.1 The model and possible realizations

Anisotropic Dirac systems occur when two Dirac cones merge in momentum space [116]. There are different materials which yield the anisotropic energy dispersion, where in one crystallographic direction the energy dispersion is Newtonian-like and in the other Dirac-like [104–111]. One of these materials is the organic charge transfer salt α-(BEDT-TTF)$_2$I$_3$ [105, 112–115]. Here, two Dirac cones merge under the application of uniaxial pressure as is explicitly shown in Sec. 7.1.1. Another material yielding this anisotropic energy dispersion is the heterostructure 5/3 TiO$_2$/VO$_2$ [108, 109]. This heterostructure has four anisotropic Dirac cones in the first Brillouin zone, which are rotated by 45 degrees with respect to each other, as can be seen in Sec. 7.1.2.

7.1.1 Mergence of two Dirac cones

Let us start our contemplation of the ADSs with the organic charge transfer salt α-(BEDT-TTF)$_2$I$_3$. Here, we follow closely the Refs. 112, 113, and 114. The two dimensional organic conductor has a unit cell which consists of four molecules on the sites A, A', B, and C, where all molecules but the ones at the sites A and A' are inequivalent. This unit cell is shown in Fig. 7.1(c). The organic conductor is described by the following Hubbard-Hamiltonian:

$$\begin{aligned}\mathcal{H}_{\alpha\text{-(BEDT-TTF)}_2\text{I}_3,\boldsymbol{r}} = &\sum_{(i\alpha,j\beta),\sigma}\left(t_{i\alpha:j\beta}\hat{a}^\dagger_{i\alpha\sigma}\hat{a}_{j\beta\sigma}+\text{h.c.}\right)\\ &+\sum_{i\alpha}U_\alpha\hat{a}^\dagger_{i\alpha\uparrow}\hat{a}^\dagger_{i\alpha\downarrow}\hat{a}_{i\alpha\downarrow}\hat{a}_{i\alpha\uparrow}+\sum_{(i\alpha:j\beta),\sigma,\sigma'}V_{\alpha\beta}\hat{a}^\dagger_{i\alpha\sigma}\hat{a}^\dagger_{j\beta\sigma'}\hat{a}_{j\beta\sigma'}\hat{a}_{i\alpha\sigma}\,,\end{aligned}\tag{7.1}$$

where the index i,j gives the site index of the unit cell, σ,σ' denotes the spin index, and the index α,β labels the position of the molecules with $\alpha,\beta\in\{A,A',B,C\}$. The hopping elements $t_{i\alpha:j\beta}$ give the energy needed for an electron to jump from the site (i,α) to the site (j,β), while U_α describes the repulsive on-site interaction, and $V_{\alpha\beta}$ the repulsive interaction between neighboring molecules. Upon going into momentum space and taking only nearest neighbor hopping into account, we obtain for the Hamiltonian

$$\begin{aligned}\mathcal{H}_{\alpha\text{-(BEDT-TTF)}_2\text{I}_3,\boldsymbol{k}} = &\sum_{k,\sigma,\alpha\beta}\epsilon_{\alpha\beta}(\boldsymbol{k})\hat{a}^\dagger_{\boldsymbol{k}\alpha\sigma}\hat{a}_{\boldsymbol{k}\beta\sigma}+\sum_{\boldsymbol{k},\boldsymbol{k}',\boldsymbol{q},\alpha}U_\alpha\hat{a}^\dagger_{\boldsymbol{k}-\boldsymbol{q}\alpha\uparrow}\hat{a}^\dagger_{\boldsymbol{k}'+\boldsymbol{q}\alpha\downarrow}\hat{a}_{\boldsymbol{k}'\alpha\downarrow}\hat{a}_{\boldsymbol{k}\alpha\uparrow}\\ &+\sum_{\boldsymbol{k},\boldsymbol{k}',\boldsymbol{q},\sigma,\sigma',\alpha,\beta}V_{\alpha\beta}(\boldsymbol{q})\hat{a}^\dagger_{\boldsymbol{k}-\boldsymbol{q}\alpha\sigma}\hat{a}^\dagger_{\boldsymbol{k}'+\boldsymbol{q}\beta\sigma'}\hat{a}_{\boldsymbol{k}'\beta\sigma'}\hat{a}_{\boldsymbol{k}\alpha\sigma}\,,\end{aligned}\tag{7.2}$$

with

$$\epsilon_{\alpha\beta}(\boldsymbol{k})=\sum_\delta t_A\mathrm{e}^{\mathrm{i}\boldsymbol{k}\cdot\boldsymbol{\delta}}\qquad\text{and}\qquad V_{\alpha\beta}(\boldsymbol{q})=\frac{1}{2}\sum_\delta V_B\mathrm{e}^{-\mathrm{i}\boldsymbol{q}\cdot\boldsymbol{\delta}}\,.\tag{7.3}$$

Here, $\boldsymbol{\delta}$ are the vectors connecting nearest-neighbor molecules while the subscript A denotes $A=c_1,c_2,\cdots,p_4$ and the subscript B is $B=c,p$ which are being defined in Fig. 7.1 (c). The explicit

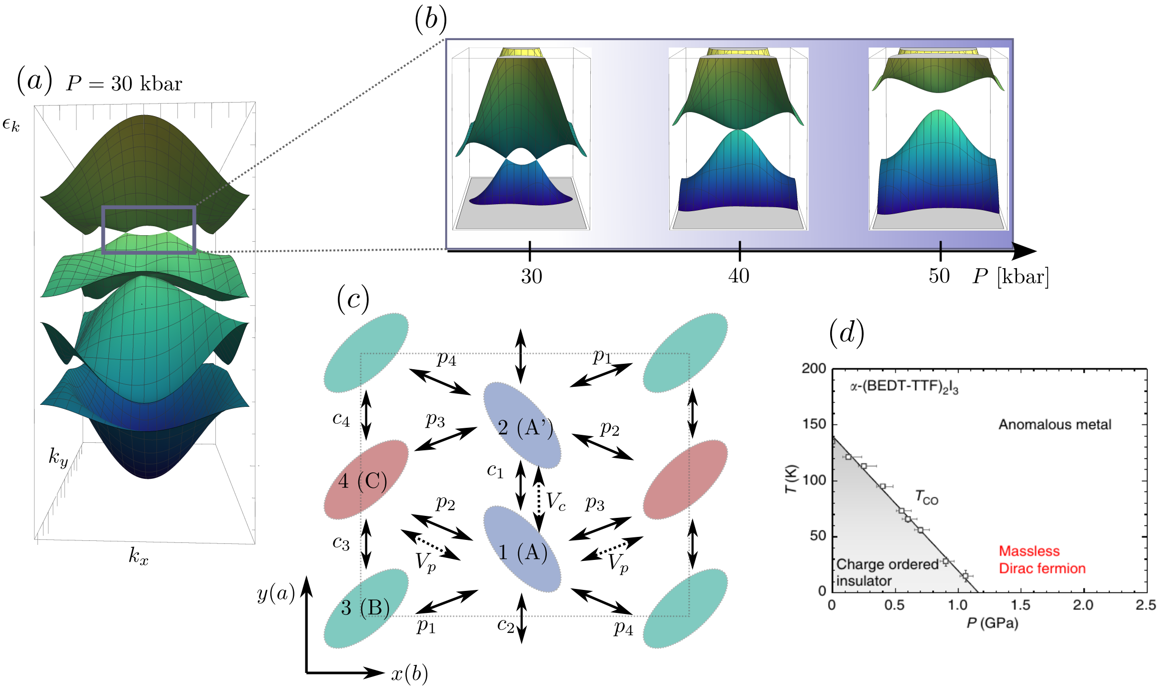

Figure 7.1: In panel (a) the four energy bands of the organic charge transfer salt α-(BEDT-TTF)$_2$I$_3$ for the uniaxial pressure $P_a = 30$kbar is shown. Panel (b) focuses on the upper two energy bands and shows the mergence of the two Dirac cones with increasing pressure. Panel (c) (adapted from [113]) shows the unit cell of α-(BEDT-TTF)$_2$I$_3$ salt which consists of four molecules. Panel(d) shows the experimental data [115] for the critical temperature of the phase transition between a charged ordered insulator and massless Dirac fermions. Panel (d) was taken from [115].

expressions of the matrix elements $\epsilon_{\alpha\beta}$ and $V_{\alpha\beta}$ are (with $\epsilon^*_{\beta\alpha} = \epsilon_{\alpha\beta}$ and $V^*_{\beta\alpha} = V_{\alpha\beta}$)

$$\begin{aligned}
\epsilon_{12}(\boldsymbol{k}) &= t_{c_1} + t_{c_2}\mathrm{e}^{-\mathrm{i}k_y} & V_{12}(\boldsymbol{q}) &= (1/2)(V_c + V_c\mathrm{e}^{\mathrm{i}q_y}) \\
\epsilon_{13}(\boldsymbol{k}) &= t_{p_1} + t_{p_4}\mathrm{e}^{\mathrm{i}k_x} & V_{13}(\boldsymbol{q}) &= (1/2)(V_p + V_p\mathrm{e}^{-\mathrm{i}q_x}) \\
\epsilon_{14}(\boldsymbol{k}) &= t_{p_2} + t_{p_3}\mathrm{e}^{\mathrm{i}k_x} & V_{14}(\boldsymbol{q}) &= (1/2)(V_p + V_p\mathrm{e}^{-\mathrm{i}q_x}) \\
\epsilon_{23}(\boldsymbol{k}) &= t_{p_4}\mathrm{e}^{\mathrm{i}k_y} + t_{p_1}\mathrm{e}^{\mathrm{i}k_x+\mathrm{i}k_y} & V_{23}(\boldsymbol{q}) &= (1/2)(V_p\mathrm{e}^{-\mathrm{i}q_y} + V_p\mathrm{e}^{-\mathrm{i}q_x-\mathrm{i}q_y}) \\
\epsilon_{24}(\boldsymbol{k}) &= t_{p_3} + t_{p_2}\mathrm{e}^{\mathrm{i}k_x} & V_{24}(\boldsymbol{q}) &= (1/2)(V_p + V_p\mathrm{e}^{-\mathrm{i}q_x}) \\
\epsilon_{34}(\boldsymbol{k}) &= t_{c_3} + t_{c_4}\mathrm{e}^{-\mathrm{i}k_y} & V_{34}(\boldsymbol{q}) &= (1/2)(V_c + V_c\mathrm{e}^{\mathrm{i}q_y})\,.
\end{aligned} \tag{7.4}$$

The hopping elements increase or decrease respectively under the application of uniaxial pressure. For a uniaxial pressure P_a along the a-axis with the units [kbar], the modified matrix elements are

$$t_A(P_a) = t_A(0)(1 + K_A P_a)\,. \tag{7.5}$$

Experimentally one finds the following values of the hopping elements: $t_{p_1}(0) = 0.140$, $t_{p_2}(0) = 0.123$, $t_{p_3}(0) = -0.025$, $t_{p_4}(0) = -0.062$, $t_{c_1}(0) = 0.048$, $t_{c_2}(0) = -0.020$, $t_{c_3}(0) = -0.028$, $t_{c_4}(0) = -0.028$ [eV], and the following slopes $K_{p_1} = 0.011$, $K_{p_2} = 0$, $K_{p_3} = 0$, $K_{p_4} = 0.032$, $K_{c_1} = 0.167$,

$K_{c_2} = -0.025$, $K_{c_3} = 0.089$, and $K_{c_4} = 0.89$ [eV/kbar]. These values are taken from Refs. 113 and 114.

Let us now discuss the phase diagram and the energy dispersion of α-(BEDT-TTF)$_2$I$_3$. At small pressure, there is a phase transition between a charged ordered insulator and massless Dirac fermions, see Refs. 114 and 115. At zero temperature, this phase transition occurs at $P_{a,c} \approx 12.5$ kbar as can be seen in the experimental data [115] shown in Fig. 7.1 (d). Hence, at zero temperature and for pressures greater than the critical value, i. e., $P_a \geq P_{a,c}$, the organic charge transfer salt is in the phase, where the system has two Dirac cones. The energy dispersion for α-(BEDT-TTF)$_2$I$_3$ at $P_a = 30$ kbar is shown in Fig. 7.1 (a). There are four energy bands, however, only the three lowest one are filled. The Fermi energy lies between the two highest energy bands. Let us now focus on these two highest energy bands. As can be seen in Fig. 7.1 (b), the two Dirac cones merge with increasing pressure. At $P_a = 40$ kbar the two Dirac cones have merged to one anisotropic Dirac cone. We can clearly see the parabolic energy dispersion along the direction from which the two Dirac cones have moved to each other. In the perpendicular direction, the energy dispersion is still linear. Upon increasing the pressure further, a gap opens in the the energy spectrum.

7.1.2 The Heterostructure TiO$_2$/VO$_2$

Another material having anisotropic Dirac cones is the heterostructure 5/3 TiO$_2$/VO$_2$. An image of the real-space representation of the heterostructure is depicted in Fig. 7.2 (a), where we see the VO$_2$ trilayer which is enclosed by 5 layers of TiO$_2$. This heterostructure has four Dirac cones in the first Brillouin zone as can be seen in Fig. 7.2 (b). The energy spectrum around these Dirac cones shows again Newtonian-like behavior along one direction and Dirac-like along the perpendicular one. But these main axis are rotated by 45 degrees with respect to each other for the different Dirac cones. This was first demonstrated by Pardo and Pickett in Ref. 108 where they calculated the energy dispersion of TiO$_2$/VO$_2$ via a first-principles density functional method. A few months later a tight-binding calculation of the dispersion relation of TiO$_2$/VO$_2$ by Banerjee *et al.* published in Ref. 109 followed. In this section, we will shortly present this tight-binding calculation. The Hamiltonian describes a three band model of spinless fermions and is given by

$$\begin{aligned}\mathcal{H}_{\mathrm{TiO_2/VO_2},\boldsymbol{r}} =& \sum_{\alpha=1}^{3}\left(\sum_i \epsilon_\alpha n_{i,\alpha} + \sum_{\langle ij\rangle} t_\alpha \left(c^\dagger_{i,\alpha}c_{j,\alpha} + h.c.\right)\right) \\ &+ \lambda_1 \sum_{\langle i\rangle,\pm}\left(c^\dagger_{i,1}c_{i\pm\hat{x},3} - c^\dagger_{i,1}c_{i\pm\hat{y},3} + h.c.\right) + \lambda_2 \sum_{\langle i\rangle,\pm}\left(c^\dagger_{i,2}c_{i\pm\hat{x},3} - c^\dagger_{i,2}c_{i\pm\hat{y},3} + h.c.\right)\,,\end{aligned} \tag{7.6}$$

where α is the band index and t_α describes intraband hopping processes. Furthermore, we assume that the third energy band is far away from the Fermi energy, which we thus assume being dispersionless, and it does not overlap with the energy bands ϵ_1 and ϵ_2 ,i. e., $\epsilon_3 \gg \epsilon_1, \epsilon_2$. The two lower bands only couple to the third energy band by an interaction which changes its sign under a rotation by 90 degrees. This interaction is modeled by the λ_1 and λ_2 terms. Next, for simplicity, we choose the hopping parameters as $t_1 = -t_2 = t$ and $\lambda_1 = \lambda_2 = t'$ and obtain in momentum space the Hamiltonian

$$\mathcal{H}_{\mathrm{TiO_2/VO_2},\boldsymbol{k}} = \sum_{\boldsymbol{k}} \hat{\Psi}^\dagger_{\boldsymbol{k}} \begin{pmatrix} \tilde{\epsilon}_{1,\boldsymbol{k}} & 0 & V_{\boldsymbol{k}} \\ 0 & \tilde{\epsilon}_{2,\boldsymbol{k}} & V_{\boldsymbol{k}} \\ V_{\boldsymbol{k}} & V_{\boldsymbol{k}} & \epsilon_3 \end{pmatrix} \hat{\Psi}_{\boldsymbol{k}}\,, \tag{7.7}$$

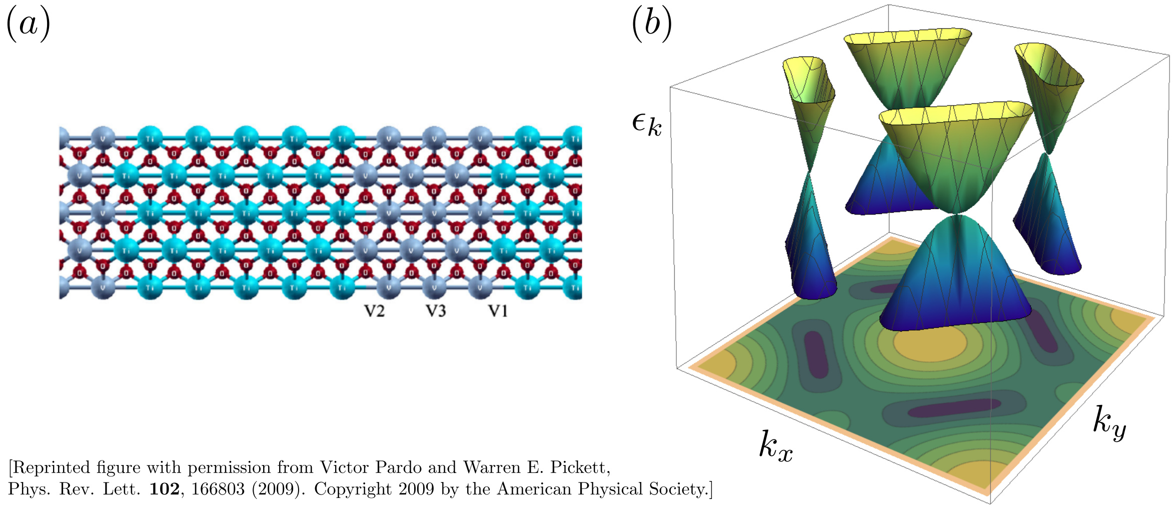

[Reprinted figure with permission from Victor Pardo and Warren E. Pickett, Phys. Rev. Lett. **102**, 166803 (2009). Copyright 2009 by the American Physical Society.]

Figure 7.2: Panel (*a*) shows the heterostructure 5/3 TiO_2/VO_2 where V2, V3, and V1 label the V ion sites. (This figure was taken from [108]). In panel (*b*), the energy dispersion of the heterostructure TiO_2/VO_2 can be seen. There are four anisotropic Dirac cones in the first Brillouin zone which are rotated by 45 degrees with respect to each other.

where $\Psi_{\boldsymbol{k}}$ is a three component fermionic field and

$$\begin{aligned}
\tilde{\epsilon}_{1,\boldsymbol{k}} &= \epsilon_1 + 2t\Big(\cos(k_x a) + \cos(k_y a)\Big) &(7.8)\\
\tilde{\epsilon}_{2,\boldsymbol{k}} &= \epsilon_2 - 2t\Big(\cos(k_x a) + \cos(k_y a)\Big) &(7.9)\\
V_{\boldsymbol{k}} &= 2t'\Big(\cos(k_x a) - \cos(k_y a)\Big)\,, &(7.10)
\end{aligned}$$

with a being the lattice constant. Since the third energy band is energetic far off, the above Hamiltonian can be downfolded to a renormalized two orbital problem with

$$\mathcal{H}_{\mathrm{TiO_2/VO_2},\boldsymbol{k}} = \sum_{\boldsymbol{k}} \hat{\psi}^\dagger_{\boldsymbol{k}} \begin{pmatrix} \tilde{\epsilon}_{1,\boldsymbol{k}} & \frac{V_{\boldsymbol{k}}^2}{\epsilon_3} \\ \frac{V_{\boldsymbol{k}}^2}{\epsilon_3} & \tilde{\epsilon}_{2,\boldsymbol{k}} \end{pmatrix} \hat{\psi}_{\boldsymbol{k}}\,. \tag{7.11}$$

The energy dispersion of TiO_2/VO_2 in the tight-binding model is thus

$$\varepsilon_{\pm\boldsymbol{k}} = \frac{\tilde{\epsilon}_{1,\boldsymbol{k}} + \tilde{\epsilon}_{2,\boldsymbol{k}}}{2} \pm \frac{1}{2}\sqrt{\Big(\tilde{\epsilon}_{1,\boldsymbol{k}} - \tilde{\epsilon}_{2,\boldsymbol{k}}\Big)^2 + 4\left(\frac{V_{\boldsymbol{k}}^2}{\epsilon_3}\right)^2}\,, \tag{7.12}$$

which is shown in Fig. 7.2 (*b*). There are four anisotropic Dirac points located at $\boldsymbol{K}_{\pm,\pm} = \frac{\pi}{2a}(\pm1,\pm1)$. As already mentioned before, the energy dispersion is linear along one axis and parabolic along the perpendicular one. However, these main axis are rotated by 45 degrees to each other for the four different Dirac cones. Next, the energy dispersions are Taylor expanded around the four Dirac points and we obtain the following Hamiltonian:

$$\begin{aligned}\mathcal{H}_{\mathrm{TiO_2/VO_2},\boldsymbol{K}_{\pm,\pm}+\boldsymbol{k}} &= \sum_k \hat{\psi}^\dagger_{\boldsymbol{K}_{+,+}+\boldsymbol{k}} \begin{pmatrix} 2(k_x+k_y)t & 4(k_x-k_y)^2t'^2 \\ 4(k_x-k_y)^2t'^2 & -2(k_x+k_y)t \end{pmatrix} \hat{\psi}_{\boldsymbol{K}_{+,+}+\boldsymbol{k}} \\ &+ \sum_k \hat{\psi}^\dagger_{\boldsymbol{K}_{-,-}+\boldsymbol{k}} \begin{pmatrix} -2(k_x+k_y)t & 4(k_x-k_y)^2t'^2 \\ 4(k_x-k_y)^2t'^2 & 2(k_x+k_y)t \end{pmatrix} \hat{\psi}_{\boldsymbol{K}_{-,-}+\boldsymbol{k}} \\ &+ \sum_k \hat{\psi}^\dagger_{\boldsymbol{K}_{+,-}+\boldsymbol{k}} \begin{pmatrix} 2(k_x-k_y)t & 4(k_x+k_y)^2t'^2 \\ 4(k_x+k_y)^2t'^2 & -2(k_x-k_y)t \end{pmatrix} \hat{\psi}_{\boldsymbol{K}_{+,-}+\boldsymbol{k}} \\ &+ \sum_k \hat{\psi}^\dagger_{\boldsymbol{K}_{-,+}+\boldsymbol{k}} \begin{pmatrix} -2(k_x-k_y)t & 4(k_x+k_y)^2t'^2 \\ 4(k_x+k_y)^2t'^2 & 2(k_x-k_y)t \end{pmatrix} \hat{\psi}_{\boldsymbol{K}_{-,+}+\boldsymbol{k}} \,.\end{aligned} \tag{7.13}$$

Due to the four rotated anisotropic Dirac cones, the above energy dispersion of the $\mathrm{TiO_2/VO_2}$ will lead to a superposition of effects arising because of the relativistic energy dispersion and of the ones arising due to the classical part of the energy spectrum. In order to distinguish clearly which physics occur because of the linear part of the energy spectrum and which due to the parabolic part, we will focus for the remainder of this thesis on systems with only one anisotropic Dirac cone per Brillouin zone. This system will be described by the Hamiltonian introduced in the next subsection.

7.1.3 The Hamiltonian

All four terms of the Hamiltonian in Eq. (7.13) can be cast into the form

$$\mathcal{H}_{0,\mathrm{ADS}} = \int d^2r \hat{\psi}^\dagger_r \left(-\frac{1}{2m}\nabla_x^2\sigma_x - \mathrm{i}v\nabla_y\sigma_y\right)\hat{\psi}_r \,. \tag{7.14}$$

Here, m is the effective mass along the x-direction and v the velocity along the y-direction. The Pauli matrices σ_x and σ_y describe the pseudo-spin space and denote the valence and conductance band. Furthermore, we introduce the momentum scale $k_0 = 2mv$. The energy spectrum originating from this Hamiltonian is

$$\epsilon_{\lambda\boldsymbol{k}} = \lambda\sqrt{\left(\frac{k_x^2}{2m}\right)^2 + \left(vk_y\right)^2} \,, \tag{7.15}$$

with the velocity of the quasiparticles $\boldsymbol{v}_{\lambda\boldsymbol{k}} = \partial\epsilon_{\lambda\boldsymbol{k}}/\partial\boldsymbol{k}$. In Fig. 7.3, the energy spectrum is shown over the equal energy contour plot. We clearly see the parabolic energy dispersion in the k_x-direction and the linear behavior along the k_y-direction. The density of states is proportional to the square root of the frequency, i. e., $\rho(\omega) = \frac{\Gamma(5/2)\sqrt{|\omega|k_0}}{4\pi^{3/2}\Gamma(3/4)v}$.

Next, we are going to define the Matsubara Green's function

$$G_{\boldsymbol{k},\mathrm{i}\omega} = \left(\mathrm{i}\omega\sigma_0 - \mathcal{H}_{0,\mathrm{ADS}}\right)^{-1} = -\frac{\mathrm{i}\omega\sigma_0 + \frac{k_x^2}{2m}\sigma_x + v\sigma_y}{\omega^2 + \epsilon^2_{\lambda\boldsymbol{k}}} \,. \tag{7.16}$$

The last quantity, we will introduce here, is the current operator. The current operator is derived by substituting $\boldsymbol{k} \to \boldsymbol{k} - e\boldsymbol{A}$ in the Hamiltonian Eq. (7.14) and taking the derivative with respect to the

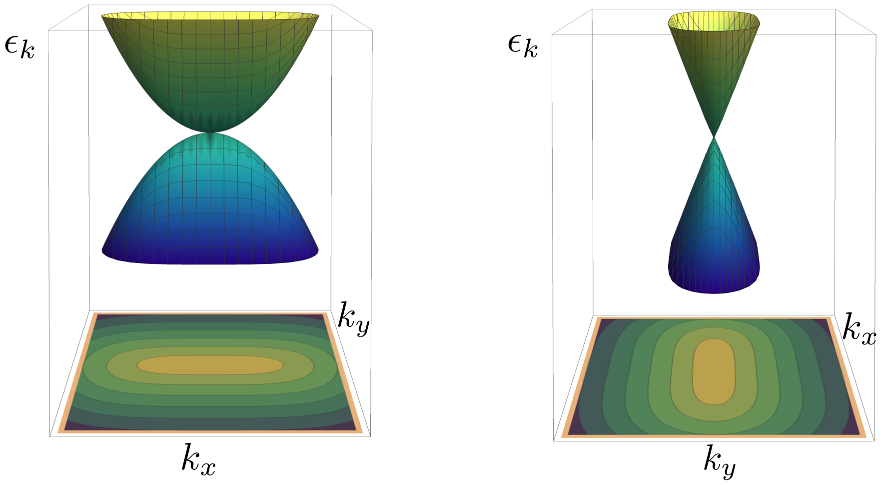

Figure 7.3: The energy dispersion of a single anisotropic Dirac cone is depicted over an equal energy contour. In the k_x-direction, the energy spectrum is parabolic, whereas in the k_y-direction the energy spectrum shows linear behavior with the velocity v.

vector potential $\boldsymbol{A}$ which yields

$$j_x = \int_{\boldsymbol{k}} \hat{\psi}^\dagger_{\boldsymbol{k}} \frac{k_x}{m} \sigma_x \hat{\psi}_{\boldsymbol{k}} \qquad \text{and} \qquad j_y = \int_{\boldsymbol{k}} \hat{\psi}^\dagger_{\boldsymbol{k}} v \sigma_y \hat{\psi}_{\boldsymbol{k}} \,. \tag{7.17}$$

After having defined the non-interacting Hamiltonian of ADSs, we are now going to include the Coulomb interaction between the quasiparticles

$$\mathcal{H}_{\mathcal{C}} = \frac{1}{2} \int_{\boldsymbol{r}} \int_{\boldsymbol{r}'} \hat{\psi}^\dagger_{\boldsymbol{r}} \hat{\psi}^\dagger_{\boldsymbol{r}'} \frac{e^2}{\epsilon |\boldsymbol{r} - \boldsymbol{r}'|} \hat{\psi}_{\boldsymbol{r}'} \hat{\psi}_{\boldsymbol{r}} \,, \tag{7.18}$$

and implement this interaction via a renormalization group (RG) analysis in the next section.

7.2 Coulomb interaction in ADS

Again we pose the question how the Coulomb interaction between the quasiparticles in ADSs influences the different transport properties. For an ADS described by the Hamiltonian $\mathcal{H}_{0,\text{ADS}} + \mathcal{H}_{\mathcal{C}}$ a renormalization group (RG) analysis in the large N limit is introduced in Sec. 7.2.1. In the same section, we will see how physical observables such as the compressibility, the heat capacity and the entropy behave upon combining scaling arguments and RG. This RG analysis will be applied both in the collisionless and in the hydrodynamic regime. However, in the hydrodynamic regime the Coulomb interaction enters the calculation one more time in form of the collision integral. Since the coupling constant of ADSs decreases under growing RG-flow, the collision integral can be obtained using perturbation theory in $1/N$. The derivation of the collision integral is elaborated in Sec. 7.2.2.

7.2.1 Large N Renormalization group analysis in the strong coupling limit

As in the previous part treating the transport properties of graphene, we want to study the influence of the Coulomb interaction on the transport properties of ADSs. Therefore, we will apply a RG analysis in the large N-limit, where N is the number of fermionic flavors. We find for the organic conductor α-(BEDT-TTF)$_2$I$_3$ $N = 2$ because of its spin degrees of freedom while for the heterostructure TiO$_2$/VO$_2$ we find $N = 8$ because of the four Dirac cones and the spin of the fermions. The RG analysis in the large N-limit is a powerful method as was previous shown for isotropic systems such as graphene in Refs. 117 and 118. The RG analysis for ADSs presented here, was published by Isobe *et al.* in Ref. 116 and we will follow closely their derivation.

Let us start with the action of ADSs treating the Coulomb interaction with the help of a Hubbard-Stratonovich field ϕ_Q with Q being the relativistic four-component momentum $Q = (\Omega, \boldsymbol{q})$. It is

$$\mathcal{S} = -\int_P \hat{\psi}_P^\dagger \left(\mathrm{i}\omega - \mathcal{H}_{0,\mathrm{ADS}}\right)\hat{\psi}_P + \mathrm{i}\sqrt{2\pi}e\int_{P,Q}\hat{\psi}^\dagger_{P+Q}\hat{\psi}_P\hat{\phi}_Q + \frac{1}{2}\int_Q |\boldsymbol{q}|\hat{\phi}_Q\hat{\phi}_Q\,. \tag{7.19}$$

Next, let us take a closer at the self-energy corrections of the bosonic fields $\hat{\phi}_Q$ and the fermionic fields $\hat{\psi}_P$ in first-order of the coupling constant α_N. The coupling constant of the system is

$$\alpha = \frac{e^2}{\hbar v} \qquad \text{and} \qquad \alpha_N = N\frac{e^2}{\hbar v}\,, \tag{7.20}$$

where α_N is finite for large N. In the following, we set again $\hbar = 1$ and restore it where needed. The self-energy of the Hubbard-Stratonovich fields is given by the polarization operator

$$\begin{aligned}\Pi(\boldsymbol{q},\omega) &= e^2\int\limits_\Omega\int\limits_{\boldsymbol{k}}\mathrm{Tr}\left(G_{\boldsymbol{k}+\boldsymbol{q},\mathrm{i}(\omega+\Omega)}G_{\boldsymbol{k},\mathrm{i}\Omega}\right)\\ &= -\alpha_N v\left[\frac{d_x\,(2m)^{-1/2}\,q_x^2}{\Delta(\omega,\boldsymbol{q})^{1/4}} + \frac{d_y\,(2m)^{1/2}\,q_y^2}{\Delta(\omega,\boldsymbol{q})^{3/4}}\right]\,,\end{aligned} \tag{7.21}$$

where $\Delta(\omega,\boldsymbol{q}) = \omega^2 + c\left(\frac{q_x^2}{2m}\right)^2 + v^2q_y^2$ and $d_x = \frac{1}{8\sqrt{\pi}}\frac{\Gamma(3/4)}{\Gamma(9/4)}$, $d_y = \frac{1}{8\sqrt{\pi}}\frac{\Gamma(5/4)}{\Gamma(7/4)}$, and $c = \left(\frac{2}{\sqrt{\pi}}\frac{\Gamma(3/4)}{\Gamma(9/4)}\right)^4$ (see Ref. 116). Thus, the full boson propagator is defined by the expression $D(\boldsymbol{q},\Omega)^{-1} = |\boldsymbol{q}| - \Pi(\boldsymbol{q},\Omega)$. Now, we can evaluate the self-energy of the ADSs at the charge neutrality point. Thereby we use the full bosonic operator and obtain

$$\Sigma(\boldsymbol{k},\omega) = -2\pi\frac{v\alpha_N}{N}\int\frac{d^2q}{(2\pi)^2}\int\frac{d\Omega}{2\pi}D(\boldsymbol{q},\Omega)G_{\boldsymbol{k}-\boldsymbol{q},\mathrm{i}(\omega-\Omega)}\,. \tag{7.22}$$

This fermionic self-energy can be parametrized in the following way

$$\Sigma(\boldsymbol{k},\omega) = (1-\mathcal{Z}_\omega)\mathrm{i}\omega + v(\mathcal{Z}_x - 1)\frac{k_x^2}{k_0}\sigma_x + v(\mathcal{Z}_y - 1)k_y\sigma_y\,, \tag{7.23}$$

with

$$\begin{aligned}\mathcal{Z}_\omega &= 1 + \frac{C_\omega}{N}\log\left(v\Lambda/k\right) + \mathcal{O}(N^{-2})\\ \mathcal{Z}_x &= 1 + \frac{C_x}{N}\log\left(v\Lambda/k\right) + \mathcal{O}(N^{-2})\\ \mathcal{Z}_y &= 1 + \frac{C_y}{N}\log\left(v\Lambda/k\right) + \mathcal{O}(N^{-2})\,,\end{aligned} \tag{7.24}$$

where $k = \max\left(k_x^2/k_0, k_y, \omega\right)$, Λ is the UV cut-off, and $C_{\omega,x,y}$ are numerical constants. The electron-plasmon vertex is again determined using the Ward-identity Eq. (4.29), i. e., $\Gamma_{\boldsymbol{k}} = e\left(1 - \frac{\partial\Sigma(\boldsymbol{k},\omega)}{\partial \mathrm{i}\omega}\right) = eZ_e$. Thus, we obtain for the action of ADS at the charge neutrality point

$$\mathcal{S} = -\int_P \hat{\psi}_P^\dagger \left(\mathrm{i}\omega - \mathcal{H}_{0,\mathrm{ADS}} - \Sigma(\boldsymbol{k},\omega)\right)\hat{\psi}_P + \mathrm{i}\sqrt{2\pi}e\int_{P,Q}\Gamma_{\boldsymbol{q}}\hat{\psi}_{P+Q}^\dagger\hat{\psi}_P\hat{\phi}_Q + \frac{1}{2}\int_Q\left(|\boldsymbol{q}| - \Pi(\boldsymbol{k},\omega)\right)\hat{\phi}_Q\hat{\phi}_Q\,. \tag{7.25}$$

which can be cast into the form Eq. (7.19) by introducing the renormalized quantities $\hat{\psi}_R = \hat{\psi}\mathcal{Z}_\omega^{1/2}$, $v_R = v\frac{\mathcal{Z}_y}{\mathcal{Z}_\omega}$, $k_{0,R} = k_0\frac{\mathcal{Z}_y}{\mathcal{Z}_x}$, and $e_R = \Gamma\mathcal{Z}_\omega^{-1} = e$, where we obtained the last relation using the Ward-identity. Now we find for the renormalized coupling constant and the momentum scale

$$\begin{aligned} \alpha_R &= \frac{e_R^2}{v_R} = \alpha\frac{\mathcal{Z}_\omega}{\mathcal{Z}_y} = \alpha\left(1 + \frac{C_\omega - C_y}{N}\log(\Lambda/k)\right) \\ k_{0,R} &= k_0\frac{\mathcal{Z}_y}{\mathcal{Z}_x} = k_0\left(1 + \frac{C_y - C_x}{N}\log(\Lambda/k)\right)\,, \end{aligned} \tag{7.26}$$

which can be cast into the following flow equations

$$\begin{aligned} \frac{d\alpha}{dl} &= \alpha\frac{C_\omega - C_y}{N} = -\gamma_v\alpha \qquad \Rightarrow \qquad \alpha(b) &= \alpha b^{-\gamma_v} \\ \frac{dk_0}{dl} &= k_0\frac{C_y - C_x}{N} = \gamma_{k_0}k_0 \qquad \Rightarrow \qquad k_0(b) &= k_0 b^{\gamma_{k_0}}\,. \end{aligned} \tag{7.27}$$

The numerical values of the coefficients C_ω, C_x, and C_y are obtained in the strong coupling limit and yield $\gamma_v = 0.3625/N$ and $\gamma_{k_0} = 0.2364/N$ [116]. With increasing RG flow, the coupling constant decreases while the momentum scale increases. What consequence does this behavior under growing RG flow have on the energy spectrum of the ADSs? To answer this question, we consider how the mass and the velocity flow under growing RG flow parameter l, i. e., $b = \mathrm{e}^l$. In the strong coupling limit, their flow equations are

$$\frac{dm}{dl} = -\frac{0.1261}{N}m = -\gamma_m\, m \qquad \text{and} \qquad \frac{dv}{dl} = \frac{0.3625}{N}v\,. \tag{7.28}$$

The anisotropy of the energy spectrum increases with increasing RG flow, since both the velocity v and the inverse mass m^{-1} will grow under the RG flow, but the velocity will increase much faster than the inverse mass. This is depicted in Fig. 7.4.

The RG in the strong coupling regime will give rise to power laws in the observables. However, in the weak coupling limit these power laws are substituted by logarithmic factors, see Ref. 116.

Physical Observables

In the following, we will combine the RG analysis in the large N-limit and in the strong coupling regime and the physical scaling arguments to determine different observables. The physical observable O is connected to their renormalized value by

$$O(k_x, k_y, \omega, \alpha) = Z_O O(Z_x(l)k_x, bk_y, Z_\omega(l)\omega, \alpha(l))\,, \tag{7.29}$$

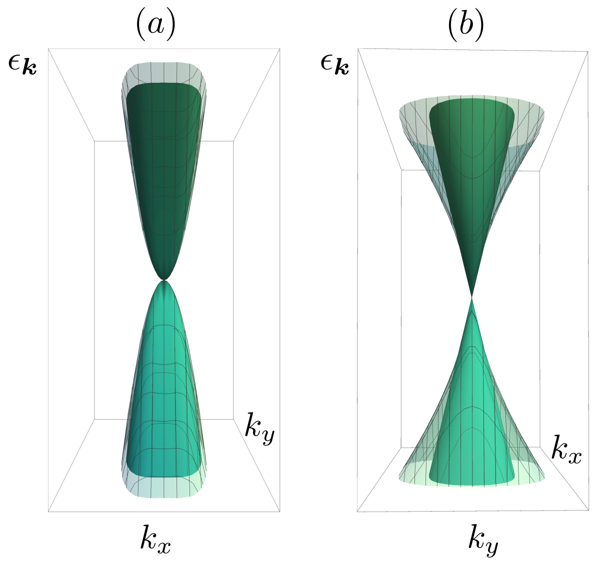

Figure 7.4: The renormalized energy spectrum (transparent one) and the unrenormalized energy spectrum are shown. Panel (a) shows the parabolic part of the energy spectrum, which is less strongly renormalized than the linear one which is shown in panel (b).

where Z_O is the scaling factor. Furthermore the momentum k_y is rescaled by $k_y \to bk_y$ with $b = \mathrm{e}^l$. The frequency and temperature are renormalized by the scaling factor Z_ω and the x-component of the momentum by Z_x. We find for these scaling factors the following RG flow equations

$$\begin{aligned} \frac{dZ_\omega}{dl} &= Z_\omega \left(1 + \frac{C_\omega - C_y}{N}\right) &\Rightarrow\quad Z_\omega &= b^{1-\gamma_v} \\ \frac{dZ_x}{dl} &= Z_x \frac{1}{2}\left(1 + \frac{C_x - C_y}{N}\right) &\Rightarrow\quad Z_x &= b^{\frac{1}{2}\left(1-\gamma_{k_0}\right)} . \end{aligned} \tag{7.30}$$

As an example let us study again, as in the case of graphene in Sec. 4.3.2, the compressibility of ADSs which is defined as the derivative of the charge carrier density with respect to the chemical potential, i. e., $\kappa = \frac{\partial n}{\partial \mu}$. Here, the particle density n has the scaling factor $Z_n = b^{-1} Z_x^{-1}$ and thus we find for the compressibility $Z_\kappa = Z_\omega/(bZ_x)$. These scaling arguments imply

$$\kappa(T) = b^{-\gamma_v - \frac{1}{2}(1-\gamma_{k_0})}\ \kappa(b^{1-\gamma_v}) \propto T^{\Phi_\kappa} , \tag{7.31}$$

with $\Phi_\kappa = \frac{1}{2} - \frac{1}{2}(\gamma_{k_0} - 3\gamma_v) = \frac{1}{2} + \frac{0.4255}{N}$. The compressibility vanishes less slowly with decreasing temperature than in the case of free anisotropic Dirac fermions $\kappa_0 \propto T^{1/2}$. The next two physical quantities being studied are the heat capacity and the entropy of the ADSs. Therefore, we first take a closer look at the free energy density with $f(T,\mu) = b^{-1} Z_x^{-1} Z_\omega\ f(Z_\omega T, Z_\omega \mu)$ which reproduces the scaling dimensions of the particle density via $n = \frac{\partial f}{\partial \mu}$. Thus, it follows for the heat capacity

$$C(T) = b^{-1} Z_x^{-1} Z_\omega^{-1} C(Z_\omega T) = b^{-\frac{1}{2}(3-\gamma_{k_0})} C(b^{1-\gamma_v} T) \propto T^{\phi_s} \tag{7.32}$$

with $\phi_s = \frac{3}{2} - \frac{1}{2}(\gamma_{k_0} - \gamma_v) = \frac{3}{2} + \frac{0.4255}{N}$. The heat capacity is connected to the entropy of the system via $C = T\frac{\partial S}{\partial T}$ and we obtain for the entropy

$$s(T) \propto T^{\phi_s} \propto T^{\frac{3}{2} + \frac{0.4255}{N}} . \tag{7.33}$$

The entropy of free anisotropic Dirac fermions is proportional to $T^{3/2}$ and due to the renormalization arising from the Coulomb interaction it also vanishes less slowly with decreasing temperature to the power $T^{0.4255/N}$.
As we have seen above due to the anisotropy of the energy spectrum, the two momentum components k_x and k_y scale differently. The anisotropy generates two different length scales in our system which are given in the hydrodynamic regime by

$$\begin{aligned}\xi_x &\propto T^{-\frac{1}{2}\left(1+\frac{0.1261}{N}\right)} \\ \xi_y &\propto T^{-(1+\frac{0.3625}{N})},\end{aligned} \tag{7.34}$$

and for the collisionless regime the temperature is substituted by frequency. The occurrence of the two different length scales will become very important in our analysis of the transport properties of ADS. They will be the reason for the beautiful and fascinating characteristics of the electrical conductivity and for the violation of the lower bound which occurs for one of the viscosity coefficients.

7.2.2 The collision integral in the hydrodynamic regime

In the hydrodynamic regime, the interaction between the electrons due to the Coulomb potential is implemented in the quantum Boltzmann equation via the collision integral I_λ^{ee}. In this section we are going to derive the collision integral for ADSs which is based on my work in collaboration with Boris N. Narozhny and Jörg Schmalian pulished in Ref. 119. Due to the previous RG analysis, we can evaluate the collision integral using perturbation theory where the small parameter is $1/N$. The collision integral due to Coulomb interaction is defined by [36]

$$I_\lambda^{ee}(\boldsymbol{k},\omega) = \Sigma_\lambda^{>}(\boldsymbol{k},\omega) G^{<}_{\lambda\boldsymbol{k},\omega} - \Sigma_\lambda^{<}(\boldsymbol{k},\omega) G^{>}_{\lambda\boldsymbol{k},\omega}, \tag{7.35}$$

where $\Sigma_\lambda^{<,>}(k,\omega)$ and $G^{<,>}_{\lambda\boldsymbol{k}\omega}$ are the lesser and greater self-energies and Green's functions. The lesser and greater Green's functions are defined as

$$G^{<}_{\lambda\lambda'\boldsymbol{k},\omega} = \mathrm{i} f_{\lambda\boldsymbol{k}} A(\boldsymbol{k},\omega)\delta_{\lambda\lambda'} \tag{7.36}$$

$$G^{>}_{\lambda\lambda'\boldsymbol{k},\omega} = \mathrm{i}[1-f_{\lambda\boldsymbol{k}}] A(\boldsymbol{k},\omega)\delta_{\lambda\lambda'}, \tag{7.37}$$

where $f_{\lambda\boldsymbol{k}}$ is the distribution function of the quasiparticles/quasiholes and $A(\boldsymbol{k},\omega)$ is the spectral function of the Green's function, which we approximate here for simplicity as $A(\boldsymbol{k},\omega) = 2\pi\delta(\omega - \lambda\epsilon_k)$. This simplification has the same temperature dependence as the general form of $A(\boldsymbol{k},\omega) = \frac{-2\,\mathrm{Im}\,\Sigma^R(\boldsymbol{k},\omega)}{(\omega-\zeta_p-\mathrm{Re}\,\Sigma^R(\boldsymbol{k},\omega))^2+(\mathrm{Im}\,\Sigma^R)^2}$. The lesser self-energy in first order of $\frac{1}{N}$ is given by

$$\Sigma_\lambda^{<}(\boldsymbol{k},\omega) = e^2 \sum_\alpha \int_{\omega'} \int_{\boldsymbol{q}} n(\omega')\,\mathrm{Im}\, D(\boldsymbol{q},\omega') G^{<}_{\alpha\boldsymbol{k},\omega} N_{\alpha\lambda}(\boldsymbol{k},\boldsymbol{k}-\boldsymbol{q}), \tag{7.38}$$

where $N_{\alpha\lambda}(\boldsymbol{k_1},\boldsymbol{k_2})$ is

$$N_{\alpha\lambda}(\boldsymbol{k}_1,\boldsymbol{k}_2) = \frac{1}{2}\left[1 + \frac{1}{\epsilon_{\alpha\boldsymbol{k_1}}\epsilon_{\lambda\boldsymbol{k_2}}}\left(\frac{k_{1,x}^2 k_{2,x}^2}{k_0^2} + k_{1,y}k_{2,y}\right)\right], \tag{7.39}$$

and Im $D(\boldsymbol{q},\omega') = \mathrm{Im}(\boldsymbol{q} - \Pi(\omega',q))^{-1}$ is the spectral function for the bosons which in the strong coupling limit has the form Im $\Pi(\boldsymbol{q},\omega')^{-1}$, see Eq. (7.21) for the explicit expression. The form of the greater self energy is analogous to the one of the lesser self energy. Hence, the collision integral describing the Coulomb interaction can be written as

$$\begin{aligned} I_\lambda^{ee}(\boldsymbol{k},\omega) &= -\int\limits_{\boldsymbol{q}} \text{Im } \Pi(\boldsymbol{q},\omega-\epsilon_{\alpha\boldsymbol{k}-\boldsymbol{q}})^{-1}\; N_{\alpha\lambda}(\boldsymbol{k},\boldsymbol{k}-\boldsymbol{q})A_\lambda(\boldsymbol{k},\omega) \\ &\times \left\{\left[1-f_{\alpha\boldsymbol{p}-\boldsymbol{q}}\right]f_{\lambda\omega}+n^0(\omega-\epsilon_{\alpha\boldsymbol{k}-\boldsymbol{q}})\left[f_{\lambda\omega}-f_{\alpha\boldsymbol{p}-\boldsymbol{q}}\right]\right\}\;, \end{aligned} \tag{7.40}$$

where $n^0(\omega)$ is the bosonic distribution function in equilibrium and we sum over equal indices. Everything is known in the above equation but the distribution functions of the quasiparticles/holes $f_{\lambda\boldsymbol{k}}$. In the linear response regime we can expand the fermionic distribution function up to first order of the source term responsible for the motion of the quasiparticles, i.e. in the case of the electrical transport the electrical field $\boldsymbol{E}$ and in the case in the hydrodynamic transport the external velocity gradient $\partial\boldsymbol{u}_\alpha/\partial\boldsymbol{x}_\beta$. Thus, we choose for the distribution function the ansatz

$$f_{\lambda\boldsymbol{k}} = f_{\lambda\boldsymbol{k}}^{(0)} + \frac{1}{T}f_{\lambda\boldsymbol{k}}^{(0)}\left(1-f_{\lambda\boldsymbol{k}}^{(0)}\right)h_{\lambda\boldsymbol{k}}\,. \tag{7.41}$$

The function $h_{\lambda\boldsymbol{k}}$ is proportional to the source term of the perturbation and to the function $g_{\lambda\boldsymbol{k}} = \sum_n \psi_n\phi_{\lambda,\boldsymbol{k}}^{(n)}$. The function $g_{\lambda\boldsymbol{k}}$ is expanded into a set of basis functions $\phi_{\lambda,\boldsymbol{k}}^{(n)}$ and the corresponding coefficients ψ_n. For ADS the basis functions $\phi_{\lambda,\boldsymbol{k}}^{(n)}$ which are the different modes of the system are given by the energy $\phi_{\lambda,\boldsymbol{k}}^{(0)} = \lambda\epsilon_{\lambda\boldsymbol{k}}$ and the band index $\phi_{\lambda,\boldsymbol{k}}^{(1)} = \lambda$. For the electrical transport and for the transport due to a velocity gradient, it is respectively [43, 46]

$$h_{\lambda\boldsymbol{k}\boldsymbol{E}} = \lambda\boldsymbol{v}_{\lambda\boldsymbol{k}}\cdot\boldsymbol{E}g_{\lambda\boldsymbol{k}}^{\boldsymbol{E}} \tag{7.42}$$

$$h_{\lambda\boldsymbol{k}\boldsymbol{u}_{\beta,\alpha}} = \lambda\left(v_{\lambda\boldsymbol{k}}^\alpha k_\beta - \delta_{\alpha\beta}\frac{\epsilon_{\lambda\boldsymbol{k}}}{2}\right)\frac{\partial\boldsymbol{u}_\beta}{\partial x_\alpha}{g_{\lambda\boldsymbol{k}}}^\beta\,. \tag{7.43}$$

Upon inserting the linearized distribution function into the collision term and integrating over the frequency with the spectral function $A(\boldsymbol{k},\omega) = 2\pi\delta\left(\omega-\epsilon_{\lambda\boldsymbol{k}}\right)$, we obtain

$$\begin{aligned} I_\lambda^{ee}(\boldsymbol{k}) =& \frac{1}{T}\int\limits_{\boldsymbol{q}} \text{Im}\,\Pi\left(\boldsymbol{q},\epsilon_{\lambda\boldsymbol{k}}-\epsilon_{\lambda\boldsymbol{k}-\boldsymbol{q}}\right)^{-1} N_{\lambda\lambda}(\boldsymbol{k},\boldsymbol{k}-\boldsymbol{q}) \\ &\times n^{(0)}(\epsilon_{\lambda\boldsymbol{k}}-\epsilon_{\lambda\boldsymbol{k}-\boldsymbol{q}})\left[1-f_{\lambda\boldsymbol{k}}^{(0)}\right]f_{\lambda\boldsymbol{k}-\boldsymbol{q}}^{(0)}\left[h_{\lambda\boldsymbol{k}}-h_{\lambda\boldsymbol{k}-\boldsymbol{q}}\right] \\ +&\frac{1}{T}\int\limits_{\boldsymbol{q}} \text{Im}\,\Pi\left(\boldsymbol{q},\epsilon_{\lambda\boldsymbol{k}}+\epsilon_{\lambda\boldsymbol{k}-\boldsymbol{q}}\right)^{-1} N_{\lambda-\lambda}(\boldsymbol{k},\boldsymbol{k}-\boldsymbol{q}) \\ &\times n^{(0)}(\epsilon_{\lambda\boldsymbol{k}}+\epsilon_{\lambda\boldsymbol{k}-\boldsymbol{q}})\left[1-f_{\lambda\boldsymbol{k}}^{(0)}\right]f_{-\lambda\boldsymbol{k}-\boldsymbol{q}}^{(0)}\left[h_{\lambda\boldsymbol{k}}-h_{-\lambda\boldsymbol{k}-\boldsymbol{q}}\right]\,. \end{aligned} \tag{7.44}$$

The first term describes intra-band scattering and the second term inter-band scattering processes mediated by the Coulomb interaction.

Now after setting the stage, we can begin to study the transport properties of ADSs. Let us start with the conductivity in the following chapter.

8

Chapter 8

The conductivity...

In Chap. 5, we discussed the conductivity of graphene in the hydrodynamic and collisionless regime. We found that in the high-frequency limit the conductivity is universal and depends neither on frequency nor on temperature with $\sigma_0(\text{Dirac}) = \frac{e^2}{4\hbar}$ [1]. However, in the hydrodynamic regime, a logarithmic temperature dependence enters via the renormalized coupling constant $\alpha(T) = \alpha/(1 + \alpha \log(\Lambda_T/T)/4)$, i. e., $\sigma_0(\text{Dirac}) = 0.0193\frac{e^2}{\hbar\alpha(T)^2}$ [19] and the conductivity approaches for increasing temperatures the value $\sigma_0 = \frac{2}{\pi^2}\frac{e^2}{\hbar}$ [95].

In this chapter, we study the conductivity of anisotropic Dirac systems (ADSs) which have with respect to the energy dispersion a lower symmetry than graphene. Thus, a natural question to ask is how does the conductivity change for systems with lower symmetry and how does the Coulomb interaction influence this transport quantity? These questions are answered in Sec. 8.1 where the conductivity is studied using the quantum Boltzmann equation in the hydrodynamic regime ($\omega \ll \tau^{-1}$). We find fascinating transport properties, since the ADSs show insulating and metallic temperature behavior depending on the direction of the applied electrical field. Using the occurrence of the two length scales, mentioned in Sec. 7.2.1, we will explain this impressive behavior of the conductivity and show the breakdown of single parameter scaling. In Sec. 8.3, the characteristics of the conductivity are studied in the collisionless regime ($\omega \gg \tau^{-1}$) where we find the same beautiful transport properties as in the hydrodynamic regime.

This chapter is based on my work in collaboration with Boris N. Narozhny and Jörg Schmalian which is published in Ref. 119.

8.1 ...in the hydrodynamic regime

Now, let us start our investigation of the conductivity in the hydrodynamic regime at the charge neutrality point, i. e., $\mu = 0$. As we have seen in Sec. 1.2 and Sec. 5.1, the quantum Boltzmann equation is used to determine the conductivity. The Boltzmann equation is given by

$$\frac{\partial f_{\lambda\boldsymbol{k}}}{\partial t} + \boldsymbol{F}\frac{\partial f_{\lambda\boldsymbol{k}}}{\partial \boldsymbol{k}} = -\frac{\delta f_{\lambda\boldsymbol{k}}}{\tau_{\text{dis}}} + I^{ee}_{\lambda}(\boldsymbol{k})\,, \tag{8.1}$$

where $\boldsymbol{F} = e\left(\boldsymbol{E} + \boldsymbol{v}_{\lambda\boldsymbol{k}} \times \boldsymbol{B}/c\right)$ is the Lorentz force with the electrical field $\boldsymbol{E}$ and the magnetic field $\boldsymbol{B}$ and τ_{dis} is the relaxation time due to impurity scattering. The derivation of the collision integral describing the scattering processes due to the Coulomb potential between the electrons can be found in Sec. 7.2.2, while the explicit expression is given in Eq. (7.44). The distribution function $f_{\lambda\boldsymbol{k}}$ is assumed to be the sum of the Fermi-Dirac distribution $f^{(0)}_{\lambda\boldsymbol{k}} = \left(1 + \mathrm{e}^{\epsilon_{\lambda\boldsymbol{k}}/T}\right)^{-1}$ describing the equilibrium part and the out-off equilibrium correction $\delta f_{\lambda\boldsymbol{k}}$. We perform our analysis in the *linear response* regime where the out-off equilibrium correction is proportional to the source of the perturbation. Thus, the distribution function is given by

$$\begin{aligned} f_{\lambda\boldsymbol{k}} &= f^{(0)}_{\lambda\boldsymbol{k}} + \delta f_{\lambda\boldsymbol{k}} \\ &= f^{(0)}_{\lambda\boldsymbol{k}} + \frac{1}{T} f^{(0)}_{\lambda\boldsymbol{k}}(1 - f^{(0)}_{\lambda\boldsymbol{k}}) h_{\lambda\boldsymbol{k}} \,. \end{aligned} \tag{8.2}$$

Thereby, we choose as ansatz for the non-equilibrium correction of the distribution function [43, 120]

$$h_{\lambda\boldsymbol{k}}{}^{\boldsymbol{E}} = \lambda \boldsymbol{v}_{\lambda\boldsymbol{k}} \cdot \boldsymbol{E}\; g^{\boldsymbol{E}}_{\lambda\boldsymbol{k}} \,, \tag{8.3}$$

where $g^{\boldsymbol{E}}_{\lambda\boldsymbol{k}}$ is an unknown function which is going to be determined by solving the Boltzmann equation. In order to determine the function $g^{\boldsymbol{E}}_{\lambda\boldsymbol{k}}$, $g^{\boldsymbol{E}}_{\lambda\boldsymbol{k}}$ is expanded in a set of basis functions $\phi^{(n)}_{\lambda\boldsymbol{k}}$ with the unknown coefficients $\psi^{\boldsymbol{E}}_n$, i. e., $g^{\parallel}_{\lambda\boldsymbol{k}} = \sum_n \psi^{\parallel}_n \phi^{(n)}_{\lambda\boldsymbol{k}}$. In general, these basis functions can be given by Chebyshev polynomials. Here however, we implemented a two-mode approximation, i. e., we describe the system only using two different basis functions. These two dominant modes are the eigenenergy of the system $\phi^{(0)}_{\lambda\boldsymbol{k}} = \lambda\epsilon_{\lambda\boldsymbol{k}}$ and the band index denoting the conductance or valence band $\phi^{(1)}_{\lambda\boldsymbol{k}} = \lambda$. Upon inserting these definitions in the Boltzmann equation Eq. (8.1), multiplying the Boltzmann equation from the left with the basis function $\phi^{(n)}_{\lambda\boldsymbol{k}}$, and after integrating and summing over the momentum $\boldsymbol{k}$ and the band index λ respectively, the Boltzmann equation can be cast into the following matrix form

$$\mathcal{M}_{\boldsymbol{E}} \boldsymbol{\psi}^{\boldsymbol{E}} = \boldsymbol{G}_{\boldsymbol{E}} \,, \tag{8.4}$$

where the matrix

$$\begin{aligned} \mathcal{M}^{ee}_{nm} = \frac{1}{T} \sum_{\lambda} \int\limits_{\boldsymbol{k},\boldsymbol{q}} & \operatorname{Im}\Pi\left(\boldsymbol{q}, \epsilon_{\lambda\boldsymbol{k}} - \epsilon_{\lambda\boldsymbol{k}-\boldsymbol{q}}\right)^{-1} N_{\lambda\lambda}(\boldsymbol{k}, \boldsymbol{k}-\boldsymbol{q}) \\ & \times n^{(0)}(\epsilon_{\lambda\boldsymbol{k}} - \epsilon_{\lambda\boldsymbol{k}-\boldsymbol{q}}) \left[1 - f^{(0)}_{\lambda\boldsymbol{k}}\right] f^{(0)}_{\lambda\boldsymbol{k}-\boldsymbol{q}} \left[\phi^{(n)}_{\lambda\boldsymbol{k}} \phi^{(m)}_{\lambda\boldsymbol{k}} - \phi^{(n)}_{\lambda\boldsymbol{k}-\boldsymbol{q}} \phi^{(m)}_{\lambda\boldsymbol{k}}\right] \\ & + \frac{1}{T} \sum_{\lambda} \int\limits_{\boldsymbol{k},\boldsymbol{q}} \operatorname{Im}\Pi\left(\boldsymbol{q}, \epsilon_{\lambda\boldsymbol{k}} + \epsilon_{\lambda\boldsymbol{k}-\boldsymbol{q}}\right)^{-1} N_{\lambda-\lambda}(\boldsymbol{k}, \boldsymbol{k}-\boldsymbol{q}) \\ & \times n^{(0)}(\epsilon_{\lambda\boldsymbol{k}} + \epsilon_{\lambda\boldsymbol{k}-\boldsymbol{q}}) \left[1 - f^{(0)}_{\lambda\boldsymbol{k}}\right] f^{(0)}_{-\lambda\boldsymbol{k}-\boldsymbol{q}} \left[\phi^{(n)}_{\lambda\boldsymbol{k}} \phi^{(m)}_{\lambda\boldsymbol{k}} - \phi^{(n)}_{-\lambda\boldsymbol{k}-\boldsymbol{q}} \phi^{(m)}_{\lambda\boldsymbol{k}}\right] \end{aligned}$$

arises due to the collision integral and the vector

$$G_{m,\boldsymbol{E}} = \frac{1}{T} \sum_{\lambda} \int_{k} \lambda \phi^{(m)}_{\lambda\boldsymbol{k}}\; f^{(0)}_{\lambda\boldsymbol{k}} \left[1 - f^{(0)}_{\lambda\boldsymbol{k}}\right] \tag{8.5}$$

consists of the terms proportional to the electrical field. Here, we assumed that no magnetic field is applied and no impurity scattering occurs. Next, the explicit expressions are given and furthermore, upon introducing dimensionless variables, $\Omega = \omega/T$, $x = \sqrt{1/(Tk_0)}k_x$, and $y = k_y/T$, the temperature dependence of the different terms is determined. Thereby, attention should be drawn to the fact that due to the anisotropy of the system the two components of the momentum scale differently with temperature. For the y-component, we find $k_y \propto T$ while for the x-component it is $k_x \propto \sqrt{T}$. The matrices are given by the expressions

$$\mathcal{M}^{ee}_{nm} = T^{3/2}\, k_0^{1/2}\, [\phi^{(m)}_{\lambda\boldsymbol{k}}][\phi^{(n)}_{\lambda\boldsymbol{k}}]\, \mathcal{C}^{ee}_{nm,\boldsymbol{E}} \tag{8.6}$$

and

$$G_{m,\boldsymbol{E}} = T^{1/2}[\phi^{(m)}_{\lambda\boldsymbol{k}}]\mathcal{C}^{f}_{m,\boldsymbol{E}}\,, \tag{8.7}$$

where $\mathcal{C}^{ee}_{nm,\boldsymbol{E}}$ and $\mathcal{C}^{f}_{m,\boldsymbol{E}}$ are numerical coefficients and the modes have the dimensionality $[\phi^{(0)}_{\lambda\boldsymbol{k}}] = [\lambda\epsilon_{\lambda\boldsymbol{k}}] = T$. Now, we can invert the matrix equation Eq. (8.4) to obtain the coefficients $\psi^{\boldsymbol{E}}_n$. These coefficients determine the electrical current

$$\boldsymbol{j} = \sum_{\lambda}\int_{\boldsymbol{k}} \boldsymbol{v}_{\lambda\boldsymbol{k}}\delta f_{\lambda\boldsymbol{k}} = \frac{e}{T}\sum_{\lambda,n}\int_{\boldsymbol{k}} \lambda\boldsymbol{v}_{\lambda\boldsymbol{k}} f^{(0)}_{\lambda\boldsymbol{k}}\left(1 - f^{(0)}_{\lambda\boldsymbol{k}}\right)\left(\boldsymbol{v}_{\lambda\boldsymbol{k}}\cdot\boldsymbol{E}\right)\psi^{\boldsymbol{E}}_n\phi^{(n)}_{\lambda\boldsymbol{k}}\,, \tag{8.8}$$

or written in components as

$$j_\alpha \;=\; \frac{e}{T}\sum_{\lambda,n}\int_{k} \lambda f^{(0)}_{\lambda\boldsymbol{k}}\left(1 - f^{(0)}_{\lambda\boldsymbol{k}}\right)\left(v^{\alpha}_{\lambda\boldsymbol{k}}\right)^2\psi^{\boldsymbol{E}}_n\phi^{(n)}_{\lambda\boldsymbol{k}}E_\alpha\,, \tag{8.9}$$

where we used the fact that the integral of the two different velocity components over the momentum is zero, i.e., $\int_{\boldsymbol{k}} v^{x}_{\lambda\boldsymbol{k}}v^{y}_{\lambda'\boldsymbol{k}} = 0$. Now, the conductivity tensor can be defined since, as we have seen in Chap. 2, the conductivity tensor connects the electrical current to the electrical field via

$$j_\alpha = \sum_{\beta}\sigma_{\alpha\beta}E_\beta\,. \tag{8.10}$$

Hence, the conductivity tensor is given at the charge neutrality point by

$$\sigma_{\alpha\alpha} = \sum_{\lambda}\int_{\boldsymbol{k}} \frac{(v^{\alpha}_{\lambda\boldsymbol{k}})^2}{T}\frac{2\mathrm{e}^{\epsilon_{\lambda\boldsymbol{k}}/T}}{\left(1 + \mathrm{e}^{\epsilon_{\lambda\boldsymbol{k}}/T}\right)^2}\psi^{\parallel}_1 \tag{8.11}$$

with $\psi^{\parallel}_1 = \frac{vk_0}{T}\frac{\mathcal{C}^{f}_{1,\boldsymbol{E}}\mathcal{C}^{ee}_{00,\boldsymbol{E}}}{\mathcal{C}^{ee}_{00,\boldsymbol{E}}\,\mathcal{C}^{ee}_{11,\boldsymbol{E}} - {\mathcal{C}^{ee}_{01,\boldsymbol{E}}}^2}$, where we used the fact that the mode $\phi^{(0)}_{\lambda\boldsymbol{k}} = \lambda\epsilon_{\lambda\boldsymbol{k}}$ does not contribute to the current. Only the mode $\phi^{(1)}_{\lambda\boldsymbol{k}} = \lambda$ determines the electrical current. Thus we find for the conductivity tensor

$$\sigma_{xx,yy}(T) \propto N\left(\frac{T}{vk_0}\right)^{\pm(\frac{1}{2}+\phi_\sigma)}\,, \tag{8.12}$$

with $\phi_\sigma = (\gamma_v + \gamma_{k_0})/2 = 0.299/N$. The off-diagonal elements of the conductivity tensor σ_{xy} and σ_{yx} are zero, since as mentioned above the integral of two different velocity components over the momentum is zero. The temperature dependence of the diagonal elements of the conductivity tensor is depicted in Fig. 8.1 (b). For decreasing temperature, σ_{xx} vanishes and we find insulating behavior, if the electrical field is aligned along the x-axis which has the parabolic energy spectrum in momentum

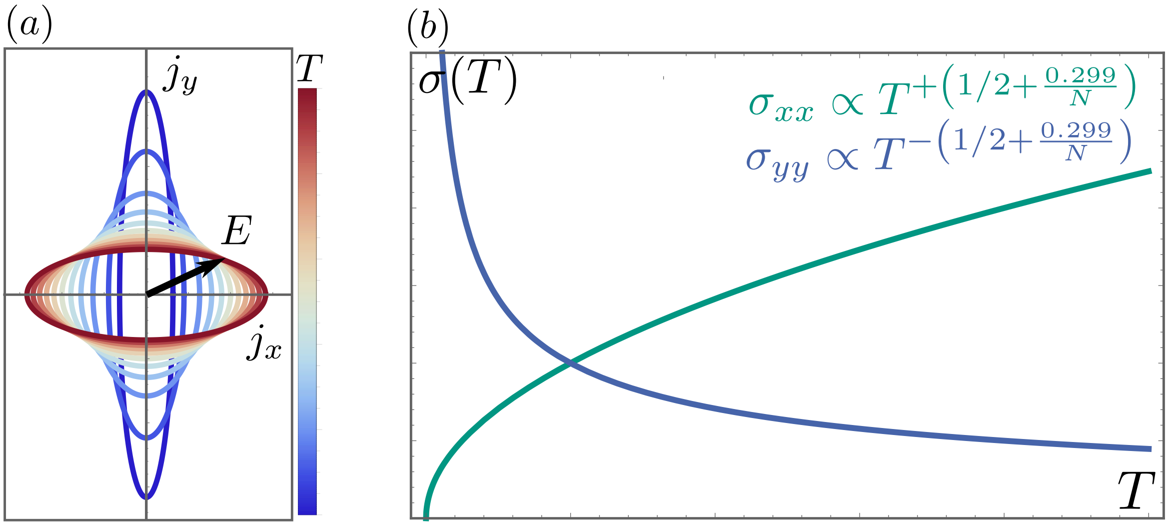

Figure 8.1: Panel (a) shows the spatial distribution of the electrical current for different temperatures. In panel (b) we see the temperature dependence of the conductivity tensor. It becomes insulating in the direction with the parabolic energy dispersion and metallic in the linear one.

space. Whereas, the σ_{yy} component of the conductivity tensor increases with decreasing temperature. Thus, the ADSs are metallic, if the electrical field is aligned along the y-axis which corresponds to the linear energy dispersion. The additional exponent ϕ_σ is obtained using the renormalization group (RG) analysis of Sec. 7.2.1 and combining it with the scaling arguments. A detailed derivation can be found in App. B.1.1. In Fig. 8.1 (a), we see the spatial distribution of the electrical current depending on the direction of the electrical field for different temperatures. For small temperatures, the j_y-component is the dominating current component as expected, while for large temperatures the j_x-component becomes more and more important and the j_y-component decreases.

Hitherto, we studied pristine ADSs systems, i. e., system with no impurity scattering. The main effect of impurities is on the σ_{yy} component of the conductivity tensor which would instead of diverging at zero temperature have a finite value. Upon implementing the impurity scattering, a self-consistent Born-approximation should be performed as in Refs. 121 and 95.

Furthermore, so far only systems with one anisotropic Dirac cone in the first Brillouin zone were investigated, as it is the case for the organic charge transfer salt α-(BEDT-TTF)$_2$I$_3$. However, in the case of the TiO$_2$/VO$_2$ heterostructure there are 4 Dirac cones in the first Brillouin zone which are rotated by 45 degrees with respect to each other. Here, the insulating behavior is not to be seen, since the diagonal elements of the conductivity tensor are a superposition of our insulating component σ_{xx} and the metallic component σ_{yy}. It is

$$\sigma_{\alpha\alpha,\mathrm{TiO_2/VO_2}} = N\left[\left(\frac{T}{vk_0}\right)^{-\left(\frac{1}{2}+\phi_\sigma\right)} + \left(\frac{T}{vk_0}\right)^{+\left(\frac{1}{2}+\phi_\sigma\right)}\right]. \tag{8.13}$$

The reason for this is simple. Due to the energy dispersion of the heterostructure, described by Eq. (7.13) the velocity components of TiO$_2$/VO$_2$ are a superposition of the velocity component $v^x_{\lambda\boldsymbol{k}}$ and $v^y_{\lambda\boldsymbol{k}}$, i. e., $v^{x,y}_{\lambda\boldsymbol{k},\mathrm{TiO_2/VO_2}} = v^y_{\lambda\boldsymbol{k}} \pm v^x_{\lambda\boldsymbol{k}}$. This superposition of the two velocity components propagates to the conductivity tensor of TiO$_2$/VO$_2$ and thus the metallic temperature behavior always dominates.

8.2 Scaling Behavior

Now let us turn back to ADSs with only one anisotropic Dirac cone in the first Brillouin zone. Here, a natural question to be asked is: how can a material be metallic and insulating depending on the direction of the applied electrical field? In order to answer this question, the scaling behavior of the conductivity for ADSs is investigated. Therefore, let us first remind ourselves of the physical scaling of the conductivity for an isotropic system such as graphene. We have seen in Sec. 2.3 that the conductivity is scale invariant under RG for an isotropic system in two dimensions. Hence, for graphene it is

$$\sigma_{\alpha\alpha}\left(T\right) = \xi^0 \sigma_{\alpha\alpha}\left(Z_T T\right) \, . \tag{8.14}$$

The temperature is rescaled by Z_T which is defined in Eq. (4.31) and the two components of the momentum are rescaled by the same length scale ξ. However for ADSs, this single parameter scaling breaks down. Due to the anisotropy of the energy dispersion, being Newtonian-like in the x-direction and Dirac-like in the y-direction, two different length scales arise with

$$\begin{aligned} \xi_x &\propto T^{-\frac{1}{2}\left(1+\frac{0.1261}{N}\right)} \, , \\ \xi_y &\propto T^{-(1+\frac{0.3625}{N})} \, , \end{aligned} \tag{8.15}$$

where the exponents proportional to $1/N$ originate from the RG analysis in the large N-limit and in the strong coupling regime, see Sec. 7.2.1 for more details of the RG. These two length scales will rescale the two components of the momentum. The k_x-component is rescaled by ξ_x which is proportional to the inverse square root of the temperature and the k_y-component by ξ_y which is proportional to the inverse temperature. The scale factor of the conductivity is the ratio of these two length scales and we find for the conductivity tensor

$$\begin{aligned} \sigma_{xx}(T) &= \frac{\xi_x}{\xi_y}\sigma_{xx}\left(\xi_y^z T\right) \propto T^{+\left(\frac{1}{2}+\frac{0.299}{N}\right)} \, , \\ \sigma_{yy}(\boldsymbol{k},T) &= \frac{\xi_y}{\xi_x}\sigma_{xx}\left(\xi_y^z T\right) \propto T^{-\left(\frac{1}{2}+\frac{0.299}{N}\right)} \, , \end{aligned} \tag{8.16}$$

where $\xi_y^z T \approx const.$ and $z = 1 - \gamma_v$ is a dynamic scaling exponent. For σ_{xx} the scaling factor is $Z_{\sigma_{xx}} = \xi_x/\xi_y$, while for the σ_{yy} component of the conductivity tensor it is the inverse $Z_{\sigma_{yy}} = \xi_y/\xi_x$. These two different scaling factors are the reason for the different temperature dependence and thus are the reason for the metallic and insulating behavior with decreasing temperature in ADSs.

8.3 ...in the collisionless regime

Now, let us see how the conductivity of ADSs at the charge neutrality point behaves in the collisionless regime. In the collisionless regime the frequency is the fastest time scale $\omega \gg \tau^{-1}$ opposed to the hydrodynamic regime where the scattering time is the the fastest scale $\omega \ll \tau^{-1}$. For the conductivity tensor in the collisionless regime the same energy dependence as in the hydrodynamic regime is expected. The only difference should be that the temperature is now substituted by the frequency. Using the Kubo-formula, we are going to check if this expectation is justified. The Kubo-formula for the conductivity is

$$\sigma_{\alpha\beta} = -\frac{\operatorname{Im}\chi_{J_{\alpha\beta}}}{\omega} \, , \tag{8.17}$$

where $\chi_{J_{\alpha\beta}}$ is the correlation function between the α- and β- component of the current operator. The current operator and the Green's function are defined in Sec. 7.1.3 in Eq. (7.17) and Eq. (7.16). The conductivity of free anisotropic Dirac fermions is given by the bare bubble diagrams

$$\begin{aligned}\chi_{J_{xx}} &= N\,T\sum_n \int_{\boldsymbol{k}} \mathrm{Tr}\left(\hat{j}_x G_{\boldsymbol{k},\mathrm{i}\omega_n} \hat{j}_x G_{\boldsymbol{k},\mathrm{i}(\omega_n+\Omega_m)}\right)\\ &= \frac{N}{m^2}\,T\sum_n \int_{\boldsymbol{k}} k_x^2\,\mathrm{Tr}\left(\sigma_x G_{\boldsymbol{k},\mathrm{i}\omega_n} \sigma_x G_{\boldsymbol{k},\mathrm{i}(\omega_n+\Omega_m)}\right)\end{aligned} \tag{8.18}$$

and

$$\begin{aligned}\chi_{J_{yy}} &= T\sum_n \int_{\boldsymbol{k}} \mathrm{Tr}\left(\hat{j}_y G_{\boldsymbol{k},\mathrm{i}\omega_n} \hat{j}_y G_{\boldsymbol{k},\mathrm{i}(\omega_n+\Omega_m)}\right)\\ &= Nv^2\sum_n \int_{\boldsymbol{k}} \mathrm{Tr}\left(\sigma_y G_{\boldsymbol{k},\mathrm{i}\omega_n} \sigma_y G_{\boldsymbol{k},\mathrm{i}(\omega_n+\Omega_m)}\right)\,.\end{aligned} \tag{8.19}$$

Again the two off-diagonal components $\chi_{J_{xy}}$ and $\chi_{J_{yx}}$ are zero due to momentum integration. The evaluation of the two remaining diagrams yields

$$\begin{aligned}\sigma_{xx}(\omega) &= N\left(\frac{\omega}{vk_0}\right)^{1/2}\mathcal{C}_{xx,1}\left[f^{(0)}\left(-\frac{\omega}{2}\right)-f^{(0)}\left(\frac{\omega}{2}\right)\right]+N\mathcal{C}_{xx,2}\left(\frac{k_BT}{vk_0}\right)^{1/2}\delta\left(\frac{\omega}{T}\right)\\ \sigma_{yy}(\omega) &= N\left(\frac{\omega}{vk_0}\right)^{-1/2}\mathcal{C}_{yy,1}\left[f^{(0)}\left(-\frac{\omega}{2}\right)-f^{(0)}\left(\frac{\omega}{2}\right)\right]+N\mathcal{C}_{yy,2}\left(\frac{k_BT}{vk_0}\right)^{-1/2}\delta\left(\frac{\omega}{T}\right)\,.\end{aligned} \tag{8.20}$$

with $\mathcal{C}_{xx,1}=\frac{2\pi^{1/2}}{5\,\Gamma(1/4)^2}$, $\mathcal{C}_{xx,2}=0.931$, $\mathcal{C}_{yy,1}=\frac{\sqrt{2}}{12\pi}K(-1)$ and $\mathcal{C}_{yy,2}=0.298$ where $K(m)$ is the complete elliptical integral of the first kind.

Let us first consider the limit of zero-frequency which corresponds to the hydrodynamic regime. We find the same temperature dependence of the conductivity as in the previous section. Hence, both formalism, the Kubo-formula and the quantum Boltzmann approach, yield two consistent results.

Next, we study the conductivity tensor at finite frequencies and find that the conductivity tensor shows the same fascinating transport properties as in the hydrodynamic regime. The σ_{xx}-component of the conductivity tensor is proportional to $\omega^{+1/2}$ and shows insulating behavior with decreasing frequency, while the σ_{yy}-component is proportional to $\omega^{-1/2}$ and thus shows metallic behavior with decreasing frequency. Next, the Coulomb interaction is included into our considerations by applying our RG analysis. The conductivity will gain again an additional power-law exponent which is proportional to $1/N$. This exponent has the same form in the collisionless regime as in the hydrodynamic. The conductivity tensor can now be expressed by

$$\sigma_{xx,yy}(\omega)\propto N\left(\frac{\omega}{vk_0}\right)^{\pm(\frac{1}{2}+\phi_\sigma)}\,, \tag{8.21}$$

with $\phi_\sigma=(\gamma_v+\gamma_{k_0})/2=0.299/N$. This calculation showed that our expectations were justified.

8.4 Summary

For graphene, a system with isotropic energy dispersion, the conductivity is universal, i. e., it neither depends on frequency nor on temperature. Only in the hydrodynamic regime a temperature dependence enters via the renormalized coupling constant and both components of the conductivity tensor behave on the same way.

In contrast to the isotropic systems, the conductivity tensor of ADSs is energy dependent. Even more, both in the hydrodynamic and in the collisionless regime, the ADSs are either insulating or metallic depending on the direction of the applied electrical field. The temperature dependence in the hydrodynamic regime and the frequency dependence in the collisionless regime are

$$\sigma_{xx,yy}(T) \propto N \left(\frac{T}{vk_0}\right)^{\pm(\frac{1}{2}+\phi_\sigma)} \qquad \text{and} \qquad \sigma_{xx,yy}(\omega) \propto N \left(\frac{\omega}{vk_0}\right)^{\pm(\frac{1}{2}+\phi_\sigma)}, \tag{8.22}$$

with $\phi_\sigma = (\gamma_v + \gamma_{k_0})/2 = 0.299/N$. These beautiful electrical transport properties occur due to the breakdown of single parameter scaling. Two different length scales govern the physics of the system and the conductivity scales as

$$\sigma_{\alpha\alpha}(\omega\backslash T) = \left(\frac{\xi_x}{\xi_y}\right)^{\varphi_\alpha} \sigma_{\alpha\alpha}(\xi_y^z\omega\backslash\xi_y^z T)\,, \tag{8.23}$$

where $\varphi_x = 1$ and $\varphi_y = -1$.

9

Chapter 9

The viscosity...

In this chapter the viscosity of anisotropic Dirac systems (ADSs) at charge neutrality is investigated. As can be seen in Chap. 3, the viscosity is a rank four tensor which connects the velocity gradient $\partial u_\delta / \partial x_\gamma$ of a fluid to its energy-stress tensor $\tau_{\alpha\beta}$. In isotropic systems the energy-stress tensor is determined by two viscosities, the bulk and the shear viscosity. In contrast to isotropic systems such as graphene, the dissipative part of the energy-stress tensor is not determined by two viscosities but by eight viscosity coefficients

$$\begin{pmatrix} \tau_{xx} \\ \tau_{xy} \\ \tau_{yx} \\ \tau_{yy} \end{pmatrix} = \begin{pmatrix} \eta_{xxxx} & 0 & 0 & \eta_{xxyy} \\ 0 & \eta_{xyyx} & \eta_{xyxy} & 0 \\ 0 & \eta_{yxyx} & \eta_{yxxy} & 0 \\ \eta_{yyxx} & 0 & 0 & \eta_{yyyy} \end{pmatrix} \begin{pmatrix} \partial u_x/\partial x \\ \partial u_x/\partial y \\ \partial u_y/\partial x \\ \partial u_y/\partial y \end{pmatrix} . \tag{9.1}$$

The viscosity coefficients are symmetric under a pairwise exchange of the indices, i. e., $\eta_{\alpha\beta\gamma\delta} = \eta_{\gamma\delta\alpha\beta}$. This is most easily seen upon studying the Kubo formula which connects the viscosity coefficients to the correlation function of two energy-stress tensors, see Eq. (3.36). Applying this symmetry property reduces the number of independent viscosity coefficients which are needed to be calculated to six.

In the course of this chapter, we will see that the six viscosity coefficients depend strongly on the flow direction and show fundamentally different temperature dependence. At low temperatures, the ratio $\eta_{\alpha\beta\gamma\delta}/s$ either diverges or stays constant for most viscosity coefficients. Most notably, one viscosity coefficient η_{xyxy} violates the famous lower bound of the ratio between viscosity and entropy η/s [18][1]. The ADSs are the first realization in condensed matter physics violating the lower bound. Further systems violating the bound can be found in anisotropic versions of a super-Yang-Mills plasma [52, 57, 67], and in ultra cold gases [59], see Sec. 3.6.2. Here, we will present a clear explanation for the violation of the lower bound and show that again the breakdown of the single parameter scaling yields this beautiful physics. A consequence of the extremely small shear viscosity can be electron turbulence, nonlocal transport and extreme sensitivity to nanoelectronics settings.

Thus, we start the contemplation of the viscosity with the derivation of the energy-stress tensor in Sec. 9.1. Thereby we use the procedure introduced in Sec. 3.2. In Sec. 9.2 the shear viscosity and its scaling is investigated in the hydrodynamic regime followed by a study of the viscosity in the collisionless regime in Sec. 9.3. In the last Sec. 9.4, the Navier-Stokes equation is going to be derived. This extremely important equation governs the flow dynamics of our quasi-particle fluid. Due to the

---

[1] The derivation of the lower bound can be found in Sec. 3.6.

smallness of the viscosity coefficient violating the lower bound, turbulent flow is expected.

This chapter is again based on my work in collaboration with Boris N. Narozhny and Jörg Schmalian published in Ref. 119.

9.1 The energy-stress tensor

Let us start with the derivation of the energy-stress tensor. Thereby, we follow the steps described in Sec. 3.2 where the energy-stress tensor is derived from the strain generators. Let us shortly repeat the most important equations. The total strain generator $\mathcal{J}_{\alpha\beta}$ consists of a summand exhibiting the transformation of the spatial coordinates $\mathcal{L}_{\alpha\beta}$ and the other summand generates the transformations in the pseudospin space $\mathcal{S}_{\alpha\beta}$, i. e., $\mathcal{J}_{\alpha\beta} = \mathcal{L}_{\alpha\beta} + \mathcal{S}_{\alpha\beta}$. These strain generators have the explicit form $\mathcal{L}_{\alpha\beta} = -x_\alpha p_\beta + \frac{\mathrm{i}}{2}\delta_{\alpha\beta}$ and $\mathcal{S}_{\alpha\beta} = -\sum_\gamma \frac{1}{4}\epsilon_{\alpha\beta\gamma}\sigma_\gamma$. The total strain generator is connected to the energy-stress tensor via the time derivative

$$T_{\alpha\beta} = -\partial_t \mathcal{J}_{\alpha\beta}\,. \tag{9.2}$$

Next, we state the expression of the energy-stress tensor due to $\mathcal{L}_{\alpha\beta}$ which is

$$T^{(\mathcal{L})}_{\alpha\beta} = -\mathrm{i}\left[\mathcal{H}_{0,\mathrm{ADS}}, \mathcal{L}_{\alpha\beta}\right] = \int_{\boldsymbol{k}} \hat{\psi}^\dagger_{\boldsymbol{k}} \begin{pmatrix} 2\frac{v}{k_0}\sigma_x k_x \\ v\sigma_y \end{pmatrix}_\alpha \begin{pmatrix} k_x \\ k_y \end{pmatrix}_\beta \hat{\psi}_{\boldsymbol{k}}\,, \tag{9.3}$$

and the expression due to $\mathcal{S}_{\alpha\beta}$

$$T^{(\mathcal{S})}_{\alpha\beta} = -\mathrm{i}[\mathcal{H}_{0,\mathrm{ADS}}, \mathcal{S}_{\alpha\beta}] = \int_{\boldsymbol{k}} \hat{\psi}^\dagger_{\boldsymbol{k}} \left[\begin{pmatrix} \frac{1}{2}\frac{v}{k_0}k_x^2 \\ \frac{1}{2}vk_y \end{pmatrix}_\alpha \sigma_\beta - \sigma_\alpha \begin{pmatrix} \frac{1}{2}\frac{v}{k_0}k_x^2 \\ \frac{1}{2}vk_y \end{pmatrix}_\beta \right] \hat{\psi}_{\boldsymbol{k}}\,. \tag{9.4}$$

The different coefficients of the energy-stress tensor have thus the form:

$$\begin{aligned}
T_{xx} &= \int_{\boldsymbol{k}} \hat{\psi}^\dagger_{\boldsymbol{k}}\; 2\frac{v}{k_0}k_x^2\sigma_x\; \hat{\psi}_{\boldsymbol{k}}\,, \\
T_{yy} &= \int_{\boldsymbol{k}} \hat{\psi}^\dagger_{\boldsymbol{k}}\; v\sigma_y k_y\; \hat{\psi}_{\boldsymbol{k}}\,, \\
T_{xy} &= \int_{\boldsymbol{k}} \hat{\psi}^\dagger_{\boldsymbol{k}} \left[\sigma_x\left(2\frac{v}{k_0}k_xk_y - \frac{1}{2}vk_y\right) + \frac{1}{2}\frac{v}{k_0}k_x^2\sigma_y\right] \hat{\psi}_{\boldsymbol{k}}\,, \\
T_{yx} &= \int_{\boldsymbol{k}} \hat{\psi}^\dagger_{\boldsymbol{k}} \left[\sigma_y\left(vk_x - \frac{1}{2}\frac{v}{k_0}k_x^2\right) + \frac{1}{2}vk_y\sigma_x\right] \hat{\psi}_{\boldsymbol{k}}\,.
\end{aligned} \tag{9.5}$$

Upon introducing the energy band representation ($\psi^\dagger_k = \gamma^\dagger_k P_k^{-1}$ and $\psi_k = P_k\gamma_k$) and using the following transformation properties of the Pauli matrices

$$P_k^{-1}\sigma_x P_k \;=\; -\frac{k_x^2}{k_0\epsilon_k}\sigma_z + \frac{k_y}{\epsilon_k}\sigma_y\,, \tag{9.6}$$

$$P_k^{-1}\sigma_y P_k \;=\; -\frac{k_y}{\epsilon_k}\sigma_z - \frac{k_x^2}{k_0\epsilon_k}\sigma_y\,, \tag{9.7}$$

we obtain the energy-stress tensor due to intra-band scattering:

$$\Pi_{\alpha\beta} = \sum_{\lambda} \int_{k} v^{\alpha}_{\lambda \boldsymbol{k}} k_{\beta} \, \hat{\gamma}^{\dagger}_{\lambda \boldsymbol{k}} \hat{\gamma}_{\lambda \boldsymbol{k}} \,, \tag{9.8}$$

which has the same form as the one we obtained from the commutator of the momentum density with the Hamiltonian and thus takes only the transformation of the spatial coordinates into account. In the following, $T_{\alpha\beta}$ will be used to determine the viscosity coefficients in the collisionless regime, whereas we use $\Pi_{\alpha\beta}$ in the hydrodynamic regime. This is justified because of the low energies in the hydrodynamic regime, interband processes are not significant. Only in the collisionless regime, the influence of the pseudospin and the interband processes is seen.

9.2 ...in the hydrodynamic regime

Now, let us investigate the viscosity in the hydrodynamic regime. The viscosity tensor connects the velocity gradient field to the dissipative part of the energy-stress tensor. Hence, we start our examination of the viscosity by calculating the average of the energy-stress tensor $\Pi_{\alpha\beta}$. In linear response, the averaged energy-stress tensor is the sum of the equilibrium part of the energy-stress tensor $\pi_{\alpha\beta}$ which is determined by the Euler equations and the dissipative part $\tau_{\alpha\beta}$. Thus, it is

$$\left\langle \Pi_{\alpha\beta} \right\rangle = \sum_{\lambda} \int_{\boldsymbol{k}} v^{\alpha}_{\lambda \boldsymbol{k}} k_{\beta} \, \left\langle \hat{\gamma}^{\dagger}_{\lambda \boldsymbol{k}} \hat{\gamma}_{\lambda \boldsymbol{k}} \right\rangle = \sum_{\lambda} \int_{\boldsymbol{k}} v^{\alpha}_{\lambda \boldsymbol{k}} k_{\beta} f_{\lambda \boldsymbol{k}} = \pi_{\alpha\beta} + \tau_{\alpha\beta} \,, \tag{9.9}$$

where $f_{\lambda \boldsymbol{k}}$ is the distribution function of the quasiparticles. The distribution function consists of an equilibrium part described by the Fermi-Dirac function, $f^{(0)}_{\lambda \boldsymbol{k}} = (1 + \mathrm{e}^{(\epsilon_{\lambda \boldsymbol{k}} + \boldsymbol{u} \cdot \boldsymbol{k})/T})^{-1}$, and a part describing the out-off equilibrium corrections $\delta f_{\lambda \boldsymbol{k}}$, i. e., $f_{\lambda \boldsymbol{k}} = f^{(0)}_{\lambda \boldsymbol{k}} + \delta f_{\lambda \boldsymbol{k}}$. The dissipative part of the energy-stress tensor is defined by this out-off equilibrium correction, i. e.,

$$\tau_{\alpha\beta} = \sum_{\lambda} \int_{\boldsymbol{k}} v^{\alpha}_{\lambda \boldsymbol{k}} k_{\beta} \delta f_{\lambda \boldsymbol{k}} \,. \tag{9.10}$$

In linear response, the out-off equilibrium correction to the distribution function can be expanded in first order to the perturbation of the system, i. e., $\delta f_{\lambda \boldsymbol{k}} = f^{(0)}_{\lambda \boldsymbol{k}} (1 - f^{(0)}_{\lambda \boldsymbol{k}}) h_{\lambda \boldsymbol{k} \boldsymbol{u}_{\beta,\alpha}} / T$. In our case, the perturbation is the gradient of the hydrodynamic velocity, $\frac{\partial \boldsymbol{u}_{\beta}}{\partial x_{\alpha}}$, and hence for $h_{\lambda \boldsymbol{k} \boldsymbol{u}_{\beta,\alpha}}$ the following ansatz is chosen

$$h_{\lambda \boldsymbol{k} \boldsymbol{u}_{\beta,\alpha}} = \sum_{\alpha\beta} \lambda \left(v^{\alpha}_{\lambda \boldsymbol{k}} k_{\beta} - \delta_{\alpha\beta} \frac{\epsilon_{\lambda \boldsymbol{k}}}{2} \right) g^{\beta}_{\lambda \boldsymbol{k}} \frac{\partial \boldsymbol{u}_{\beta}}{\partial x_{\alpha}} \,. \tag{9.11}$$

A detailed derivation of this ansatz can be found in Sec. 3.5. The function $g^{\beta}_{\lambda \boldsymbol{k}}$ is expanded into a set of basis functions weighted with coefficients ψ^{β}_{n}, i. e., $g^{\beta}_{\lambda \boldsymbol{k}} = \sum_{n} \psi^{\beta}_{n} \phi^{(n)}_{\lambda \boldsymbol{k}}$. These basis functions are different modes of the system. In ADSs the dominant modes are given by the energy $\phi^{(0)}_{\lambda \boldsymbol{k}} = \lambda \epsilon_{\lambda \boldsymbol{k}}$ and the band index $\phi^{(1)}_{\lambda \boldsymbol{k}} = \lambda$. What remains to be done is to identify the coefficients ψ^{β}_{n}. They pin down the out-off equilibrium correction $\delta f_{\lambda \boldsymbol{k}}$ and thus fix the dissipative part of the energy-stress tensor. In order to determine $\delta f_{\lambda \boldsymbol{k}}$, the above described ansatz of the distribution function is inserted into the quantum Boltzmann equation

$$\frac{\partial f_{\lambda \boldsymbol{k}}}{\partial t} + \boldsymbol{v}_{\lambda \boldsymbol{k}} \frac{\partial f_{\lambda \boldsymbol{k}}}{\partial \boldsymbol{x}} = I^{ee}_{\lambda} \,. \tag{9.12}$$

Upon multiplying the quantum Boltzmann equation with the mode $\phi^{(m)}_{\lambda\boldsymbol{k}}$ and integrating and summing over the momentum and the band index respectively, the Boltzmann equation can be cast into a matrix form

$$\begin{pmatrix} \mathcal{M}^{ee}_{u_{x,y}} & 0 \\ 0 & \mathcal{M}^{ee}_{u_{y,x}} \end{pmatrix} \begin{pmatrix} \boldsymbol{\psi}^x \\ \boldsymbol{\psi}^y \end{pmatrix} = \begin{pmatrix} \boldsymbol{G}_{u_{x,y}} \\ \boldsymbol{G}_{u_{y,x}} \end{pmatrix} , \tag{9.13}$$

where the matrix $\mathcal{M}^{ee}_{u_{\alpha,\beta}}$ corresponds to the collision integral due to the Coulomb potential between the quasiparticles and the vector $\boldsymbol{G}_{u_{\alpha,\beta}}$ corresponds to the term proportional to $\boldsymbol{v}_{\lambda\boldsymbol{\alpha}}$ in the Boltzmann equation Eq. (9.12). The vector $\boldsymbol{\psi}^\alpha$ consists of the coefficients ψ_n and is given by $\boldsymbol{\psi}^\alpha = (\psi^\alpha_0, \psi^\alpha_1)$. (For simplicity it was assumed that the distribution function is time independent. However, a time dependence of the distribution function can easily be implemented in this procedure.) The explicit expressions of these terms can be found in App. B.2. Upon introducing dimensionless variables, $\Omega = \omega/T$, $x = \sqrt{1/(Tk_0)}\, k_x$, and $y = k_y/T$, the temperature dependence of the different terms are found

$$\begin{aligned} \mathcal{M}^{ee}_{nm,u_{x,y}} &= T^2 \left[\phi^{(m)}_{\lambda\boldsymbol{k}}\right] \left[\phi^{(n)}_{\lambda\boldsymbol{k}}\right] \mathcal{C}^{ee}_{nm,u_{x,y}} , \\ \mathcal{M}^{ee}_{nm,u_{y,x}} &= T^3 \left[\phi^{(m)}_{\lambda\boldsymbol{k}}\right] \left[\phi^{(n)}_{\lambda\boldsymbol{k}}\right] \mathcal{C}^{ee}_{nm,u_{y,x}} , \end{aligned} \tag{9.14}$$

and

$$\begin{aligned} G_{m,u_{x,y}} &= T\ [\phi^{(m)}_{\lambda\boldsymbol{k}}]\ \mathcal{G}_{m,u_{x,y}} , \\ G_{m,u_{y,x}} &= T^2\ [\phi^{(m)}_{\lambda\boldsymbol{k}}]\ \mathcal{G}_{m,u_{y,x}} , \end{aligned} \tag{9.15}$$

where $\mathcal{C}^{ee}_{nm,u_{x,y}}$, $\mathcal{C}^{ee}_{nm,u_{y,x}}$, $\mathcal{G}_{m,u_{x,y}}$, and $\mathcal{G}_{m,u_{y,x}}$ are numerical coefficients. The modes have the following temperature behavior $[\phi^{(0)}_{\lambda\boldsymbol{k}}] = [\lambda\epsilon_{\lambda\boldsymbol{k}}] = T$ and $[\phi^{(1)}_{\lambda\boldsymbol{k}}] = [\lambda] = 1$. Upon inverting the matrix equation Eq. (9.13), the coefficients ψ^β_n and their temperature dependence are determined. The components of the shear viscosity tensor can now be calculated by

$$\eta_{\alpha\beta\gamma\delta} = \sum_\lambda \int_{\boldsymbol{k}} \lambda v^\alpha_{\lambda\boldsymbol{k}} k_\beta \left(v^\gamma_{\lambda\boldsymbol{k}} k_\delta - \delta_{\gamma\delta} \frac{\epsilon_{\lambda\boldsymbol{k}}}{2} \right) g^\beta_{\lambda\boldsymbol{k}} f^{(0)}_{\lambda\boldsymbol{k}} (1 - f^{(0)}_{\lambda\boldsymbol{k}})/T . \tag{9.16}$$

The resulting shear viscosities at the charge neutrality point are given by

$$\eta_{\alpha\beta\gamma\delta} = N\ \mathcal{C}_{\alpha\beta\gamma\delta} \frac{k_0^2}{\hbar} \left(\frac{T}{vk_0} \right)^{\phi_{\alpha\beta\gamma\delta}} , \tag{9.17}$$

which are proportional to the fermionic flavor N and the numerical constants $\mathcal{C}_{\alpha\beta\gamma\delta}$ of order unity. The temperature of the viscosity coefficients η_{xyxy} and η_{yxyx} scale with the exponents

$$\begin{aligned} \phi_{xyxy} &= \frac{5}{2} + \frac{1}{2} \left(\gamma_{k_0} + 5\gamma_v \right) = \frac{5}{2} + \frac{1.02445}{N} , \\ \phi_{yxyx} &= \frac{1}{2} - \frac{1}{2} \left(3\gamma_{k_0} - \gamma_v \right) = \frac{1}{2} - \frac{0.17335}{N} . \end{aligned} \tag{9.18}$$

The remaining viscosity coefficients η_{ijkl} scale with the exponent

$$\phi_s = \frac{3}{2} - \frac{1}{2} \left(\gamma_{k_0} - 3\gamma_v \right) = \frac{3}{2} + \frac{0.4255}{N} , \tag{9.19}$$

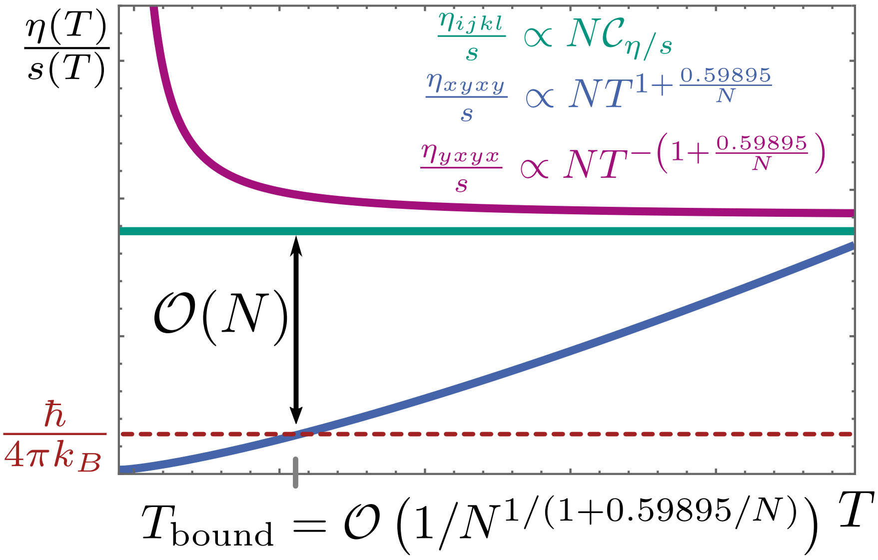

Figure 9.1: The temperature dependence of the ratio of the viscosity coefficients over the entropy is shown. The lower bound of this ratio [18] is given by the red dashed line. For most viscosity coefficients η_{ijkl} the ratio is proportional to N and thus constant, whereas for the coefficient η_{yxyx} the ratio diverges. For η_{xyxy} the ratio violates the lower bound at T_{bound}.

which is the same exponent governing the entropy as is shown in the next section. Note that we switched the notation from Greek to Roman letters. Every time this occurs, all viscosity coefficients but η_{xyyx} and η_{yxxy} are meant. The factors proportional to N^{-1} arise due to the renormalization group (RG) analysis. In order to characterize how perfect the fluid is, the viscosity coefficients are compared to the entropy of the system.

9.2.1 The lower bound

As seen in Sec. 3.6, the ratio of the viscosity over the entropy of the system indicates how perfect a fluid is. (A fluid whose viscosity is zero is referred to as a perfect fluid.) This ratio has an universal lower bound $\eta/s \geq \frac{\hbar}{4\pi k_{\text{B}}}$ which was derived by Kovtun, Son, and Starinets in Ref. 18 where they used the correspondence between strongly coupled gauge theories and gravity. For ADSs the entropy is (see Sec. 7.2.1)

$$s(T) \propto T^{\phi_s} \propto T^{\frac{3}{2}+\frac{0.4255}{N}} \,. \tag{9.20}$$

The ratio of the viscosity coefficients over the entropy is depicted in Fig. 9.1, where the red dashed line indicates the value of the lower bound. For most viscosity coefficients the ratio is constant. However, for the viscosity coefficient η_{yxyx} the ratio diverges at low temperatures with $T^{-(1+0.59895/N)}$ and even more fascinating, for the coefficient η_{xyxy} the ratio violates the lower bound at $T_{\text{bound}} = \mathcal{O}\left(1/(N^{1/(1+0.59895/N)})\right)$ and vanishes for decreasing temperatures as $T^{+(1+0.59895/N)}$. Hence, the ADSs are to our knowledge the first realization in condensed matter physics which violates the lower bound.

How can in the same material some viscosity coefficients fulfill the lower bound, while for one coefficient the ratio diverges and for another the lower bound is violated? To answer this question, the flow of different momentum components is studied. The viscosity tensor connects the dissipative part of the energy-stress tensor to the hydrodynamic velocity gradient, $\tau_{\alpha\beta} = \sum_{\gamma\delta} \eta_{\alpha\beta\gamma\delta} \partial u_\delta / \partial x_\gamma$, see Eq. (3.4). This velocity gradient $\partial u_\delta / \partial x_\gamma$ is depicted in Fig. 9.2 (0) by the purple arrows. Because of the gradient, the momentum component k_δ, which is parallel to u_δ, is transported with the velocity component $v^\gamma_{\lambda\boldsymbol{k}}$ into the γ-direction. Simultaneously, the momentum component k_β is transported with the velocity component $v^\alpha_{\lambda\boldsymbol{k}}$ into the α-direction. Due to the anisotropic energy dispersion shown by the equal energy contourplots in Fig. 9.2 (a)-(d), the velocity component $v^y_{\lambda\boldsymbol{k}}$ is larger than $v^x_{\lambda\boldsymbol{k}}$ for small temperatures. Hence, for the components η_{yxxy} the momentum k_x flows with $v^y_{\lambda\boldsymbol{k}}$ in the y-direction and the momentum k_y with $v^x_{\lambda\boldsymbol{k}}$ in the x-direction and similar behavior we see for η_{xyyx}. So both momentum components flow respectively with the smaller and the larger velocity component and thus do not violate the lower bound. In contrast, we find for η_{yxyx} that the momentum component k_x flows twice with the larger velocity $v^y_{\lambda\boldsymbol{k}}$ and thus the ratio diverges. While for η_{xyxy}, the momentum k_y flows twice with the smaller velocity $v^x_{\lambda\boldsymbol{k}}$ in the x-direction and thus violates the lower bound.

Another explanation can be given by studying the scaling of the viscosity, which is done in the next section.

9.2.2 Scaling of the viscosity tensor

Before we explore the scaling behavior of the viscosity of ADSs, let us repeat how this transport property behaves for isotropic systems as graphene. For graphene the viscosity and entropy scale as

$$\begin{aligned} \eta(T) &= \xi^{-2} \eta(Z_T T)\,, \\ s(T) &= \xi^{-2} s(Z_T T)\,. \end{aligned} \tag{9.21}$$

(see Sec. 3.4 for a detailed derivation of the viscosity's scaling in isotropic systems.) Since there is only one length scale $\xi = b = \mathrm{e}^l$ in the system, we find single-parameter scaling. The ratio η/s is scale invariant under a RG analysis because the two scaling factors $Z_\eta = \xi^{-2}$ and $Z_s = \xi^{-2}$ cancel each other. However, for ADSs the situation is a different one. The single parameter scaling breaks down due to the occurrence of the two different length scales arising from the anisotropic energy dispersion. The scaling factors of the different viscosity coefficients are given by

$$\begin{aligned} Z_{\eta_s} &= \xi_x^{-1} \xi_y^{-1}\,, \\ Z_{\eta_{xyxy}} &= \xi_x \xi_y^{-3}\,, \\ Z_{\eta_{yxyx}} &= \xi_x^{-3} \xi_y\,, \end{aligned} \tag{9.22}$$

while we find for the entropy the scaling factor

$$Z_s = \xi_x^{-1} \xi_y^{-1}\,. \tag{9.23}$$

The scaling factors Z_η are derived from the Kubo-formula for the viscosity coefficients, i. e., $\eta_{\alpha\beta\gamma\delta} = \omega \, \mathrm{Im} \left\langle [\mathcal{J}_{\alpha\beta}, \mathcal{J}_{\gamma\delta}] \right\rangle$. Thereby, the scaling factor of the total strain generator $\mathcal{J}_{\alpha\beta}$ is equal to the particle density times the scaling of the space coordinate x_α and the momentum p_β, since the total strain generator only differs from the particle density by the product of x_α and p_β, i. e., $\mathcal{J}_{\alpha\beta} = \int_{\boldsymbol{x}} \hat{\psi}^\dagger_{\boldsymbol{x}} x_\alpha p_\beta \hat{\psi}_{\boldsymbol{x}}$. The detailed derivation can be found in App. B.1.2. Hence, the ratio of the viscosity coefficient over entropy for ADSs is determined by the following quotient of the two length scales

$$\frac{\eta_{\alpha\beta\gamma\delta}}{s} \propto N \frac{\hbar}{k_\mathrm{B}} \left(\frac{\xi_x}{\xi_y} \right)^{\varphi}\,, \tag{9.24}$$

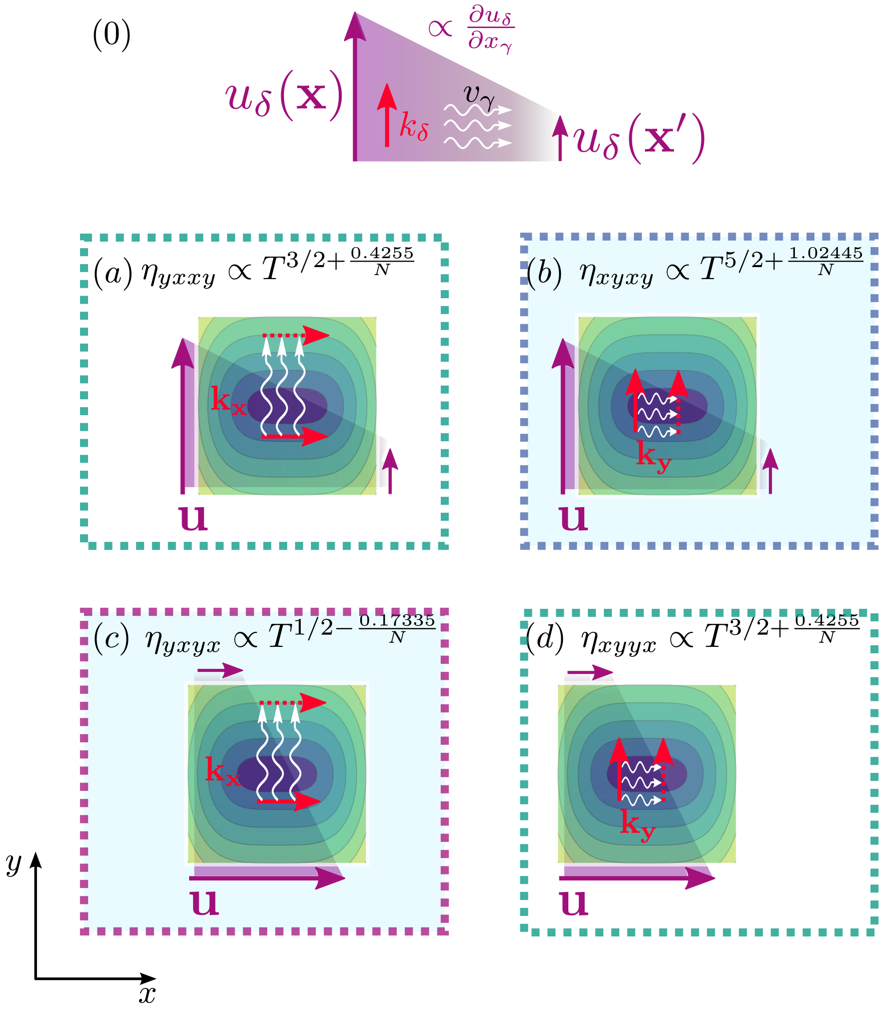

Figure 9.2: The momentum flow of the different viscosity coefficients is shown. Panel (0) shows one part of the momentum flow due to the velocity gradient $\partial u_\delta/\partial x_\gamma$ which is implicit assumed in the panels (a) to (d), where the momentum k_δ flows with $v^\gamma_{\lambda\boldsymbol{k}}$ in the γ-direction. Simultaneously the momentum k_β (red arrows) flow with the velocity component $v^\alpha_{\lambda\boldsymbol{k}}$ (white, wiggled line) in the α-direction. For the coefficient η_{yxyx} the ratio diverges, while η_{xyxy} violates the lower bound. Note that in panel (a) and (b) the velocity gradient $\partial u_y/\partial x_y$ is applied, while in the panels (c) and (d) we find the velocity gradient $\partial u_x/\partial x_x$.

where we find $\varphi = 0$, 2, and -2 depending on the values for $\alpha, \beta, \dots \in \{x, y\}$. For $\varphi = 0$, the ratio is constant, while we find $\varphi = -2$ for the diverging coefficient η_{yxyx} and $\varphi = 2$ for the coefficient violating the lower bound.

9.3 ...in the collisionless regime

Let us now investigate the viscosity tensor at the charge neutrality point in the collisionless regime. In the collisionless regime the excitation frequency is the fastest time scale, i. e., $\omega \gg \tau^{-1}$, while in the hydrodynamic regime it is the scattering time, i. e., $\tau^{-1} \gg \omega$. We use the Kubo-formula to determine the viscosity tensor which is given for finite frequencies by

$$\eta_{\alpha\beta\gamma\delta} \propto \frac{\operatorname{Im} \chi_{\tau_{\alpha\beta}\tau_{\gamma\delta}}}{\omega} \,, \tag{9.25}$$

where $\chi_{\tau_{\alpha\beta}\tau_{\gamma\delta}}$ is the correlation function between two energy-stress tensors. For non-interacting anisotropic Dirac fermions the correlation function is given by the bare bubble diagram which is

$$\chi_{\tau_{\alpha\beta}\tau_{\gamma\delta}} = NT \sum_n \int_{\boldsymbol{k}} \operatorname{Tr}\left(T_{\alpha\beta} G_{\boldsymbol{k},\mathrm{i}\omega_n} T_{\gamma\delta} G_{\boldsymbol{k},\mathrm{i}(\omega_n+\Omega_m)} \right) \,, \tag{9.26}$$

with the Matsubara Green's function given in Eq. (7.16) and the energy-stress tensor defined in Eq. (9.5). Upon evaluating the correlation function by analytical continuation and taking the imaginary part, we find for the different viscosity coefficients the following expressions

$$\eta_{xxxx} = +\sqrt{\frac{k_0}{v}} \frac{1}{v} \frac{K(-1)}{21\sqrt{2}\pi} \, \omega^{3/2} \left[f^{(F)}_{-\omega/2} - f^{(F)}_{\omega/2} \right] , \tag{9.27}$$

$$\eta_{yyyy} = +\sqrt{\frac{k_0}{v}} \frac{1}{v} \frac{K(-1)}{84\sqrt{2}\pi} \, \omega^{3/2} \left[f^{(F)}_{-\omega/2} - f^{(F)}_{\omega/2} \right] , \tag{9.28}$$

$$\eta_{xxyy} = -\sqrt{\frac{k_0}{v}} \frac{1}{v} \frac{K(-1)}{42\sqrt{2}\pi} \, \omega^{3/2} \left[f^{(F)}_{-\omega/2} - f^{(F)}_{\omega/2} \right] , \tag{9.29}$$

$$\eta_{xyxy} = \left(\sqrt{\frac{v}{k_0}} \frac{1}{v^3} \frac{15\sqrt{\pi}}{1024\Gamma\left(\frac{9}{4}\right)\Gamma\left(\frac{13}{4}\right)} \, \omega^{5/2} + \sqrt{\frac{k_0}{v}} \frac{1}{v} \frac{\Gamma\left(\frac{5}{4}\right)^2}{16\pi^{3/2}} \, \omega^{3/2} \right) \left[f^{(F)}_{-\omega/2} - f^{(F)}_{\omega/2} \right] , \tag{9.30}$$

$$\eta_{yxyx} = \left(\sqrt{\frac{k_0}{v}} k_0 \frac{3\sqrt{\pi}}{20\Gamma\left(\frac{1}{4}\right)^2} \, \omega^{1/2} + \sqrt{\frac{k_0}{v}} \frac{1}{v} \frac{\Gamma\left(\frac{5}{4}\right)^4}{\pi^{3/2}\Gamma\left(\frac{1}{4}\right)^2} \, \omega^{3/2} \right) \left[f^{(F)}_{-\omega/2} - f^{(F)}_{\omega/2} \right] , \tag{9.31}$$

$$\eta_{xyyx} = -\sqrt{\frac{k_0}{v}} \frac{1}{v} \frac{37\Gamma\left(\frac{5}{4}\right)}{672\sqrt{2\pi}\Gamma\left(\frac{3}{4}\right)} \, \omega^{3/2} \left[f^{(F)}_{-\omega/2} - f^{(F)}_{\omega/2} \right] , \tag{9.32}$$

where $f^{(F)}_{\lambda\omega} = (1 + \mathrm{e}^{\lambda\omega/(k_\mathrm{B}T)})^{-1}$ is the Fermi-Dirac function and $K(x)$ is the complete elliptic integral of the first kind. Let us first focus on the first three components of the viscosity tensor η_{xxxx}, η_{yyyy}, and η_{xxyy}. These three coefficients determine the bulk viscosity ζ of the system, since it is $\zeta = \eta_{xxxx} + \eta_{yyyy} + 2\eta_{xxyy}$. Hence, the ADSs have a finite bulk viscosity with $\zeta = \sqrt{\frac{k_0}{v}} \frac{1}{v} \frac{K(-1)}{84\sqrt{2}\pi} \, \omega^{3/2}$ at zero temperature. This stands in contrast to graphene which has no bulk viscosity but only a shear viscosity. Furthermore, the components η_{xyxy} and η_{yxyx}, for which in the hydrodynamic regime the ratio of η/s is either diverging or vanishing, have an additional factor proportional to $\omega^{3/2}$. This additional factor originates in interband processes which are not taken into account in the hydrodynamic regime. However, the energy-stress tensor $T_{\alpha\beta}$ derived from the total strain generator, $\mathcal{J}_{\alpha\beta} = \mathcal{L}_{\alpha\beta} + \mathcal{S}_{\alpha\beta}$, includes both inter- and intraband processes. Upon applying the RG analysis of Sec. 7.2.1 to the above viscosity coefficient, the same exponents are found as in the hydrodynamic regime. It is

$$\begin{aligned}\phi_s &= \frac{3}{2} + \frac{1}{2}\Big(3\gamma_v - \gamma_{k_0}\Big) = \frac{3}{2} + \frac{0.4255}{N}\\ \phi_{xyxy} &= \frac{5}{2} + \frac{1}{2}\Big(5\gamma_v + \gamma_{k_0}\Big) = \frac{5}{2} + \frac{0.14455}{N}\\ \phi_{yxyx} &= \frac{1}{2} + \frac{1}{2}\Big(\gamma_v - 3\gamma_{k_0}\Big) = \frac{1}{2} - \frac{0.17335}{N}\,.\end{aligned} \tag{9.33}$$

For the viscosity coefficients with the exponent 3/2 and 5/2, the viscosity coefficients grow faster with increasing frequencies due to the additional factor exhibited by the Coulomb interaction. Whereas, the viscosity coefficient with the exponent 1/2 grows more slowly with increasing frequency due to the Coulomb interaction.

9.4 Navier-Stokes equation

How can the viscosity coefficients be measured? What is the influence of the viscosity on the dynamics of the fluid? To answer these questions, the quantum Boltzmann equation is used to set the particle density n, the energy density n_ϵ, and the momentum density $n_{\boldsymbol{k}}$ into relation to their respective current. The continuity equation of the momentum density is known as Navier-Stokes equation. The Navier-Stokes equation governs the flow dynamics of a fluid and determines if the flow is laminar or turbulent. Thus, let us derive this important equation in this section. We start by defining the different densities. The number of carriers in the upper and lower energy band is given by

$$n_+ = N\int_{\boldsymbol{k}} f_{+\boldsymbol{k}} \qquad \text{and} \qquad n_- = N\int_{\boldsymbol{k}} f_{-\boldsymbol{k}}\,, \tag{9.34}$$

with the total charge (or carrier) density $n = n_+ - n_-$ and the "imbalace" density $n_I = n_+ + n_-$ which corresponds to the total number of quasiparticles. The energy density n_ϵ and the momentum density $n_{\boldsymbol{k}}$ are

$$n_\epsilon = N\sum_\lambda\int_{\boldsymbol{k}} \epsilon_{\lambda\boldsymbol{k}} f_{\lambda\boldsymbol{k}} - n_{\epsilon 0} \qquad \text{and} \qquad n_{\boldsymbol{k}} = N\sum_\lambda\int_{\boldsymbol{k}} \boldsymbol{k} f_{\lambda\boldsymbol{k}} \tag{9.35}$$

with $n_{\epsilon 0} = N\int_{\boldsymbol{k}} \epsilon_{-\boldsymbol{k}}$ being the energy of a filled valence band. Upon multiplying the quantum Boltzmann equation by the momentum $\boldsymbol{k}$ and the energy $\epsilon_{\lambda\boldsymbol{k}}$ and summing and integrating over the band index and the momentum respectively, the following continuity equations for the different densities are obtained

$$\partial_t n + \boldsymbol{\nabla}_{\boldsymbol{r}}\cdot\boldsymbol{j} = 0, \tag{9.36a}$$

$$\partial_t n_\epsilon + \boldsymbol{\nabla}_{\boldsymbol{r}}\cdot\boldsymbol{j}_\epsilon = e\boldsymbol{E}\cdot\boldsymbol{j}, \tag{9.36b}$$

$$\partial_t n_{\boldsymbol{k}}^\alpha + \nabla_{\boldsymbol{r}}^\beta \Pi_{\beta\alpha} - enE^\alpha - \frac{e}{c}\big[\boldsymbol{j}\times\boldsymbol{B}\big]^\alpha = -\frac{n_{\boldsymbol{k}}^\alpha}{\tau_{\text{dis}}}. \tag{9.36c}$$

In the first continuity equation Eq. (9.36a) the total charge n of the system is conserved and the time derivative of the total charge density is set equal to the divergence of the electrical current. The total charge carrier density can only change, if the electrical current flows in or out of a certain volume. The second continuity equation Eq. (9.36b) relates the energy density n_ϵ and the energy current j_ϵ to the product of the electrical current $\boldsymbol{j}$ with the electrical field $\boldsymbol{E}$. The last equation Eq. (9.36c) is the continuity equation of the α-component of momentum density $\boldsymbol{n_k}$. Here, the time derivative of the momentum density is not only equal to the divergence of the energy-stress tensor $\Pi_{\alpha\beta}$, but also depends on the product of the particle density with the α-component of the electrical field and on the cross product of the electrical current with the magnetic field[2]. In the following, we want to express the densities and currents by the hydrodynamic velocity $\boldsymbol{u}$ (which is also called drift velocity) and the pressure P of the system. Therefore, for simplicity the magnetic field $\boldsymbol{B}$ is set to zero and we assume that the ADSs are pristine, i. e., $\tau_{\text{dis}}^{-1} = 0$. The drift velocity enters the calculation by the local equilibrium distribution function which is given by $f^{(0)}_{\lambda\boldsymbol{k}}(\boldsymbol{r}) = \left(1 + \exp\left[\frac{\epsilon_{\lambda\boldsymbol{k}} - \mu_\lambda(\boldsymbol{r}) - \boldsymbol{u}(\boldsymbol{r})\cdot\boldsymbol{k}}{T(\boldsymbol{r})}\right]\right)^{-1}$. In order to evaluate the different densities and currents, this local equilibrium distribution function is expanded in a power series in $\boldsymbol{u}$, where $\boldsymbol{u}$ is small compared to either v or the velocity of the parabolic direction. It holds

$$f^{(0)}_{\lambda\boldsymbol{k}} \approx f^{(F)}_{\lambda\boldsymbol{k}} - \boldsymbol{u}\cdot\boldsymbol{k}\frac{\partial f^{(F)}_{\lambda\boldsymbol{k}}}{\partial\epsilon_{\lambda\boldsymbol{k}}} + \frac{1}{2}\left(\boldsymbol{u}\cdot\boldsymbol{k}\right)^2\frac{\partial^2 f^{(F)}_{\lambda\boldsymbol{k}}}{\partial\epsilon^2_{\lambda\boldsymbol{k}}} + \cdots\,. \tag{9.37}$$

At the charge neutrality point we find for the imbalance density and the energy density

$$n_I = N\frac{2\sqrt{k_0}}{\pi^2 v^{3/2}}K(-1)X_{1/2}\,T^{3/2} \qquad \text{and} \qquad n_\epsilon = N\frac{2\sqrt{k_0}}{\pi^2 v^{3/2}}K(-1)X_{3/2}\,T^{5/2}\,, \tag{9.38}$$

with $X_{1/2} = \frac{1}{2}\left(1 - \sqrt{\frac{\pi}{2}}\zeta(3/2)\right)$, $X_{3/2} = \frac{3}{4}\left(1 - \frac{\sqrt{2}}{4}\right)\sqrt{\pi}\zeta(5/2)$, and K being the complete elliptic integral of the first kind. We see that the imbalance density is proportional to $T^{3/2}$, while the energy density has a $T^{5/2}$ temperature dependence. Now, for the momentum density of ADSs it is

$$n^x_{\boldsymbol{k}} = m_* n_I\; u_x \qquad \text{and} \qquad n^y_{\boldsymbol{k}} = \frac{5}{3v}n_\epsilon\; u_y\,, \tag{9.39}$$

with $m_* = 3[E(-1) - K(-1)]/K(-1)m \approx 1.37m$. The two components of the momentum density have a different temperature behavior exhibited due to the anisotropy of the energy spectrum. Next, we focus on the currents of the ADSs. They are given by the expression

$$\boldsymbol{j} = n\boldsymbol{u} + \delta\boldsymbol{j} \qquad \text{and} \qquad \boldsymbol{j}_\epsilon = \frac{5}{3}n_\epsilon\boldsymbol{u} + \delta\boldsymbol{j}_\epsilon\,, \tag{9.40}$$

where $\delta\boldsymbol{j}$ and $\delta\boldsymbol{j}_\epsilon$ are the dissipative corrections to the (energy-) current defined by the out-of-equilibrium distribution function $\delta f_{\lambda\boldsymbol{k}}$. What still remains to be expressed by the densities and the drift velocity is the energy-stress tensor of the ADSs which was defined in Eq. (9.9) with $\Pi_{\alpha\beta} = N\sum_\lambda\int\frac{d^2k}{(2\pi)^2}\boldsymbol{v}_{k\boldsymbol{\alpha}}k^\beta f_{\lambda\boldsymbol{k}}$. This energy-stress tensor can be related to the pressure of the systems, as seen

---

[2] The minus sign before the terms proportional to the electrical and the magnetic field in Eq. (9.36c) arises due to integration-by-parts of the Boltzmann equation

in Sec. 3.2, by $P = \frac{1}{2}\,\mathrm{Tr}\,\Pi_{\alpha\beta} - \boldsymbol{n_k} \cdot \boldsymbol{u}$. Hence, under the assumption of local equilibrium, the energy-stress tensor is given by

$$\begin{aligned}
\Pi_{xx} &= \frac{2}{3}n_\epsilon + \frac{3}{2}m_* n_I u_x^2 + \frac{5}{6v^2}n_\epsilon u_y^2 + \tau_{xx} = P + m_* n_I u_x^2 + \tau_{xx} \\
\Pi_{yy} &= \frac{2}{3}n_\epsilon + \frac{1}{2}m_* n_I u_x^2 + \frac{5}{2v^2}n_\epsilon u_y^2 + \tau_{yy} = P + \frac{5}{3v^2}n_\epsilon u_y^2 + \tau_{yy} \\
\Pi_{xy} &= m_* n_I u_x u_y + \tau_{xy} \\
\Pi_{yx} &= \frac{5}{3v^2}n_\epsilon u_x u_y + \tau_{yx} \,,
\end{aligned} \tag{9.41}$$

where $\tau_{\alpha\beta}$ is the dissipative part of the energy-stress tensor which is proportional to the gradient of the drift velocity and to the viscosity tensor. Upon inserting these definitions into the continuity equation of the momentum density Eq. (9.36c) and applying the remaining continuity equations Eq. (9.36), we find the Navier-Stokes equation. If the system flows with u_x along the parabolic dispersion, the Navier-Stokes equation is

$$m_* \; n_I \left(\partial_t u_x + \sum_\gamma u_\gamma \partial_\gamma u_x \right) + \partial_x P = \mathcal{F}_{s,x} + eE_x n + \sum_\gamma m_* \; n_I \; \partial_{x_\gamma} \delta j_\gamma \,, \tag{9.42}$$

with $\mathcal{F}_{s,\alpha} = \sum_\beta \partial_\beta \tau_{\beta\alpha} = \sum_{\beta\gamma\delta} \partial_\beta \eta_{\beta\alpha\gamma\delta} \frac{\partial u_\delta}{\partial x_\gamma}$. Here, $\mathcal{F}_{s,\alpha}$ is the dissipative Stokes-force and it is defined as the gradient of the dissipative part of the energy-stress tensor. This Navier-Stokes equation for the velocity component u_x has the same form as a Naiver-Stokes equation of a Galilean invariant system [43]. The velocity terms are multiplied by the mass m_* of the parabolic energy dispersion and the imbalance density. However, the Navier-Stokes equation of u_y shows relativistic characteristics with

$$w \left(\partial_t u_y + \sum_\gamma u_\gamma \partial_\gamma u_y \right) + \partial_y P + u_y \partial_t P = \mathcal{F}_{s,y} + en \left(E_y - u_y \sum_\gamma u_\gamma E_\gamma \right) - \sum_\gamma u_y E_\gamma \delta j_\gamma + \sum_\gamma u_y \partial_{x_\gamma} \delta j_{\epsilon,\gamma} \,. \tag{9.43}$$

As in graphene [20, 21] which is, as previously shown, a relativistic system, the additional time derivative of the pressure appears. Furthermore, the velocity terms on the left-hand side of the equation are now multiplied by the enthalpy density, $w = n_\epsilon + P$, instead of $m_* n_I$. This enthalpy density can be related by the Gibbs-Duhem relation to the entropy of the system at the charge neutrality point, i. e., $w = Ts$. These two equations will rule the flow dynamics of our quasi-particle fluid. Due to the smallness of the viscosity coefficient η_{xyxy} for small temperatures, turbulent flow dynamic is expected as well as an extreme sensitivity to boundary conditions. A further analysis of the Navier-Stokes equation will give access to experimentally measurable quantities which are sensitive to the different viscosity coefficients and to the violation of the lower bound. One of these quantities are the shear modes with the corresponding shear frequencies depicted in Fig. 9.3. If the incident momentum is pointing along the "relativistic" y-direction, the two shear frequencies $\omega_+ = \mathrm{i} q_y \eta_{yxyx}/(m_* n_I) \propto 1/T$ and $\omega_- = \mathrm{i} q_y v^2 \eta_{yyyy}/(Ts) \propto 1/T$ are proportional to the inverse temperature. These viscosity coefficients do not violate the lower bound. However, for incident momenta pointing along the "parabolic" x-direction the two shear frequencies $\omega_+ = \mathrm{i} q_x^2 \eta_{xxxx}/(m_* n_I)$ and $\omega_- = \mathrm{i} q_x^2 v^2 \eta_{xyxy}/(Ts)$ are constant. Hence, the temperature independence of the shear frequency ω_- is a consequence of the violation of

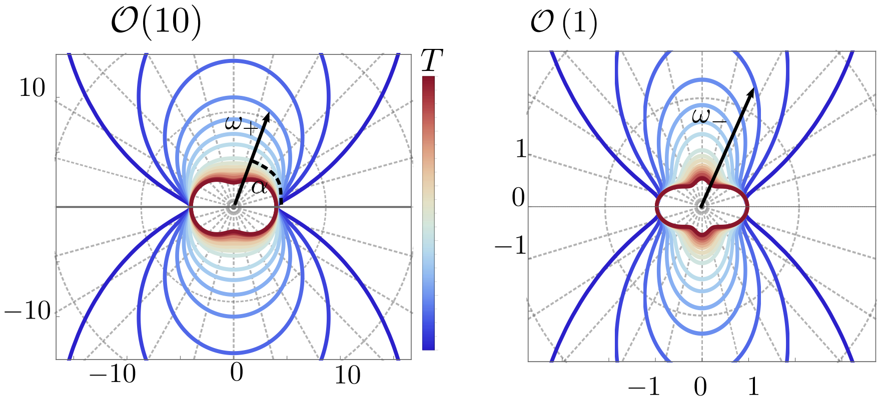

Figure 9.3: This figure shows the polar plot of the shear frequencies ω_+ and ω_- for different temperatures and the absolute value of the momentum $\boldsymbol{q} = 1$. The shear frequencies are constant for incident q_x momentum and are proportional to the inverse temperature if the momentum is aligned along the y-direction.

the lower bound. The explicit formula of the shear frequencies for general incident momenta is

$$\begin{aligned}\omega_\pm =& \mathrm{i}\frac{q_x^2}{2}\left(\frac{v^2\eta_{xyxy}}{sT}+\frac{\eta_{xxxx}}{m_* n_I}\right)+i\frac{q_y^2}{2}\left(\frac{v^2\eta_{yyyy}}{sT}+\frac{\eta_{yxyx}}{m_* n_I}\right)\\ &\pm\mathrm{i}\frac{1}{2m_* n_I sT}\Bigg[4(\eta_{xxyy}+\eta_{yxxy})(\eta_{yyxx}+\eta_{xyyx})m_* n_I q_x^2 q_y^2 v^2 sT\\ &+\Big(q_x^2(\eta_{xxxx}sT-\eta_{xyxy}v^2 m_* n_I)+q_y^2(\eta_{yxyx}sT-\eta_{yyyy}v^2 m_* n_I)\Big)^2\Bigg]^{1/2}.\end{aligned} \tag{9.44}$$

Another way to measure the viscosity coefficients individually is to apply external pressure and use the relation $\partial_\alpha P = \sum_{\beta\gamma\delta}\partial_\beta\eta_{\beta\alpha\gamma\delta}\partial u_\delta/\partial x_\gamma$ to analyze the anisotropic version of the Poiseuille flow.

9.5 Summary

In this chapter the viscosity tensor of ADSs was investigated both in the hydrodynamic and in the collisionless regime. In the hydrodynamic regime the components of the viscosity tensor are given by

$$\eta_{\alpha\beta\gamma\delta} = N\mathcal{C}_{\alpha\beta\gamma\delta}\frac{k_0^2}{\hbar}\left(\frac{T}{vk_0}\right)^{\phi_{\alpha\beta\gamma\delta}}, \tag{9.45}$$

where $\mathcal{C}_{\alpha\beta\gamma\delta}$ are numerical coefficients and the exponents have the form

$$\begin{aligned}\phi_{xyxy} &= \frac{5}{2}+\frac{1}{2}\left(\gamma_{k_0}+5\gamma_v\right)=\frac{5}{2}+\frac{1.02445}{N},\\ \phi_{yxyx} &= \frac{1}{2}-\frac{1}{2}\left(3\gamma_{k_0}-\gamma_v\right)=\frac{1}{2}-\frac{0.17335}{N}\\ \phi_s &= \frac{3}{2}-\frac{1}{2}\left(\gamma_{k_0}-3\gamma_v\right)=\frac{3}{2}+\frac{0.4255}{N}.\end{aligned} \tag{9.46}$$

The viscosity coefficient η_{xyxy} violates the famous lower bound of $\eta/s \geq \hbar/(4\pi k_\mathrm{B})$ [18] for low temperatures due to the breakdown of the single parameter scaling. The actual bound for the matrix elements should be

$$\frac{\eta_{\alpha\beta\gamma\delta}}{s} \geq \frac{\hbar}{4\pi k_\mathrm{B}} \left(\frac{\xi_x}{\xi_y} \right)^{\varphi} \tag{9.47}$$

with $\varphi = -2, 0, 2$ depending on the values for $\alpha, \beta \cdots \in \{x, y\}$. This is to our knowledge the first condensed matter realization which violates the lower bound. Furthermore, the Navier-Stokes equation was derived for ADSs. The anisotropy of the energy dispersion propagates to this equation, since the u_x component of the drift velocity obeys a Navier-Stokes equation of a Galilean invariant system whereas the u_y component has a relativistic Navier-Stokes equation. The smallness of the viscosity coefficient will lead to extreme turbulent flow dynamics. The different components of the viscosity tensor will become experimentally accessible by studying the shear frequencies of the system.

In the collisionless regime the temperature dependence of the viscosity tensor is replaced by a frequency dependence. The components η_{xyxy} and η_{yxyx} gain an additional term proportional to ω^{ϕ_s} due to interband processes which are not taken into account in the hydrodynamic regime.

Conclusions

This thesis is devoted to the ***Transport in isotropic and anisotropic Dirac systems*** where we focused on the *electrical conductivity* σ and the *viscosity* η in the *collisionless* ($\omega \gg \tau^{-1}$) and in the *hydrodynamic regime* ($\omega \ll \tau^{-1}$) and determined the influence of the *Coulomb interaction* on them.

These transport properties behave very differently in the two regimes, since the physical processes dominating the transport of the quasiparticles are quite distinct in the corresponding regimes. In the *hydrodynamic regime*, $\omega \ll \tau^{-1}$, the relaxation time τ due to collisions is the fastest time scale and hence collision processes dominate the transport. On the other hand, in the *collisionless regime*, $\omega \gg \tau^{-1}$, the excitation frequency sets the fastest time scale and collision processes can be neglected. The two regimes are accessed by different methods: the hydrodynamic regime by the Boltzmann equation, and the collisionless regime by the Kubo formalism.

However, the two different regimes are not the only aspect of transport between we want to distinguish. The nature of the transport described by the *electrical conductivity* and the *viscosity* is a very different one and we elaborate this in more detail.

The *electrical conductivity* σ describes how the quasiparticles in a material behave in the presence of an applied electric field. It is a very important quantity which characterizes different materials, since it can be used to distinguish between insulators, semi-conductors, and metals. We showed that the electrical conductivity for a two dimensional (2D) system is scale invariant by using the Ward identity which describes the charge conservation of the system. The consequence of this scale invariance is that in a renormalization group (RG) analysis, the conductivity turns out to be independent of the rescaled temperature and the rescaled frequency.

The other important transport quantity is the *viscosity* η. The viscosity of a fluid describes energy dissipation due to internal friction between particles with different velocities. It plays an important role in the dynamical behavior of a fluid. Since the quasiparticles in a material can be described under certain conditions (very clean sample and no phonons in the material) as a fluid, the viscosity determines the dynamics of the quasiparticle fluid. If the viscosity of a system is very small, the flow dynamics become turbulent. The quantity which indicates whether the viscosity is large or not is the ratio of viscosity over entropy. Kovtun *et al.* postulated that this ratio has a lower bound [18] which can be understood as a lower bound to the validity of the quasiparticle picture. Up till now, all condensed matter systems fulfilled the lower bound and only some systems in cosmology [52–57] and ultra cold gases [58, 59] violated it. With the anisotropic Dirac system, we found the first condensed matter realization which violates the lower bound.

Furthermore, the viscosity is a rank four tensor which relates the gradient of the drift velocity to the energy-stress tensor $T_{\alpha\beta}$. Bradlyn *et al.* [42] showed that this energy-stress tensor is equal to the time derivative of the total strain generator $\mathcal{J}_{\alpha\beta}$, i. e., $T_{\alpha\beta} = -\partial_t \mathcal{J}_{\alpha\beta}$. The strain generators are the generators of the unitary transformation which describes the deformation of the fluid. Bradlyn *et al.* showed that the strain generator acting on the spatial coordinates is given by $\mathcal{L}_{\alpha\beta} = \{x_\alpha, p_\beta\}/2$. In this work, we extended this description to lattices with a pseudospin which describes the multi-atomic basis of a lattice. We show that the strain generator $\mathcal{S}_{\alpha\beta}$ acting on the pseudospin space is crucial in order to fulfill the symmetry properties of the viscosity tensor that are expected for a rotationally invariant system, as was demonstrated using graphene as an example. Hence, the total strain generator consists of a contribution acting on the spatial coordinates, while the other acts in the pseudospin space, i. e.,

$$\begin{aligned}\mathcal{J}_{\alpha\beta} &= \mathcal{L}_{\alpha\beta} + \mathcal{S}_{\alpha\beta} \\ &= \{x_\alpha, p_\beta\}/2 + \mathrm{i}[S_\alpha, S_\beta]/2\,.\end{aligned} \tag{10.1}$$

After setting the stage, we now turned to the question why the electrical conductivity and the viscosity are investigated in *isotropic and anisotropic Dirac systems* (ADSs). The special feature of the Dirac systems is their energy spectrum. The energy dispersion is linear and gapless which leads to quasi-relativistic behavior of these systems. The system is *quasi*-relativistic, since the particles move with the Fermi velocity v_F and not with the speed of light c. This leads to the fact that the Coulomb interaction can be regarded as instantaneous. The effect of the linear energy dispersion relation is seen in the transport properties and a summary of the results in the different regimes is shown in Fig. 10.1 where the transport properties colored in gray recapitulate results obtained by other authors, whereas the results marked in black present my own work.

Graphene A very important example for an isotropic Dirac system is graphene whose transport properties are studied in this thesis. Graphene is a fascinating material due to its many beautiful properties. It is the thinnest material of the world consisting only of one layer of carbon atoms, has a very high charge carrier density at room temperature, has a high transmissivity of light [22], and is very strong and very flexible.

In the *hydrodynamic regime*, where the Coulomb interaction is responsible for the scattering processes, Fritz *et al.* [120] found that the collinear scattering regime exhibits a logarithmic divergence in the collision integral which leads to the fact that only a few modes, such as the energy and the band index, are needed to describe the hydrodynamics in graphene. Furthermore, they find that the conductivity depends on the inverse of the coupling squared constant and higher correction terms in the coupling constant are of order $\mathcal{O}([\log\alpha(T)]^{-1})$, i. e.,

$$\sigma(T) = \frac{0.760}{\alpha(T)^2}\frac{e^2}{h}\,, \tag{10.2}$$

with the renormalized coupling constant $\alpha(T) = \alpha/(1+\frac{1}{4}\alpha\log(\Lambda/T))$. Furthermore, Müller *et al.* [19] showed that the quasiparticles in graphene behave as a nearly perfect fluid. The ratio of viscosity over entropy

$$\eta(T)/s(T) = \frac{0.00815}{\alpha(T)^2} \tag{10.3}$$

approaches the lower bound with increasing temperature. A consequence of this behavior is that the flow dynamics are very sensitive to boundary conditions and that vortices for the viscous flow are to be expected [31].

In this thesis, we complete the picture of transport in graphene by the calculation of the two transport properties in the collisionless regime. In the *collisionless regime*, the *electrical conductivity* of graphene behaves differently than in the hydrodynamic regime. Most notably, we resolve a long controversy about the question how the Coulomb interaction influences the optical conductivity of graphene. Details on our calculation can be found in Ref. 16. Different groups studied this question and found (at the end) two different answers to this question, namely two different values of the correction coefficient $\mathcal{C}_\sigma$ of the optical conductivity to leading order in the coupling constant, i. e.,

$$\sigma(\omega) = \frac{e^2}{4\hbar}\left(1 + \mathcal{C}_\sigma\ \alpha(\omega)\right) , \tag{10.4}$$

where $\alpha(\omega) = \alpha/(1 + \frac{1}{4}\alpha \log(\Lambda/\omega))$ is the renormalized coupling constant. The origin of these different values for the same physical quantity lies in the fact that the different Feynman diagrams contributing to the correction coefficient –the self-energy diagram and the vertex diagram– are individually logarithmically divergent upon evaluating them within the Dirac model and hence need to be regularized. However, the different regularization schemes yield different results and it is by no means obvious which regularization scheme is the correct one. In order to settle this question, we implemented a tight-binding calculation of the correction coefficient, since in the tight-binding description the lattice constant automatically regularizes the Feynman diagrams. Furthermore, we showed where some of the regularization schemes used in the Dirac model went wrong and which subtleties needed to be taken into account, where we proceeded as follows. First, we studied the non-interacting optical conductivity in the tight-binding description and found that the conductivity has an additional frequency-dependent correction

$$\sigma^{(0)}(\omega) = \frac{e^2}{4\hbar}\left[1 + \frac{1}{9}\left(\frac{\omega}{t}\right)^2\right] , \tag{10.5}$$

where t is the hopping constant. Here, we corrected the result for the optical conductivity obtained by Stauber *et al.* [101], who predicted the prefactor of the frequency correction to be $1/36$ instead of $1/9$. Then, we determined the self-energy diagram and the vertex diagram in the tight-binding description and found that the value of the correction coefficient $\mathcal{C}_\sigma$ is

$$\mathcal{C}_\sigma = \frac{19 - 6\pi}{12} \simeq 0.01 . \tag{10.6}$$

Moreover, we showed that this value is universal and does not depend on microscopic quantities such as the size of the Wannier orbitals of the carbon atoms. Furthermore, we demonstrated how the dimensional regularization (DR) scheme is used correctly when the correction coefficient is calculated in the Dirac model. Either the DR has to be combined with a continuum-renormalization scheme, the minimal subtraction scheme, when no UV cut-off is introduced to the system. Alternatively, the DR can be combined with the Wilson RG which has an implicit UV cut-off. If the latter is the case, the UV cut-off has to be kept till the very end of the calculation in order to avoid the UV quirk.

Now let us return to the question how the Coulomb potential influences the optical conductivity. We have evaluated that the correction coefficient has the value $\mathcal{C}_\sigma \simeq 0.01$ and thus is quite small. Hence, the influence of the Coulomb interaction is relatively small besides the logarithmic correction of the coupling constant.

But this is not the case for all transport quantities in graphene. Indeed, we found that the Coulomb interaction has a big influence for the *viscosity* η in the *collisionless regime*. To demonstrate this, we used that fact that the viscosity can be calculated as the correlation function between two energy-stress tensors over the frequency. In the course of the calculation, it became clear that there has to be a strain generator acting in the pseudospin space of graphene in order to obtain the correct symmetric form of the energy-stress tensor and thus a viscosity tensor which has the symmetry properties of a rotationally invariant system. We found that the viscosity of graphene described by non-interacting Dirac fermions is proportional to the frequency squared,

$$\eta^{(0)}(\omega) = \frac{\omega^2}{64}\frac{\hbar}{v_{\mathrm{F}}} . \tag{10.7}$$

In order to determine the influence of the Coulomb interaction, the correction coefficient $\mathcal{C}_\eta$ is calculated using the same approach as in the determination of $\mathcal{C}_\sigma$ of the optical conductivity in the Dirac model. A special feature in the determination of the correction coefficient $\mathcal{C}_\eta$ for the viscosity is that –in addition to the self-energy diagram and the vertex diagram– a third diagram is needed to cancel the logarithmic divergences of the individual diagrams. This third diagram is dubbed the honey diagram and describes the interacting part of the energy-stress tensor. We find

$$\eta(\omega) = \frac{\omega^2}{64}\frac{\hbar}{v_\mathrm{F}}\left(1 + \frac{89 - 20\pi}{40}\alpha(\omega)\right) , \tag{10.8}$$

where the correction coefficient has the value $\mathcal{C}_\eta = (89 - 20\pi)/40 \simeq 0.65$ and is thus quite large. In conclusion, the viscosity is a transport quantity which is, in contrast to the optical conductivity, greatly influenced by the Coulomb interaction. These results are to be published in Ref. 46.

Anisotropic Dirac systems Does the transport behavior of the electrical conductivity and the viscosity change when we lower the symmetry of the systems? Indeed, in anisotropic Dirac systems (ADSs), we find fascinating transport properties which differ strongly from the transport quantities of graphene.

The ADSs have an anisotropic energy dispersion which arises when two Dirac cones merge. In the direction where the fusion of the Dirac cones occurred, the energy dispersion is parabolic, whereas in the perpendicular direction the energy dispersion is still linear. Two examples exhibiting such an anisotropic energy dispersion are the organic charge transfer salt α-(BEDT-TTF)$_2$I$_3$ and the heterostructure 5/3 $\mathrm{TiO_2/VO_2}$. In the case of the organic charge transfer salt, two Dirac cones merge under the application of uniaxial pressure and for $P = 40$kbar there exists one Dirac cone with the anisotropic energy dispersion relation. In the case of the heterostructure $\mathrm{TiO_2/VO_2}$, there are four anisotropic Dirac cones in the first Brillouin zone which are rotated by 45 degrees with respect to each other.[3]

Both in the *hydrodynamic* and in the *collisionless regime*, the *conductivity tensor* shows a very interesting behavior. In the direction of the parabolic energy dispersion relation, we find insulating behavior, while in the direction of the linear energy dispersion, we find metallic behavior, i. e.,

$$\begin{aligned} \sigma_{xx,yy}(T) &\propto N\left(\frac{T}{vk_0}\right)^{\pm(\frac{1}{2}+\frac{0.299}{N})} \qquad \text{in the hydrodynamic regime}\,, \text{ and} \\ \sigma_{xx,yy}(\omega) &\propto N\left(\frac{\omega}{vk_0}\right)^{\pm(\frac{1}{2}+\frac{0.299}{N})} \qquad \text{in the collisionless regime}\,. \end{aligned} \tag{10.9}$$

Hence, we find in the same material insulating or metallic behavior depending on the direction of the electrical field. Fascinatingly, the Coulomb interaction even enhances this behavior. The influence of the Coulomb potential is taken into account by an RG analysis in the large-N limit and in the strong-coupling regime. It gives rise to the additional exponents proportional to $1/N$, where N is the fermionic flavor. In the case of the organic charge transfer salt, $N = 2$ because of the two spin degrees of freedom, while for the heterostructure $\mathrm{TiO_2/VO_2}$ we have $N = 8$, since there are four Dirac cones in the first Brillouin zone with two spin degrees of freedom each.

---

[3] For the purpose of this thesis, we focused on just one anisotropic Dirac cone in the first Brillouin zone. Due to the rotation of the Dirac cones, we find a superposition of the transport properties arising due to the linear and due to the parabolic energy dispersion in the heterostructure $\mathrm{TiO_2/VO_2}$.

The *viscosity tensor* of an ADS differs from the viscosity of graphene even more strongly and has some fascinating properties. Due to the anisotropy of the energy spectrum, the system is not described by the shear viscosity η anymore, but by a viscosity tensor consisting of eight independent viscosity coefficients. The functional temperature (frequency) dependence of these viscosity coefficients in the hydrodynamic (collisionless) regime depends on the momentum flow and reads for the different viscosity coefficients as

$$\begin{aligned}
\eta_{\alpha\beta\gamma\delta}(T) &= N C_{\alpha\beta\gamma\delta} \frac{k_0^2}{\hbar} \left(\frac{T}{v k_0} \right)^{\phi_{\alpha\beta\gamma\delta}} && \text{in the hydrodynamic regime}\,, \text{ and} \\
\eta_{\alpha\beta\gamma\delta}(\omega) &= N C_{1,\alpha\beta\gamma\delta} \frac{k_0^2}{\hbar} \left(\frac{\omega}{v k_0} \right)^{\phi_{\alpha\beta\gamma\delta}} + N C_{2,\alpha\beta\gamma\delta} \frac{k_0^2}{\hbar} \left(\frac{\omega}{v k_0} \right)^{\phi_s} && \text{in the collisionless regime}\,,
\end{aligned} \tag{10.10}$$

where N is the fermionic flavor, and $C_{\alpha\beta\gamma\delta}$, $C_{1,\alpha\beta\gamma\delta}$, and $C_{2,\alpha\beta\gamma\delta}$ are numerical constants with $\alpha \cdots \delta \in \{x, y\}$. (In our notation, the parabolic energy dispersion is aligned along the x-axis and the linear one along the y-axis.) In the *collisionless regime*, the additional term proportional to $C_{2,\alpha\beta\gamma\delta}$ arises due to interband processes. These interband processes do not occur in the *hydrodynamic regime* where only intraband processes dominate and thus there is no such term.

But now let us focus on the exponents of the viscosity coefficients. The exponents of η_{xyxy} and η_{yxyx} are given by

$$\begin{aligned}
\phi_{xyxy} &= \frac{5}{2} + \frac{1.02445}{N}\,, \\
\phi_{yxyx} &= \frac{1}{2} - \frac{0.17335}{N}\,,
\end{aligned} \tag{10.11}$$

while the exponent of the remaining viscosity coefficient η_{ijkl} is

$$\phi_{ijkl} = \phi_s = \frac{3}{2} + \frac{0.4255}{N}\,. \tag{10.12}$$

Again, the Coulomb potential enhances the temperature dependence for all viscosity coefficients but for the viscosity coefficient η_{yxyx} where the Coulomb potential reduces the exponent.

In order to see, whether the viscosity coefficients are large or not, we compare these coefficients with the entropy of the system whose exponent is proportional to ϕ_s. We find that all viscosity coefficients η_{ijkl} fulfill the lower bound to the ratio of viscosity over entropy and we further find that for the viscosity coefficient η_{yxyx} the ratio diverges with decreasing temperature. However, the viscosity coefficient η_{xyxy} violates the lower bound. This violation of the lower bound in ADSs is, up to our knowledge, the first condensed-matter realization of the violation. The physical interpretation of the lower bound to the ratio η/s can be given by the Heisenberg uncertainty principle. But now that this lower bound is violated, does this mean that the Heisenberg uncertainty principle is not valid anymore? The answer to this question is no. The reason for the violation of the lower bound is the following: due to the anisotropy of the system, two different length scales ξ_x and ξ_y arise which rescale the x- and y-component of the momentum differently. Hence, we introduced a version of the lower bound applicable to anisotropic systems which depends on these length scales and is

$$\frac{\eta_{\alpha\beta\gamma\delta}}{s} \geq \frac{\hbar}{4\pi k_{\mathrm{B}}} \left(\frac{\xi_x}{\xi_y} \right)^{\varphi}\,, \tag{10.13}$$

with $\varphi = 0, 2, -2$ depending on the values for $\alpha, \beta, \dots \in \{x, y\}$.

Nevertheless, the extreme smallness of the viscosity coefficient will lead to extreme flow behavior. Experimentally measurable quantities which give access to these viscosity coefficients can be obtained using the Navier-Stokes equation. The Navier-Stokes equation for the velocity component in the direction of the parabolic energy dispersion is the Navier-Stokes equation of a Galilean invariant system, while for the velocity component in the direction with the linear energy dispersion, we find the Navier-Stokes equation of a relativistic system. This set of equations governs the flow dynamics and the extremely small viscosity coefficient leads to extremely turbulent flow. We also presented other experimental quantities showing signs of the violation of the lower bound: the shear frequencies and shear modes of the system.

All these fascinating transport properties of ADSs are to be published in Ref. 119.

As can be seen in Fig. 10.1, this thesis gives a complete picture of the *electrical conductivity* σ and the *viscosity* η in the *collisionless* and *hydrodynamic* regime of *isotropic and anisotropic Dirac systems*. As a common theme, we investigated the influence of the *Coulomb interaction* on the two transport properties in the two different regimes.

This does by no way mean that it is an exhaustive picture of the transport in graphene and ADSs. There exist different effects which lead to possible corrections of these transport properties. One example is an applied magnetic field which modifies the electrical conductivity and the viscosity. While there have already been works on the magnetotransport in graphene [81], the effect on the conductivity of ADS is an interesting aspect that remains to be studied. Another example are impurities in the system. In order to study the correction due to defects, a self-consistent Born approximation should be performed. For the conductivity of an ADS, we expect that the metallic temperature dependence of one contribution of the conductivity tensor becomes constant, while the insulating contribution stays insulating.

However, all these additional effects will only lead to corrections of our results which are recovered in the limit of zero magnetic field/clear system. Hence, with this thesis we lay a foundation for the behavior of the different transport properties, σ and η, in the different regimes on which we can build in the future.

—Frei nach meinem Opi:

Hätte ich mit dieser Seite angefangen zu schreiben,
wäre ich gleich fertig gewesen.

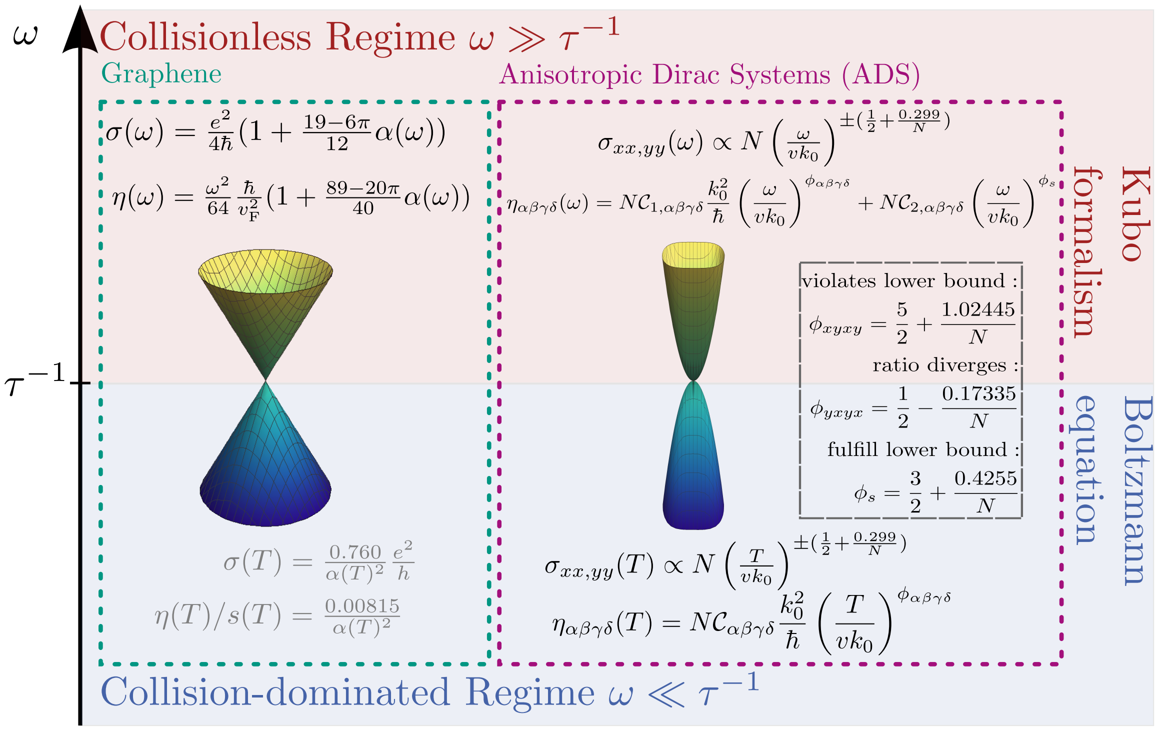

Figure 10.1: Overview of the results. In this thesis, we determine the conductivity σ and the viscosity η of graphene and ADSs as a function of frequency and temperature. Both materials are studied at the charge neutrality point, i. e., their chemical potential μ is zero. The red area indicates the collisionless regime where the Kubo formalism is used, while the blue area indicates the hydrodynamic regime where the transport quantities are calculated using the Boltzmann equation. The equations colored in gray represent results obtained by other authors, while the equations in black represent the results obtained by me and my collaborators.

Appendix A

Graphene

A.1 Derivation of the Transmission coefficient

In this section we derive the formula which relates the transmission coefficient $T(\omega)$ of the incident light to the optical conductivity $\sigma(\omega)$ of the system. This derivation follows the calculation of Stauber *et al.* [101].

We will focus on a situation, where p-polarized light scatters between two media that are separated by a graphene flake, see figure A.1. The graphene flake lays in the x-y-plane. It separates the two media characterized by the electrical permittivity $\epsilon_i \epsilon_0$ with $i = 1, 2$, where ϵ_0 is the vacuum permittivity, and ϵ_1 and ϵ_2 are the relative permittivity of the two media. The incident electrical field given by $\boldsymbol{E} = \big(E_x, 0, E_z\big)$ propagates in the direction $\boldsymbol{k} = \big(k_x, 0, k_z\big)$. When the incident light scatters on the graphene flake, it has to fulfill the electrical boundary conditions which are

$$\begin{aligned} \big(\boldsymbol{D}_2 - \boldsymbol{D}_1\big)\, \boldsymbol{n} &= \rho\,, & \text{(A.1)} \\ \boldsymbol{n} \times \big(\boldsymbol{E}_2 - \boldsymbol{E}_1\big) &= 0\,. & \text{(A.2)} \end{aligned}$$

Here, $\boldsymbol{D}_i$ is the electrical displacement field in the medium i, and ρ is the charge density of graphene. The vector $\boldsymbol{n}$ is perpendicular to the plane of the graphene flake. The electrical field in medium 1 consists of the incident electrical field E_i and the reflected field $E_r = rE_i$, i. e., $\boldsymbol{E}_1 = \boldsymbol{E}_i + \boldsymbol{E}_r$, while

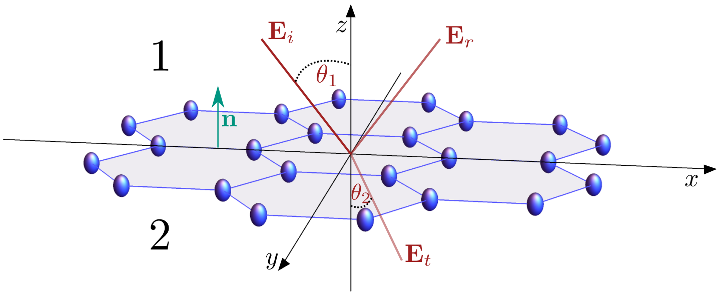

Figure A.1: The incident p-polarized light E_i scatters between two media which are separated by a graphene flake. After scattering on the graphene flake, the light is either reflected E_r or transmitted E_t.

in the second medium the transmitted field $E_2 = E_t = tE_i$ is found. Using these definitions of the electrical field, we can cast the electrical boundary conditions in the form

$$\begin{aligned} -\epsilon_0\epsilon_2 E_t \sin\theta_2 + \epsilon_0\epsilon_1 \big(E_i + E_r\big)\sin\theta_1 &= \rho && \text{(A.3)} \\ \big(E_i - E_r\big)\cos\theta_1 &= E_t \cos\theta_2\,, && \text{(A.4)} \end{aligned}$$

where θ_1 and θ_2 are the incident and refracted angle respectively. Next, we use the continuity equation

$$\frac{\partial\rho}{\partial t} + \nabla\boldsymbol{j} = 0 \tag{A.5}$$

which describes the charge conservation of the system. In the momentum space it has the form

$$\rho(\omega) = \frac{k_x}{\omega} j_x(\omega)\,, \tag{A.6}$$

where we used the fact that the incoming light is p-polarized with $\boldsymbol{E} = (E_x, 0, E_z)$ inducing only a current in the x-direction of the graphene flake. Furthermore, inserting Ohm's law

$$j_x(\omega) = \sigma(\omega)E_x = \sigma(\omega)E_t\cos\theta_2\,, \tag{A.7}$$

and Snell's law

$$\sqrt{\epsilon_1}\sin\theta_1 = \sqrt{\epsilon_2}\sin\theta_2 \tag{A.8}$$

into the above electrical boundary equations (A.3) and (A.4) yields the following expression for the transmission coefficient

$$t(\omega) = \frac{2\epsilon_0\epsilon_1\cos\theta_1}{\epsilon_0\epsilon_1\cos\theta_2 + \sqrt{\epsilon_1\epsilon_2}\cos\theta_1 + \sqrt{\epsilon_1}\sigma(\omega)/c\cos\theta_1\cos\theta_2}\,. \tag{A.9}$$

This expression simplifies further for a normal incident of the light and we obtain the transmission probability

$$T(\omega) = \big|t(\omega)\big|^2\frac{k_z^t}{k_z^i} = \sqrt{\frac{\epsilon_2}{\epsilon_1}}\frac{4\left(\epsilon_1\epsilon_0\right)^2}{\left|\left(\sqrt{\epsilon_1\epsilon_2}+\epsilon_1\right)\epsilon_0 + \sqrt{\epsilon_1}\sigma(\omega)/c\right|^2}\,. \tag{A.10}$$

If both media are vacuum, we find that the transmissivity is given by

$$T(\omega) = \left(1 + \frac{\sigma(\omega)}{2\,c\epsilon_0}\right)^{-2}\,, \tag{A.11}$$

which relates the transmission coefficient to the optical conductivity. Calculating the conductivity of graphene at half filling using noninteracting Dirac fermions, the above expression simplifies even further and we find

$$T(\omega) = \left(1 + \frac{\pi}{2}\alpha_{\text{QED}}\right)^{-2}\,, \tag{A.12}$$

where $\alpha_{\text{QED}} = \frac{e^2}{4\pi\epsilon_0 c\hbar} = \frac{1}{137}$.

A.2 The optical conductivity of graphene

In this part of the appendix, details of the calculation of the optical conductivity presented in Chap. 5 are given. In order to determine the optical conductivity, the Kubo formula (2.5) is used, $\sigma_{\alpha\beta}(\omega) = \pi D_{\alpha\beta}\delta(\omega) - \operatorname{Im}\chi_{J_\alpha J_\beta}(\omega)/\omega$. The current-current correlation function χ_J can be expanded in the coupling constant $\alpha(\omega)$ after performing a renormalization group (RG) analysis, i. e., $\chi_J = \chi_J^{(0)} + \chi_J^{(1)} + \cdots$. In the first part of this section, we demonstrate how the non-interacting part $\chi_J^{(0)}$ of the correlation function is calculated in the *Dirac model* and in the *tight-binding description*, before we turn to the calculation of $\chi_J^{(1)}$ in the tight-binding model, which determines the correction coefficient $\mathcal{C}_\sigma$.

A.2.1 The non-interacting part of the optical conductivity

Let us start determining the non-interaction part of the optical conductivity, where we first shortly summarize the calculation in the Dirac model and than give the details for the tight-binding description.

The Dirac model

The current-current correlation function is given by the following expression

$$\chi_J^{(0)}(\mathrm{i}\omega) = \frac{N_{sv}}{2}\sum_\mu \int \frac{d\epsilon}{2\pi}\int \frac{d^2k}{(2\pi)^2}\,\mathrm{Tr}\left(\hat{j}_{x+y}G_{\boldsymbol{k},\mathrm{i}(\epsilon+\omega)}\hat{j}_{x+y}G_{\boldsymbol{k},\mathrm{i}\epsilon}\right)\,, \tag{A.13}$$

where the Green's function $G_{\boldsymbol{k},\mathrm{i}\epsilon}$ is defined in (4.19) and the current operator, $\hat{j}_{x+y} = \hat{j}_x + \hat{j}_y$, with the x- and y- components of the current are defined in (4.20). Inserting these definitions, and performing the angle integration yields

$$\begin{aligned}\chi_J^{(0)}(\mathrm{i}\omega) &= \frac{N_{sv}}{2}\sum_\mu \int \frac{d\epsilon}{2\pi}\int \frac{d^2k}{(2\pi)^2}\,\mathrm{Tr}\left(\hat{j}_{x+y}G_{\boldsymbol{k},\mathrm{i}(\epsilon+\omega)}\hat{j}_{x+y}G_{\boldsymbol{k},\mathrm{i}\epsilon}\right)\\ &= -\frac{N_{sv}}{2}\int \frac{d\epsilon}{2\pi}\int \frac{d^2k}{(2\pi)^2}\frac{4\epsilon(\epsilon+\omega)}{\left((v_\mathrm{F}k)^2+\epsilon^2\right)\left((v_\mathrm{F}k)^2+(\epsilon+\omega)^2\right)}\\ &= -\frac{N_{sv}}{2}\int \frac{d^2k}{(2\pi)^2}\frac{4v_\mathrm{F}k}{(2v_\mathrm{F}k)^2+\omega^2}\,.\end{aligned} \tag{A.14}$$

After analytical continuation $\mathrm{i}\omega_n \to \omega + \mathrm{i}\delta$, which is given by

$$\frac{1}{4(v_\mathrm{F}k)^2 - (\mathrm{i}\omega_n)} \to P.V.\frac{1}{4(v_\mathrm{F}k)^2-\omega} + \frac{\mathrm{i}\pi}{2\omega}\delta(2p-\omega) + \frac{\mathrm{i}\pi}{2\omega}\delta(2p+\omega) \tag{A.15}$$

and taking the imaginary part of the correlation function, we obtain

$$\sigma_0 = \frac{N_{sv}}{16}\frac{e^2}{\hbar}\,, \tag{A.16}$$

for the conductivity [1] with $N_{sv} = 4$.

The tight-binding description

The current-current correlation in the tight-binding description has the same structure as found in (A.13). Only the expressions of the current operator and the Green's function are replaced by the corresponding expression in the tight-binding description. Setting $\mu = \nu = y$ yields:

$$\begin{aligned}\chi_J^{(0)}(\mathrm{i}\omega) &= -\frac{T}{2}\sum_{\boldsymbol{k},\epsilon,\nu} \mathrm{Tr}\left[\mathcal{J}_{\boldsymbol{k}}^{\nu}\mathcal{G}_{\boldsymbol{k},\mathrm{i}\epsilon}\mathcal{J}_{\boldsymbol{k}}^{\nu}\mathcal{G}_{\boldsymbol{k},\mathrm{i}(\epsilon+\omega)}\right] \\ &= -\frac{1}{2}\sum_{\boldsymbol{k},\nu} \frac{\left(h_{\boldsymbol{k}}{}^{*} j_{\nu,\boldsymbol{k}} - h_{\boldsymbol{k}} j^{*}_{\nu,\boldsymbol{k}}\right)^2}{t\ |h_{\boldsymbol{k}}|\left(4|h_{\boldsymbol{k}}|^2 + \omega^2/t^2\right)}\,, \end{aligned} \tag{A.17}$$

In the second line we evaluated the frequency integration and performed the trace in the pseudospin space. Next, we rewrite the current-component $j_y(\boldsymbol{k})$, defined in Eq. (4.12a), as:

$$j_y(\boldsymbol{k}) \;=\; \frac{-\mathrm{i}ta}{2}\left[h_{\boldsymbol{k}} - 3\right] \tag{A.18}$$

$$j_y^{*}(\boldsymbol{k}) \;=\; \frac{\mathrm{i}ta}{2}\left[h_{\boldsymbol{k}}{}^{*} - 3\right]\,, \tag{A.19}$$

and obtain for our retarded current correlator:

$$\chi_J^{(0)}(\mathrm{i}\Omega) = \frac{ta^2}{4}\int_{BZ}\frac{d^2k}{(2\pi)^2}\frac{18|h_{\boldsymbol{k}}|^2 + 4|h_{\boldsymbol{k}}|^4 - 12|h_{\boldsymbol{k}}|^2\left(h_{\boldsymbol{k}} + h_{\boldsymbol{k}}{}^{*}\right) + 9\left(h_{\boldsymbol{k}}^2 + h_{\boldsymbol{k}}^{*\,2}\right)}{|h_{\boldsymbol{k}}|(4|h_{\boldsymbol{k}}|^2 + \Omega^2/t^2)}. \tag{A.20}$$

Upon analytically continuing $\mathrm{i}\Omega \to \omega + \mathrm{i}\delta$,

$$\frac{1}{4|h_{\boldsymbol{k}}|^2 + \Omega^2} \to \mathrm{P.V.}\frac{1}{4|h_{\boldsymbol{k}}|^2 - \omega^2} + \mathrm{i}\frac{\pi}{2\omega}\delta(\omega - 2|h_{\boldsymbol{k}}|) + \mathrm{i}\frac{\pi}{2\omega}\delta(\omega + 2|h_{\boldsymbol{k}}|)\,, \tag{A.21}$$

with P.V. denoting the principal value, assuming $\omega > 0$, and taking the imaginary part of the above expression, we obtain for the retarded correlator:

$$\begin{aligned}\chi_J^{(0)}(\omega) &= \sum_k\left(\frac{ta^2\pi}{32}\right)\left[18 + 4|h_{\boldsymbol{k}}|^2 + 18\frac{[\mathrm{Re}\,h_{\boldsymbol{k}}]^2 - [\mathrm{Im}\,h_{\boldsymbol{k}}]^2}{|h_{\boldsymbol{k}}|^2} - 24[\mathrm{Re}\,h_{\boldsymbol{k}}]\right]\delta\left(|h_{\boldsymbol{k}}| - \frac{\omega}{2t}\right) \\ &= \sum_k\left(\frac{ta^2\pi}{32}\right) g\left(h_{\boldsymbol{k}}\right)\ \delta\left(|h_{\boldsymbol{k}}| - \frac{\omega}{2t}\right)\,. \end{aligned} \tag{A.22}$$

In this expression, we have kept the dimensionful quantities a and t, although henceforth we shall set them to unity and measure the frequency relative to t. Due to the delta function constraint, we can integrate the above expression analytically. Therefore, we split up the function $g\left(h_{\boldsymbol{k}}\right)$ into two functions and define:

$$g_1(|h_{\boldsymbol{k}}|) \;=\; 18 + 4|h_{\boldsymbol{k}}|^2 \tag{A.23}$$

$$g_2\left(h_{\boldsymbol{k}}\right) \;=\; 18\frac{[\mathrm{Re}\,h_{\boldsymbol{k}}]^2 - [\mathrm{Im}\,h_{\boldsymbol{k}}]^2}{|h_{\boldsymbol{k}}|^2} - 24[\mathrm{Re}\,h_{\boldsymbol{k}}]\,. \tag{A.24}$$

Firstly, we evaluate the expression:

$$\chi^{(0)}_{J,1}(\omega) = \frac{\pi}{16}\sum_{\boldsymbol{k}} g_1(|h_{\boldsymbol{k}}|)\delta(2|h_{\boldsymbol{k}}| - \omega)\,. \tag{A.25}$$

To this end, we introduce the density of state per unit cell as

$$\begin{aligned}\rho(E) &= \int \frac{d^2k}{(2\pi)^2}\delta(E - |h_{\boldsymbol{k}}|)\\ &= \int \frac{d^2k}{(2\pi)^2}\sum_{i=1}^{4}\frac{1}{|\partial_{k_{x,i}}|h(k_{x,i},k_y)||}\delta(k_x - k_{x,i})\,,\end{aligned} \tag{A.26}$$

with the $k_{x,i}$ being the solution to $E = |h_{\boldsymbol{k}}|$:

$$k_{x,i} = \pm\frac{2}{\sqrt{3}}\arccos\left[\frac{1}{4}(-2\cos\left(\frac{3k_y}{2}\right) \pm \sqrt{2}\sqrt{2E^2 - 1 + \cos\left(3k_y\right)})\right], \tag{A.27}$$

describing curves that encircle the Dirac points at $\boldsymbol{k}_R = \frac{4\pi}{3a}(\frac{1}{2\sqrt{3}}\hat{x} + \frac{1}{2}\hat{y})$ and $\boldsymbol{k}_L = \frac{4\pi}{3a}(-\frac{1}{2\sqrt{3}}\hat{x} + \frac{1}{2}\hat{y})$ when the y component is restricted to $k_{y,-} < k_y < k_{+,y}$ with

$$k_{y,\pm}(E) = \frac{2\pi}{3} \pm \frac{\arccos\left(1 - 2E^2\right)}{3}\,. \tag{A.28}$$

We can evaluate the density of states analytically and obtain:

$$\rho(E) = \frac{1}{(2\pi)^2}\frac{32\ E\ \sqrt{1 - \frac{E}{3}}\ K\left[-\frac{16E}{(E-3)(1+E)^3}\right]}{3(3-E)(1+E)^{3/2}}\,, \tag{A.29}$$

where $K[m]$ is the complete elliptic integral of the first kind. One part of the correlation function is thus given by:

$$\begin{aligned}\chi^{(0)}_{J,1}(\omega) &= \frac{\pi}{32}\sum_{\boldsymbol{k}} g_1(|h_{\boldsymbol{k}}|)\delta(|h_{\boldsymbol{k}}| - \omega/2)\\ &= \frac{\pi}{32}\rho\left(\frac{\omega}{2}\right)g\left(\frac{\omega}{2}\right)\\ &= \frac{\pi}{32}\rho\left(\frac{\omega}{2}\right)(18 + \omega^2)\,.\end{aligned} \tag{A.30}$$

In order to evaluate the expression:

$$\chi^{(0)}_{J,2}(\omega) = \frac{\pi}{16}\sum_{\boldsymbol{k}} g_2(h_{\boldsymbol{k}})\delta(2|h_{\boldsymbol{k}}| - \omega)\,, \tag{A.31}$$

we expand the above formula near the node, $h_{\boldsymbol{k_R}+\boldsymbol{k}}$, and write the deviation from the node in polar coordinates $\boldsymbol{k} = (k,\theta)$,

$$|h_{\boldsymbol{k_R}+\boldsymbol{k}}| \simeq \frac{3}{128}k(64 - 7k^2 + 16k\cos 3\theta - k^2\cos 6\theta), \tag{A.32}$$

valid to $\mathcal{O}(k^3)$. The approximate solution to $\omega = 2|h_{\boldsymbol{k_R}+\boldsymbol{k}}|$ is:

$$k_1(\theta,\omega) = \frac{1}{3}\omega - \frac{1}{36}\omega^2\cos 3\theta + \frac{1}{1728}[7 + 8\cos^2 3\theta + \cos 6\theta]\omega^3\,, \tag{A.33}$$

that is valid to $\mathcal{O}(\omega^3)$. The factor $g_2(h_{\boldsymbol{k}})$ is, to the same order,

$$\begin{aligned} g_2(\boldsymbol{k}_R + \boldsymbol{k}) \simeq \frac{9}{32}\Big[& k^3(-\cos 11\theta) + 3(5k^2 - 16)k\cos\theta + \left(64 - 20k^2\right)\cos 2\theta \\ &+ 2k\Big(2\left(k^2 - 16\right)\cos 3\theta - 8(\cos 5\theta + 3k) \\ &+ k(8\cos 4\theta + 8\cos 6\theta + 3k\cos 5\theta + 2\cos 8\theta(1 - 2k\cos\theta))\Big)\Big]\,. \end{aligned} \tag{A.34}$$

From the delta function, we also need

$$\frac{d}{dk}|h_{\boldsymbol{k_R}+\boldsymbol{k}}| = \frac{3}{64}\left(64 + 32k\cos 3\theta - 21k^2 - 3k^2\cos 6\theta\right)\,. \tag{A.35}$$

Then, assuming the same contribution comes from each node (which we have verified), we'll have:

$$\chi^{(0)}_{J,2}(\omega) \;=\; \frac{\pi}{8}\int_0^{2\pi} d\theta \int_0^{\infty} dk\; k\; g_2(\boldsymbol{k})\delta(2|h_{\boldsymbol{k}}| - \omega) \tag{A.36}$$

$$\;=\; \frac{\pi}{8}\int_0^{2\pi} d\theta\; k_1(\theta,\omega)\frac{1}{|\frac{d}{dk_1}2|h_{\boldsymbol{k_R}+\boldsymbol{k_1}}||}g_2(\boldsymbol{k}_R + \boldsymbol{k}_1)\,, \tag{A.37}$$

where we evaluated the radial k integral. To evaluate the integral, we simply insert $k_1(\theta,\omega)$ into the factors Eq. (A.35) and Eq. (A.36), insert them into the integrand and Taylor expand order by order in ω before evaluating the angle integrations. We obtain:

$$\chi^{(0)}_{J,2}(\omega) = -\frac{\omega}{8}\frac{\omega^2}{36}\,. \tag{A.38}$$

Upon inserting the combined result into Eq. (5.38), we find the frequency-dependent conductivity given by the formula:

$$\sigma(\omega) \;=\; \frac{\pi}{32\omega}\rho\left(\frac{\omega}{2}\right)(18 + \omega^2) - \frac{1}{8}\frac{\omega^2}{36} \tag{A.39}$$

$$\;\approx\; \sigma_0\left(1 + \frac{1}{9}\omega + \mathcal{O}(\omega^3)\right)\,, \tag{A.40}$$

with σ_0 the zero-frequency limit (reinserting correct factors of e^2 and $\hbar$, previously set to unity).

$$\sigma_0 = \frac{N}{8}\frac{e^2}{\hbar}. \tag{A.41}$$

In comparing to the known result for the conductivity of N_{sv} species of Dirac fermions, $\sigma_0 = \frac{N_{sv}}{16}\frac{e^2}{\hbar}$, recall that here we have $N = 2$, since we are considering the spinless case (but have summed over two nodes).

A.2.2 Correction coefficient in tight-binding description

After having calculated the non-interacting part of the optical conductivity in the tight-binding description, the influence of the Coulomb interaction is investigated. To this end, we evaluate the Feynman diagrams contributing to $\chi_J^{(1)}$, namely the self-energy diagram and the vertex diagram, and thus determine the value of the correction coefficient $\mathcal{C}_\sigma$.

Self-energy diagram

For the self-energy type diagrams contributing to order $\alpha(\omega)$, we obtain

$$\begin{aligned}\chi_J^{(1,bc)}(i\omega) &= -T^2 \sum_{\boldsymbol{k}\epsilon\epsilon'\nu} \int \frac{d^2q}{(2\pi)^2} V(\boldsymbol{q}) \operatorname{Tr}\Big(\mathcal{J}_{\boldsymbol{k}}^{\nu} \mathcal{G}_{\boldsymbol{k},\mathrm{i}(\omega+\epsilon)} \mathcal{J}_{\boldsymbol{k}}^{\nu} \mathcal{G}_{\boldsymbol{k},\mathrm{i}\epsilon} M_{\boldsymbol{q}} \mathcal{G}_{\boldsymbol{k}+\boldsymbol{q},\mathrm{i}\epsilon'} M_{-\boldsymbol{q}} \mathcal{G}_{\boldsymbol{k},\mathrm{i}\epsilon}\Big) \\ &= -T^2 \sum_{\boldsymbol{k}\epsilon\epsilon'\nu} \int \frac{d^2q}{(2\pi)^2} \operatorname{Tr}\Big(\mathcal{J}_{\boldsymbol{k}}^{\nu} \mathcal{G}_{\boldsymbol{k},\mathrm{i}(\omega+\epsilon)} \mathcal{J}_{\boldsymbol{k}}^{\nu} \mathcal{G}_{\boldsymbol{k},\mathrm{i}\epsilon} \Sigma(\boldsymbol{k}) \mathcal{G}_{\boldsymbol{k},\mathrm{i}\epsilon}\Big) \,,\end{aligned} \tag{A.42}$$

where to get to the second line we identified the self energy subdiagram. Inserting the Green's function and evaluating the frequency summation at $T = 0$, we find

$$\chi_J^{(1,bc)}(i\omega) = -\sum_{\boldsymbol{p}} \int \frac{d\omega}{2\pi} \frac{1}{(\omega-\Omega)^2 + |h_{\boldsymbol{p}}|^2} \frac{1}{(\omega^2 + |h_{\boldsymbol{p}}|^2)^2} \times \operatorname{Tr}\Big[\cdots j_\mu \cdots j_\mu \cdots\Big] \,, \tag{A.43}$$

where in the following we proceed to evaluate the trace and sum over the xx and yy components which yields

$$\operatorname{Tr}\Big[\cdots j_x \cdots j_x \cdots\Big] + Tr\Big[\cdots j_y \cdots j_y \cdots\Big] = T_1 + \omega T_2 + \omega^2 T_3 \,. \tag{A.44}$$

The trace is given by

$$\begin{aligned}&\operatorname{Tr}\left[\begin{pmatrix} -\mathrm{i}(\omega-\Omega) & h_{\boldsymbol{p}}^* \\ h_{\boldsymbol{p}} & -\mathrm{i}(\omega-\Omega)\end{pmatrix}\begin{pmatrix} 0 & j_{\boldsymbol{p}}^* \\ j_{\boldsymbol{p}} & 0\end{pmatrix}\begin{pmatrix} -\mathrm{i}\omega & h_{\boldsymbol{p}}^* \\ h_{\boldsymbol{p}} & -\mathrm{i}\omega\end{pmatrix}\begin{pmatrix} 0 & \Sigma_{21} \\ \Sigma_{12} & 0\end{pmatrix}\begin{pmatrix} -\mathrm{i}\omega & h_{\boldsymbol{p}}^* \\ h_{\boldsymbol{p}} & -\mathrm{i}\omega\end{pmatrix}\begin{pmatrix} 0 & j_{\boldsymbol{p}}^* \\ j_{\boldsymbol{p}} & 0\end{pmatrix}\right] \\ &= {h_{\boldsymbol{p}}^*}^3 (j_x^2 + j_y^2)\Sigma_{12} + h_{\boldsymbol{p}}^3 ({j_x^*}^2 + {j_y^*}^2)\Sigma_{21} + 2\omega\Omega\Big[h_{\boldsymbol{p}}^*(j_x j_x^* + j_y j_y^*)\Sigma_{12} + h_{\boldsymbol{p}}(j_x j_x^* + j_y j_y^*)\Sigma_{21}\Big] \\ &+ \omega^2\Big[\Sigma_{12}\Big(-2h_{\boldsymbol{p}}^*(j_x j_x^* + j_y j_y^*) - h_{\boldsymbol{p}}({j_x^*}^2 + {j_y^*}^2)\Big) + \Sigma_{21}\Big(-2h_{\boldsymbol{p}}(j_x j_x^* + j_y j_y^*) - h_{\boldsymbol{p}}^*({j_x}^2 + {j_y}^2)\Big)\Big] \\ &= T_1 + \omega T_2 + \omega^2 T_3 \,,\end{aligned} \tag{A.45}$$

where we identify the following expressions for T_1, T_2, and T_3

$$\begin{aligned}T_1 &= {h_{\boldsymbol{p}}^*}^3 (j_x^2 + j_y^2)\Sigma_{12} + h.c. \\ T_2 &= 2\Omega\Big[h_{\boldsymbol{p}}^*(j_x j_x^* + j_y j_y^*)\Sigma_{12}\Big] + h.c. \\ T_3 &= \Sigma_{12}\Big(-2h_{\boldsymbol{p}}^*(j_x j_x^* + j_y j_y^*) - h_{\boldsymbol{p}}({j_x^*}^2 + {j_y^*}^2)\Big) + h.c. \,.\end{aligned} \tag{A.46}$$

Thus, we have to calculate the following frequency integral:

$$\begin{aligned} I_\Sigma &= \int \frac{d\omega}{2\pi} \frac{1}{(\omega-\Omega)^2+|h_{\boldsymbol{p}}|^2} \frac{1}{(\omega^2+|h_{\boldsymbol{p}}|^2)^2} \left[T_1+\omega T_2+\omega^2 T_3\right] \\ &= \frac{1}{4|h_{\boldsymbol{p}}|^3(4|h_{\boldsymbol{p}}|^2+\Omega^2)^2} \left[(12|h_{\boldsymbol{p}}|^2+\Omega^2)T_1+(4|h_{\boldsymbol{p}}|^2\Omega)T_2+(4|h_{\boldsymbol{p}}|^4+3|h_{\boldsymbol{p}}|^2\Omega^2)T_3\right] . \end{aligned} \tag{A.47}$$

The self-energy contribution to the current-current correlation function is (summing over xx and yy terms and including the overall minus):

$$\begin{aligned} \chi_J^{(1,bc)}(\mathrm{i}\omega) &= -\sum_{\boldsymbol{p}} \frac{1}{4|h_{\boldsymbol{p}}|^3} \frac{1}{(4|h_{\boldsymbol{p}}|^2+\Omega^2)^2} \left[(4|h_{\boldsymbol{p}}|^2+\Omega^2)D_1(\boldsymbol{p})+(4|h_{\boldsymbol{p}}|^2-\Omega^2)D_2(\boldsymbol{p})\right] \\ &= -\sum_{\boldsymbol{p}} \frac{1}{4|h_{\boldsymbol{p}}|^3} \left[\frac{D_1(\boldsymbol{p})}{4|h_{\boldsymbol{p}}|^2+\Omega^2}+D_2(\boldsymbol{p})\frac{4|h_{\boldsymbol{p}}|^2-\Omega^2}{(4|h_{\boldsymbol{p}}|^2+\Omega^2)^2}\right] , \end{aligned} \tag{A.48}$$

where

$$D_1(\boldsymbol{p}) = 2(h^*\Sigma_{12}-h\Sigma_{21}) \left[(h^*)^2\left(j_x^2+j_y^2\right)-h^2\left((j_x^*)^2+(j_y^*)^2\right)\right] , \tag{A.49}$$

$$D_2(\boldsymbol{p}) = (h^*\Sigma_{12}+h\Sigma_{21}) \left[(h^*)^2(j_x^2+j_y^2)+h^2\left((j_x^*)^2+(j_y^*)^2\right)-2\left(j_x j_x^*+j_y j_y^*\right)|h|^2\right] . \tag{A.50}$$

Next, we analytically continue $i\Omega \to \omega + i\delta$ to get:

$$\frac{1}{4|h|^2+\Omega^2} = \frac{1}{4|h|}\left[\frac{1}{2|h|+i\Omega}+\frac{1}{2|h|-i\Omega}\right] \to \frac{1}{4|h|}\left[\frac{1}{2|h|+\omega+i\delta}+\frac{1}{2|h|-\omega-i\delta}\right] , \tag{A.51}$$

and

$$\frac{4|h|^2-\Omega^2}{(4|h|^2+\Omega^2)^2} = \frac{d}{d\Omega}\frac{\Omega}{4|h|^2+\Omega^2} \to \frac{d}{d\omega}\frac{\omega}{4|h|}\left[\frac{1}{2|h|+\omega+i\delta}+\frac{1}{2|h|-\omega-i\delta}\right] , \tag{A.52}$$

which, after taking the imaginary part (and assuming $\omega > 0$), leads to:

$$\operatorname{Im}\chi_J^{(1,bc)}(\omega) = -\pi\sum_{\boldsymbol{p}}\frac{1}{16|h_{\boldsymbol{p}}|^4}D_1(\boldsymbol{p})\delta\left(\omega-2|h_{\boldsymbol{p}}|\right) - \pi\frac{d}{d\omega}\sum_{\boldsymbol{p}}\frac{\omega}{16|h_{\boldsymbol{p}}|^4}D_2(\boldsymbol{p})\delta\left(\omega-2|h_{\boldsymbol{p}}|\right) . \tag{A.53}$$

The delta functions in each term will pin $\omega = 2|h_{\boldsymbol{p}}|$. Using the delta function which leads to (A.27) and (A.28), we obtain

$$\begin{aligned} \operatorname{Im}\chi_J^{(1,bc)}(\omega) = &-\pi A \sum_{i=1}^{4} \int_{p_{y,-}}^{p_{y,+}} \frac{dp_y}{(2\pi)^2} \frac{1}{2|(\partial_{p_x}|h_{\boldsymbol{p}}|)|_{p_{x,i}}|} \frac{D_1(p_{x,i},p_y)}{\omega^4} \\ &+\pi A \frac{d}{d\omega} \sum_{i=1}^{4} \int_{p_{y,-}}^{p_{y,+}} \frac{dp_y}{(2\pi)^2} \frac{1}{2|(\partial_{p_x}|h_{\boldsymbol{p}}|)|_{p_{x,i}}|} \frac{D_2(p_{x,i},p_y)}{\omega^3} , \end{aligned} \tag{A.54}$$

where A is the area of a unit cell in real-space. This is the contribution of the self-energy diagram to the correction coefficient $\mathcal{C}_\sigma$. Now let us turn to the vertex diagram.

Vertex-Diagram

To calculate the correction of the conductivity due to the vertex correction, we have to evaluate the expression:

$$\chi_J^{(1,d)}(\mathrm{i}\omega) = \sum_{\boldsymbol{p}} \int \frac{d^2 q}{(2\pi)^2} \hat{V}(\boldsymbol{q}) \,\mathrm{Tr}\left[I_\mu(\boldsymbol{p}, \mathrm{i}\Omega) M_{\boldsymbol{q}} I_\mu(\boldsymbol{p}+\boldsymbol{q}, -\mathrm{i}\Omega) M_{-\boldsymbol{q}} \right], \tag{A.55}$$

where $I_\mu(\boldsymbol{p}, \mathrm{i}\Omega)$ is given by:

$$\begin{aligned} I_\mu(\boldsymbol{p}, \mathrm{i}\Omega) &= T \sum_\omega \mathcal{G}_{\boldsymbol{p},\mathrm{i}\omega} \mathcal{J}^\mu_{\boldsymbol{p}} \mathcal{G}_{\boldsymbol{p},\mathrm{i}(\omega-\Omega)} \\ &= T \sum_\omega \frac{1}{(\omega-\Omega)^2 + |h_{\boldsymbol{p}}|^2} \frac{1}{\omega^2 + |h_{\boldsymbol{p}}|^2} \begin{pmatrix} -\mathrm{i}\omega & h^*_{\boldsymbol{p}} \\ h_{\boldsymbol{p}} & -\mathrm{i}\omega \end{pmatrix} \begin{pmatrix} 0 & j^*_\mu \\ j_\mu & 0 \end{pmatrix} \begin{pmatrix} -\mathrm{i}(\omega-\Omega) & h^*_{\boldsymbol{p}} \\ h_{\boldsymbol{p}} & -\mathrm{i}(\omega-\Omega) \end{pmatrix} \\ &= T \sum_\omega \frac{1}{(\omega-\Omega)^2 + |h_{\boldsymbol{p}}|^2} \frac{1}{\omega^2 + |h_{\boldsymbol{p}}|^2} \left[M_0 + \omega M_1 + \omega^2 M_2 \right] \end{aligned} \tag{A.56}$$

with

$$M_0 = \begin{pmatrix} \mathrm{i} h^*_{\boldsymbol{p}} \, j_\mu \, \Omega & h^{*\,2}_{\boldsymbol{p}} \, j_\mu \\ h^2_{\boldsymbol{p}} \, j^*_\mu & +\mathrm{i} h_{\boldsymbol{p}} \, j^*_\mu \, \Omega \end{pmatrix}, \tag{A.57}$$

$$M_1 = \begin{pmatrix} -\mathrm{i}\left[h^*_{\boldsymbol{p}} j_\mu + h_{\boldsymbol{p}} j^*_\mu \right] & j^*_\mu \Omega \\ j_\mu \Omega & -\mathrm{i}\left[h^*_{\boldsymbol{p}} j_\mu + h_{\boldsymbol{p}} j^*_\mu \right] \end{pmatrix}, \tag{A.58}$$

$$M_2 = \begin{pmatrix} 0 & -j^*_\mu \\ -j_\mu & 0 \end{pmatrix}. \tag{A.59}$$

Next, we take again the zero temperature limit $T \to 0$, which means that the sum over the Matsubara frequencies becomes an integral $T \sum\limits_\omega \to \int \frac{d\omega}{2\pi}$. Thus, we have to evaluate the following frequency integrals:

$$\int\limits_{-\infty}^{+\infty} \frac{d\omega}{2\pi} \frac{1}{(\omega-\Omega)^2 + |h_{\boldsymbol{p}}|^2} \frac{1}{\omega^2 + |h_{\boldsymbol{p}}|^2} = \frac{1}{4|h_{\boldsymbol{p}}|^2 + \Omega^2} \frac{1}{|h_{\boldsymbol{p}}|}, \tag{A.60}$$

$$\int\limits_{-\infty}^{+\infty} \frac{d\omega}{2\pi} \frac{\omega}{(\omega-\Omega)^2 + |h_{\boldsymbol{p}}|^2} \frac{1}{\omega^2 + |h_{\boldsymbol{p}}|^2} = \frac{\Omega}{4|h_{\boldsymbol{p}}|^2 + \Omega^2} \frac{1}{2|h_{\boldsymbol{p}}|}, \tag{A.61}$$

$$\int\limits_{-\infty}^{+\infty} \frac{d\omega}{2\pi} \frac{\omega^2}{(\omega-\Omega)^2 + |h_{\boldsymbol{p}}|^2} \frac{1}{\omega^2 + |h_{\boldsymbol{p}}|^2} = \frac{2|h_{\boldsymbol{p}}|^2 + \Omega^2}{4|h_{\boldsymbol{p}}|^2 + \Omega^2} \frac{1}{2|h_{\boldsymbol{p}}|}. \tag{A.62}$$

Using these frequency integrals, the matrix $I_\mu(\boldsymbol{p},\Omega)$ has the form:

$$\begin{aligned} I_\mu(\boldsymbol{p},\mathrm{i}\Omega) &= \frac{1}{|h_{\boldsymbol{p}}|}\frac{1}{\Big(4|h_{\boldsymbol{p}}|^2+\Omega^2\Big)}\begin{pmatrix} \mathrm{i}\Omega\frac{1}{2}\Big[h^*_{\boldsymbol{p}}j_\mu - h_{\boldsymbol{p}}j^*_\mu\Big] & h^*(\boldsymbol{p})^2 j_\mu - |h_{\boldsymbol{p}}|^2 j^*_\mu \\ h(\boldsymbol{p})^2 j^*_\mu - |h_{\boldsymbol{p}}|^2 j_\mu & i\Omega\frac{1}{2}\Big[h_{\boldsymbol{p}}j^*_\mu - h^*_{\boldsymbol{p}}j_\mu\Big] \end{pmatrix} \\ &= \frac{1}{|h_{\boldsymbol{p}}|}\frac{1}{\Big(4|h_{\boldsymbol{p}}|^2+\Omega^2\Big)}V_\mu(\boldsymbol{p},\Omega)\,. \end{aligned} \tag{A.63}$$

Now, we can rewrite our expression for the vertex diagram in the following form:

$$\chi_J^{(1,d)}(\mathrm{i}\omega) = \sum_{\boldsymbol{p}} \frac{1}{|h_{\boldsymbol{p}}|\Big(4|h_{\boldsymbol{p}}|^2+\Omega^2\Big)}\,\mathrm{Tr}\,\Big[V_\mu(\boldsymbol{p},\Omega)Q_\mu(\boldsymbol{p},-\Omega)\Big]\,, \tag{A.64}$$

where

$$Q_\mu(\boldsymbol{p},-\Omega) = \int \frac{d^2q}{(2\pi)^2}\hat{V}(\boldsymbol{q})\frac{M_{\boldsymbol{q}}V_\mu(\boldsymbol{p}+\boldsymbol{q},-\Omega)M_{-\boldsymbol{q}}}{|h_{\boldsymbol{p}+\boldsymbol{q}}|\Big(4|h_{\boldsymbol{p}+\boldsymbol{q}}|^2+\Omega^2\Big)}\,. \tag{A.65}$$

We now write $Q_\mu(\boldsymbol{R},-\Omega)$ as a Fourier series:

$$Q_\mu(\boldsymbol{p},-\Omega) = A\sum_{\boldsymbol{R}} e^{+i\boldsymbol{p}\cdot\boldsymbol{R}}Q_\mu(\boldsymbol{R},-\Omega), \tag{A.66}$$

$$Q_\mu(\boldsymbol{R},-\Omega) = \sum_{\boldsymbol{p}} e^{-i\boldsymbol{p}\cdot\boldsymbol{R}}Q_\mu(\boldsymbol{p},-\Omega). \tag{A.67}$$

Next, we simplify $Q_\mu(\boldsymbol{R},-\Omega)$:

$$Q_\mu(\boldsymbol{R},-\Omega) = \sum_{\boldsymbol{p}} e^{-i\boldsymbol{p}\cdot\boldsymbol{R}}\int \frac{d^2q}{(2\pi)^2}\hat{V}(\boldsymbol{q})\frac{M_{\boldsymbol{q}}V_\mu(\boldsymbol{p}+\boldsymbol{q},-\Omega)M_{-\boldsymbol{q}}}{|h_{\boldsymbol{p}+\boldsymbol{q}}|\Big(4|h_{\boldsymbol{p}+\boldsymbol{q}}|^2+\Omega^2\Big)} \tag{A.68}$$

$$= \sum_{\boldsymbol{p}} \int \frac{d^2q}{(2\pi)^2} e^{-i(\boldsymbol{p}-\boldsymbol{q})\cdot\boldsymbol{R}}\hat{V}(\boldsymbol{q})\frac{M_{\boldsymbol{q}}V_\mu(\boldsymbol{p},-\Omega)M_{-\boldsymbol{q}}}{|h_{\boldsymbol{p}}|\Big(4|h_{\boldsymbol{p}}|^2+\Omega^2\Big)}, \tag{A.69}$$

where in the second line we switched the order of integration and shifted $\boldsymbol{p}\rightarrow\boldsymbol{p}-\boldsymbol{q}$, using the periodicity of the integrand. As the next step, we introduce the Fourier transform of the Coulomb potential

$$\int \frac{d^2q}{(2\pi)^2}\hat{V}(\boldsymbol{q})e^{+i\boldsymbol{q}\cdot\boldsymbol{R}} = \int_0^\infty \frac{dq}{(2\pi)^2}q\int_0^{2\pi} d\theta\frac{2\pi}{q}e^{+iqR\cos(\theta)} = \frac{1}{|\boldsymbol{R}|}\,, \tag{A.70}$$

in order to calculate the following expression

$$\begin{aligned} \int \frac{d^2q}{(2\pi)^2}e^{+i\boldsymbol{q}\cdot\boldsymbol{R}}M_{\boldsymbol{q}}V_\mu(\boldsymbol{p},-\Omega)M_{-\boldsymbol{q}} &= \int \frac{d^2q}{(2\pi)^2}\hat{V}(\boldsymbol{q})e^{+i\boldsymbol{q}\cdot\boldsymbol{R}}\begin{pmatrix} V_{\mu,11} & V_{\mu,12}e^{+iq_ya} \\ V_{\mu,21}e^{-iq_ya} & V_{\mu,22} \end{pmatrix} \\ &= \begin{pmatrix} V_{\mu,11}\frac{1}{|\boldsymbol{R}|} & V_{\mu,12}\frac{1}{|\boldsymbol{R}+a\hat{y}|} \\ V_{\mu,21}\frac{1}{|\boldsymbol{R}-a\hat{y}|} & V_{\mu,22}\frac{1}{|\boldsymbol{R}|} \end{pmatrix}\,, \end{aligned} \tag{A.71}$$

where we wrote out the explicit four components of $V_\mu(\boldsymbol{p}, -\Omega)$. The current-current correlation function of the vertex-correction can now be written as:

$$\begin{aligned}\chi_J^{(1,d)}(\mathrm{i}\omega) =& A\sum_{\boldsymbol{R}}\sum_{\boldsymbol{p},\boldsymbol{k}} \frac{1}{|h_{\boldsymbol{p}}|(4|h_{\boldsymbol{p}}|^2+\Omega^2)} \frac{1}{|h_{\boldsymbol{k}}|(4|h_{\boldsymbol{k}}|^2+\Omega^2)} \cdot e^{+i(\boldsymbol{p}-\boldsymbol{k})\cdot\boldsymbol{R}} \\ &\cdot \mathrm{Tr}\left[\begin{pmatrix} V_{\mu,11}(\boldsymbol{p},\Omega) & V_{\mu,12}(\boldsymbol{p},\Omega) \\ V_{\mu,21}(\boldsymbol{p},\Omega) & V_{\mu,22}(\boldsymbol{p},\Omega)\end{pmatrix} \begin{pmatrix} V_{\mu,11}(\boldsymbol{k},-\Omega)\frac{e^2}{|\boldsymbol{R}|} & V_{\mu,12}(\boldsymbol{k},-\Omega)\frac{e^2}{|\boldsymbol{R}+a\hat{y}|} \\ V_{\mu,21}(\boldsymbol{k},-\Omega)\frac{1}{|\boldsymbol{R}-a\hat{y}|} & V_{\mu,22}(\boldsymbol{k},-\Omega)\frac{1}{|\boldsymbol{R}|}\end{pmatrix}\right] .\end{aligned} \tag{A.72}$$

Evaluating the trace gives:

$$\begin{aligned}\chi_J^{(1,d)}(\mathrm{i}\omega) = e^2 A\sum_{\boldsymbol{R}}\sum_{\boldsymbol{p},\boldsymbol{k}} e^{+i(\boldsymbol{p}-\boldsymbol{k})\cdot\boldsymbol{R}} &\frac{1}{|h_{\boldsymbol{p}}|(4|h_{\boldsymbol{p}}|^2+\Omega^2)} \frac{1}{|h_{\boldsymbol{k}}|(4|h_{\boldsymbol{k}}|^2+\Omega^2)} \\ \times \Big[&\frac{V_{\mu,11}(\boldsymbol{p},\Omega)V_{\mu,11}(\boldsymbol{k},-\Omega) + V_{\mu,22}(\boldsymbol{p},\Omega)V_{\mu,22}(\boldsymbol{k},-\Omega)}{|\boldsymbol{R}|} \\ + &\frac{V_{\mu,12}(\boldsymbol{p},\Omega)V_{\mu,21}(\boldsymbol{k},-\Omega)}{|\boldsymbol{R}-a\hat{y}|} + \frac{V_{\mu,21}(\boldsymbol{p},\Omega)V_{\mu,12}(\boldsymbol{k},-\Omega)}{|\boldsymbol{R}+a\hat{y}|}\Big] .\end{aligned} \tag{A.73}$$

The matrix elements are given by:

$$\begin{aligned}V_{\mu,11}(\boldsymbol{p},\Omega)V_{\mu,11}(\boldsymbol{k},-\Omega) + V_{\mu,22}(\boldsymbol{p},\Omega)V_{\mu,22}(\boldsymbol{k},-\Omega) &= \frac{1}{2}\Omega^2\left[h^*_{\boldsymbol{p}}j_{\mu,\boldsymbol{p}} - h_{\boldsymbol{p}}j_{\mu,\boldsymbol{p}}{}^*\right]\left[h_{\boldsymbol{k}}{}^*j_{\mu,\boldsymbol{k}} - h_{\boldsymbol{k}}j_{\mu,\boldsymbol{k}}{}^*\right] \\ &= \frac{1}{2}\Omega^2\left[h_{\boldsymbol{p}}j_{\mu,\boldsymbol{p}}{}^* - h^*_{\boldsymbol{p}}j_{\mu,\boldsymbol{p}}\right]\left[h_{\boldsymbol{k}}j_{\mu,\boldsymbol{k}}{}^* - h_{\boldsymbol{k}}{}^*j_{\mu,\boldsymbol{k}}\right] ,\end{aligned} \tag{A.74}$$

$$\begin{aligned}V_{\mu,12}(\boldsymbol{p},\Omega)\cdot V_{\mu,21}(\boldsymbol{k},-\Omega)\frac{1}{|\boldsymbol{R}-a\hat{y}|} &= \frac{1}{|\boldsymbol{R}-a\hat{y}|}h_{\boldsymbol{k}}h^*_{\boldsymbol{p}}\left[h_{\boldsymbol{k}}j^*_\mu(\boldsymbol{k}) - h_{\boldsymbol{k}}{}^*j_{\mu,\boldsymbol{k}}\right]\left[h^*_{\boldsymbol{p}}j_{\mu,\boldsymbol{p}} - h_{\boldsymbol{p}}j^*_{\mu,\boldsymbol{p}}\right] \\ &= -\frac{h^*_{\boldsymbol{p}}h_{\boldsymbol{k}}}{|\boldsymbol{R}-a\hat{y}|}\left[h_{\boldsymbol{k}}j_{\mu,\boldsymbol{k}}{}^* - h_{\boldsymbol{k}}{}^*j_{\mu,\boldsymbol{k}}\right]\left[h_{\boldsymbol{p}}j_{\mu,\boldsymbol{p}}{}^* - h^*_{\boldsymbol{p}}j_{\mu,\boldsymbol{p}}\right] ,\end{aligned} \tag{A.75}$$

$$\begin{aligned}V_{\mu,21}(\boldsymbol{p},\Omega)V_{\mu,12}(\boldsymbol{k},-\Omega)\frac{1}{|\boldsymbol{R}+a\hat{y}|} &= \frac{1}{|\boldsymbol{R}+a\hat{y}|}h_{\boldsymbol{k}}{}^*h_{\boldsymbol{p}}\left[h_{\boldsymbol{k}}{}^*j_{\mu,\boldsymbol{k}} - h_{\boldsymbol{k}}j^*_\mu(\boldsymbol{k})\right]\left[h_{\boldsymbol{p}}j^*_\mu(\boldsymbol{p}) - h^*_{\boldsymbol{p}}j_{\mu,\boldsymbol{p}}\right] \\ &= -\frac{h_{\boldsymbol{p}}h_{\boldsymbol{k}}{}^*}{|\boldsymbol{R}+a\hat{y}|}\left[h_{\boldsymbol{k}}j_{\mu,\boldsymbol{k}}{}^* - h_{\boldsymbol{k}}{}^*j_{\mu,\boldsymbol{k}}\right]\left[h_{\boldsymbol{p}}j_{\mu,\boldsymbol{p}}{}^* - h^*_{\boldsymbol{p}}j_{\mu,\boldsymbol{p}}\right] .\end{aligned} \tag{A.76}$$

Next, we define the function

$$-\mathrm{i}\eta_\mu(\boldsymbol{p}) = h_{\boldsymbol{p}}j^*_{\mu,\boldsymbol{p}} - h^*_{\boldsymbol{p}}j_{\mu,\boldsymbol{p}} \tag{A.77}$$

and the coefficients:

$$C_{1,\mu}(\boldsymbol{R},\omega) = \text{P.V.}\sum_{\boldsymbol{p}} \frac{\eta_\mu(\boldsymbol{p})}{|h_{\boldsymbol{p}}|\left(4|h_{\boldsymbol{p}}|^2 - \Omega^2\right)} \cos\left(\boldsymbol{p}\cdot\boldsymbol{R}\right) \in \mathbb{R}\,, \tag{A.78}$$

$$C_{2,\mu}(\boldsymbol{R},\omega) = \text{P.V.}\sum_{\boldsymbol{p}} \frac{\eta_\mu(\boldsymbol{p})h_{\boldsymbol{p}}}{|h_{\boldsymbol{p}}|\left(4|h_{\boldsymbol{p}}|^2 - \Omega^2\right)} \cos\left(\boldsymbol{p}\cdot\boldsymbol{R}\right) \in \mathbb{R}\,, \tag{A.79}$$

$$S_{1,\mu}(\boldsymbol{R},\omega) = \text{P.V.}\sum_{\boldsymbol{p}} \frac{\eta_\mu(\boldsymbol{p})}{|h_{\boldsymbol{p}}|\left(4|h_{\boldsymbol{p}}|^2 - \Omega^2\right)} \sin\left(\boldsymbol{p}\cdot\boldsymbol{R}\right) = 0\,, \tag{A.80}$$

$$S_{2,\mu}(\boldsymbol{R},\omega) = \text{P.V.}\sum_{\boldsymbol{p}} \frac{\eta_\mu(\boldsymbol{p})h_{\boldsymbol{p}}}{|h_{\boldsymbol{p}}|\left(4|h_{\boldsymbol{p}}|^2 - \Omega^2\right)} \sin\left(\boldsymbol{p}\cdot\boldsymbol{R}\right) \in i\mathbb{R}\,, \tag{A.81}$$

where P.V. indicates that the corresponding integrals are principal value integrals. The principal value integrals are calculated by introducing the small parameter ϵ the following way:

$$\begin{aligned} C_{1,\mu}(\boldsymbol{R},\omega) &= \text{P.V.}\sum_{\boldsymbol{p}} \frac{\eta_\mu(\boldsymbol{p})}{|h_{\boldsymbol{p}}|\left(4|h_{\boldsymbol{p}}|^2 - \Omega^2\right)} \cos\left(\boldsymbol{p}\cdot\boldsymbol{R}\right) \in \mathbb{R} \\ &= \sum_{\boldsymbol{p}} \frac{\eta_\mu(\boldsymbol{p})}{|h_{\boldsymbol{p}}|}\frac{1}{4|h_{\boldsymbol{p}}|}\left(\frac{1}{2|h_{\boldsymbol{p}}| - \omega + i\epsilon} + \frac{1}{2|h_{\boldsymbol{p}}| + \omega}\right)\cos\left(\boldsymbol{p}\cdot\boldsymbol{R}\right)\,. \end{aligned} \tag{A.82}$$

We introduce the real functions

$$E_{j,\mu}(\boldsymbol{R},\omega) = C_{j,\mu}(\boldsymbol{R},\omega) - \mathrm{i}S_{j,\mu}(\boldsymbol{R},\omega) \in \mathbb{R}\,, \tag{A.83}$$

which are explicitly given by $E_{1,\mu} = C_{1,\mu}$ and $E_{2,\mu} = \mathrm{Re}(C_{2,\mu}) + \mathrm{Im}(S_{2,\mu})$. Using these definitions, we can rewrite the current-current correlator as:

$$\begin{aligned} \mathrm{Im}\,\chi_J^{(1,d)}(\omega) &= 2e^2A\sum_{\boldsymbol{R}}\sum_{\boldsymbol{p}} \frac{\eta_\mu(\boldsymbol{p})}{|h_{\boldsymbol{p}}|}\frac{\pi}{2\omega}\delta(\omega - 2|h_{\boldsymbol{p}}|) \\ &\times\left[\frac{\omega^2}{2|\boldsymbol{R}|}\cos\left(\boldsymbol{pR}\right)C_{1,\mu}(\boldsymbol{R},\omega) + \frac{2}{|\boldsymbol{R} - a\hat{y}|}E_{2,\mu}(\boldsymbol{R},\omega)\,\mathrm{Re}\left(e^{-\mathrm{i}\boldsymbol{pR}}h_{\boldsymbol{p}}\right)\right]\,. \end{aligned} \tag{A.84}$$

Defining now the functions:

$$\Gamma_{1,\mu}(\boldsymbol{p},\omega) = \sum_{\boldsymbol{R}} \frac{1}{2|\boldsymbol{R}|}C_{1,\mu}(\boldsymbol{R},\omega)\cos(\boldsymbol{pR}) \tag{A.85}$$

$$\Gamma_{2,\mu}(\boldsymbol{p},\omega) = \frac{1}{\omega^2}\sum_{\boldsymbol{R}} \frac{2}{|\boldsymbol{R} - a\hat{y}|}E_{2,\mu}(\boldsymbol{R},\omega)\,\mathrm{Re}\left(h_{\boldsymbol{p}}e^{-\mathrm{i}\boldsymbol{pR}}\right)\,, \tag{A.86}$$

we can rewrite

$$\mathrm{Im}\,\chi_J^{(1,d)}(\omega) = 2e^2A\sum_{\boldsymbol{p}} \frac{\eta_\mu(\boldsymbol{p})}{|h_{\boldsymbol{p}}|}\frac{\pi}{2\omega}\delta(\omega - 2|h_{\boldsymbol{p}}|)\omega^2\{\Gamma_{1,\mu}(\boldsymbol{p},\omega) + \Gamma_{2,\mu}(\boldsymbol{p},\omega)\}\,. \tag{A.87}$$

Evaluating the $\delta-$function gives

$$\begin{aligned}\operatorname{Im}\chi_J^{(1,d)}(\omega) &= 2e^2A\sum_{i=1}^{4}\int_{p_{y,-}}^{p_{y,+}}\frac{dp_y}{(2\pi)^2}\frac{\pi\eta_\mu(\boldsymbol{p})}{2|\partial_{p_x}|h_{\boldsymbol{p}}|\big|_{p_{x,i}}|}\{\Gamma_{1,\mu}(\boldsymbol{p},\omega)+\Gamma_{2,\mu}(\boldsymbol{p},\omega)\} \\ &= e^2A\sum_{i=1}^{4}\int_{p_{y,-}}^{p_{y,+}}\frac{dp_y}{4\pi}\frac{\eta_\mu(\boldsymbol{p})}{|\partial_{p_x}|h_{\boldsymbol{p}}|\big|_{p_{x,i}}|}\{\Gamma_{1,\mu}(\boldsymbol{p},\omega)+\Gamma_{2,\mu}(\boldsymbol{p},\omega)\}\,.\end{aligned} \tag{A.88}$$

Hence, to determine the contribution of the vertex diagram to the correction coefficient, the above expression has been evaluated.

A.2.3 Correction coefficient in the Dirac model

Here, we present a calculation of the correction coefficient in the Dirac model by combining a soft cut-off acting on the Coulomb interaction, $V(\boldsymbol{r}) \to V_\eta(\boldsymbol{r})$, and the dimensional regularization (DR), $d = 2-\epsilon$, and demonstrate explicitly that the order of limits of the two parameters η and ϵ does not commute. We refer to this non commuting of the order of limits as the UV quirk.

The Coulomb potential and the self-energy

The deformed Coulomb interaction is given by the potential

$$V(\boldsymbol{r}) = \frac{e^2}{r}\left(\frac{r}{r_0}\right)^{\eta}\left(\frac{r}{r_0}\right)^{\epsilon}. \tag{A.89}$$

where we introduced the length scale r_0 in such a way that the dimensionality of the Coulomb potential stays unchanged. The Fourier transform of this potential in $d = 2-\epsilon$ dimensions is

$$V(\boldsymbol{q}) = \frac{2\pi e^2 r_0^{-(\eta+\epsilon)}\zeta_{\eta\epsilon}}{q^{1+\eta}} \qquad \text{with} \qquad \zeta_{\eta\epsilon} = \frac{2^\eta\pi^{-\epsilon/2}\Gamma\left(\frac{1+\eta}{2}\right)}{\Gamma\left(\frac{1-\eta-\epsilon}{2}\right)}\,. \tag{A.90}$$

Next, we define the parameter dependent coupling constant

$$\alpha_{\eta\epsilon} = \alpha r_0^{-(\eta+\epsilon)}\zeta_{\eta\epsilon}\,. \tag{A.91}$$

As the next step, the self-energy is evaluated by using the Feynman parametrization[1] and a shift in momentum $\boldsymbol{q} \to \boldsymbol{q} - y\boldsymbol{p}$ which yields

$$\begin{aligned}\Sigma(\boldsymbol{p}) &= \Phi(p)\boldsymbol{p}\boldsymbol{\sigma} \\ &= -2\pi\alpha_{\eta\epsilon}\int\frac{d\omega}{2\pi}\frac{d^dq}{(2\pi)^d}\frac{1}{|\boldsymbol{p}-\boldsymbol{q}|^{1+\eta}}G_{\boldsymbol{q},\mathrm{i}\omega} \\ &= \frac{\pi\alpha_{\eta\epsilon}}{(4\pi)^{d/2}}\frac{\Gamma\left(1+\frac{\eta}{2}-\frac{D}{2}\right)\Gamma\left(\frac{d+1}{2}\right)\Gamma\left(\frac{D-\eta-1}{2}\right)}{\Gamma\left(\frac{1}{2}+\frac{\eta}{2}\right)\Gamma\left(\frac{1}{2}\right)\Gamma\left(d-\frac{\eta}{2}\right)}\frac{\boldsymbol{p}\cdot\boldsymbol{\sigma}}{|\boldsymbol{p}|^{2+\eta-d}}\,,\end{aligned} \tag{A.92}$$

---

[1] Here, the Feynman parametrization is given by $\frac{1}{A^\alpha B^\beta} = \frac{\Gamma(\alpha+\beta)}{\Gamma(\alpha)\Gamma(\beta)}\int_0^1 dy\,\frac{y^{\alpha-1}(1-y)^{\beta-1}}{[yA+(1-y)B]^{\alpha+\beta}}$. Furthermore, in the following we use the Feynman integrals $\int\frac{d^dl}{(2\pi)^d}\frac{1}{(l^2+\Delta)^n} = \frac{\Gamma(n-d/2)}{(4\pi)^{d/2}\Gamma(n)}\frac{1}{\Delta^{n-d/2}}$ and $\int\frac{d^dl}{(2\pi)^d}\frac{l^2}{(l^2+\Delta)^n} = \frac{1}{(4\pi)^{d/2}}\frac{d}{2}\frac{\Gamma(n-1-d/2)}{\Gamma(n)}\frac{1}{\Delta^{n-1-d/2}}$.

with $d = 2 - \epsilon$. Thus, $\Phi(p)$ is defined as

$$\Phi(p) = A_{\eta\epsilon} \cdot p^{D-2-\eta} \tag{A.93}$$

with

$$A_{\eta\epsilon} = \frac{\pi\alpha r_0^{-(\eta+\epsilon)}}{(4\pi)^{d/2}} \frac{2^{\eta}\pi^{-\epsilon/2}\Gamma\left(1+\frac{\eta-D}{2}\right)\Gamma\left(\frac{d+1}{2}\right)\Gamma\left(\frac{d-\eta-1}{2}\right)}{\Gamma\left(\frac{1-\eta-\epsilon}{2}\right)\Gamma\left(\frac{1}{2}\right)\Gamma\left(d-\frac{\eta}{2}\right)} . \tag{A.94}$$

Now, we can start to evaluate the self-energy diagram and the vertex diagram. Let us start with the self-energy diagram.

The self-energy diagram

In order to calculate the correction of the conductivity due to the self energy, we evaluate the corresponding Feynman diagram. The diagram is thus given by the following expression:

$$\begin{aligned} \chi_J^{(1,bc)}(\mathrm{i}\Omega) &= -2N_{sv} \int_{\boldsymbol{p}} \int_{\omega} \mathrm{Tr}\left(G_{\boldsymbol{p},\mathrm{i}(\omega+\Omega)} j_\mu G_{\boldsymbol{p},\mathrm{i}\omega} \Sigma(\boldsymbol{p}) G_{\boldsymbol{p},\mathrm{i}\omega} j_\mu\right) \\ &= -2N_{sv} \int \frac{d^dp}{(2\pi)^d} \frac{d\omega}{2\pi} \frac{\Phi(p)}{p^2+(\omega+\Omega)^2} \frac{1}{\left(p^2+\omega^2\right)^2} \\ &\quad \times \mathrm{Tr}\left[(\mathrm{i}\omega+\boldsymbol{\sigma p})(i(\omega+\Omega)+2\sigma_x p_x-\boldsymbol{\sigma}\cdot\boldsymbol{p})(\mathrm{i}\omega+\boldsymbol{\sigma}\cdot\boldsymbol{p})\boldsymbol{\sigma}\cdot\boldsymbol{p}\right] , \end{aligned} \tag{A.95}$$

where $\Phi(p)$ is determined by the self-energy and is defined in equation (A.93). Next, we perform the trace over the Pauli matrices. Thereby, it is important to take into account that the Pauli matrices living in d dimensions are defined by the Clifford algebra $\{\sigma_a, \sigma_b\} = 2\delta_{a,b}$. Using the Clifford algebra, the following relations can be derived

$$\begin{aligned} &\sum_a \sigma_a\sigma_\mu\sigma_a = d\ \delta_{0,\mu}\sigma_0 + (2-d)\sum_a \sigma_a\delta_{a,\mu} , \\ &\sum_a \sigma_a^2 = d\sigma_0 , \quad \mathrm{Tr}(\sum_a \sigma_a^2 = d^2) , \quad \mathrm{Tr}(\sigma_0) = d , \quad \mathrm{Tr}(\sigma_a) = 0 , \end{aligned} \tag{A.96}$$

where Roman letters are spatial indices and Greek letters denote spacetime indices. Upon applying these relations, we can perform the trace over the Pauli matrices which yields

$$\chi_J^{(1,bc)}(\mathrm{i}\Omega) = -2N_{sv} \int \frac{d^dp}{(2\pi)^d} \frac{d\omega}{2\pi} \frac{\Phi(p)}{p^2+(\omega+\Omega)^2} \frac{d}{\left(p^2+\omega^2\right)^2} \left\{-2\omega(\omega+\Omega)p^2 + \left(1-\frac{2}{d}\right)\left(\omega^2-p^2\right)p^2\right\} . \tag{A.97}$$

Next, we integrate over the frequency and obtain

$$\chi_J^{(1,bc)}(\mathrm{i}\Omega) = 2N_{sv} d\left(1-\frac{1}{d}\right) \int \frac{d^dp}{(2\pi)^d} \frac{\Phi(p)p(4p^2-\Omega^2)}{(4p^2+\Omega^2)^2} . \tag{A.98}$$

Inserting $\Phi(p) = A_{\eta\epsilon} p^{D-2-\eta}$ yields

$$\begin{aligned} \chi_J^{(1,bc)}(\mathrm{i}\Omega) &= 2N_{sv} d(1-1/d) \int \frac{d^dp}{(2\pi)^d} \frac{A_{\eta\epsilon} p^{d-2-\eta}\ p(4p^2-\Omega^2)}{(4p^2+\Omega^2)^2} \\ &= 4N_{sv} d(1-1/d) \frac{\pi^{d/2} A_{\eta\epsilon}}{(2\pi)^d \Gamma\left(d/2\right)} \int_0^\infty dp \frac{p^{2d-2-\eta}(4p^2-\Omega^2)}{(4p^2+\Omega^2)^2} . \end{aligned} \tag{A.99}$$

Since we want to calculate the imaginary part on the real axis, the zero frequency part is subtracted and we find

$$\chi_J^{(1,bc)}(\mathrm{i}\Omega) - \chi_J^{(1,bc)}(0) = -\frac{N_{sv} d(1-1/d)\pi^{d/2} A_{\eta\epsilon}}{(2\pi)^d \Gamma(d/2)} \int_0^\infty dp \frac{p^{-4+2d-\eta}\Omega^2(12p^2+\Omega^2)}{(4p^2+\Omega^2)^2} \,. \tag{A.100}$$

Substituting $x = p/\Omega$ yields

$$\begin{aligned} \chi_J^{(1,bc)}(\mathrm{i}\Omega) - \chi_J^{(1,bc)}(0) &= -\frac{N_{sv} d(1-1/d)\pi^{d/2} A_{\eta\epsilon}\Omega\Omega^{-4+2d-\eta}}{(2\pi)^d \Gamma(d/2)} \int_0^\infty dx \frac{(12x^2+1)x^{-4+2D-\eta}}{(4x^2+1)^2} \\ &= -\frac{N d(1-1/d)\pi^{d/2} A_{\eta\epsilon}\Omega\Omega^{-4+2d-\eta}}{(2\pi)^d \Gamma(d/2)} 2^{2-2d+\eta}\pi(2d-2-\eta)\sec\left(d\pi - \frac{\pi\eta}{2}\right) . \end{aligned} \tag{A.101}$$

In $d = 2$ dimensions the expression $(\chi_J^{(1,bc)}(\mathrm{i}\Omega) - \chi_J^{(1,bc)}(0))/\Omega$ is dimensionless. But if we go to $d = 2-\epsilon$ dimensions, the expression gains the dimension L^ϵ, where L is a length scale. Hence, before expanding the expression, we have to multiply it with the factor $r_0^{-\epsilon}$. Now, we set $d = 2-\epsilon$ in the above expression and expand our result for small but finite ϵ and η. This yields

$$\begin{aligned} r_0^{-\epsilon} \cdot \frac{\chi_J^{(1,bc)}(\mathrm{i}\Omega) - \chi_J^{(1,bc)}(0)}{\Omega} \approx &- \frac{N_{sv}\alpha}{32(\eta+\epsilon)} + \\ &+ \frac{N\alpha}{32(\epsilon+\eta)} \Big[\eta\{\gamma - \log(4/(r_0\Omega))\} + \\ &\quad + \epsilon\{1 + 2\gamma - 2\log\left(4/(r_0\Omega)\right) + 1/2(2-\gamma-\log(4\pi))\}\Big] . \end{aligned} \tag{A.102}$$

The self-energy diagram is divergent in $1/(\epsilon+\eta)$ for $\eta, \epsilon \to 0$. The vertex diagram cancels this divergence.

The vertex diagram

The vertex diagram is defined as

$$\chi_J^{(1,d)}(\mathrm{i}\Omega) = N_{sv} \int \frac{d^d p}{(2\pi)^d} \frac{d\omega}{2\pi} \int \frac{d^d q}{(2\pi)^d} \frac{d\omega'}{2\pi\alpha_{\eta\epsilon}} \frac{2\pi\alpha_{\eta\epsilon}}{|\boldsymbol{p}-\boldsymbol{q}|^{(1+\eta)}} \operatorname{Tr}\left[G_{\boldsymbol{p},\mathrm{i}\omega} j_\mu G_{\boldsymbol{p},\mathrm{i}(\omega+\Omega)} G_{\boldsymbol{q},\mathrm{i}(\omega'+\Omega)} j_\mu G_{\boldsymbol{q},\mathrm{i}\omega'}\right] . \tag{A.103}$$

Performing the trace over the Pauli matrices and the frequency integration yields

$$\begin{aligned} \chi_J^{(1,d)}(\mathrm{i}\Omega) = 2\pi N_{sv}\alpha_{\eta\epsilon} \int \frac{d^D p}{(2\pi)^D} \int \frac{d^d q}{(2\pi)^d} \frac{1}{|\boldsymbol{p}-\boldsymbol{q}|^{1+\eta}} \frac{d}{pq(4p^2+\Omega^2)(4q^2+\Omega^2)} \times \\ \times \left[\Omega^2(p_x q_x - \boldsymbol{pq}) + 4(p_x q_x \boldsymbol{pq} + p^2q^2 - p^2q_x^2 - p_x^2q^2)\right] . \end{aligned} \tag{A.104}$$

As for the self-energy diagram, we have to subtract the zero-frequency part of the correlation function which results in

$$\begin{aligned} \chi_J^{(1,d)}(\mathrm{i}\Omega) - \chi_J^{(1,d)}(0) = -N_{sv} \int \frac{d^d p}{(2\pi)^d} \int \frac{d^d q}{(2\pi)^d} \frac{2\pi\alpha_{\eta\epsilon}}{|\boldsymbol{p}-\boldsymbol{q}|^{1+\eta}} \frac{d\ \Omega^2}{4p^3q^3(4p^2+\Omega^2)(4q^2+\Omega^2)} \times \\ \times \left\{4p^2q^2(\boldsymbol{pq} - p_x q_x) + (\boldsymbol{pq} q_x p_x + p^2q^2 - p_x^2q^2 - p^2q_x^2)(\Omega^2 + 4(p^2+q^2))\right\} , \end{aligned} \tag{A.105}$$

or equivalently

$$\begin{aligned}\chi_J^{(1,d)}(\mathrm{i}\Omega) - \chi_J^{(1,d)}(0) = -N_{sv}\int \frac{d^dp}{(2\pi)^d}\frac{d^dq}{(2\pi)^d}&\frac{\pi\alpha_{\eta\epsilon} d\;\Omega}{8p^3q^3\left(p^2+(\Omega/2)^2\right)\left(q^2+(\Omega/2)^2\right)}\\ &\frac{p^2q^2(\boldsymbol{pq}-q_xp_x)+(\boldsymbol{qp}q_xp_x+p^2q^2-p_x^2q^2-p^2q_x^2)(p^2+q^2+(\Omega/2)^2)}{|\boldsymbol{p}-\boldsymbol{q}|^{1+\eta}}\,.\end{aligned} \tag{A.106}$$

Next, we split up this integral in two separate integrals. (One integral contains the divergent part while the other is convergent for $\eta = 0$ and $\epsilon = 0$.) These integrals are defined as

$$\left.\frac{\chi_J^{(1,d)}(\mathrm{i}\Omega) - \chi_J^{(1,d)}(0)}{\Omega}\right|_1 = \frac{-N_{sv}\pi\alpha_{\eta\epsilon} d\;\Omega}{8}\int \frac{d^dp}{(2\pi)^d}\frac{d^dq}{(2\pi)^d}\frac{\boldsymbol{pq}-q_xp_x}{pq(p^2+(\Omega/2)^2)(q^2+(\Omega/2)^2)|\boldsymbol{p}-\boldsymbol{q}|^{1+\eta}}\,, \tag{A.107}$$

and

$$\begin{aligned}\left.\frac{\chi_J^{(1,d)}(\mathrm{i}\Omega) - \chi_J^{(1,d)}(0)}{\Omega}\right|_2 = -N_{sv}\int \frac{d^dp}{(2\pi)^d}\frac{d^dq}{(2\pi)^d}&\frac{\pi\alpha_{\eta\epsilon} d\;\Omega}{8p^3q^3\left(p^2+(\Omega/2)^2\right)\left(q^2+(\Omega/2)^2\right)}\\ &\frac{(\boldsymbol{qp}q_xp_x+p^2q^2-p_x^2q^2-p^2q_x^2)(p^2+q^2+(\Omega/2)^2)}{|\boldsymbol{p}-\boldsymbol{q}|^{1+\eta}}\,.\end{aligned} \tag{A.108}$$

We split the last integral in three different parts by adding and subtracting $(\Omega/2)^2$. By this procedure, we separate the diverging part of the above integral from the convergent one. It reads

$$\begin{aligned}\left.\frac{\chi_J^{(1,d)}(\mathrm{i}\Omega) - \chi_J^{(1,d)}(0)}{\Omega}\right|_{2,a} &= -N_{sv}\int \frac{d^dp}{(2\pi)^d}\frac{d^dq}{(2\pi)^d}\frac{\pi\alpha_{\eta\epsilon}\; d\;\Omega}{8p^3q^3\left(p^2+(\Omega/2)^2\right)\left(q^2+(\Omega/2)^2\right)}\\ &\qquad\frac{(\boldsymbol{qp}q_xp_x+p^2q^2-p_x^2q^2-p^2q_x^2)(p^2+(\Omega/2)^2+q^2+(\Omega/2)^2)}{|\boldsymbol{p}-\boldsymbol{q}|^{1+\eta}}\\ &= \frac{-\pi\alpha_{\eta\epsilon}\; d\;\Omega}{4}\int \frac{d^dp}{(2\pi)^d}\frac{d^dq}{(2\pi)^d}\frac{\boldsymbol{pq}q_xp_x+p^2q^2-p_x^2q^2-p^2q_x^2}{p^3q^3(q^2+(\Omega/2)^2)|\boldsymbol{p}-\boldsymbol{q}|^{1+\eta}}\,,\end{aligned} \tag{A.109}$$

$$\left.\frac{\chi_J^{(1,d)}(\mathrm{i}\Omega) - \chi_J^{(1,d)}(0)}{\Omega}\right|_{2,b} = \frac{+N_{sv}\pi\alpha_{\eta\epsilon} d\;\Omega^3}{32}\int \frac{d^dp}{(2\pi)^d}\frac{d^dq}{(2\pi)^d}\frac{1}{pq(p^2+(\Omega/2)^2)(q^2+(\Omega/2)^2)|\boldsymbol{p}-\boldsymbol{q}|^{1+\eta}}\,, \tag{A.110}$$

and

$$\begin{aligned}\left.\frac{\chi_J^{(1,d)}(\mathrm{i}\Omega) - \chi_J^{(1,d)}(0)}{\Omega}\right|_{2,c} &= \frac{+N_{sv}\pi\alpha_{\eta\epsilon}\; d\;\Omega^3}{32}\int \frac{d^dp}{(2\pi)^d}\frac{d^dq}{(2\pi)^d}\frac{\boldsymbol{pq}p_xq_x-p_x^2q^2-p^2q_x^2}{p^3q^3(p^2+(\Omega/2)^2)(q^2+(\Omega/2)^2)|\boldsymbol{p}-\boldsymbol{q}|^{1+\eta}}\\ &= \frac{+N_{sv}\pi\alpha_{\eta\epsilon}\; d\;\Omega^3}{32}\int \frac{d^dp}{(2\pi)^d}\frac{d^dq}{(2\pi)^d}\frac{\boldsymbol{pq}p_xq_x-2p^2q_x^2}{p^3q^3(p^2+(\Omega/2)^2)(q^2+(\Omega/2)^2)|\boldsymbol{p}-\boldsymbol{q}|^{1+\eta}},\,,\end{aligned} \tag{A.111}$$

where we used rotational symmetry. The integral $[\chi_J^{(1,d)}(\mathrm{i}\Omega)-\chi_J^{(1,d)}(0)]/\Omega|_{2,a}$ is divergent for $(\eta,\epsilon)\to 0$, while the remaining integrals exhibit a finite value for $eta, \epsilon = 0$. This finite value is

$$\left.\frac{\chi_J^{(1,d)}(\mathrm{i}\Omega) - \chi_J^{(1,d)}(0)}{\Omega}\right|_1 + \left.\frac{\chi_J^{(1,d)}(\mathrm{i}\Omega) - \chi_J^{(1,d)}(0)}{\Omega}\right|_{2,b} + \left.\frac{\chi_J^{(1,d)}(\mathrm{i}\Omega) - \chi_J^{(1,d)}(0)}{\Omega}\right|_{2,c} = \frac{N_{sv}\alpha}{32}\left(\pi-\frac{8}{3}\right)\,. \tag{A.112}$$

Now let us calculate the divergent part, which corresponds to the integral (A.109). The Feynman parametrization[2] and the shift in momentum is again used to solve this integral which leads to the following expression

$$\begin{aligned}
\left.\frac{\chi_J^{(1,d)}(\mathrm{i}\Omega)-\chi_J^{(1,d)}(0)}{\Omega}\right|_{2,a} &= \frac{-N_{sv}\pi\alpha_{\eta\epsilon}\ d\ \Omega}{4}\int\frac{d^dp}{(2\pi)^d}\frac{d^dq}{(2\pi)^d}\frac{\boldsymbol{p}\boldsymbol{q}q_xp_x+p^2q^2-p_x^2q^2-p^2q_x^2}{p^3q^3(q^2+(\Omega/2)^2)|\boldsymbol{p}-\boldsymbol{q}|^{1+\eta}} \\
&= \frac{-N_{sv}\pi\alpha_{\eta\epsilon}\ d\ \Omega}{4}\frac{2\Gamma[3+\eta/2]}{\sqrt{\pi}\Gamma\left[\frac{1+\eta}{2}\right]}\int_0^1 dx\int_0^{1-x}dy(1-x-y)^{1/2}x^{-1/2+\eta/2}\times \\
&\times\int\frac{d^dp}{(2\pi)^d}\frac{d^dl}{(2\pi)^d}\underbrace{\frac{p^2-p_x^2}{p^3}}_{=(1-1/d)\frac{1}{p}}\frac{x^2p^2+(1-1/d)l^2}{\left[l^2+p^2x(1-x)+y(\Omega/2)^2\right]^{3+\eta/2}} \\
&= -\frac{\pi\alpha_{\eta\epsilon}N_{sv}2^{3-2d+\eta}\Omega^{2d-4-\eta}\ d\ (1-1/d)}{(4\pi)^d\sqrt{\pi}}\times \\
&\times\frac{\Gamma\left[\frac{d+1}{2}\right]\Gamma\left[\frac{5}{2}-d+\frac{\eta}{2}\right]\Gamma\left[d-\frac{3}{2}-\frac{\eta}{2}\right]\Gamma\left[1-\frac{d}{2}+\frac{\eta}{2}\right]\Gamma\left[\frac{d-1-\eta}{2}\right]}{\Gamma\left[\frac{1+\eta}{2}\right]\Gamma\left[\frac{d}{2}\right]\Gamma\left[d-\frac{\eta}{2}\right]}\,.
\end{aligned} \tag{A.113}$$

Next, we expand the dimensionless expression for small η and ϵ and obtain

$$\begin{aligned}
r_0^{-\epsilon}\left.\frac{\chi_J^{(1,d)}(\mathrm{i}\Omega)-\chi_J^{(1,d)}(0)}{\Omega}\right|_{2,a} \approx &-\frac{N_{sv}\alpha}{32(\eta+\epsilon)}+ \\
&+\frac{N_{sv}\alpha}{32(\epsilon+\eta)}\Big[\eta(-1/2+\gamma-\log(4/(r_0\Omega)))+ \\
&+\epsilon\{2\gamma-2\log\left(4/(r_0\Omega)\right)+1/2(2-\gamma-\log(4\pi))\}\Big]\,.
\end{aligned} \tag{A.114}$$

Also the vertex diagram is divergent in $1/(\eta+\epsilon)$ for $(\eta,\epsilon)\to 0$. This divergence cancels the divergence of the self-energy diagram and we obtain a finite correction value.

The correction coefficient

Upon adding the vertex diagram and the self-energy, we find the following correction coefficient

$$\mathcal{C}_\sigma(\eta,\epsilon)=\frac{1}{\eta+\epsilon}\left(\frac{(16-6\pi)(\eta+\epsilon)+3\eta+6\epsilon}{12}\right)\,. \tag{A.115}$$

Depending if we first set $\eta\to 0$ and then $\epsilon\to 0$ or vice versa, we either obtain $\tilde{\mathcal{C}_\sigma}$ or $\mathcal{C}_\sigma$. Only when we take the limit $\eta\to 0$ at the very end of the calculation, the correct value $\mathcal{C}_\sigma=(19-6\pi)/12$ is found.

---

[2] The Feynman parametrization is given by $\frac{1}{A^\alpha B^\beta C^\gamma}=\frac{\Gamma[\alpha+\beta+\gamma]}{\Gamma[\alpha]\Gamma[\beta]\Gamma[\gamma]}\int_0^1 dx\int_0^{1-x}dy\frac{(1-x-y)^{\alpha-1}x^{\beta-1}y^{\gamma-1}}{[(1-x-y)A+xB+yC]^{\alpha+\beta+\gamma}}$.

A.3 Viscosity in the collisionless regime

In this section we give a detailed description of the calculation of the viscosity of graphene in the collisionless regime. In order to determine the viscosity, the Kubo formula (3.36), $\eta_{\alpha\beta\gamma\delta} = \operatorname{Im}\chi_{T_{\alpha\beta}T_{\gamma\delta}}/\omega$, is used. As for the optical conductivity, we expand the correlation function between the energy-stress tensor $T_{\alpha\beta}$ to leading order in the renormalized coupling constant $\alpha(\omega)$, i. e., $\chi_{T_{xy}T_{xy}} = \chi^{(0)}_{T_{xy}T_{xy}} + \chi^{(1)}_{T_{xy}T_{xy}}$. First, we start with the calculation of the viscosity described by free Dirac fermions $\eta_0(\omega)$, before we determine the Feynman diagrams in leading order of $\alpha(\omega)$ which contribute to the correction coefficient $\mathcal{C}_\eta$. This calculation is performed in the Dirac model.

A.3.1 Non-interacting part of the viscosity

In order to calculate the shear viscosity η of graphene, we have to use the symmetrized energy-stress $T^{(0)}_{\alpha\beta}(\boldsymbol{k})$, as we have seen in Sec. 6.2.1. The correlation function in zeroth order of the coupling constant is given by

$$\begin{aligned}
\chi_{T^{(0)}_{xy},T^{(0)}_{xy}}(\mathrm{i}\omega) &= N_{sv}\int_{\boldsymbol{p}}\int_{\omega} \operatorname{Tr}\left[G_{\boldsymbol{p},\mathrm{i}(\omega+\Omega)}T^{(0)}_{xy}(\boldsymbol{p})G_{\boldsymbol{p},\mathrm{i}\omega}T^{(0)}_{xy}(\boldsymbol{p})\right] \\
&= N_{sv}\int_{\boldsymbol{p}}\int_{\omega} \frac{1}{4}\frac{1}{p^2+(\omega+\Omega)^2}\frac{1}{p^2+\omega^2}\operatorname{Tr}\left[\mathcal{M}\right] \\
&= \int_{\boldsymbol{p}}\int_{\omega} \frac{N_{sv}}{p^2+(\omega+\Omega)^2}\frac{1}{p^2+\omega^2}\left[p_x^4 + p_x^2\left(\omega(\omega+\Omega)-6p_y^2\right)+p_y^2\left(p_y^2+\omega(\omega+\Omega)\right)\right] ,
\end{aligned} \tag{A.116}$$

where $\mathcal{M}$ is

$$\mathcal{M} = \begin{pmatrix} \mathrm{i}(\omega+\Omega) & p_x-\mathrm{i}p_y \\ p_x+\mathrm{i}p_y & \mathrm{i}(\omega+\Omega)\end{pmatrix}\begin{pmatrix} 0 & p_y-\mathrm{i}p_x \\ p_y+\mathrm{i}p_x & 0\end{pmatrix}\begin{pmatrix} \mathrm{i}\omega & p_x-\mathrm{i}p_y \\ p_x+\mathrm{i}p_y & \mathrm{i}\omega\end{pmatrix}\begin{pmatrix} 0 & p_y-\mathrm{i}p_x \\ p_y+\mathrm{i}p_x & 0\end{pmatrix} . \tag{A.117}$$

Performing the frequency and angle integration, yields

$$\begin{aligned}
\chi_{T^{(0)}_{xy},T^{(0)}_{xy}}(\mathrm{i}\omega) &= \frac{N_{sv}}{2}\int\frac{d^2p}{(2\pi)^2}\frac{p^2\left(p_x^2+p_y^2\right)+p_x^4-6p_x^2p_y^2+p_y^4}{p\left(4p^2+\Omega^2\right)} \\
&= \frac{N_{sv}}{2}\int_0^\infty\frac{dp}{2\pi}\frac{p^4}{\left(4p^2+\Omega^2\right)} .
\end{aligned} \tag{A.118}$$

Now, we use the analytical continuation $\mathrm{i}\Omega \to \omega + \mathrm{i}\delta$ and obtain

$$\frac{1}{4p^2+\Omega^2} = \mathrm{P.V.}\left[\frac{1}{4p^2-\omega^2}\right] + \frac{\mathrm{i}\pi}{2\omega}\delta(2p+\omega) + \frac{\mathrm{i}\pi}{2\omega}\delta(2p-\omega) . \tag{A.119}$$

Taking the imaginary part of the correlation function and choosing $\omega > 0$, gives

$$\begin{aligned}
\operatorname{Im}\chi_{T^{(0)}_{xy},T^{(0)}_{xy}}(\omega) &= \frac{N_{sv}}{2}\int_0^\infty\frac{dp}{2\pi}\,p^4\frac{\pi}{2\omega}\delta(2p-\omega) \\
&= \frac{N_{sv}}{256}\omega^3 .
\end{aligned} \tag{A.120}$$

The shear viscosity for the non-interacting graphene is thus

$$\mathrm{Re}\;\eta(\omega) = \frac{\omega^2}{64}\frac{\hbar}{v_{\mathrm{F}}^2}\,, \tag{A.121}$$

where we reinstalled $\hbar$ and v_{F} which were set to one during the calculation and we inserted that $N_{sv} = 4$, since there are two spin degrees of freedom and two Dirac cones.

A.3.2 Correction coefficient of the viscosity in the collisionless regime

Now let us answer the question how the Coulomb interaction influences the viscosity. To this end, we have (as shown in Sec. 6.2.2) to evaluate the *self-energy diagram*, the *vertex diagram* and the *honey diagram*. In this section, we give a detailed presentation of the calculation of the different diagrams. To evaluate the different diagrams, we introduce a soft cut-off to the Coulomb interaction $V_\eta(\boldsymbol{q}) = 2\pi\alpha/\boldsymbol{q}^{1+\eta}$ where the parameter η regularizes the integrals.

The self-energy diagram

We start with the evaluation of the self-energy diagram. The self-energy is given by

$$\Sigma(\boldsymbol{k}) = \phi(\boldsymbol{k})\boldsymbol{k}\cdot\boldsymbol{\sigma} \tag{A.122}$$

with

$$\phi(\boldsymbol{k}) = \mathcal{A}k^{-\eta} = \alpha r_0^{-\eta}\frac{2^\eta\,\Gamma\left(\frac{\eta}{2}\right)}{8\,\Gamma\left(\frac{4-\eta}{2}\right)}k^{-\eta}\,, \tag{A.123}$$

where the parameter η regularizes the self energy. Now the correlation function of the self-energy diagram is defined as

$$\begin{aligned}\chi^{(1,bc)}_{T^{(0)}_{xy}T^{(0)}_{xy}}(\mathrm{i}\Omega) &= -2\int_P \mathrm{Tr}\left[G_{\boldsymbol{p},\mathrm{i}(\omega+\Omega)}T^{(0)}_{xy}(\boldsymbol{p})G_{\boldsymbol{p},\mathrm{i}\omega}\Sigma(\boldsymbol{p})G_{\boldsymbol{p},\mathrm{i}\omega}T^{(0)}_{xy}(\boldsymbol{p})\right]\\ &= -\alpha r_0^{-\eta}\frac{1}{2}\frac{2^\eta\,\Gamma\left(\frac{\eta}{2}\right)}{8\,\Gamma\left(\frac{4-\eta}{2}\right)}\int\frac{\mathrm{d}^2k}{(2\pi)^2}\int\frac{\mathrm{d}\omega}{2\pi}\frac{p^{-\eta}}{(k^2+(\omega+\Omega)^2)}\frac{1}{(k^2+\omega^2)^2}\,\mathrm{Tr}(\mathcal{B})\end{aligned} \tag{A.124}$$

with

$$\begin{aligned}&\mathrm{Tr}(\mathcal{B})\\ &= \mathrm{Tr}\Big[(\mathrm{i}(\omega+\Omega)\sigma_0 + k_x\sigma_x + k_y\sigma_y)(k_x\sigma_y + k_y\sigma_x)(\mathrm{i}\omega\sigma_0 + k_x\sigma_x + k_y\sigma_y)(k_x\sigma_x + k_y\sigma_y)\\ &\times(\mathrm{i}\omega\sigma_0 + k_x\sigma_x + k_y\sigma_y)(k_x\sigma_y + k_y\sigma_x)\Big]\\ &= -2k_x(k_x+k_y)\Big(k_x^4 + k_x^2\Big[\omega(\omega+2\Omega) - 10k_y^2\Big] + k_y^2\Big[5\left(k_y^2+\omega^2\right) + 2\omega\Omega\Big]\Big)\,.\end{aligned} \tag{A.125}$$

After performing the frequency integral and the integration over the angle, we obtain

$$\chi^{(1,bc)}_{T^{(0)}_{xy}T^{(0)}_{xy}}(\mathrm{i}\Omega) = \int_0^\infty \mathrm{d}k\frac{2^{\eta-6}\Gamma\left(\frac{\eta}{2}\right)k^{4-\eta}\left(4k^2-\Omega^2\right)}{\pi\Gamma\left(2-\frac{\eta}{2}\right)\left(4k^2+\Omega^2\right)^2}\,. \tag{A.126}$$

Next, we have to calculate the difference

$$f^{(1,bc)}_{xyxy}(\mathrm{i}\Omega) = \frac{\chi_{T^{(0)}_{xy}T^{(0)}_{xy}}(\mathrm{i}\Omega) - \chi_{T^{(0)}_{xy}T^{(0)}_{xy}}(0)}{\Omega^2} = -\int_0^\infty \mathrm{d}k \frac{2^{\eta-8}\Gamma\left(\frac{\eta}{2}\right) k^{2-\eta}\left(12k^2+\Omega^2\right)}{\pi\Gamma\left(2-\frac{\eta}{2}\right)\left(4k^2+\Omega^2\right)^2} \tag{A.127}$$

and

$$\begin{aligned}\frac{f^{(1,bc)}_{xyxy}(\mathrm{i}\Omega) - f^{(1,bc)}_{xyxy}(0)}{\Omega} &= \int_0^\infty \mathrm{d}k \frac{2^{\eta-10}\Omega\Gamma\left(\frac{\eta}{2}\right) k^{-\eta}\left(20k^2+3\Omega^2\right)}{\pi\Gamma\left(2-\frac{\eta}{2}\right)\left(4k^2+\Omega^2\right)^2} \\ &= -\frac{4^{\eta-6}(\eta-4)\Omega\left(\frac{1}{\Omega^2}\right)^{\frac{\eta+1}{2}}\sec\left(\frac{\pi\eta}{2}\right)\Gamma\left(\frac{\eta}{2}\right)}{\Gamma\left(2-\frac{\eta}{2}\right)} \\ &\approx \frac{N_{sv}\alpha}{512\eta} + N_{sv}\alpha\frac{-4\log(r_o\Omega) - 4\gamma + 1 + 4\log(4)}{2048} + \mathcal{O}(\eta)\,,\end{aligned} \tag{A.128}$$

where we reinserted N_{sv} and the coupling constant α in the last step. The self-energy diagram diverges when we take the limit $\eta \to 0$. The other two Feynman diagrams are going to cancel this divergence.

The vertex diagram

In this section we focus on the vertex diagram. First we introduce a coupling constant which depends on our regularization parameter η

$$\alpha_\eta = \alpha_0\, r_0^{-\eta}\zeta_\eta \tag{A.129}$$

with

$$\zeta_\eta = \frac{2^\eta\Gamma\left(\frac{1+\eta}{2}\right)}{\Gamma\left(\frac{1-\eta}{2}\right)}\,, \tag{A.130}$$

where we introduced the length scale r_0 in such a way that the unit of Coulomb interaction remains unchanged. Now, we can calculate the correlation function of the vertex correction. This function is defined as

$$\chi^{(1,d)}_{T^{(0)}_{xy}T^{(0)}_{xy}}(\mathrm{i}\Omega) = -\frac{N_{sv}\alpha_\eta}{4}\int_{\boldsymbol{p},\omega}\int_{\boldsymbol{k},\omega'}\frac{2\pi}{|\mathbf{p}-\mathbf{k}|^{1+\eta}}\,\mathrm{Tr}\left[G_{\boldsymbol{p},\mathrm{i}\omega}T^{(0)}_{xy}(\boldsymbol{p})G_{\boldsymbol{p},\mathrm{i}(\omega+\Omega)}G_{\boldsymbol{k},\mathrm{i}(\omega'+\Omega)}T^{(0)}_{xy}(\boldsymbol{k})G_{\boldsymbol{k},\mathrm{i}\omega'}\right]. \tag{A.131}$$

After inserting the corresponding expressions of the Green's functions and the energy-stress tensor and performing the two frequency integrals, we find

$$\begin{aligned}\chi^{(1,d)}_{T^{(0)}_{xy}T^{(0)}_{xy}}(\mathrm{i}\Omega) = &-\frac{N_{sv}\alpha_\eta}{4}\int\frac{d^2p}{(2\pi)^2}\int\frac{d^2q}{(2\pi)^2}\frac{2\pi}{|\mathbf{p}-\mathbf{q}|^{1+\eta}}\frac{2}{pq\left(4p^2+\Omega^2\right)\left(4q^2+\Omega^2\right)}\\ &\times\{p^2\left(p_xq_x\left(q^2+q_x^2-3q_y^2\right)+p_yq_y\left(q^2-3q_x^2+q_y^2\right)\right)\\ &+p_x^3q_x\left(q^2+q_x^2-3q_y^2\right)+p_x^2\left(\Omega^2\left(q_y^2-q_x^2\right)-3p_yq_y\left(q^2-3q_x^2+q_y^2\right)\right)\\ &-3p_xp_y^2q_x\left(q^2+q_x^2-3q_y^2\right)+p_y^2\left(p_yq_y\left(q^2-3q_x^2+q_y^2\right)+\Omega^2(q_x-q_y)(q_x+q_y)\right)\}\,.\end{aligned} \tag{A.132}$$

Next, we subtract the zero-frequency part from the above expression to obtain

$$f^{(1,d)}_{xyxy}(\mathrm{i}\Omega) = \frac{\chi^{(1,d)}_{T^{(0)}_{xy}T^{(0)}_{xy}}(\mathrm{i}\Omega)-\chi^{(1,d)}_{T^{(0)}_{xy}T^{(0)}_{xy}}(0)}{\Omega^2}\,. \tag{A.133}$$

To finally determine the contribution to the correction coefficient, we have to (as explained in Sec. 6.2.2) subtract again the zero-frequency part which yields

$$\frac{f^{(1,d)}_{xyxy}(\mathrm{i}\Omega)-f^{(1,d)}_{xyxy}(0)}{\Omega} = Q_1+Q_2+Q_3\,, \tag{A.134}$$

where Q_1 and Q_2 are convergent for $\eta = 0$, whereas the integral Q_3 is divergent for $\eta \to 0$. In the following, we demonstrate how the different integrals are evaluated.

Calulation of Q_1 First, we calculate the Q_1 integral. The integral is given by

$$\begin{aligned}Q_1 &= -\frac{N_{sv}\alpha_\eta}{8}\frac{2}{(2\pi)^2}\Omega^{-\eta}\int\limits_0^\infty dp\int\limits_0^\infty dq\int\limits_0^\pi d\varphi\frac{pq}{32p^2q^2\left(4p^2+1\right)\left(4q^2+1\right)}\frac{4pq\cos(2\varphi)+16p^2q^2\cos(\varphi)\cos(2\varphi)}{\left(p^2+q^2-2pq\cos(\varphi)\right)^{\frac{1+\eta}{2}}}\\ &= -\frac{N_{sv}\alpha_\eta}{8}\frac{1}{(2\pi)^2}\Omega^{-\eta}\int\limits_0^\infty dp\frac{1}{p(4p^2+1)}\int\limits_0^\infty dq\frac{1}{q(4q^2+1)}\int\limits_0^\pi d\varphi\frac{\frac{1}{4}pq\cos(2\varphi)+p^2q^2\cos(\varphi)\cos(2\varphi)}{\left(p^2+q^2-2pq\cos(\varphi)\right)^{\frac{1+\eta}{2}}}\,.\end{aligned} \tag{A.135}$$

Next, we substitute the variable q the following way: $q = xp$ and obtain:

$$Q_1 = -\frac{N_{sv}\alpha_\eta}{8}\frac{1}{(2\pi)^2}\Omega^{-\eta}\int\limits_0^\infty dp\frac{1}{p(4p^2+1)}\int\limits_0^\infty dx\frac{1}{(4x^2p^2+1)}\int\limits_0^\pi d\varphi\frac{\frac{1}{4}p^2\cos(2\varphi)+xp^4\cos(\varphi)\cos(2\varphi)}{p^{1+\eta}\left(1+x^2-2x\cos(\varphi)\right)^{\frac{1+\eta}{2}}}\,. \tag{A.136}$$

This integral is convergent for $\eta = 0$ and we thus have to evaluate the following integral:

$$Q_1 = -\frac{N_{sv}\alpha_\eta}{8}\frac{1}{(2\pi)^2}\Omega^{-\eta}\int\limits_0^\infty dp\frac{1}{(4p^2+1)}\int\limits_0^\infty dx\frac{1}{(4x^2p^2+1)}\int\limits_0^\pi d\varphi\frac{\frac{1}{4}\cos(2\varphi)+xp^2\cos(\varphi)\cos(2\varphi)}{\sqrt{1+x^2-2x\cos(\varphi)}}\,. \tag{A.137}$$

The integration over p can be done and gives:

$$\begin{aligned} \int\limits_0^\infty dp \frac{1}{4p^2+1}\frac{1}{4x^2p^2+1} &= \frac{\pi}{4(1+x)} && \text{(A.138)} \\ \int\limits_0^\infty dp \frac{1}{4p^2+1}\frac{p^2}{4x^2p^2+1} &= \frac{\pi}{16x(1+x)}\,. && \text{(A.139)} \end{aligned}$$

What remains to be evaluated is the following:

$$Q_1 = -\frac{N_{sv}\alpha_\eta}{8}\frac{\pi}{(2\pi)^2}\Omega^{-\eta}\frac{1}{16}\int\limits_0^\infty dx \frac{1}{(1+x)\sqrt{1+x^2-2x\cos(\varphi)}}\int\limits_0^\pi d\varphi\,\Big[\cos(2\varphi)+\cos(\varphi)\cos(2\varphi)\Big]\,. \tag{A.140}$$

Next we evaluate the x-integral and than the angular integral:

$$\begin{aligned} Q_1 &= -\frac{N_{sv}\alpha_\eta}{8}\frac{\pi}{(2\pi)^2}\Omega^{-\eta}\frac{1}{16}\int\limits_0^\pi d\varphi\,\Big[\cos(2\varphi)+\cos(\varphi)\cos(2\varphi)\Big]\log\left(\cot\left(\frac{\varphi}{4}\right)\right)\sec\left(\frac{\varphi}{2}\right) \\ &= -\frac{N_{sv}\alpha_\eta}{960}\,. \end{aligned} \tag{A.141}$$

Calulation of Q_2 Next we evaluate the integral Q_2. It is given by the expression:

$$\begin{aligned} Q_2 = &-\frac{N_{sv}\alpha_\eta}{8}\int_0^\infty \frac{dp\;p}{(2\pi)^2}\int_0^\infty \frac{dq\;q}{(2\pi)^2}\int_0^{2\pi} d\varphi \frac{2\pi}{|\mathbf{p}-\mathbf{q}|^{1+\eta}}\frac{\Omega^{-\eta}}{32p^2q^2\left(4p^2+1\right)\left(4q^2+1\right)} \\ &\times\left\{16p^3q\cos(2\varphi)+16pq^3\cos(2\varphi)\right\} && \text{(A.142)} \\ = &-\frac{N_{sv}\alpha_\eta}{8}\frac{2*2}{2}\frac{\Omega^{-\eta}}{(2\pi)^2}\int\limits_0^\infty dp\frac{1}{p(4p^2+1)}\int\limits_0^\infty dq\frac{1}{q(4q^2+1)}\int\limits_0^\pi d\varphi\frac{p^3q\cos(2\varphi)}{(p^2+q^2-2pq\cos(\varphi))^{\frac{1+\eta}{2}}}\,. \end{aligned}$$

One additional factor of 2 arises because the expression is symmetric under exchange of $\mathbf{p}$ and $\mathbf{q}$. The other factor 2 arises because the cosine is symmetric in the interval $[0,2\pi]$ and thus the angle integral can be changed to $\int\limits_0^{2\pi} d\varphi = 2\int\limits_0^{\pi} d\varphi$. Next, we substitute the variable again $q = xp$ and obtain:

$$\begin{aligned} Q_2 &= -\frac{N_{sv}\alpha_\eta}{4}\frac{\Omega^{-\eta}}{(2\pi)^2}\int\limits_0^\infty dp\frac{p^{2-\eta}}{4p^2+1}\int\limits_0^\infty dx\frac{1}{4x^2p^2+1}\int\limits_0^\pi d\varphi\frac{\cos(2\varphi)}{\left(1+x^2-2x\cos(\varphi)\right)^{\frac{1+\eta}{2}}} \\ &= -\frac{N_{sv}\alpha_\eta}{4}\frac{\Omega^{-\eta}}{(2\pi)^2}2^{\eta-4}\pi\sec\left(\frac{\pi\eta}{2}\right)\int\limits_0^\infty dx\frac{1-x^{\eta-1}}{x^2-1}\int\limits_0^\pi d\varphi\frac{\cos(2\varphi)}{\left(1+x^2-2x\cos(\varphi)\right)^{\frac{1+\eta}{2}}} && \text{(A.143)} \\ &= q\int\limits_0^\infty dx\frac{1-x^{\eta-1}}{x^2-1}\int\limits_0^\pi d\varphi\frac{2\cos(\varphi)^2-1}{\left(1+x^2-2x\cos(\varphi)\right)^{\frac{1+\eta}{2}}}\,, \end{aligned}$$

with

$$q = -\frac{N_{sv}\alpha_\eta}{4}\frac{\Omega^{-\eta}}{(2\pi)^2}2^{\eta-4}\pi\sec\left(\frac{\pi\eta}{2}\right)\,. \tag{A.144}$$

Again we split up the integral in two parts. The two integrals are defined as:

$$Q_{2,a} = 2q\int_0^\infty dx\frac{1-x^{\eta-1}}{x^2-1}\int_0^\pi d\varphi\frac{\cos(\varphi)^2}{\Big(1+x^2-2x\cos(\varphi)\Big)^{\frac{1+\eta}{2}}} \tag{A.145}$$

$$Q_{2,b} = -q\int_0^\infty dx\frac{1-x^{\eta-1}}{x^2-1}\int_0^\pi d\varphi\frac{1}{\Big(1+x^2-2x\cos(\varphi)\Big)^{\frac{1+\eta}{2}}}\,. \tag{A.146}$$

Analysis of $Q_{2,a}$ Now, we analyze the integral $Q_{2,a}$. This integral can be split in a singular and a non-singular contribution $Q_{2,a} = Q^s_{2,a} + Q^{ns}_{2,a}$, where

$$\begin{aligned} Q^s_{2,a} &= 2q\int_0^\infty dx\frac{1-x^{\eta-1}}{x^2-1}\int_0^\pi d\varphi\cos(\varphi)^2 \\ &= 2q\frac{\pi}{2}\cot\Big(\frac{\pi}{2}\eta\Big)\frac{\pi}{2}\,. \end{aligned} \tag{A.147}$$

Next, the non-singular contribution is analyzed, which is defined as

$$\begin{aligned} Q^{ns}_{2,a} &= Q_{2,a} - Q^s_{2,a} \\ &= 2q\int_0^\infty dx\frac{1-x^{\eta-1}}{x^2-1}\int_0^\pi d\varphi\cos(\varphi)^2\left(\frac{1}{[1+x^2-2x\cos(\varphi)]^{\frac{1+\eta}{2}}}-1\right)\,. \end{aligned} \tag{A.148}$$

Since this integral is convergent for $\eta = 0$, it can be evaluated in this limit. We find

$$\begin{aligned} Q^{ns}_{2,a} &= 2q\int_0^\infty dx\frac{1}{x(1+x)}\int_0^\pi d\varphi\cos(\varphi)^2\left(\frac{1}{\sqrt{1+x^2-2x\cos(\varphi)}}-1\right) \\ &= 2q\frac{\pi}{12}\big(11-6\pi+\log(4096)\big)\,, \end{aligned} \tag{A.149}$$

where we performed first the x-integral and than the φ-integral.

Analysis of $Q_{2,b}$ Next, we analyze the $Q_{2,b}$ integral analogous to the previous one. We can again split it up into a singular and a non-singular contribution. The singular contribution is given by

$$\begin{aligned} Q^s_{2,b} &= -q\int_0^\infty dx\frac{1-x^{\eta-1}}{x^2-1}\int_0^\pi d\varphi\;1 \\ &= -q\frac{\pi}{2}\cot\left(\frac{\pi}{2}\eta\right)\pi\,. \end{aligned} \tag{A.150}$$

The non-singular part reads

$$\begin{aligned} Q_{2,b}^{ns} &= Q_{2,b} - Q_{2,b}^{s} \\ &= -q \int_0^\infty dx \frac{1-x^{\eta-1}}{x^2-1} \int_0^\pi d\varphi \left(\frac{1}{[1+x^2-2x\cos(\varphi)]^{\frac{1+\eta}{2}}} - 1 \right) . \end{aligned} \tag{A.151}$$

This integral can again be evaluated in the limit $\eta = 0$ and yields:

$$\begin{aligned} Q_{2,b}^{ns} &= -q \int_0^\infty dx \frac{1}{x(1+x)} \int_0^\pi d\varphi \left(\frac{1}{\sqrt{1+x^2-2x\cos(\varphi)}} - 1 \right) \\ &= +q\frac{\pi}{2}\big(\pi - 2\log(4)\big) . \end{aligned} \tag{A.152}$$

Result of Q_2 Thus, upon combining $Q_{2,a}$ and $Q_{2,b}$, we obtain for the Q_2 integral the following value:

$$\begin{aligned} Q_2 &= Q_{2,a} + Q_{2,b} \\ &= q[\frac{\pi^2}{2}\cot\left(\frac{\pi}{2}\eta\right) + \frac{\pi}{6}\big(11 - 6\pi + \log(4096)\big) - \frac{\pi^2}{2}\cot\left(\frac{\pi}{2}\eta\right) + \frac{\pi}{2}\big(\pi - 2\log(4)\big)] \\ &= q\frac{\pi}{6}(11-3\pi) \\ &= -\frac{N_{sv}\alpha_\eta}{4}\frac{\Omega^{-\eta}}{(2\pi)^2}2^{\eta-4}\pi\sec\left(\frac{\pi\eta}{2}\right)\frac{\pi}{6}(11-3\pi) \\ &\approx -\frac{N_{sv}\alpha}{2}\left(\frac{11}{768} - \frac{\pi}{256}\right) . \end{aligned} \tag{A.153}$$

Calulation of Q_3 In this section we analyze the divergent diagram Q_3. This integral is given by the expression:

$$\begin{aligned} Q_3 = &-\frac{N_{sv}\alpha_\eta}{8}\frac{1}{(2\pi)^2}\frac{\Omega^{-\eta}}{32}\int_0^\infty dp \frac{p}{p^2(4p^2+1)}\int_0^\infty dq\frac{q}{q^2(4q^2+1)}\int_0^{2\pi}d\varphi\frac{\cos(\varphi)\cos(2\varphi)}{\Big(p^2+q^2-2pq\cos(\varphi)\Big)^{\frac{1+\eta}{2}}} \\ &\times\{4p^2(4p^2+1)+4q^2(4q^2+1)\} \\ = &-\frac{N_{sv}\alpha_\eta}{8}\frac{1}{(2\pi)^2}\frac{\Omega^{-\eta}}{32}\int_0^\infty dp\frac{8p^3(4p^2+1)}{p^2(4p^2+1)}\int_0^\infty dq\frac{q}{q^2(4q^2+1)}\int_0^{2\pi}d\varphi\frac{\cos(\varphi)\cos(2\varphi)}{\Big(p^2+q^2-2pq\cos(\varphi)\Big)^{\frac{1+\eta}{2}}} \\ = &-\frac{N_{sv}\alpha_\eta}{32}\frac{\Omega^{-\eta}}{(2\pi)^2}\int_0^\infty dp\ p\int_0^\infty dq\frac{1}{q(4q^2+1)}\int_0^{2\pi}d\varphi\frac{\cos(\varphi)\cos(2\varphi)}{\Big(p^2+q^2-2pq\cos(\varphi)\Big)^{\frac{1+\eta}{2}}} . \end{aligned} \tag{A.154}$$

Next, we substitute the integration variable p by $p = xq$ and obtain:

$$Q_3 = -\frac{N_{sv}\alpha_\eta}{32}\frac{\Omega^{-\eta}}{(2\pi)^2}\int_0^\infty dq\frac{q^{-\eta}}{4q^2+1}\int_0^\infty dx\int_0^{2\pi}d\varphi\frac{x\cos(\varphi)\cos(2\varphi)}{\Big(1+x^2-2x\cos(\varphi)\Big)^{\frac{1+\eta}{2}}} . \tag{A.155}$$

In the following step we use the identity:

$$|\mathbf{k}|^{-(1+\eta)} = \Gamma\left(\frac{1+\eta}{2}\right)^{-1} \int_0^\infty dz \frac{e^{-k^2 z}}{z^{\frac{1-\eta}{2}}} \,, \tag{A.156}$$

and obtain[3]

$$\begin{aligned} Q_3 &= -\frac{N_{sv}\alpha_\eta}{32}\frac{\Omega^{-\eta}}{(2\pi)^2}2^{-2+\eta}\pi\frac{\sec\left(\frac{\pi\eta}{2}\right)}{\Gamma\left(\frac{1+\eta}{2}\right)}\int_0^\infty dx\int_0^{2\pi} d\varphi\int_0^\infty dz\frac{x}{z^{\frac{1-\eta}{2}}}\cos(\varphi)\cos(2\varphi)e^{-\left(1+x^2-2x\cos(\varphi)\right)z} \\ &= -\frac{N_{sv}\alpha_\eta}{32}\frac{\Omega^{-\eta}}{(2\pi)^2}2^{-2+\eta}\pi\frac{\sec\left(\frac{\pi\eta}{2}\right)}{\Gamma\left(\frac{1+\eta}{2}\right)}\int_0^\infty dx\int_0^\infty dz\frac{x}{z^{\frac{1-\eta}{2}}}2\pi e^{-(1+x^2)z}xz[\,{}_1\tilde{F}_1(2;x^2;z^2) - \,{}_1\tilde{F}_1(3;x^2;z^2)] \\ &= -\frac{N_{sv}\alpha_\eta}{32}\frac{\Omega^{-\eta}}{(2\pi)^2}2^{-2+\eta}\pi\frac{\sec\left(\frac{\pi\eta}{2}\right)}{\Gamma\left(\frac{1+\eta}{2}\right)}\int_0^\infty dz\frac{1}{2}\pi^{3/2}e^{-\frac{z}{2}}z^{\frac{\eta}{2}-2}\left(zI_0\left(\frac{z}{2}\right)+(z-2)I_1\left(\frac{z}{2}\right)\right) \\ &= -\frac{N_{sv}\alpha_\eta}{32}\frac{\Omega^{-\eta}}{(2\pi)^2}2^{-2+\eta}\pi\frac{\sec\left(\frac{\pi\eta}{2}\right)}{\Gamma\left(\frac{1+\eta}{2}\right)}\frac{\pi(\eta+2)\Gamma\left(\frac{1}{2}-\frac{\eta}{2}\right)\Gamma\left(\frac{\eta}{2}\right)}{4\Gamma\left(3-\frac{\eta}{2}\right)} \\ &\approx -\frac{\alpha}{1024\eta} - \frac{\alpha(4\log(r_0\Omega)+4\gamma-5-8\log(2))}{4096} + \mathcal{O}(\eta)\,. \end{aligned} \tag{A.157}$$

Result of the vertex diagram Combining all three integral gives

$$\frac{f^{(1,d)}_{xyxy}(\mathrm{i}\Omega) - f^{(1,d)}_{xyxy}(0)}{\Omega} = \frac{\alpha(20\eta\log(\Omega r_0) + 40\pi\eta + 20\gamma\eta - 193\eta - 40\eta\log(2) - 20)}{20480\,\eta}\,. \tag{A.158}$$

The vertex diagram is also divergent for $\eta \to 0$, but does not fully cancel the divergence of the self-energy diagram. A third Feynman diagram is needed to cancel all divergences.

The Honey diagram

The last diagram contributing to the correction coefficient $\mathcal{C}_\eta$ is the *honey diagram.* It takes the interacting part of the energy-stress tensor into account. This interacting part of the energy-stress tensor is determined by calculating the commutator between the Coulomb potential and the strain generator. We find for the interacting energy-stress tensor in real space

$$\begin{aligned} T^{int}_{\alpha\beta}(\boldsymbol{R},\tau) &= [\mathcal{H}_{\mathcal{C}},\mathcal{L}_{\alpha\beta}] \\ &= -\int_{\boldsymbol{x},\boldsymbol{r}} \hat{\psi}^\dagger_{\boldsymbol{x}}(\tau)\hat{\psi}^\dagger_{\boldsymbol{r}}(\tau)\hat{\psi}_{\boldsymbol{r}}(\tau)x_\alpha\frac{\partial}{\partial x_\beta}\Big(V(\boldsymbol{r},\boldsymbol{x})\Big)\hat{\psi}_{\boldsymbol{x}}(\tau) - \int_{\boldsymbol{x},\boldsymbol{r'}} \hat{\psi}^\dagger_{\boldsymbol{x}}(\tau)\hat{\psi}^\dagger_{\boldsymbol{r'}}(\tau)\hat{\psi}_{\boldsymbol{r'}}(\tau)x_\alpha\frac{\partial}{\partial x_\beta}\Big(V(\boldsymbol{x},\boldsymbol{r'})\Big)\hat{\psi}_{\boldsymbol{x}}(\tau) \\ &= \frac{1}{2}(1-\eta)r_0^{-\eta}\int_{\boldsymbol{r_1},\boldsymbol{r_2}} \hat{\psi}^\dagger_{\boldsymbol{r_1}}(\tau)\hat{\psi}^\dagger_{\boldsymbol{r_2}}(\tau)\hat{\psi}_{\boldsymbol{r_2}}(\tau)\hat{\psi}_{\boldsymbol{r_1}}(\tau)\frac{(\boldsymbol{r_1}-\boldsymbol{r_2})_\alpha(\boldsymbol{r_1}-\boldsymbol{r_2})_\beta}{|\boldsymbol{r_1}-\boldsymbol{r_2}|^{3-\eta}}\,, \end{aligned} \tag{A.159}$$

---

[3] where ${}_1\tilde{F}_1(a;b;c)$ is the regularized confluent hypergeometric function and $I_n(x)$ are the modified Bessel functions of the first kind.

where we assumed the Coulomb potential to have the form $V(\boldsymbol{r},\boldsymbol{r'}) = \frac{r_0^{-\eta}}{|\boldsymbol{r}-\boldsymbol{r'}|^{1-\eta}}$. This result is in agreement with the expression of the interacting energy-stress tensor which we obtained in the derivation analogous to the Martin and Schwinger calculation [49]. The Fourier transform is

$$\begin{aligned}T^{int}_{\alpha\beta}(\boldsymbol{q}=0,\tau) =&\frac{1}{2}(1-\eta)r_0^{-\eta}2^{1-\eta}\pi\frac{\Gamma\left(\frac{3+\eta}{2}\right)}{\Gamma\left(\frac{3-\eta}{2}\right)}\int\limits_{\boldsymbol{k},\boldsymbol{p},\boldsymbol{l}}\frac{l_\alpha l_\beta}{|\boldsymbol{l}|^{3+\eta}}\hat{\psi}^\dagger_{\boldsymbol{k}}(\tau)\hat{\psi}^\dagger_{\boldsymbol{p}}(\tau)\hat{\psi}_{\boldsymbol{p}-\boldsymbol{l}}(\tau)\hat{\psi}_{\boldsymbol{k}+\boldsymbol{l}}(\tau)\\ =&\frac{1}{2}(1-\eta)r_0^{-\eta}2^{1-\eta}\pi\frac{\Gamma\left(\frac{3+\eta}{2}\right)}{\Gamma\left(\frac{3-\eta}{2}\right)}\int\limits_{\boldsymbol{l}}\frac{l_\alpha l_\beta}{|\boldsymbol{l}|^{3+\eta}}n(\boldsymbol{l},\tau)n(-\boldsymbol{l},\tau)\,,\end{aligned} \tag{A.160}$$

with

$$n(\boldsymbol{l},\tau) = \int\limits_{\boldsymbol{p}}\hat{\psi}^\dagger_{\boldsymbol{p}}(\tau)\hat{\psi}_{\boldsymbol{p}+\boldsymbol{l}}(\tau)\,. \tag{A.161}$$

After having calculated the interacting part of the energy-stress tensor $T^{int}_{\alpha\beta}$, the additional diagram contributing to the correction coefficient is determined by the correlator between the non-interacting and interacting energy-stress tensor $\left\langle T^{int}_{\alpha\beta}, T^{(0)}_{\alpha\beta}\right\rangle$. Just to remind ourselves, $T^{(0)}_{\alpha\beta}$ is for graphene $T^{(0)}_{\alpha\beta} = \frac{1}{2}\int\limits_{\boldsymbol{q}}\hat{\psi}^\dagger_{\boldsymbol{q}}\left(q_\alpha\sigma_\beta + q_\beta\sigma_\alpha\right)\hat{\psi}_{\boldsymbol{q}}$. Thus, the following four contractions have to been evaluated:

$$\begin{aligned}&(a)\\ &\frac{1}{4}(1-\eta)r_0^{-\eta}2^{1+\eta}\pi\int\limits_{\boldsymbol{k},\boldsymbol{p},\boldsymbol{l},\boldsymbol{q}}(q_\gamma\sigma_\delta+q_\delta\sigma_\gamma)_{cd}\frac{l_\alpha l_\beta}{|\boldsymbol{l}|^{3+\eta}}\wick{\c1{\hat{\psi}}^\dagger_{\boldsymbol{k},a}(\tau)\c2{\hat{\psi}}^\dagger_{\boldsymbol{p},b}(\tau)\c2{\hat{\psi}}_{\boldsymbol{p}-\boldsymbol{l},b}(\tau)\c3{\hat{\psi}}_{\boldsymbol{k}+\boldsymbol{l},a}(\tau)\c3{\hat{\psi}}^\dagger_{\boldsymbol{q},c}(0)\c1{\hat{\psi}}_{\boldsymbol{q},d}(0)}\\ &(b)\\ &\frac{1}{4}(1-\eta)r_0^{-\eta}2^{1+\eta}\pi\int\limits_{\boldsymbol{k},\boldsymbol{p},\boldsymbol{l},\boldsymbol{q}}(q_\gamma\sigma_\delta+q_\delta\sigma_\gamma)_{cd}\frac{l_\alpha l_\beta}{|\boldsymbol{l}|^{3+\eta}}\wick{\c1{\hat{\psi}}^\dagger_{\boldsymbol{k},a}(\tau)\c2{\hat{\psi}}^\dagger_{\boldsymbol{p},b}(\tau)\c3{\hat{\psi}}_{\boldsymbol{p}-\boldsymbol{l},b}(\tau)\c1{\hat{\psi}}_{\boldsymbol{k}+\boldsymbol{l},a}(\tau)\c3{\hat{\psi}}^\dagger_{\boldsymbol{q},c}(0)\c2{\hat{\psi}}_{\boldsymbol{q},d}(0)}\\ &(c)\\ &\frac{1}{4}(1-\eta)r_0^{-\eta}2^{1+\eta}\pi\int\limits_{\boldsymbol{k},\boldsymbol{p},\boldsymbol{l},\boldsymbol{q}}(q_\gamma\sigma_\delta+q_\delta\sigma_\gamma)_{cd}\frac{l_\alpha l_\beta}{|\boldsymbol{l}|^{3+\eta}}\wick{\c1{\hat{\psi}}^\dagger_{\boldsymbol{k},a}(\tau)\c2{\hat{\psi}}^\dagger_{\boldsymbol{p},b}(\tau)\c3{\hat{\psi}}_{\boldsymbol{p}-\boldsymbol{l},b}(\tau)\c2{\hat{\psi}}_{\boldsymbol{k}+\boldsymbol{l},a}(\tau)\c3{\hat{\psi}}^\dagger_{\boldsymbol{q},c}(0)\c1{\hat{\psi}}_{\boldsymbol{q},d}(0)}\\ &(d)\\ &\frac{1}{4}(1-\eta)r_0^{-\eta}2^{1+\eta}\pi\int\limits_{\boldsymbol{k},\boldsymbol{p},\boldsymbol{l},\boldsymbol{q}}(q_\gamma\sigma_\delta+q_\delta\sigma_\gamma)_{cd}\frac{l_\alpha l_\beta}{|\boldsymbol{l}|^{3+\eta}}\wick{\c1{\hat{\psi}}^\dagger_{\boldsymbol{k},a}(\tau)\c2{\hat{\psi}}^\dagger_{\boldsymbol{p},b}(\tau)\c1{\hat{\psi}}_{\boldsymbol{p}-\boldsymbol{l},b}(\tau)\c3{\hat{\psi}}_{\boldsymbol{k}+\boldsymbol{l},a}(\tau)\c3{\hat{\psi}}^\dagger_{\boldsymbol{q},c}(0)\c2{\hat{\psi}}_{\boldsymbol{q},d}(0)}\end{aligned} \tag{A.162}$$

Only these four contractions will result in connected diagrams. In principal, there are two more contractions possible which lead to disconnected diagrams, which we do not take into account here. The first two diagrams emerging from contractions (a) and (b) are both equal to zero. Let me demonstrate exemplary why they are zero at the contraction (a). We find for this contraction

$$\begin{aligned}
\chi^{(a)}_{T^{int}_{\alpha\beta},T^{(0)}_{\alpha\beta}} &= \frac{1}{4}(1-\eta)r_0^{-\eta}2^{1+\eta}\pi\frac{\Gamma\left(\frac{3+\eta}{2}\right)}{\Gamma\left(\frac{3-\eta}{2}\right)}\int_{\boldsymbol{q},\boldsymbol{k},\boldsymbol{p},\boldsymbol{l}} \frac{l_\alpha l_\beta}{|\boldsymbol{l}|^{3+\eta}}\left(q_\gamma\sigma_\delta + q_\delta\sigma_\alpha\right)_{cd} \\
&\times \left(G_{\boldsymbol{p},0}\right)_{bb}\left(G_{\boldsymbol{k}+\boldsymbol{l},+\tau}\right)_{ac}\left(G_{\boldsymbol{k},-\tau}\right)_{da}\delta(\boldsymbol{k}-\boldsymbol{q})\delta(\boldsymbol{p}-\boldsymbol{p}+\boldsymbol{l})\delta(\boldsymbol{k}+\boldsymbol{l}-\boldsymbol{q}) \\
&= \frac{1}{4}(1-\eta)r_0^{-\eta}2^{1+\eta}\pi\frac{\Gamma\left(\frac{3+\eta}{2}\right)}{\Gamma\left(\frac{3-\eta}{2}\right)}\int_{\boldsymbol{k},\boldsymbol{p},\boldsymbol{l}} \frac{l_\alpha l_\beta}{|\boldsymbol{l}|^{3+\eta}}\operatorname{Tr}(G_{\boldsymbol{p},0})\operatorname{Tr}(G_{\boldsymbol{k}+\boldsymbol{l},+\tau}\left(k_\gamma\sigma_\delta + k_\delta\sigma_\alpha\right)G_{\boldsymbol{k},-\tau})\delta(\boldsymbol{l}) \\
&= 0\,.
\end{aligned} \tag{A.163}$$

Upon evaluating the $\boldsymbol{l}$ momentum integral, the correlation function vanishes. The contraction (b) has an analogous expression which will be zero for the same reasons. Now, we turn to the contractions (c) and (d) and the resulting diagrams. The correlation function resulting from the contraction (c) is given by

$$\begin{aligned}
\chi^{(c)}_{T^{int}_{\alpha\beta},T^{(0)}_{\alpha\beta}}(\tau) &= -\frac{1}{4}(1-\eta)r_0^{-\eta}2^{1+\eta}\pi\frac{\Gamma\left(\frac{3+\eta}{2}\right)}{\Gamma\left(\frac{3-\eta}{2}\right)}\int_{\boldsymbol{q},\boldsymbol{k},\boldsymbol{p},\boldsymbol{l}} \frac{l_\alpha l_\beta}{|\boldsymbol{l}|^{3+\eta}}\left(q_\gamma\sigma_\delta + q_\delta\sigma_\alpha\right)_{cd} \\
&\times (G_{\boldsymbol{p},0})_{ab}(G_{\boldsymbol{p}-\boldsymbol{l},\tau})_{bc}(G_{\boldsymbol{k},-\tau})_{da}\delta(\boldsymbol{k}-\boldsymbol{q})\delta(\boldsymbol{k}+\boldsymbol{l}-\boldsymbol{p})\delta\left(\boldsymbol{p}-\boldsymbol{l}-\boldsymbol{q}\right) \\
&= -\frac{1}{4}(1-\eta)r_0^{-\eta}2^{1+\eta}\pi\frac{\Gamma\left(\frac{3+\eta}{2}\right)}{\Gamma\left(\frac{3-\eta}{2}\right)}\int_{\boldsymbol{k},\boldsymbol{l}} \frac{l_\alpha l_\beta}{|\boldsymbol{l}|^{3+\eta}}\operatorname{Tr}\left[G_{\boldsymbol{k}+\boldsymbol{l},0}G_{\boldsymbol{k},\tau}\left(k_\gamma\sigma_\delta + k_\delta\sigma_\gamma\right)G_{\boldsymbol{k},-\tau}\right]\,.
\end{aligned} \tag{A.164}$$

Next, we will re-expresses the above expression by Matsubara frequencies. It holds

$$\begin{aligned}
\chi^{(c)}_{T^{int}_{\alpha\beta},T^{(0)}_{\alpha\beta}}(\mathrm{i}\nu_r) &= -\frac{1}{4}(1-\eta)r_0^{-\eta}2^{1+\eta}\pi\frac{\Gamma\left(\frac{3+\eta}{2}\right)}{\Gamma\left(\frac{3-\eta}{2}\right)} \\
&\times \int_{\boldsymbol{k},\boldsymbol{l},n,m,s}\int_0^\beta d\tau \frac{l_\alpha l_\beta}{|\boldsymbol{l}|^{3+\eta}}\operatorname{Tr}\left[G_{\boldsymbol{k}+\boldsymbol{l},\mathrm{i}\omega_s}G_{\boldsymbol{k},\mathrm{i}\omega_n}\left(k_\gamma\sigma_\delta + k_\delta\sigma_\gamma\right)G_{\boldsymbol{k},\mathrm{i}\omega_m}\right]\mathrm{e}^{\mathrm{i}(\nu_r-\omega_n+\omega_m)\tau} \\
&= -\frac{1}{4}(1-\eta)r_0^{-\eta}2^{1+\eta}\pi\frac{\Gamma\left(\frac{3+\eta}{2}\right)}{\Gamma\left(\frac{3-\eta}{2}\right)}\int_{\boldsymbol{k},\boldsymbol{l},m,s} \frac{l_\alpha l_\beta}{|\boldsymbol{l}|^{3+\eta}}\operatorname{Tr}\left[G_{\boldsymbol{k}+\boldsymbol{l},\mathrm{i}\omega_s}G_{\boldsymbol{k},\mathrm{i}(\omega_m+\nu_r)}\left(k_\gamma\sigma_\delta + k_\delta\sigma_\gamma\right)G_{\boldsymbol{k},\mathrm{i}\omega_m}\right]\,.
\end{aligned} \tag{A.165}$$

The last contraction (d) yields exactly the same expression. Thus, the additional diagram to the correction coefficient (the honey diagram) is twice the above expression and reads

$$\chi_{T^{int}_{\alpha\beta},T^{(0)}_{\alpha\beta}}(\mathrm{i}\nu_r) = -\frac{1}{2}(1-\eta)r_0^{-\eta}2^{1+\eta}\pi\frac{\Gamma\left(\frac{3+\eta}{2}\right)}{\Gamma\left(\frac{3-\eta}{2}\right)}\int_{\boldsymbol{k},\boldsymbol{l},m,s} \frac{l_\alpha l_\beta}{|\boldsymbol{l}|^{3+\eta}}\operatorname{Tr}\left[G_{\boldsymbol{k}+\boldsymbol{l},\mathrm{i}\omega_s}G_{\boldsymbol{k},\mathrm{i}(\omega_m+\nu_r)}\left(k_\gamma\sigma_\delta + k_\delta\sigma_\gamma\right)G_{\boldsymbol{k},\mathrm{i}\omega_m}\right]\,. \tag{A.166}$$

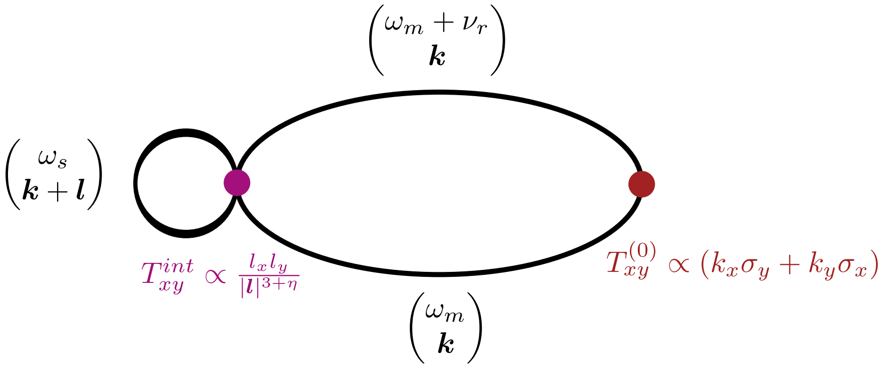

Figure A.2: The honey diagram.

Let us now evaluate this Feynman diagram. It is depicted in Fig. A.2. Upon rewriting the above expression explicitly with the corresponding expressions of the Green's functions, we find

$$\chi_{T^{int}_{\alpha\beta},T^{(0)}_{\alpha\beta}}(\mathrm{i}\nu_r) = -\frac{1}{2}(1-\eta)r_0^{-\eta}2^{1+\eta}\pi\frac{\Gamma\left(\frac{3+\eta}{2}\right)}{\Gamma\left(\frac{3-\eta}{2}\right)}\int_{\boldsymbol{k},\boldsymbol{l},\boldsymbol{m},\boldsymbol{s}}\frac{l_\alpha l_\beta}{|\boldsymbol{l}|^{3+\eta}}\frac{\mathrm{Tr}[\mathcal{A}]}{(\omega'^2+|\boldsymbol{l}+\boldsymbol{k}|^2)(k^2+\omega^2)(k^2+(\omega+\Omega)^2)}\,, \tag{A.167}$$

where the trace is given by

$$\begin{aligned}&\mathrm{Tr}[\mathcal{A}] =\\ &\mathrm{Tr}\Big([\mathrm{i}\omega'\sigma_0+(k_x+l_x)\sigma_x+(k_y+l_y)\sigma_y][\mathrm{i}(\omega+\Omega)\sigma_0+k_x\sigma_x+k_y\sigma_y][k_x\sigma_y+k_y\sigma_x][\mathrm{i}\omega\sigma_0+k_x\sigma_x+k_y\sigma_y]\Big)\\ &=-2\bigg((k_x+l_x)k_y\left(-3k_x^2+k_y^2+\omega(\omega+\Omega)\right)+(k_y+l_y)k_x\left(k_x^2-3k_y^2+\omega(\omega+\Omega)\right)+2k_xk_y\omega'(2\omega+\Omega)\bigg)\,.\end{aligned} \tag{A.168}$$

Next, we perform the two frequency integrations and find

$$\begin{aligned}\chi_{T^{int}_{\alpha\beta},T^{(0)}_{\alpha\beta}}(\mathrm{i}\nu_r) =&\frac{1}{2}(1-\eta)r_0^{-\eta}2^{1+\eta}\pi\frac{\Gamma\left(\frac{3+\eta}{2}\right)}{\Gamma\left(\frac{3-\eta}{2}\right)}\frac{1}{(2\pi)^4}\\ &\times\int_0^\infty \mathrm{d}k\int_0^\infty \mathrm{d}l\int_0^{2\pi}\mathrm{d}\alpha\int_0^{2\pi}\mathrm{d}\beta\frac{k^3\sin(2\alpha)\cos(2\beta)l^{1-\eta}\sin(\alpha-\beta)}{\left(4k^2+\Omega^2\right)\sqrt{k^2+2kl\cos(\alpha-\beta)+l^2}}\,.\end{aligned} \tag{A.169}$$

Then the Matsubara frequency is analytically continued, i. e., $\mathrm{i}\Omega \to \omega + \mathrm{i}\delta$, which yields

$$\frac{1}{4k^2+\Omega} \to P.V.\frac{1}{4k^2-\omega^2}+\frac{\mathrm{i}\pi}{4\omega}\delta\left(k-\frac{\omega}{2}\right)+\frac{\mathrm{i}\pi}{4\omega}\delta\left(k+\frac{\omega}{2}\right)\,. \tag{A.170}$$

The imaginary part of the correlation function can now be cast into the form

$$\begin{aligned}\operatorname{Im}\chi_{T^{int}_{\alpha\beta},T^{(0)}_{\alpha\beta}}(\mathrm{i}\nu_r) =&\frac{1}{2}(1-\eta)r_0^{-\eta}2^{1+\eta}\pi\frac{\Gamma\left(\frac{3+\eta}{2}\right)}{\Gamma\left(\frac{3-\eta}{2}\right)}\frac{1}{(2\pi)^4}\\ &\times\int\limits_0^\infty \mathrm{d}l\int\limits_0^{2\pi}\mathrm{d}\alpha\int\limits_0^{2\pi}\mathrm{d}\beta\frac{\pi\omega^2\sin(2\alpha)\cos(2\beta)l^{1-\eta}\sin(\alpha-\beta)}{16\sqrt{4l^2+4l\omega\cos(\alpha-\beta)+\omega^2}}\,.\end{aligned}\tag{A.171}$$

Next, we substitute the angle $\alpha\to\varphi+\beta$ and perform the β integration and obtain

$$\operatorname{Im}\chi_{T^{int}_{\alpha\beta},T^{(0)}_{\alpha\beta}}(\mathrm{i}\nu_r) = \frac{1}{2}(1-\eta)r_0^{-\eta}2^{1+\eta}\pi\frac{\Gamma\left(\frac{3+\eta}{2}\right)}{\Gamma\left(\frac{3-\eta}{2}\right)}\frac{1}{(2\pi)^4}\int\limits_0^\infty \mathrm{d}l\int\limits_0^{2\pi}\mathrm{d}\varphi\frac{\pi^2\omega^2l^{1-\eta}\sin^2(\varphi)\cos(\varphi)}{16\sqrt{l^2+l\omega\cos(\varphi)+\omega^2/4}}\,.\tag{A.172}$$

Upon using the relation

$$|\boldsymbol{k}|^{1-\eta}=\Gamma\left(\frac{1+\eta}{2}\right)^{-1}\int\limits_0^\infty\mathrm{d}z\frac{\mathrm{e}^{-k^2z}}{z^{\frac{1-\eta}{2}}}\,,\tag{A.173}$$

we obtain

$$\begin{aligned}\operatorname{Im}\chi_{T^{int}_{\alpha\beta},T^{(0)}_{\alpha\beta}}(\mathrm{i}\nu_r) =&\frac{1}{2}(1-\eta)r_0^{-\eta}2^{1+\eta}\pi\frac{\Gamma\left(\frac{3+\eta}{2}\right)}{\Gamma\left(\frac{3-\eta}{2}\right)}\frac{1}{(2\pi)^4}\\ &\times\int\limits_0^\infty \mathrm{d}l\int\limits_0^{2\pi}\mathrm{d}\varphi\int\limits_0^\infty\mathrm{d}z\pi^{3/2}\omega^2l^{1-\eta}\sin^2(\varphi)\cos(\varphi)\frac{\mathrm{e}^{-z\left(l^2+l\omega\cos(\varphi)+\frac{\omega^2}{4}\right)}}{16\sqrt{z}}\,.\end{aligned}\tag{A.174}$$

After performing the last angle-integration, it is

$$\operatorname{Im}\chi_{T^{int}_{\alpha\beta},T^{(0)}_{\alpha\beta}}(\mathrm{i}\nu_r) =\frac{1}{2}(1-\eta)r_0^{-\eta}2^{1+\eta}\pi\frac{\Gamma\left(\frac{3+\eta}{2}\right)}{\Gamma\left(\frac{3-\eta}{2}\right)}\frac{1}{(2\pi)^4}\int\limits_0^\infty \mathrm{d}l\int\limits_0^\infty\mathrm{d}z\frac{\pi^{5/2}\omega l^{-\eta}e^{-\frac{1}{4}z\left(4l^2+\omega^2\right)}I_2(lz\omega)}{8z^{3/2}}\,,\tag{A.175}$$

where $I_n(z)$ is the modified Bessel function of the first kind. Next, we integrate over the momentum $\boldsymbol{l}$ and find

$$\begin{aligned}\operatorname{Im}\chi_{T^{int}_{\alpha\beta},T^{(0)}_{\alpha\beta}}(\mathrm{i}\nu_r) =&\frac{1}{2}(1-\eta)r_0^{-\eta}2^{1+\eta}\pi\frac{\Gamma\left(\frac{3+\eta}{2}\right)}{\Gamma\left(\frac{3-\eta}{2}\right)}\frac{1}{(2\pi)^4}\\ &\times\int\limits_0^\infty\mathrm{d}z\frac{1}{128}\pi^{5/2}\omega^3\Gamma\left(\frac{3}{2}-\frac{\eta}{2}\right)z^{\frac{\eta+1}{2}-\frac{3}{2}}\,{}_1F_1\left(\frac{\eta+3}{2};3;-\frac{1}{4}\left(z\omega^2\right)\right)\,,\end{aligned}\tag{A.176}$$

where ${}_1F(a,b,z)$ is the Kummer confluent hypergeometric function. Hence, the imaginary part of the correlation function is given by

$$\operatorname{Im}\chi_{T^{int}_{\alpha\beta},T^{(0)}_{\alpha\beta}}(\mathrm{i}\nu_r) = \frac{2^{2\eta-11}(\eta-1)\omega^3\left(\omega^2\right)^{-\frac{\eta}{2}}\Gamma\left(\frac{\eta}{2}\right)}{\Gamma\left(3-\frac{\eta}{2}\right)}\,.\tag{A.177}$$

When we expand the above expression for small η, we find

$$\operatorname{Im}\chi_{T^{int}_{\alpha\beta},T^{(0)}_{\alpha\beta}}(\mathrm{i}\nu_r) = -\frac{\omega^3}{2048\eta} - \frac{-4\omega^3\log(r_0) - 4\gamma\omega^3 - \omega^3 + 8\omega^3\log(2) - 2\omega^3\log\left(\omega^2\right)}{8192} + \mathcal{O}(\eta)\,. \tag{A.178}$$

We have to multiply the above expression by a factor of 2, since the correlation function $\left\langle T^{int}_{\alpha\beta}, T^{(0)}_{\gamma\delta}\right\rangle$ and $\left\langle T^{(0)}_{\alpha\beta}, T^{int}_{\gamma\delta}\right\rangle$ give the same result and both combinations contribute to the correction coefficient. Thus, the final contribution to the correction coefficient due to the honey diagram is

$$\operatorname{Im}\chi_{T^{int}_{\alpha\beta},T^{(0)}_{\alpha\beta}}(\mathrm{i}\nu_r) = -\frac{1}{1024\eta} - \frac{-4\log(r_0) - 4\log(\Omega) - 4\gamma - 1 + 8\log(2)}{4096} \tag{A.179}$$

The honey diagram is also divergent for $\eta \to 0$. When all three diagrams are summed up, these divergences cancel each other.

The correction coefficient

Upon combining all three Feynman diagrams, we find for the correction coefficient $\mathcal{C}_\eta$

$$\mathcal{C}_\eta = \frac{89 - 20\pi}{40} \simeq 0.65\,. \tag{A.180}$$

This is a relatively large correction coefficient and hence, the impact of the Coulomb interaction on the shear viscosity of graphene in the collisionless regime is large.

Appendix B

B Anisotropic Dirac System (ADS)

B.1 Derivation of the Scaling behavior of the Conductivity and the Viscosity tensor

In this section, we derive the scaling behavior of the conductivity and the viscosity tensor for an anisotropic Dirac system (ADS). Thereby, we build on the foundation laid in Sec. 7.2.1 where we introduced how physical observables behave under a Wilson renormalization group (RG) analysis. The observable is related to their renormalized value by [116]

$$O(k_x, k_y, \omega, \alpha) = Z_O O(Z_x(l)k_x, bk_y, Z_\omega(l)\omega, \alpha(l))\,, \tag{B.1}$$

where Z_O is the scaling factor and the scaling factor Z_x and Z_ω are given by

$$Z_x = b^{1-\gamma_v} \qquad \text{and} \qquad Z_\omega = b^{\frac{1}{2}(1-\gamma_{k_0})} \tag{B.2}$$

with

$$\gamma_v = \frac{0.3625}{N} \qquad \text{and} \qquad \gamma_{k_0} = \frac{0.2364}{N}\,. \tag{B.3}$$

Now, let us see how the conductivity $\sigma_{\alpha\beta}$ and the viscosity $\eta_{\alpha\beta\gamma\delta}$ behave under an RG flow.

B.1.1 Derivation of the Scaling of the Conductivity

We want to determine the scaling dimension of the electrical conductivity $\sigma_{\alpha\alpha}$ with $\alpha \in x, y$. Therefore, we consider the optical conductivity $\sigma_{\alpha\alpha}$ in the collisionless regime. The same power laws are expected for the temperature dependent conductivity in the collision dominated regime. We use the Kubo-formula (2.8)

$$\sigma_{\alpha\alpha} = \lim_{\boldsymbol{q}\to 0} \frac{\omega}{q_\alpha^2} \chi_\rho \left(\boldsymbol{q}, \omega\right) \tag{B.4}$$

with the charge susceptibility χ_ρ. The charge susceptibility is proportional to the compressibility in the limit of zero momentum and frequency

$$\chi_\rho \left(\boldsymbol{q} \to 0, \omega = 0\right) = \kappa\,. \tag{B.5}$$

Hence, we can assume that the charge susceptibility has the same scaling dimension as the compressibility, i. e., $Z_{\chi_\rho} = Z_\kappa = Z_\omega/(bZ_x)$. This implies that we find for the conductivity the following scaling dimensions

$$\sigma_{xx} = \frac{Z_x}{b}\sigma_{xx}\left(Z_\omega T\right) \tag{B.6}$$

$$\sigma_{yy} = \frac{b}{Z_x}\sigma_{yy}\left(Z_\omega T\right) . \tag{B.7}$$

Inserting (B.2) into the above scaling equations, we find for the conductivity in the collision dominated regime the following temperature dependence

$$\sigma_{xx,yy}(T) \propto \left(\frac{T}{vk_0}\right)^{\pm(\frac{1}{2}+\phi_\sigma)} , \tag{B.8}$$

with $\phi_\sigma = \frac{1}{2}(\gamma_v + \gamma_{k_0}) = 0.299/N$. The Coulomb interaction enhances the metallic and insulating temperature dependence.

B.1.2 Derivation of the Scaling of the Shear viscosity

Now, let us turn to the scaling behavior of the viscosity where we expect the same power laws for the temperature dependent viscosity $\eta_{\alpha\beta\gamma\delta}(T)$ as for $\eta_{\alpha\beta\gamma\delta}(\omega)$. The shear viscosity $\eta_{\alpha\beta\gamma\delta}$ is defined by the Kubo-formula (3.36)

$$\eta_{\alpha\beta\gamma\delta} \propto \frac{1}{\omega}\,\mathrm{Im}\,\chi_{T_{\alpha\beta}T_{\gamma\delta}} , \tag{B.9}$$

where $\mathrm{Im}\,\chi_{T_{\alpha\beta}T_{\gamma\delta}}$ is the correlation function between the energy-stress tensors. However, in order to derive the scaling behavior of the viscosity tensor, we are going to use a different version of the Kubo formula for the viscosity. This is possible, as seen in Sec. 3.2, since the energy-stress tensor can also be expressed by the time derivative of the strain generator $\mathcal{J}_{\alpha\beta} = \mathcal{L}_{\alpha\beta} + \mathcal{S}_{\alpha\beta}$, where

$$\mathcal{L}_{\alpha\beta} = x_\alpha p_\beta + \frac{i}{2}\delta_{\alpha\beta} \quad \text{and} \quad \mathcal{S}_{\alpha\beta} = -\frac{1}{4}\epsilon_{\alpha\beta\gamma}\sigma_\gamma . \tag{B.10}$$

Using this fact, the Kubo formula, (3.37), for the viscosity is given by the following expression

$$\eta_{\alpha\beta\gamma\delta} \propto \ \omega \ \mathrm{Im}\Big\langle[\mathcal{J}_{\alpha\beta}, \mathcal{J}_{\gamma\delta}]\Big\rangle . \tag{B.11}$$

For further details of the derivation of this expression for the viscosity tensor, we refer to Sec. 3.3. Next, we assume that the operator $\mathcal{S}_{\alpha\beta}$ has the same dimensionality as the particle density, $Z_{\mathcal{S}_{\alpha\beta}} = Z_n$. Upon assuming for the operator $\mathcal{L}_{\alpha\beta}$ the same dimensionality as the particle density times the momentum and the corresponding spatial coordinate, which has the dimensionality of the inverse momentum, we find

$$Z_{\mathcal{L}_{xx}} = Z_n , \tag{B.12}$$

$$Z_{\mathcal{L}_{yy}} = Z_n , \tag{B.13}$$

$$Z_{\mathcal{L}_{xy}} = \frac{Z_x}{b}Z_n , \tag{B.14}$$

$$Z_{\mathcal{L}_{yx}} = \frac{b}{Z_x}Z_n , \tag{B.15}$$

$$Z_{\mathcal{S}_{ab}} = Z_n . \tag{B.16}$$

These scaling factors are used to determine the scaling factors of the two point correlation function of the strain generators. They are given by

$$
\begin{aligned}
Z_{\left\langle \mathcal{L}_{xx}\mathcal{L}_{xx}\right\rangle} &= Z_\kappa = \frac{Z_\omega}{bZ_x}\,, && \text{(B.17)}\\
Z_{\left\langle \mathcal{L}_{yy}\mathcal{L}_{yy}\right\rangle} &= Z_\kappa = \frac{Z_\omega}{bZ_x}\,, && \text{(B.18)}\\
Z_{\left\langle \mathcal{L}_{xx}\mathcal{L}_{yy}\right\rangle} &= Z_\kappa = \frac{Z_\omega}{bZ_x}\,, && \text{(B.19)}\\
Z_{\left\langle \mathcal{L}_{xy}\mathcal{L}_{xy}\right\rangle} &= Z_\kappa \frac{Z_x^2}{b^2} = \frac{Z_\omega}{b^3 Z_x}\,, && \text{(B.20)}\\
Z_{\left\langle \mathcal{L}_{yx}\mathcal{L}_{yx}\right\rangle} &= Z_\kappa \frac{b^2}{Z_x^2} = \frac{Z_\omega}{b Z_x^3}\,, && \text{(B.21)}\\
Z_{\left\langle \mathcal{L}_{xy}\mathcal{L}_{yx}\right\rangle} &= Z_\kappa = \frac{Z_\omega}{bZ_x}\,, && \text{(B.22)}\\
Z_{\left\langle \mathcal{S}_{\alpha\beta}\mathcal{S}_{\gamma\delta}\right\rangle} &= Z_\kappa = \frac{Z_\omega}{bZ_x}\,. && \text{(B.23)}
\end{aligned}
$$

We do not study the combination $\left\langle \mathcal{L}_{ab}\mathcal{S}_{cd}\right\rangle$, since these terms are always zero because of the momentum integration. Now, all scaling factors needed to determine the scaling behavior of the viscosity are known, and upon inserting them into the Kubo formula (3.37), we find the following scaling factors of the viscosity coefficients

$$
\begin{aligned}
Z_{\eta_1} &= Z_{\eta_{xyyx}} = Z_x^{-1} b^{-1}\,, && \text{(B.24)}\\
Z_{\eta_2} &= Z_{\eta_{xyxy}} = \begin{cases} Z_x b^{-3} \text{ for the } \left\langle \mathcal{L}_{xy}\mathcal{L}_{xy}\right\rangle \text{ -part} \\ Z_x^{-1} b^{-1} \text{ for the } \left\langle \mathcal{S}_{xy}\mathcal{S}_{xy}\right\rangle \text{ -part} \end{cases}, && \text{(B.25)}\\
Z_{\eta_3} &= Z_{\eta_{yxyx}} = \begin{cases} Z_x^{-3} b \text{ for the } \left\langle \mathcal{L}_{xy}\mathcal{L}_{xy}\right\rangle \text{ -part} \\ Z_x^{-1} b^{-1} \text{ for the } \left\langle \mathcal{S}_{xy}\mathcal{S}_{xy}\right\rangle \text{ -part} \end{cases}. && \text{(B.26)}
\end{aligned}
$$

The scaling implies for the temperature dependence of the viscosity coefficients

$$
\begin{aligned}
\eta_{xyxy}(T) &= b^{-\frac{5}{2}-\frac{1}{2}\gamma_{k_0}}\ \eta_{2,\mathcal{L}}(b^{1-\gamma_v}T) + b^{-\frac{3}{2}+\frac{1}{2}\gamma_{k_0}}\ \eta_{2,\mathcal{S}}(b^{1-\gamma_v}T)\,, && \text{(B.27)}\\
\eta_{yxyx}(T) &= b^{-\frac{1}{2}+\frac{3}{2}\gamma_{k_0}}\ \eta_{3,\mathcal{L}}(b^{1-\gamma_v}T) + b^{-\frac{3}{2}+\frac{1}{2}\gamma_{k_0}}\ \eta_{3,\mathcal{S}}(b^{1-\gamma_v}T)\,, && \text{(B.28)}\\
\eta_{abcd}(T) &= b^{-\frac{3}{2}+\frac{1}{2}\gamma_{k_0}}\ \eta_{1,\mathcal{L}+\mathcal{S}}(b^{1-\gamma_v}T)\,, && \text{(B.29)}
\end{aligned}
$$

where η_{abcd} are all possible combinations of $a, b, c, d \in \{x, y\}$ but the coefficients η_{xyyx} and η_{yxxy}. Also, we exclude the coefficients η_{aaab}, $\eta_{aaba}, \cdots$, since these are the Hall viscosity coefficients which are zero due to the momentum integration. The explicit temperature dependence for the coefficients are thus

$$\begin{aligned}
\eta_{abcd}(T) &= \left(\frac{T}{vk_0}\right)^{3/2-1/2\gamma_{k_0}+3/2\gamma_v} \frac{k_0^2}{\hbar}\,\mathcal{C}_1 = \left(\frac{T}{vk_0}\right)^{3/2+\frac{0.4255}{N}} \frac{k_0^2}{\hbar}\,\mathcal{C}_1\,, && \text{(B.30)}\\
\eta_{xyxy}(T) &= \left(\frac{T}{vk_0}\right)^{5/2+1/2\gamma_{k_0}+5/2\gamma_v} \frac{k_0^2}{\hbar}\,\mathcal{C}_{2,\mathcal{L}} + \left(\frac{T}{vk_0}\right)^{3/2+\frac{0.4255}{N}} \frac{k_0^2}{\hbar}\,\mathcal{C}_{2,\mathcal{S}}\\
&= \left(\frac{T}{vk_0}\right)^{5/2+\frac{1.02445}{N}} \frac{k_0^2}{\hbar}\,\mathcal{C}_{2,\mathcal{L}} + \left(\frac{T}{vk_0}\right)^{3/2+\frac{0.4255}{N}} \frac{k_0^2}{\hbar}\,\mathcal{C}_{2,\mathcal{S}}\,, && \text{(B.31)}\\
\eta_{yxyx}(T) &= \left(\frac{T}{vk_0}\right)^{1/2-3/2\gamma_{k_0}+1/2\gamma_v} \frac{k_0^2}{\hbar}\,\mathcal{C}_{3,\mathcal{L}} + \left(\frac{T}{vk_0}\right)^{3/2-1/2\gamma_{k_0}+3/2\gamma_v} \frac{k_0^2}{\hbar}\,\mathcal{C}_{3,\mathcal{S}}\\
&= \left(\frac{T}{vk_0}\right)^{1/2-\frac{0.17335}{N}} \frac{k_0^2}{\hbar}\,\mathcal{C}_{3} + \left(\frac{T}{vk_0}\right)^{3/2+\frac{0.4255}{N}} \frac{k_0^2}{\hbar}\,\mathcal{C}_{3,\mathcal{S}}\,. && \text{(B.32)}
\end{aligned}$$

The Coulomb interaction enhances exponent of the temperature and only for η_{yxxy} it becomes reduced.

B.2 The viscosity derived by the Boltzmann equation

In this section, we give the explicit form of the matrix $\mathcal{M}^{ee}_{nm,\,u_{\beta,\alpha}}$ and the vector $G_{m,\,u_{\beta,\alpha}}$ which were introduced in Sec. 9.2. This matrix and vector appear when we multiply the Boltzmann equation which depends on the modes $\phi^{(n)}_{\lambda\boldsymbol{k}}$ with the mode $\phi^{(m)}_{\lambda\boldsymbol{k}}$ and integrate and sum over the respective quantum numbers. The matrix $\mathcal{M}^{ee}_{nm,\,u_{\beta,\alpha}}$ describes the scattering processes due to Coulomb interaction, while the vector $\boldsymbol{G}_{u_{\beta,\alpha}}$ arises from the term in the Boltzmann equation which is proportional to the spatial derivative of the distribution function and thus proportional to the gradient of the drift velocity $u_{\beta,\alpha}$. The matrix is given by the expression

$$\begin{aligned}
\mathcal{M}^{ee}_{nm,\,u_{\beta,\alpha}} = {} & \frac{N}{T}\sum_{\lambda}\int\frac{d^2k}{(2\pi)^2}\sum_{q}\operatorname{Im}\Pi\left(\boldsymbol{q},\epsilon_{\lambda\boldsymbol{k}}-\epsilon_{\lambda\boldsymbol{k}-\boldsymbol{q}}\right)^{-1} N_{\lambda\lambda}(\boldsymbol{k},\boldsymbol{k}-\boldsymbol{q})n^{(0)}(\epsilon_{\lambda\boldsymbol{k}}-\epsilon_{\lambda\boldsymbol{k}-\boldsymbol{q}})\left[1-f^{(0)}_{\lambda\boldsymbol{k}}\right]f^{(0)}_{\lambda\boldsymbol{k}-\boldsymbol{q}}\\
& \times\left[\lambda\left(v^{\alpha}_{\lambda\boldsymbol{k}}k_{\beta}-\frac{1}{2}\delta_{\alpha\beta}\epsilon_{\lambda\boldsymbol{k}}\right)\phi^{(n)}_{\lambda\boldsymbol{k}}\phi^{(m)}_{\lambda\boldsymbol{k}}-\lambda\left(v^{\alpha}_{\lambda\boldsymbol{k}-\boldsymbol{q}}(\boldsymbol{k}-\boldsymbol{q})_{\beta}-\frac{1}{2}\delta_{\alpha\beta}\epsilon_{\lambda\boldsymbol{k}-\boldsymbol{q}}\right)\phi^{(n)}_{\lambda\boldsymbol{k}-\boldsymbol{q}}\phi^{(m)}_{\lambda\boldsymbol{k}}\right]\\
& +\frac{N}{T}\sum_{\lambda}\int\frac{d^2k}{(2\pi)^2}\sum_{q}\operatorname{Im}\Pi(\boldsymbol{q},\epsilon_{\lambda\boldsymbol{k}}+\epsilon_{\lambda\boldsymbol{k}-\boldsymbol{q}})^{-1}N_{\lambda-\lambda}(\boldsymbol{k},\boldsymbol{k}-\boldsymbol{q})n^{(0)}(\epsilon_{\lambda\boldsymbol{k}}+\epsilon_{\lambda\boldsymbol{k}-\boldsymbol{q}})\left[1-f^{(0)}_{\lambda\boldsymbol{k}}\right]f^{(0)}_{-\lambda\boldsymbol{k}-\boldsymbol{q}}\\
& \times\left[\lambda\left(v^{\alpha}_{\lambda\boldsymbol{k}}k_{\beta}-\frac{1}{2}\delta_{\alpha\beta}\epsilon_{\lambda\boldsymbol{k}}\right)\phi^{(n)}_{\lambda\boldsymbol{k}}\phi^{(m)}_{\lambda\boldsymbol{k}}-\lambda\left(v^{\alpha}_{\lambda\boldsymbol{k}-\boldsymbol{q}}(\boldsymbol{k}-\boldsymbol{q})_{\beta}-\frac{1}{2}\delta_{\alpha\beta}\epsilon_{\lambda\boldsymbol{k}-\boldsymbol{q}}\right)\phi^{(n)}_{-\lambda\boldsymbol{k}-\boldsymbol{q}}\phi^{(m)}_{\lambda\boldsymbol{k}}\right]\,,
\end{aligned} \tag{B.33}$$

and the vector $\boldsymbol{G}_{u_{\beta,\alpha}}$ by

$$G_{m,\,u_{\beta,\alpha}}=\frac{N}{T}\sum_{\lambda}\int\frac{d^2k}{(2\pi)^2}\phi^{(m)}_{\lambda\boldsymbol{k}}f^{(0)}_{\lambda\boldsymbol{k}}\left[1-f^{(0)}_{\lambda\boldsymbol{k}}\right]\left(v^{\alpha}_{\lambda\boldsymbol{k}}k_{\beta}-\frac{1}{2}\delta_{\alpha\beta}\epsilon_{\lambda\boldsymbol{k}}\right)\,. \tag{B.34}$$

The temperature dependence of these quantities determines at the end the temperature dependence of the conductivity, as we have shown in the corresponding Sec. 9.2.

Bibliography

[1] A. W. W. Ludwig, M. P. A. Fisher, R. Shankar, and G. Grinstein, “Integer quantum hall transition: An alternative approach and exact results,” *Phys. Rev. B*, vol. 50, pp. 7526–7552, Sep 1994.
(Cited on pages vi, 50, 87, 99, and 131.)

[2] N. Stander, B. Huard, and D. Goldhaber-Gordon, “Evidence for klein tunneling in graphene p–n junctions,” *Phys. Rev. Lett.*, vol. 102, p. 026807, Jan 2009.
(Cited on pages vi and 39.)

[3] Y. Zhang, Y.-W. Tan, H. L. Stormer, and P. Kim, “Experimental observation of the quantum hall effect and berry’s phase in graphene,” *Nature*, vol. 438, pp. 201–204, Nov. 2005.
(Cited on pages vi and 39.)

[4] X. Du, I. Skachko, F. Duerr, A. Luican, and E. Y. Andrei, “Fractional quantum hall effect and insulating phase of dirac electrons in graphene,” *Nature*, vol. 462, pp. 192–195, Nov. 2009.
(Cited on pages vii and 39.)

[5] K. I. Bolotin, F. Ghahari, M. D. Shulman, H. L. Stormer, and P. Kim, “Observation of the fractional quantum hall effect in graphene,” *Nature*, vol. 462, pp. 196–199, Nov. 2009.
(Cited on pages vii and 39.)

[6] D. C. Elias, R. V. Gorbachev, A. S. Mayorov, S. V. Morozov, A. A. Zhukov, P. Blake, L. A. Ponomarenko, I. V. Grigorieva, K. S. Novoselov, F. Guinea, and A. K. Geim, “Dirac cones reshaped by interaction effects in suspended graphene,” *Nat Phys*, vol. 7, pp. 701–704, Sept. 2011.
(Cited on pages vii, 33, 39, 43, and 44.)

[7] I. F. Herbut, V. Juričić, and O. Vafek, “Coulomb interaction, ripples, and the minimal conductivity of graphene,” *Phys. Rev. Lett.*, vol. 100, p. 046403, Jan 2008.
(Cited on pages vii, 45, 49, 51, 52, and 54.)

[8] E. G. Mishchenko, “Minimal conductivity in graphene: Interaction corrections and ultraviolet anomaly,” *EPL (Europhysics Letters)*, vol. 83, no. 1, p. 17005, 2008.
(Cited on pages 53, 54, 64, and 69.)

[9] D. E. Sheehy and J. Schmalian, “Optical transparency of graphene as determined by the fine-structure constant,” *Phys. Rev. B*, vol. 80, p. 193411, Nov 2009.
(Cited on pages 53 and 54.)

[10] V. Juričić, O. Vafek, and I. F. Herbut, “Conductivity of interacting massless dirac particles in graphene: Collisionless regime,” *Phys. Rev. B*, vol. 82, p. 235402, Dec 2010.
(Cited on pages 53, 54, and 64.)

[11] A. Golub and B. Horovitz, “Shot noise in graphene with long-range coulomb interaction and local fermi distribution,” *Phys. Rev. B*, vol. 81, p. 245424, Jun 2010.
(Not cited.)

[12] S. H. Abedinpour, G. Vignale, A. Principi, M. Polini, W.-K. Tse, and A. H. MacDonald, “Drude weight, plasmon dispersion, and ac conductivity in doped graphene sheets,” *Phys. Rev. B*, vol. 84, p. 045429, Jul 2011.
(Not cited.)

[13] I. Sodemann and M. M. Fogler, “Interaction corrections to the polarization function of graphene,” *Phys. Rev. B*, vol. 86, p. 115408, Sep 2012.
(Cited on pages 53 and 54.)

[14] B. Rosenstein, M. Lewkowicz, and T. Maniv, “Chiral anomaly and strength of the electron-electron interaction in graphene,” *Phys. Rev. Lett.*, vol. 110, p. 066602, Feb 2013.
(Cited on pages 53, 54, and 56.)

[15] S. Teber and A. V. Kotikov, “Interaction corrections to the minimal conductivity of graphene via dimensional regularization,” *EPL (Europhysics Letters)*, vol. 107, no. 5, p. 57001, 2014.
(Cited on pages 45, 53, 54, and 64.)

[16] J. M. Link, P. P. Orth, D. E. Sheehy, and J. Schmalian, “Universal collisionless transport of graphene,” *Phys. Rev. B*, vol. 93, p. 235447, Jun 2016.
(Cited on pages viii, 46, 53, 54, 64, 87, and 122.)

[17] D. L. Boyda, V. V. Braguta, M. I. Katsnelson, and M. V. Ulybyshev, “Many-body effects on graphene conductivity: Quantum monte carlo calculations,” *Phys. Rev. B*, vol. 94, p. 085421, Aug 2016.
(Cited on pages vii, 45, 49, 51, and 54.)

[18] P. K. Kovtun, D. T. Son, and A. O. Starinets, “Viscosity in strongly interacting quantum field theories from black hole physics,” *Phys. Rev. Lett.*, vol. 94, p. 111601, Mar 2005.
(Cited on pages vii, 17, 26, 27, 28, 74, 75, 84, 87, 107, 111, 119, and 121.)

[19] L. Fritz, J. Schmalian, M. Müller, and S. Sachdev, “Quantum critical transport in clean graphene,” *Phys. Rev. B*, vol. 78, p. 085416, Aug 2008.
(Cited on pages vii, 45, 46, 48, 71, 87, 99, and 122.)

[20] M. Müller, J. Schmalian, and L. Fritz, “Graphene: A nearly perfect fluid,” *Phys. Rev. Lett.*, vol. 103, p. 025301, Jul 2009.
(Cited on pages viii, 73, 74, 75, 84, 87, and 117.)

[21] U. Briskot, M. Schütt, I. V. Gornyi, M. Titov, B. N. Narozhny, and A. D. Mirlin, “Collision-dominated nonlinear hydrodynamics in graphene,” *Phys. Rev. B*, vol. 92, p. 115426, Sep 2015.
(Cited on pages viii, 39, 73, 75, 84, and 117.)

[22] R. R. Nair, P. Blake, A. N. Grigorenko, K. S. Novoselov, T. J. Booth, T. Stauber, N. M. R. Peres, and A. K. Geim, “Fine structure constant defines visual transparency of graphene,” *Science*, vol. 320, no. 5881, pp. 1308–1308, 2008.
(Cited on pages 3, 45, 49, 60, 64, and 122.)

[23] D. A. Siegel, C.-H. Park, C. Hwang, J. Deslippe, A. V. Fedorov, S. G. Louie, and A. Lanzara, "Many-body interactions in quasi-freestanding graphene," *Proceedings of the National Academy of Sciences*, vol. 108, no. 28, pp. 11365–11369, 2011.
(Cited on pages 3, 33, and 39.)

[24] K. Elk and W. Gasser, *Die Methode der Greenschen Funktionen in der Festkrperphysik.* Berlin: Akademie-Verl., 1979.
(Cited on pages 4, 5, and 79.)

[25] P. J. W. Moll, P. Kushwaha, N. Nandi, B. Schmidt, and A. P. Mackenzie, "Evidence for hydrodynamic electron flow in pdcoo2," *Science*, vol. 351, no. 6277, pp. 1061–1064, 2016.
(Cited on pages 6 and 7.)

[26] R. N. Gurzhi, "Hydrodynamic effects in solids at low temperature," *Soviet Physics Uspekhi*, vol. 11, no. 2, p. 255, 1968.
(Cited on page 6.)

[27] D. Vollhardt and P. Wölfle, *The superfluid phases of helium 3.* London [u.a.]: Taylor & Francis, 1990.
(Cited on page 7.)

[28] J. Crossno, J. K. Shi, K. Wang, X. Liu, A. Harzheim, A. Lucas, S. Sachdev, P. Kim, T. Taniguchi, K. Watanabe, T. A. Ohki, and K. C. Fong, "Observation of the dirac fluid and the breakdown of the wiedemann-franz law in graphene," *Science*, vol. 351, no. 6277, pp. 1058–1061, 2016.
(Cited on pages 7, 33, and 39.)

[29] R. Franz and G. Wiedemann, "Ueber die wärme-leitungsfähigkeit der metalle," *Annalen der Physik*, vol. 165, no. 8, pp. 497–531, 1853.
(Cited on page 7.)

[30] D. A. Bandurin, I. Torre, R. K. Kumar, M. Ben Shalom, A. Tomadin, A. Principi, G. H. Auton, E. Khestanova, K. S. Novoselov, I. V. Grigorieva, L. A. Ponomarenko, A. K. Geim, and M. Polini, "Negative local resistance caused by viscous electron backflow in graphene," *Science*, vol. 351, no. 6277, pp. 1055–1058, 2016.
(Cited on pages 7, 33, and 39.)

[31] L. Levitov and G. Falkovich, "Electron viscosity, current vortices and negative nonlocal resistance in graphene," *Nat Phys*, vol. 12, pp. 672–676, July 2016.
(Cited on pages 7, 73, 76, 77, and 122.)

[32] M. Titov, R. V. Gorbachev, B. N. Narozhny, T. Tudorovskiy, M. Schütt, P. M. Ostrovsky, I. V. Gornyi, A. D. Mirlin, M. I. Katsnelson, K. S. Novoselov, A. K. Geim, and L. A. Ponomarenko, "Giant magnetodrag in graphene at charge neutrality," *Phys. Rev. Lett.*, vol. 111, p. 166601, Oct 2013.
(Cited on pages 7, 33, and 39.)

[33] M. J. M. de Jong and L. W. Molenkamp, "Hydrodynamic electron flow in high-mobility wires," *Phys. Rev. B*, vol. 51, pp. 13389–13402, May 1995.
(Cited on page 7.)

[34] B. N. Narozhny, I. V. Gornyi, A. D. Mirlin, and J. Schmalian, “Hydrodynamic approach to electronic transport in graphene,” *ArXiv e-prints*, Apr. 2017.
(Cited on pages 7 and 39.)

[35] A. Kamenev, *Field theory of non-equilibrium systems.* Cambridge

u.a.

: Cambridge Univ. Press, 1. publ. ed., 2011. Hier auch später erschienene, unveränderte Nachdrucke.
(Cited on page 7.)

[36] P. Danielewicz, “Quantum theory of nonequilibrium processes, i,” *Annals of Physics*, vol. 152, no. 2, pp. 239 – 304, 1984.
(Cited on pages 7 and 97.)

[37] P. Drude, “Zur elektronentheorie der metalle,” *Annalen der Physik*, vol. 306, no. 3, pp. 566–613, 1900.
(Cited on page 11.)

[38] P. Drude, “Zur elektronentheorie der metalle; ii. teil. galvanomagnetische und thermomagnetische effecte,” *Annalen der Physik*, vol. 308, no. 11, pp. 369–402, 1900.
(Cited on page 11.)

[39] G. D. Mahan, *Many-particle physics.* Physics of solids and liquids, New York [u.a.]: Kluwer Academic, Plenum Publ., 3. ed. ed., 2000. Includes bibliographical references and index.
(Cited on pages 12 and 36.)

[40] Egor Kiselev, *Rigorous Bounds on Pomeranchuk l=1 Instabilities from Ward Identities.* PhD thesis, Karlsruhe Institute of Technology, 21 Jan. 2016.
(Cited on pages 14 and 24.)

[41] M. E. Peskin and D. V. Schroeder, *An introduction to quantum field theory.* The advanced book program, Boulder, Colo. [u.a.]: Westview Pr., [nachdr.] ed., 2006.
(Cited on pages 14, 24, and 66.)

[42] B. Bradlyn, M. Goldstein, and N. Read, “Kubo formulas for viscosity: Hall viscosity, ward identities, and the relation with conductivity,” *Phys. Rev. B*, vol. 86, p. 245309, Dec 2012.
(Cited on pages 17, 19, 22, and 121.)

[43] L. D. Landau and E. M. Lifšic, *Course of theoretical physics*, vol. 6: Fluid mechanics. Oxford [u.a.]: Butterworth-Heinemann, 2. ed., repr. with corr. ed., 1998. Aus d. Russ. bers.
(Cited on pages 17, 18, 98, 100, and 117.)

[44] E. M. Lifvcic and L. P. Pitaevskij, *Course of theoretical physics*, vol. 10: Physical kinetics of *Pergamon international library of science, technology, engineering and social studies.* Oxford [u.a.]: Pergamon Pr., 1. ed. ed., 1981.
(Cited on pages 18 and 78.)

[45] D. Forcella, J. Zaanen, D. Valentinis, and D. van der Marel, “Electromagnetic properties of viscous charged fluids,” *Phys. Rev. B*, vol. 90, p. 035143, Jul 2014.
(Cited on page 19.)

[46] Julia M. Link, Daniel E. Sheehy, Boris N. Narozhny, and Jörg Schmalian, “Viscosity in lattices with pseudospin.”.
(Cited on pages 19, 74, 98, and 124.)

[47] M. Mecklenburg and B. C. Regan, “Spin and the honeycomb lattice: Lessons from graphene,” *Phys. Rev. Lett.*, vol. 106, p. 116803, Mar 2011.
(Cited on pages 20, 21, and 78.)

[48] M. Mecklenburg, J. Woo, and B. C. Regan, “Tree-level electron-photon interactions in graphene,” *Phys. Rev. B*, vol. 81, p. 245401, Jun 2010.
(Cited on page 21.)

[49] P. C. Martin and J. Schwinger, “Theory of many-particle systems. i,” *Phys. Rev.*, vol. 115, pp. 1342–1373, Sep 1959.
(Cited on pages 21, 81, and 154.)

[50] C. Itzykson and J.-B. Zuber, *Quantum field theory.* International series in pure and applied physicsMcGraw-Hill international editions : physics series, New York: McGraw-Hill, 4. print. ed., 1988.
(Cited on page 22.)

[51] L. D. Landau and E. M. Lifsvic, *Course of theoretical physics*, vol. 2: The classical theory of fields of *Pergamon international library.* Oxford: Pergamon Press, 4., rev. english ed. ed., 1975.
(Cited on page 22.)

[52] A. Rebhan and D. Steineder, “Violation of the holographic viscosity bound in a strongly coupled anisotropic plasma,” *Phys. Rev. Lett.*, vol. 108, p. 021601, Jan 2012.
(Cited on pages 26, 28, 107, and 121.)

[53] M. Brigante, H. Liu, R. C. Myers, S. Shenker, and S. Yaida, “Viscosity bound violation in higher derivative gravity,” *Phys. Rev. D*, vol. 77, p. 126006, Jun 2008.
(Cited on page 28.)

[54] M. Brigante, H. Liu, R. C. Myers, S. Shenker, and S. Yaida, “Viscosity bound and causality violation,” *Phys. Rev. Lett.*, vol. 100, p. 191601, May 2008.
(Cited on page 28.)

[55] Y. Kats and P. Petrov, “Effect of curvature squared corrections in ads on the viscosity of the dual gauge theory,” *Journal of High Energy Physics*, vol. 2009, no. 01, p. 044, 2009.
(Cited on page 28.)

[56] A. Buchel, R. C. Myers, and A. Sinha, “Beyond eta/s = 1/4 pi,” *Journal of High Energy Physics*, vol. 2009, no. 03, p. 084, 2009.
(Cited on page 28.)

[57] S. CREMONINI, "The shear viscosity to entropy ratio: A status report," *Modern Physics Letters B*, vol. 25, no. 23, pp. 1867–1888, 2011.
(Cited on pages 26, 107, and 121.)

[58] T. Schäfer and D. Teaney, "Nearly perfect fluidity: from cold atomic gases to hot quark gluon plasmas," *Reports on Progress in Physics*, vol. 72, no. 12, p. 126001, 2009.
(Cited on pages 26, 28, and 121.)

[59] R. Samanta, R. Sharma, and S. P. Trivedi, "The Shear Viscosity in an Anisotropic Unitary Fermi Gas," *ArXiv e-prints*, July 2016.
(Cited on pages 26, 28, 107, and 121.)

[60] J. Maldacena, "The large-n limit of superconformal field theories and supergravity," *International Journal of Theoretical Physics*, vol. 38, pp. 1113–1133, Apr 1999.
(Cited on page 26.)

[61] S. Gubser, I. Klebanov, and A. Polyakov, "Gauge theory correlators from non-critical string theory," *Physics Letters B*, vol. 428, no. 1, pp. 105 – 114, 1998.
(Not cited.)

[62] E. Witten, "Anti De Sitter Space And Holography," *Advances in Theoretical and Mathematical Physics*, 1998.
(Not cited.)

[63] O. Aharony, S. S. Gubser, J. Maldacena, H. Ooguri, and Y. Oz, "Large n field theories, string theory and gravity," *Physics Reports*, vol. 323, no. 3-4, pp. 183 – 386, 2000.
(Cited on page 26.)

[64] G. Policastro, D. T. Son, and A. O. Starinets, "Shear viscosity of strongly coupled $n = 4$ supersymmetric yang-mills plasma," *Phys. Rev. Lett.*, vol. 87, p. 081601, Aug 2001.
(Cited on pages 26 and 27.)

[65] G. T. Horowitz and A. Strominger, "Black strings and p-branes," *Nuclear Physics B*, vol. 360, no. 1, pp. 197 – 209, 1991.
(Cited on page 27.)

[66] D. T. Son and A. O. Starinets, "Viscosity, black holes, and quantum field theory," *Annual Review of Nuclear and Particle Science*, vol. 57, no. 1, pp. 95–118, 2007.
(Cited on page 27.)

[67] S. Jain, R. Samanta, and S. P. Trivedi, "The shear viscosity in anisotropic phases," *Journal of High Energy Physics*, vol. 2015, p. 28, Oct 2015.
(Cited on pages 28 and 107.)

[68] C. Chin, R. Grimm, P. Julienne, and E. Tiesinga, "Feshbach resonances in ultracold gases," *Rev. Mod. Phys.*, vol. 82, pp. 1225–1286, Apr 2010.
(Cited on page 28.)

[69] A. H. Castro Neto, F. Guinea, N. M. R. Peres, K. S. Novoselov, and A. K. Geim, "The electronic properties of graphene," *Rev. Mod. Phys.*, vol. 81, pp. 109–162, Jan 2009.
(Cited on pages 33 and 37.)

[70] A. K. Geim and K. S. Novoselov, “The rise of graphene,” *Nat Mater*, vol. 6, pp. 183–191, Mar. 2007.
(Cited on page 33.)

[71] M. Vozmediano, M. Katsnelson, and F. Guinea, “Gauge fields in graphene,” *Physics Reports*, vol. 496, no. 4, pp. 109 – 148, 2010.
(Cited on page 33.)

[72] N. D. Mermin, “Crystalline order in two dimensions,” *Phys. Rev.*, vol. 176, pp. 250–254, Dec 1968.
(Cited on page 33.)

[73] P. R. Wallace, “The band theory of graphite,” *Phys. Rev.*, vol. 71, pp. 622–634, May 1947.
(Cited on page 33.)

[74] J. W. McClure, “Diamagnetism of graphite,” *Phys. Rev.*, vol. 104, pp. 666–671, Nov 1956.
(Cited on page 33.)

[75] J. C. Slonczewski and P. R. Weiss, “Band structure of graphite,” *Phys. Rev.*, vol. 109, pp. 272–279, Jan 1958.
(Cited on page 33.)

[76] K. S. Novoselov, A. K. Geim, S. V. Morozov, D. Jiang, Y. Zhang, S. V. Dubonos, I. V. Grigorieva, and A. A. Firsov, “Electric field effect in atomically thin carbon films,” *Science*, vol. 306, no. 5696, pp. 666–669, 2004.
(Cited on page 33.)

[77] R. Peierls, “Zur theorie des diamagnetismus von leitungselektronen,” *Zeitschrift für Physik*, vol. 80, pp. 763–791, Nov 1933.
(Cited on page 36.)

[78] V. P. GUSYNIN, S. G. SHARAPOV, and J. P. CARBOTTE, “Ac conductivity of graphene: From tight-binding model to 2 + 1-dimensional quantum electrodynamics,” *International Journal of Modern Physics B*, vol. 21, no. 27, pp. 4611–4658, 2007.
(Cited on pages 37 and 38.)

[79] J. L. Mañes, F. Guinea, and M. A. H. Vozmediano, “Existence and topological stability of fermi points in multilayered graphene,” *Phys. Rev. B*, vol. 75, p. 155424, Apr 2007.
(Cited on page 37.)

[80] K. S. Novoselov, A. K. Geim, S. V. Morozov, D. Jiang, M. I. Katsnelson, I. V. Grigorieva, S. V. Dubonos, and A. A. Firsov, “Two-dimensional gas of massless dirac fermions in graphene,” *Nature*, vol. 438, pp. 197–200, Nov. 2005.
(Cited on page 39.)

[81] B. N. Narozhny, I. V. Gornyi, M. Titov, M. Schütt, and A. D. Mirlin, “Hydrodynamics in graphene: Linear-response transport,” *Phys. Rev. B*, vol. 91, p. 035414, Jan 2015.
(Cited on pages 39, 76, and 126.)

[82] S. M. Sze and K. K. Ng, “Physics of semiconductor devices,” 2007. Dateiformat Volltext: PDF; This classic reference provides detailed information on the underlying physics and operational characteristics of all major bipolar, unipolar, special microwave, and optoelectronic devices. It integrates nearly 1,000 references to important original research papers and review articles, and includes more than 650 high-quality technical illustrations and 25 tables of material parameters for device analysis.
(Cited on page 39.)

[83] J. E. Drut and T. A. Lähde, “Lattice field theory simulations of graphene,” *Phys. Rev. B*, vol. 79, p. 165425, Apr 2009.
(Cited on page 40.)

[84] J. E. Drut and T. A. Lähde, “Critical exponents of the semimetal-insulator transition in graphene: A monte carlo study,” *Phys. Rev. B*, vol. 79, p. 241405, Jun 2009.
(Cited on page 40.)

[85] Antonio H. Castro Neto, “Viewpoint: Pauling’s dreams for graphene,” *Physics*, vol. 2, 20 Apr. 2009.
(Cited on page 40.)

[86] L. P. Kadanoff, “Scaling laws for Ising models near T(c),” *Physics*, vol. 2, pp. 263–272, 1966.
(Cited on page 40.)

[87] K. G. Wilson, “Renormalization group and critical phenomena. 2. Phase space cell analysis of critical behavior,” *Phys. Rev.*, vol. B4, pp. 3184–3205, 1971.
(Cited on page 40.)

[88] K. G. Wilson, “Renormalization group and critical phenomena. 1. Renormalization group and the Kadanoff scaling picture,” *Phys. Rev.*, vol. B4, pp. 3174–3183, 1971.
(Cited on page 40.)

[89] R. Shankar, “Renormalization-group approach to interacting fermions,” *Rev. Mod. Phys.*, vol. 66, pp. 129–192, Jan 1994.
(Cited on page 41.)

[90] J. González, F. Guinea, and M. A. H. Vozmediano, “Marginal-fermi-liquid behavior from two-dimensional coulomb interaction,” *Phys. Rev. B*, vol. 59, pp. R2474–R2477, Jan 1999.
(Cited on page 42.)

[91] S. Das Sarma, E. H. Hwang, and W.-K. Tse, “Many-body interaction effects in doped and undoped graphene: Fermi liquid versus non-fermi liquid,” *Phys. Rev. B*, vol. 75, p. 121406, Mar 2007.
(Cited on page 42.)

[92] D. T. Son, “Quantum critical point in graphene approached in the limit of infinitely strong coulomb interaction,” *Phys. Rev. B*, vol. 75, p. 235423, Jun 2007.
(Cited on page 42.)

[93] D. E. Sheehy and J. Schmalian, “Quantum critical scaling in graphene,” *Phys. Rev. Lett.*, vol. 99, p. 226803, Nov 2007.
(Cited on pages 42, 43, and 44.)

[94] J. Martin, N. Akerman, G. Ulbricht, T. Lohmann, J. H. Smet, K. von Klitzing, and A. Yacoby, "Observation of electron-hole puddles in graphene using a scanning single-electron transistor," *Nat Phys*, vol. 4, pp. 144–148, Feb. 2008.
(Cited on pages 43 and 44.)

[95] P. M. Ostrovsky, I. V. Gornyi, and A. D. Mirlin, "Electron transport in disordered graphene," *Phys. Rev. B*, vol. 74, p. 235443, Dec 2006.
(Cited on pages 45, 48, 71, 99, and 102.)

[96] D. N. Basov, R. D. Averitt, D. van der Marel, M. Dressel, and K. Haule, "Electrodynamics of correlated electron materials," *Rev. Mod. Phys.*, vol. 83, pp. 471–541, Jun 2011.
(Cited on page 50.)

[97] K. Damle and S. Sachdev, "Nonzero-temperature transport near quantum critical points," *Phys. Rev. B*, vol. 56, pp. 8714–8733, Oct 1997.
(Cited on page 50.)

[98] G. Gazzola, A. L. Cherchiglia, L. A. Cabral, M. C. Nemes, and M. Sampaio, "Conductivity of coulomb interacting massless dirac particles in graphene: Regularization-dependent parameters and symmetry constraints," *EPL (Europhysics Letters)*, vol. 104, no. 2, p. 27002, 2013.
(Cited on pages 53 and 54.)

[99] B. Rosenstein, H. C. Kao, and M. Lewkowicz, "Long-range electron-electron interactions in graphene make its electrodynamics nonlocal," *Phys. Rev. B*, vol. 90, p. 045137, Jul 2014.
(Cited on page 53.)

[100] J. Grönqvist, T. Stroucken, M. Lindberg, and S. Koch, "Wannier excitons signalling strong coulomb coupling in graphene," *The European Physical Journal B*, vol. 85, p. 395, Dec 2012.
(Cited on page 55.)

[101] T. Stauber, N. M. R. Peres, and A. K. Geim, "Optical conductivity of graphene in the visible region of the spectrum," *Phys. Rev. B*, vol. 78, p. 085432, Aug 2008.
(Cited on pages 60, 71, 123, and 129.)

[102] G. M. Bruun and H. Smith, "Shear viscosity and damping for a fermi gas in the unitarity limit," *Phys. Rev. A*, vol. 75, p. 043612, Apr 2007.
(Cited on page 74.)

[103] T. Schäfer, "Ratio of shear viscosity to entropy density for trapped fermions in the unitarity limit," *Phys. Rev. A*, vol. 76, p. 063618, Dec 2007.
(Cited on page 74.)

[104] G. Montambaux, F. Piéchon, J.-N. Fuchs, and M. O. Goerbig, "A universal hamiltonian for motion and merging of dirac points in a two-dimensional crystal," *Eur. Phys. J. B*, vol. 72, no. 4, pp. 509–520, 2009.
(Cited on pages 87 and 88.)

[105] G. Montambaux, F. Piéchon, J.-N. Fuchs, and M. O. Goerbig, "Merging of dirac points in a two-dimensional crystal," *Phys. Rev. B*, vol. 80, p. 153412, Oct 2009.
(Cited on page 88.)

[106] P. Dietl, F. Piéchon, and G. Montambaux, “New magnetic field dependence of landau levels in a graphenelike structure,” *Phys. Rev. Lett.*, vol. 100, p. 236405, Jun 2008.
(Not cited.)

[107] M. Ezawa, “Topological origin of quasi-flat edge band in phosphorene,” *New Journal of Physics*, vol. 16, no. 11, p. 115004, 2014.
(Not cited.)

[108] V. Pardo and W. E. Pickett, “Half-metallic semi-dirac-point generated by quantum confinement in tio$_2$/vo$_2$ nanostructures,” *Phys. Rev. Lett.*, vol. 102, p. 166803, Apr 2009.
(Cited on pages 87, 88, 90, and 91.)

[109] S. Banerjee, R. R. P. Singh, V. Pardo, and W. E. Pickett, “Tight-binding modeling and low-energy behavior of the semi-dirac point,” *Phys. Rev. Lett.*, vol. 103, p. 016402, Jul 2009.
(Cited on pages 87, 88, and 90.)

[110] P. Delplace and G. Montambaux, “Semi-dirac point in the hofstadter spectrum,” *Phys. Rev. B*, vol. 82, p. 035438, Jul 2010.
(Not cited.)

[111] S. Banerjee and W. E. Pickett, “Phenomenology of a semi-dirac semi-weyl semimetal,” *Phys. Rev. B*, vol. 86, p. 075124, Aug 2012.
(Cited on pages 87 and 88.)

[112] A. Kobayashi, S. Katayama, K. Noguchi, and Y. Suzumura, “Superconductivity in charge ordered organic conductor,” *Journal of the Physical Society of Japan*, vol. 73, no. 11, pp. 3135–3148, 2004.
(Cited on pages 87 and 88.)

[113] A. Kobayashi, S. Katayama, Y. Suzumura, and H. Fukuyama, “Massless fermions in organic conductor,” *Journal of the Physical Society of Japan*, vol. 76, no. 3, p. 034711, 2007.
(Cited on pages 88, 89, and 90.)

[114] A. Kobayashi, Y. Suzumura, F. Piéchon, and G. Montambaux, “Emergence of dirac electron pair in the charge-ordered state of the organic conductor α-(bedt-ttf)$_2$i$_3$,” *Phys. Rev. B*, vol. 84, p. 075450, Aug 2011.
(Cited on pages 88 and 90.)

[115] M. Hirata, K. Ishikawa, K. Miyagawa, M. Tamura, C. Berthier, D. Basko, A. Kobayashi, G. Matsuno, and K. Kanoda, “Observation of an anisotropic dirac cone reshaping and ferrimagnetic spin polarization in an organic conductor,” *Nature Communications*, vol. 7, pp. 12666–, 31 Aug. 2016.
(Cited on pages 87, 88, 89, and 90.)

[116] H. Isobe, B.-J. Yang, A. Chubukov, J. Schmalian, and N. Nagaosa, “Emergent Non-Fermi-Liquid at the Quantum Critical Point of a Topological Phase Transition in Two Dimensions,” *Phys. Rev. Lett.*, vol. 116, p. 076803, Feb 2016.
(Cited on pages 88, 94, 95, and 159.)

[117] D. T. Son, “Quantum critical point in graphene approached in the limit of infinitely strong coulomb interaction,” *Phys. Rev. B*, vol. 75, p. 235423, Jun 2007.
(Cited on page 94.)

[118] M. S. Foster and I. L. Aleiner, "Graphene via large n: A renormalization group study," *Phys. Rev. B*, vol. 77, p. 195413, May 2008.
(Cited on page 94.)

[119] J. M. Link, B. N. Narozhny, and J. Schmalian, "Out-of-bounds hydrodynamics in anisotropic Dirac fluids," *ArXiv e-prints*, Aug. 2017.
(Cited on pages 97, 99, 108, and 126.)

[120] M. Müller, L. Fritz, and S. Sachdev, "Quantum-critical relativistic magnetotransport in graphene," *Phys. Rev. B*, vol. 78, p. 115406, Sep 2008.
(Cited on pages 100 and 122.)

[121] J. Klier, I. V. Gornyi, and A. D. Mirlin, "Transversal magnetoresistance in weyl semimetals," *Phys. Rev. B*, vol. 92, p. 205113, Nov 2015.
(Cited on page 102.)

List of Figures

1 Structure of the Thesis ix

2.1 Conductivity 12

3.1 Definition of the viscosity. 18
3.2 The ratio η/s for different fluids 28

4.1 The honeycomb lattice of graphene. 34
4.2 The energy dispersion of graphene in the tight-binding description 35
4.3 The semi-metal to insulator transition in graphene. 40
4.4 The concept of the Wilson RG. 41
4.5 Quantum critical phase diagram of graphene. 43
4.6 Measurements of the renormalized velocity and inverse compressibility. 44

5.1 Temperature dependence of the dc conductivity of graphene in the hydrodynamic regime 48
5.2 Measurement of the transmissivity of light through a graphene sheet 49
5.3 Contributions to the current-current correlation function up to first order in α 51
5.4 The self-energy of graphene in the tight-binding description. 58
5.5 Conductivity of graphene in the tight-binding description and in the optical regime . . . 60
5.6 Correction coefficient of the conductivity in the tight-binding description 62
5.7 Optical transmission through graphene as a function of the wavelength λ_ω. 63

6.1 Graphene a nearly perfect fluid. 75
6.2 Viscous flow of graphene 77
6.3 Feynman diagrams for the viscosity in graphene 79
6.4 The frequency dependence of the shear viscosity of graphene in the collisionless regime . 83

7.1 The organic charge transfer salt α-(BEDT-TTF)$_2$I$_3$, its phase diagram and its energy dispersion. 89
7.2 The heterostructure TiO_2/VO_2 and its energy dispersion. 91
7.3 The energy-dispersion of an anisotropic Dirac system. 93
7.4 The renormalized energy-spectrum of ADS. 96

8.1 The conductivity tensor of ADS. 102

9.1 Violation of the lower bound 111
9.2 Momentum flow of the different viscosity coefficients 113
9.3 Shear frequency 118

10.1 Overview of the final results 127

A.1 Derivation of the transmission coefficient. 129
A.2 The honey diagram. 156

Acronyms

2D two dimensional

ADS anisotropic Dirac system

AdS/CFT anti-de Sitter/conformal field theory

DR dimensional regularization

RG renormalization group

SYM super-symmetric Yang-Mills

Danksagung

Es ist ein lobenswerter Brauch:
Wer was Gutes bekommt,
Der bedankt sich auch.

—Wilhelm Busch

Und genau so möchte ich es an dieser Stelle halten. Ich habe vier wundervolle Jahre am Institut für Theorie der Kondensierten Materie (TKM) verbracht.

Dabei gilt natürlich ganz besonderen Dank meinem Doktorvater Prof. Jörg Schmalian, der mir die Möglichkeit gab und gibt in seiner Arbeitsgruppe mich der Forschung von isotropen und anisotropen Dirac-Systemen zu widmen und mich als Forscherin weiterzuentwicklen. Ich habe viel von ihm gelernt, die vielen physikalischen Diskussionen genossen und es sehr wert geschätzt, dass ich jederzeit mit Fragen und Problemen zu ihm kommen konnte, was bei weitem nicht selbstverständlich ist.

Außerdem möchte ich mich bei PD. Boris N. Narozhny für unsere Zusammenarbeit und den vielen Diskussionen bedanken und besonders dass er sich bereit erklärt hat Korreferent dieser Arbeit zu sein.

Des weiteren danke ich Prof. Peter P. Orth herzlich, in dessen Nachwuchsgruppe ich meine Promotion begonnen habe und der mich im Ringen um die richtige Bestimmung des Korrekturkoeffizienten der optischen Leitfähigkeit begleitet und unterstüzt hat.

Further, I want to thank Prof. Daniel E. Sheehy for the great collaboration and especially for having given me the opportunity to visit him for two months at the Louisiana State University in Baton Rouge. I enjoyed this research stay a lot and learned plenty.

Zudem möchte ich mich auch sehr herzlich bei der Carl-Zeiss Stiftung für die zwei-einhalb jährige finanzielle Unterstützung während meiner Promotion bedanken.

In dieser Arbeit werden sich noch ein paar kleine Fehlerteufel vestecken. Dazu dass die Anzahl dieser Fehler kleiner wurde, haben Matthias Bard, Andrea Bergschneider, Mareike Hoyer, Nikolaos Kainaris, Nefta Kanilmaz, Janina Klier, Markus Klug, Jasmin Link und Tim Ludwig beigetragen, die diese Arbeit Korrektur gelesen haben.

Außerdem wäre diese Arbeit ohne den großartige Computer-Support von Andreas Poenicke nicht möglich gewesen und vielen Dank gilt Christian Seiler, der mir bei Programmier-Fragen mit Rat und Tat zur Seite stand.

Natürlich möchte ich mich auch für die großartige Atmosphäre am Institut bedanken, zu der ihr alle beitragt. Vielen Dank euch allen! Dabei möchte ich mich besonders bei Fabienne Flatter und Sonja König bedanken, die den Papierkram so weit wie möglich von uns fern halten und den vielen Skat-Spielern Stefan Beyl, Pia Gagel, Alexander Gawrilow, Patrik Hlobil, Mareike Hoyer, Nefta Kanilmaz, Lars Lauke, Martin Lietz, Tim Ludwig, Pablo Schad und Philip Wollfarth, die meine Pausen immer bereichert haben. Ich habe euch gerne mit Punkten und Süßigkeiten versorgt! Ich habe während der vier-einhalb Jahre in Karlsuhe und am TKM wircklich gute und wahre Freunde gefunden. Vielen Dank an Mathias Scheurer, Ulf Briskot, Philip Wollfahrt, Patrik Hlobil und Una Karahasanovic

für gemeinsame Kino-Besuche, Kochabende und Parties. Besonders möchte ich hier Tim Ludwig und Mareike Hoyer danken, mit denen ich viele gute Stunden mit Tanzen, Theater, Feiern und vielem mehr verbracht habe, die aber auch in schweren Zeiten für mich da waren. Das gleiche gilt natürlich auch für meine Heidelberger Freunde Andrea Bergschneider, Emer Brady und Caroline Heneka. Was wäre ich nur ohne euch alle?

Zum Schluss möchte ich meiner Familie und besonders meiner Mama Birgit, meinem Papa Hubert und meiner Schwester Jasmin danken. Ihr seid die beste Familie, die ich mir vorstellen kann! Vielen Dank dafür, dass ihr immer für mich da seid, mich bedingungslos unterstützt und ich mich immer auf euch verlassen kann!

Falls ich in dieser Danksagung jemanden vergessen habe, möchte ich mich entschuldigen und dem oder derjenigen trotzdem danken! ;)